HIGH RESOLUTION SPECTROSCOPIC STUDY OF ATMOSPHERIC TRACE GASES WITH CLIMATE RESEARCH APPLICATION

ROBAB HASHEMI
Bachelor of Science, University of Mohaghegh Ardebili, Ardebil, Iran
Master of Science, University of Guilan, Rasht, Iran

A Thesis
Submitted to the School of Graduate Studies
of the University of Lethbridge
in Partial Fulfillment of the
Requirements for the Degree

DOCTOR OF PHILOSOPHY

Department of Physics and Astronomy
University of Lethbridge
LETHBRIDGE, ALBERTA, CANADA

HIGH RESOLUTION SPECTROSCOPIC STUDY OF ATMOSPHERIC TRACE GASES WITH CLIMATE RESEARCH APPLICATION

ROBAB HASHEMI

Date of Defence: November 23, 2018

Dr. B. Billinghurst Supervisor	Senior Scientist	Ph.D.
Dr. C. Coburn Thesis Examination Committee Member	Associate Professor	Ph.D.
Dr. B. Seyed-Mahmoud Thesis Examination Committee Member	Associate Professor	Ph.D.
Dr. A. Akbary-Majdabadno Internal Examiner	Professor	Ph.D.
Dr. D. Wunch External Examiner	Assistant Professor	Ph.D.
Dr. S. Kienzle Chair of Thesis Examination	Professor	Ph.D.

Dedication

To Dr. Adriana Predoi-Cross

Abstract

The presented research was conducted to collect, and analyze the laboratory spectroscopic data together with theoretical calculations of the line shape parameters for the HITRAN (High Resolution Transmission) molecular spectroscopic database. The most updated version of this database is HITRAN2016 [1], and this research has contributed to this database by adding improved laboratory results to it. There is a demand for accurate retrieval of concentration values for carbon dioxide and methane (with accuracy better than 0.3 percent) which requires accurate line shape parameters. These line shape parameters are invaluable for modelling and interpreting spectra of Earth and planetary atmospheres.

It is necessary to measure advanced line shape parameters such as the speed-dependence (to explain the impact of the speed of colliding molecules) and line mixing (where there is interference of neighbouring transitions) for all the transitions in the databases. The molecules of interest for the present research are atmospheric trace gases; acetylene (C_2H_2), methane (CH_4) and carbon monoxide (CO).

For C_2H_2, the goal is to determine the fundamental Boltzmann constant based on a line shape analysis of $\nu_1 + \nu_3$ band recorded using a tunable diode laser. The next focus of the thesis is the examination of different line profiles on the absorption spectra of the CO-CO_2 in the $2-0$ band and CH_4-air in 2.3 μm. A standard multispectrum non-linear least squares fitting technique is used to measure line width and line shift coefficients, and their temperature dependencies considering the effect of speed dependence and line mixing.

Acknowledgments

First of all, I should thank my supervisor, Dr. Brant Billighurst for his support and giving me directions. I found him very kind, patient, and helpful. I could never ask for a better one. My special thanks to Dr. Adriana Predoi-Cross, my former supervisor, who I started my graduate journey with her and she supported me in every way during these years. I further appreciate Dr. Behnam Seyed-Mahmoud and Dr. Craig Coburn for their excellent guidance through this project as my committee members. I am also pleased to have Dr. Akbary, Dr. Wunch and Dr. Kienzle in my examination committee.

I am grateful to Dr. Vander Auwera from the University of Brussels, Belgium, who helped me during my internship. He is a very knowledgeable person and also he is a great supervisor. Additionally, I appreciate Dr. Iouli Gordon who supported me during my second internship in Harvard-Smithsonian Centre for Astrophysics, Cambridge, Boston, USA. Furthermore, I would like to thank Dr. Malathy Devi and Dr. Chris Benner, collaborators at the College of William and Mary, for their guidance and teaching me how to use the Labfit software.

I would also like to thank my best friend and my love, Hossein, for his everyday companionship and support. Thanks to my friends at the University of Lethbridge, Saeedeh, Behroo, Shaghayegh, Navvab, Ostad Nima, Hirad & Kourosh kuchulu, Seyed, Chad, Hoimonti and Mazid for being my best friends and supporting me.

I am also grateful for my funding sources; the Natural Sciences and Engineering Research Council of Canada, the NSERC CREATE AMETHYST, the Alberta Innovates Technology Futures (AITF), the SGS Dean's Scholarship, Department of Physics and Astronomy, and SGS University of Lethbridge.

Contents

List of Tables

List of Figures

Chapter 1

Introduction

1.1 Overview

There is a logarithmic trend between the increase of atmospheric temperature and growth of carbon-bearing gas emissions (CO_2 and CH_4), as reported by the Intergovernmental Panel on Climate Change (IPCC) [17, 18]. The temperature measurements carried out by a team at NASAs Goddard Institute for Space Studies showed that since 1880, there has been 0.8 degree Celsius increase in the Earth's average surface temperature [19]. The knowledge of the increasing rate of the surface temperature and its measurement accurately is crucial, since even half a degree increase of the average surface temperature, can cause more intense climate change such as rainstorms, rising the sea levels, longer heat waves, and degradation of tropical coral reefs [17]. Because of the non-negligible role of carbon-bearing gases in increasing the average surface temperature, the effort should be made in order to measure these gases as accurate as possible.

Over the recent decades, scientists have carried out numerous studies to monitor atmospheric concentrations of CO_2 and CH_4 to quantify the emission of these gases and understand their environmental impact using the remotely sensed spectroscopy techniques [20–25]. Remote sensing refers to the means of collecting data about a particular object without being in direct contact with it. This technique is based on recording energy transmitted, reflected, or emitted by the target and interpreting that data. In many remote sensing techniques, the data are gained through interaction between electromagnetic (EM) radiation and the object of interest. The absorption, emission, and scattering emerging from the interaction of EM radiation with the target produce changes in the spectral features of the original radiation. Examining the spectral signatures and to recognize the characteristics of the object is spectroscopy's role. Spectroscopy is hence the foundation of remote sensing [26].

In a broader view, remote sensing has applicability in various areas, including aeronomy, astrophysics, weather forecasting and climate research. A fair amount of information and perception about global change processes in the Earth's atmosphere originates from remote sensing observations (for local smaller scales, ground-based in-situ measurements are more accurate since air pollution affects mainly the lowest layers of the atmosphere). To collect data remotely, scientists use different platforms such as ground-based stations (e.g., the Network for the Detection of Stratospheric Changes (NDSC) [27], balloon-borne measurements (the IASIballoon experiment [28]), and satellite-based observations (the Atmospheric Chemistry Experiment (ACE) [23]. Developing space-born satellites was a revolution in remote sensing measurements as most of the information about the planetary atmosphere is obtained using satellites. Typically, satellites observe the light reflected by Earth's atmosphere. By analyzing the strengths of the collected spectra in different wavelengths, the atmospheric concentrations of those gases can be estimated.

In practice interpreting satellite observed spectra is very complicated due to having varying temperature and pressures in different altitudes. Also, the satellite observes all the present gases by single measurement. Thats why we need to measure the spectroscopic line parameters in controlled laboratory measurements.

For most of the atmospheric spectroscopic studies, a simple Voigt line shape model was used to analyze the experimental data [29] (this profile will be described later in this chapter). The Voigt line shape, however, ignores physical effects like velocity changing collisions [30], speed dependence of spectroscopic parameters [31–33] and line mixing impact of overlapping spectral lines [34]. Development of highly accurate spectroscopic experimental techniques allows studying molecules with weak transition [35]. Hence, for analyzing the spectroscopic measurements accurately, more robust theoretical line shape models are required to include all the known physical effects [36].

This research is conducted to measure spectroscopic line-by-line parameters for some of the missing transitions in the reference databases as well as updating some of the line-shape parameters that have been previously measured with older, and less accurate methods. I used highly accurate experimental techniques as well as using better theoretical models for spectral modelling. Having access to such accurate spectroscopic data is necessary when studying the trace gases in Earth's atmosphere, quantitatively evaluating climate models, and studying the extra exoplanet atmospheres. Trace gases (which are listed in Section 1.2) have lower quantity on the order of part per million or part per billion, but they are very active in chemical reactions and dynamic of planetary atmosphere. This study intends to extend the standard spectroscopic parameters databases with more accurate spectroscopic parameters for trace gases and to add further absorption parameters to the database using advanced line profiles.

The question is with how much accuracy the spectroscopic parameters can be obtained, and the answer lies in (i) experimental tools and techniques of the measurements, and (ii) the data analysis and modelling methods where more realistic physical effects are considered [37]. The objective of the present study is to improve the uncertainty of already existing parameters by at least one order of magnitude for most of the parameters of the target molecules to achieve better accuracy in the concentration retrievals. Therefore, in addition to improve the existing coefficients (line positions, intensities, line broadening and pressure-induced line shifts), some extra parameters like the temperature dependencies of coefficients required. For this purpose, high-resolution laboratory spectra were used for sample temperature and pressure conditions close to real situations in the measurement environment.

In this chapter, first, the importance of remote sensing measurements and spectral line shape study in atmospheric and astrophysics research will be discussed, and the research

Table 1.1: The wavelength of different portion of EM radiation

γR	XR	UV	V	IR	Ref_{IR}	Ther_{IR}	MW	RW
<0.03	0.03-30	0.03-0.4	0.4-0.7	0.7-100	0.7-3	3-14	0.1-100	>100
nm	nm	μm	μm	μm	μm	μm	cm	cm

objectives will be listed. Then, a few applications of satellite remote sensing data are presented. After explaining popular line shape functions and line parameters which are used in standard spectroscopic databases, the HITRAN database [1] together with the current stage of its development will be introduced. The main application of spectroscopic line shape studies will be discussed, and in the end, the outline of this dissertation will be presented.

1.2 Motivations for remote sensing of the atmosphere

Molecular spectroscopy expands our knowledge about the interaction between EM radiation and molecules. The amount of energy that can be absorbed by a molecule is quantized and is related to the structure of a molecule. When the radiation passes through a sample, it can be absorbed by the sample over a range of frequencies. By viewing the spectrum, the type of the components in the sample together with their quantity can be determined [2].

The visible part of EM radiation is only a small portion of the whole range of the radiation (0.0035%). EM radiation includes radio waves (RW), microwaves (MW), infrared (IR, including reflected and thermal IR), visible (V), ultraviolet (UV), X-rays (XR), and gamma rays (γR) as presented in Table 1.1.

Some molecules absorb light in the infrared region and absorption of this energy by molecules results in the rotation or vibration of the molecule. This will be expanded upon in Chapter 2.

The components of the Earth's atmosphere are mainly nitrogen (78.08 %) and oxygen (20.95 %); argon is about 0.93 % of the air. The other gases such as water vapour, ozone, methane, nitrous oxide, and carbon dioxide are called trace-gases, which have lower volume mixing ratios (VMR). For example, the VMRs of carbon monoxide (CO), nitrous oxide (N_2O), methane (CH_4) and carbon dioxide (CO_2) are 0.1 ppm, 0.3 ppm, 1.8 ppm, and 400 ppm, respectively [38].

The amount of the trace-gases varies in the atmosphere due to various factors such as altitude, latitude, time (like seasonal changes) and geographical area, where it can be the ocean, forest, lands or urban areas. For example, CO is more abundant in the northern hemisphere than the southern hemisphere because of the number of population living in the northern hemisphere and creating higher emissions due to burning of fossil fuel. The other reason is due to the short lifetime of CO (two months), it cannot ultimately make the transfer to the southern hemisphere [39]. Among the trace gases, water vapour (H_2O) has the highest VMR which varies in the atmosphere (between 0.1 to 4 %).

These trace-gases mentioned above are called greenhouse gases since they can absorb and emit infrared radiation. When the sunlight reaches the Earth's surface, a portion of it is absorbed by the surface of Earth and atmosphere (about 23% is absorbed by the atmosphere and about 48% by the surface [40]) and emitted as infrared radiation into the atmosphere. Because of the structure of greenhouse gases, this infrared radiation is absorbed and trapped in the atmosphere warming it [26] and causing the increase in the global average surface temperature. The main component of Earth's atmosphere, N_2, has stable amount because it is not infrared active molecules.

The ability of greenhouse gas to absorb radiation is called "global warming potential (GWP)," which is the ratio of the trapped heat by that specific greenhouse gas compared to the trapped heat by the equal amount of CO_2 in a specified period. As an example, in the time interval of 100 years, the global warming potential for methane is 25, indicating that CH_4 is 25 times more potent than CO_2 [41]. The global warming potential is time dependent because of different life-time of the atmospheric molecules. In shorter time intervals, the GWP of the molecules with shorter life-time will be higher, meaning that they may have greater impact in the short time span.

1.2.1 Justification of the research

Infrared spectroscopic study of trace gases namely acetylene (C_2H_2), carbon monoxide (CO), and methane (CH_4) is the foundation of this thesis.

Laser spectroscopy can be used as an optical method for measuring the Boltzmann constant (k_B). Since k_B is well-known the result of this type of measurements can be used to provide the most probable sources of uncertainty by performing detailed error analysis. The $\nu_1 + \nu_3$ band of C_2H_2 is a strong absorption band, and therefore, it is appropriate for measurements of fundamental physical constants such as k_B.

CO is an atmospheric pollutant which does not show greenhouse gas effect, but, it takes part in chemical reactions leading to greenhouse gas effect. For instance, the oxidation of CO leads to the formation of ozone and CO_2. In presence of the OH radical, CO, directly affect the oxidation capacity of the atmosphere [42]. CO is emitted as a result of biomass burning or combustion of fossil fuels [43]. Another cause of CO formation is the reaction of volatile organic compounds with the OH radical [38].

Furthermore, CO is present in the atmosphere of Venus [44], where CO_2 has high abundance [45] atmosphere. Hence, studying the mixture of CO and CO_2 will support the research on the carbon cycle and greenhouse gas effect. The relative uncertainty of the previously reported parameters for CO-CO_2 [10] was not adequate to be used for obtaining CO concentration, and the effect of the speed dependence and line mixing parameters were not included in modelling the spectra. For the temperature dependence of CO in HITRAN, all the values were fixed to 0.6 for all the lines (the average value measured and reported in Ref: [10]); however, the study by Chu et al. [46], as an example, showed that using a single value is an approximation and is not a nearly accurate value to be used in the atmospheric retrievals.

Methane (CH_4) is produced naturally (e.g., wetlands, biomass burning) and anthropogenically (e.g., fossil fuel mining, rice cultivation, livestocks). Being an infrared-active molecule, this gas absorbs and emits infrared EM radiation. The main factors, such as concentration, lifetime, and the infrared absorptivity play a role in the greenhouse gases' global warming potential. Methane is an abundant molecule that is also found in the atmosphere of other planets; it is present on Titan's atmosphere [47], as well as atmospheres of Mars [48] and Jupiter [49, 50].

The methane band system in the 2.3 microns spectral region is of interest for measurements of the Earth's atmospheric methane profiles because it is covered by several satellites and ground-based spectroscopic remote sensing instruments [24, 51], simultaneously, observing methane and few other greenhouse gases.

1.2.2 Example applications of satellite-based remote sensing

Three examples of space-based measurements are presented here. These missions are listed because of their application in retrieving concentration of greenhouse gases such as CH_4, CO_2, and CO.

The first example is GOSAT satellite; there are several surface concentration measurements of CH_4 collected by different networks such as NOAA ESRL (National Oceanic and Atmospheric Administration Earth System Research Laboratory) [52]. These data present useful information on local emissions [53]; yet, for many significant emission areas (e.g., the tropics), there are not enough measurements available.

GOSAT, the Greenhouse Gases Observing Satellite [54], developed by the Japanese Ministry of the Environment (MOE), Japan Aerospace Exploration Agency (JAXA), and National Institute for Environmental Studies (NIES) is a space mission to observe the concentrations of CH_4 and CO_2. The satellite was launched in 2009 and is still collecting data [24]. GOSAT includes sensors in the near infrared and thermal region, detecting solar light reflected from the surface of Earth together with the emitted thermal radiance. The GOSAT observations make it possible to analyze the CH_4 and CO_2 distribution, and those data can be used to monitor the seasonal changes in the sources and sinks globally and locally. This spacecraft's findings enable understanding of global warming and its causes. Besides, this team has developed GOSAT-2 launched on October 2018 to continue the measurements of greenhouse gases and finding the significance of climate change on the carbon cycle [55]. Nikitin et al. [56] have performed laboratory studies in the 5550-6240 cm^{-1} range of methane using the Fourier transform spectrometer to provide a line list (including 12150 transitions) for obtaining the column concentration of CH_4.

The second mission is OCO-2 satellite, which was launched on June 2014. Typical carbon pools such as oceans, plants and soils on land absorb carbon (carbon sinks). The question that Orbiting Carbon Observatory-2 (OCO-2) data was designed to answer is related to the location and distribution of these carbon sinks, therefore, modelling the carbon concentration is necessary. NASAs current mission for OCO-2 [57, 58], produces original data about the processes governing the transfer of carbon among the carbon sinks. By studying and analyzing OCO-2 measurements, scientists can explain the altering carbon content stored by vegetation, and they can also describe the effect of ocean temperature on the absorption of carbon dioxide.

To obtain information about the amount of CO_2 measured at a given location, the OCO-2 instrument measures the sunlight intensity reflected off the Earth's surface. The gases present in the Earth's atmosphere leave a fingerprint that can be detected by OCO-2 spectrometers. The OCO-2 instrument assembles the measurements in two separate regions of the CO_2 (1.61 and 2.06 microns) and O_2 spectra as a reference (0.765 microns) [57]. OCO-2 mission flies with a 16-day repeat cycle. The OCO-2 data are processed initially at the Jet Propulsion Lab and then distributed and stored at the Goddard Earth Science Data and Information Services Center. All OCO-2 data products are free for users [59].

Laboratory measurements can produce precise spectroscopic line parameters of CO_2 and O_2 to explain the taken atmospheric spectral measurements. Benner et al 2016 [60], did an example laboratory study to examine the CO_2 spectra in the 4700 to 4930 wavenumber region using a Fourier transform spectrometer to calculate the line parameters of CO_2 to be used in generating the absorption coefficients for the OCO-2 retrieval algorithm. By simultaneously fitting a large number of experimental spectra, they have tried to reduce the random errors in the analysis.

To monitor carbon sources and sinks in the Earth's atmosphere, NASA plans to prepare another space-born technology. The OCO-3 mission is programmed for launching into space in 2019 to gather daily information on carbon dioxide as a complementary tool for OCO-2 data.

The last example is SOIR mission to cover the planetary research interest of the thesis. Remote measurement devices can determine the compositions of the outer planets. SOIR (Solar Occultation in the InfraRed) instrument on board the ESA Venus Express spacecraft [61], as an example, probes the atmosphere of Venus, where the dominant element is carbon [44, 62] within the IR region. As one of the nearby planets to Earth, Venus is considered as a good destination for space exploration since the greenhouse effect is discovered first for Venus. The recording of SOIR spectra in 2.3 μm region of the CO and CO_2 spectra is within a suitable range to measure the concentration of CO. SOIR uses solar occultation techniques and a spectrometer with range 2.3 to 4.2 μm.

SOIR takes occultation measurements at sunrise or sunset. The way the SOIR occultation works to measure a transmitted spectrum is that, approaching the sunset, the light path proceeds deep into the atmosphere, and the absorption pattern can be observed [63]. The recorded spectrum is calibrated to include several corrections such as nonlinearity of the detector and spectral calibration. Then by taking the ratio of the spectrum of the atmosphere of Venus and the non-attenuated solar spectrum (observed above the atmosphere), the transmittance can be achieved. For analyzing the spectra obtained by SOIR, synthetic spectra are calculated, and then line-by-line simulations are performed based on Venus's atmospheric conditions to retrieve concentrations of gaseous species and temperature profiles. The example laboratory spectroscopic line parameters for CO in 2.3 μm region can be found in Ref. [64, 65].

These examples are only three of many missions that have been launched for measurement of trace gases, and there are many missions under development and investigation stage.

1.3 Absorption spectroscopy

By measuring the spectra of molecules and registering the frequency of the absorbed or emitted radiation, the fingerprint of the molecule can be obtained to allow for characterizing the nature of the molecular system. Using different line shape functions, we can describe the spectral features of a system [2, 8].

Beer-Lambert's law is used to obtain the transmitted intensity after interaction of light with target molecules (based on the length of the cell and amount of the sample molecules),

$$I(\tilde{\nu}) = I_0(\tilde{\nu})exp[-\alpha(\tilde{\nu})l] = I_0(\tilde{\nu})exp[-\sigma(\tilde{\nu})Nl]. \tag{1.1}$$

In the above equation, $I_0(\tilde{\nu})$ and $I(\tilde{\nu})$ are the spectral irradiance (in Wm^{-2}) of incident light before and after interaction with the sample of interest and $\tilde{\nu}$ is the wavenumber (in cm^{-1}). Also, $\alpha(\tilde{\nu})$ (in cm^{-1}) and $\sigma(\tilde{\nu})$ (in cm^{2}molecule^{-1}) are the wavenumber-dependent absorption coefficient and absorption cross section of the sample of particle density N (in molecule cm^{-3}). At standard pressure ($P = 1$ atm) and temperature ($T = 273.15$ K), N (also called Loschmidt number) is $n_L = 2.6867661(47) \times 10^{19}$ molecule cm^{-3} atm^{-1}. Variable l represents the absorption path length with units of cm.

Considering molecules in thermal equilibrium, we can use the Boltzmann distribution to obtain the particle density (population). For a given level j with energy of E_j (considering two energy levels j and k for molecules with energies E_j and E_k),

$$N_j = [N/Q(T)]g_j exp[-hcE_j/k_BT]. \tag{1.2}$$

The degeneracy of the level is shown by g_j, $Q(T)$ presents the total internal partition function, and the total particle density is presented by N. We can write $N = n_L(T_0/T)P$, with n_L introducing the Loschmidt number, $T_0 = 273.15$ K, T is the temperature, and P is the pressure. In the gas phase, molecules interact with radiation of spectral energy density $\rho_{\tilde{\nu}}(\tilde{\nu})$; Planck's radiation law describes the radiant energy density in a wavenumber interval $d\tilde{\nu}$ around wavenumber $\tilde{\nu}$,

$$\rho_{\tilde{\nu}}(\tilde{\nu}) = \frac{8\pi hc\tilde{\nu}^3}{exp[hc\tilde{\nu}/k_BT] - 1}. \tag{1.3}$$

In the above equation, k_B shows the Boltzmann constant. Molecules in level k can decay to the lower level j spontaneously, with emission of a photon of energy $hc\tilde{\nu}_{jk} = E_k - E_j$. The variation per second of the population of level k in this process is shown by the following relationship,

$$dN_k/dt = -A_{kj}N_k. \tag{1.4}$$

Parameter A_{kj} (in s^{-1}) is called the Einstein coefficient (subscripts k and j on A mean the upper and lower levels). Besides spontaneous emission, absorption and stimulated emission occur. In the absorption process the change in time for the population of the two levels j and k is

$$dN_j/dt = -B_{jk}N_j\rho_{\tilde{\nu}}(\tilde{\nu}_{jk}). \tag{1.5}$$

Here, B_{jk} presents the Einstein coefficient for absorption with unit of sg^{-1}. Similarly, for stimulated emission we can write

$$dN_k/dt = -B_{kj}N_k\rho_{\tilde{\nu}}(\tilde{\nu}_{jk}). \tag{1.6}$$

Again, B_{kj} is the Einstein coefficients of stimulated emission (in $\mathrm{s\,g}^{-1}$). The coefficients $B_{jk}\rho_{\tilde{\nu}}(\tilde{\nu}_{jk})$ and $B_{kj}\rho_{\tilde{\nu}}(\tilde{\nu}_{jk})$ are the transition probabilities in unit of time. If the system is at thermodynamical equilibrium, we can obtain the relations among the three Einstein coefficients.

1.4 Well-known line shape profiles

By assuming molecules with two levels j and k of energies E_j and E_k, where $E_j < E_k$, we can introduce $\alpha_{jk}(\tilde{\nu})$ as the absorption coefficient corresponding to the transition $E_j \rightarrow E_k$ and $\alpha_{jk} = \int \alpha_{jk}(\tilde{\nu}) d\tilde{\nu}$ as the integrated absorption coefficient. We can write

$$\alpha(\tilde{\nu}) = I_{jk} g(\tilde{\nu} - \tilde{\nu}_{jk}). \tag{1.7}$$

The area subtended by that profile is I_{jk} and $g(\tilde{\nu} - \tilde{\nu}_{jk})$ is the normalized line profile function around the central line position $\tilde{\nu}_{jk}$ such that

$$hc\tilde{\nu}_{jk} = E_k - E_j. \tag{1.8}$$

Here h is Planck's constant and c is the speed of light in vacuum. Figure 1.1, presents some of parameters for the line profiles.

When the molecules are in the gas phase, they have motion, and they collide with each other. These collisions affect the way they interact with light and change their internal degrees of freedom. In gases at low pressures, the effects of collisions on the internal degrees of freedom and the translational motion of the molecules can be neglected. In such an approximation, the shape of spectral lines depends upon the velocity distribution of the molecules defined by a Gauss function. Then the main contributor to the shape of absorption lines arises due to the Doppler shift of the apparent wavenumber of the radiation resulting from the thermal motion of the molecules: it is increased for molecules moving towards the source and decreased moving away (this type of Doppler shift is called longitudinal Doppler effect). [1] Thus, if the radiation beam travels along the z-direction, a molecule having velocity V will absorb a photon on the transition $E_j \rightarrow E_k$ if its wavenumber is equal

---

[1] In case of perpendicular motion where there is transverse Doppler effect, nearing object will seem blue-shifted (shorter), and the receding one will be red-shifted (longer). In case having moving object and light source at the same time, there will not be any changes in the frequency.

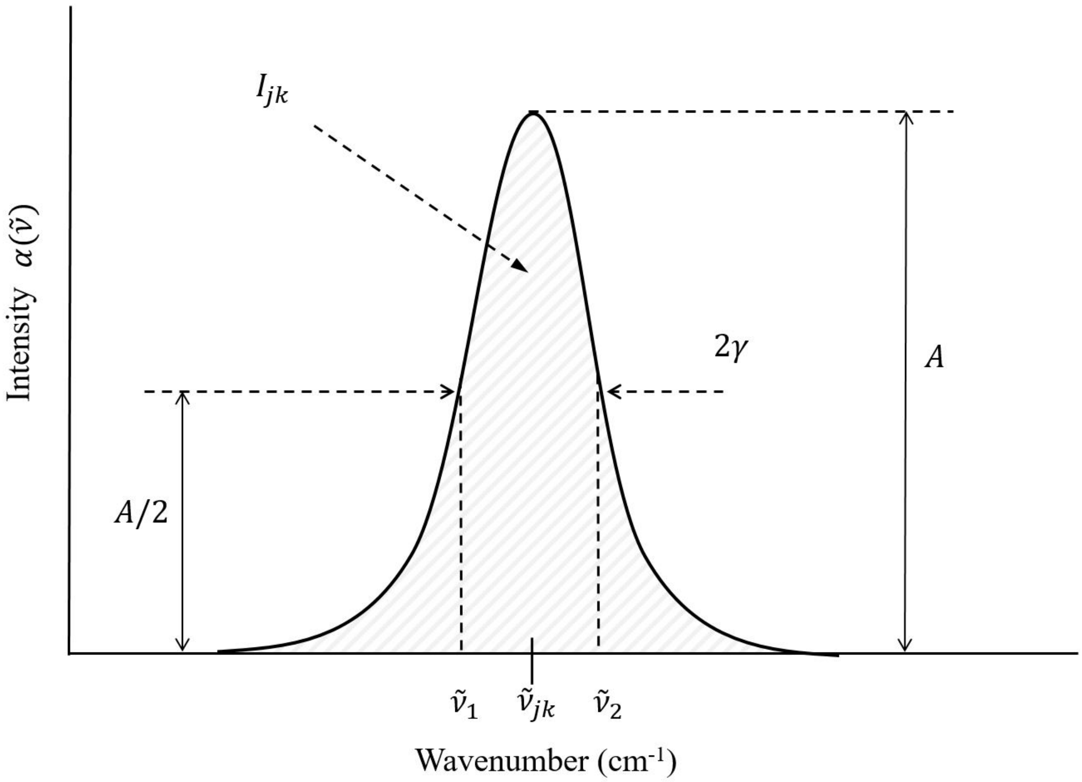

Figure 1.1: The parameters needed for characterizing line shape functions. Line position $\tilde{\nu}_{jk}$, intensity I_{jk}, the amplitude A, and the half width at half maximum or broadening $\gamma = 0.5|\tilde{\nu}_1 - \tilde{\nu}_2|$ are presented. This figure is reproduced based on information provided in Ref. [2].

to

$$\tilde{\nu} = \tilde{\nu}_{jk}[1 + v/c]. \tag{1.9}$$

The velocity components v of the molecules obey a one-dimension Maxwell-Boltzmann distribution rule at thermodynamical equilibrium. This velocity distribution causes an inhomogenous broadening of the line and leads to a Gaussian line profile (where pressure is less than 0.001 atmosphere).

$$g_D(\tilde{\nu} - \tilde{\nu}_{jk}) = \sqrt{\frac{ln2}{\pi}} \frac{1}{\gamma_D} exp{-}ln2(\frac{\tilde{\nu} - \tilde{\nu}_{jk}}{\gamma_D})^2. \tag{1.10}$$

The Doppler width γ_D is given by

$$\gamma_D = \sqrt{ln2}(v_P/c)\tilde{\nu}_{jk} = 3.581 \times 10^{-7}\tilde{\nu}_{jk}\sqrt{T/M}, \tag{1.11}$$

where $v_p = \sqrt{2RT/M}$ is the most probable speed as defined in the Maxwell-Boltzmann distribution, γ_D is expressed in cm^{-1}, T in Kelvin and M in $g.mol^{-1}$.

For the higher pressures, taking the collisions into account, various approximations can be made for describing the shape of spectral lines. The binary impacts approach is one of the famous models that ignores the translational effects of collisions and neglects velocity-changes due to collisions. In this case, Doppler broadening is uncorrelated with collisional broadening.

Spontaneous emission leads to an exponential decay. For a given level j, population of the exponential delay is given by $\tau_j = \Sigma_n(1/A_{in})$, where A_{in} is the Einstein coefficient. Implementing the time-dependent Fourier transformation for the transition $E_j \rightarrow E_k$, leads to the Lorentz line profile [66] with $\gamma = (\frac{1}{4\pi c})(1/\tau_j + 1/\tau_k)$ as the natural width of the line.

$$g_L(\tilde{\nu} - \tilde{\nu}_{jk}) = \frac{1}{\pi} \frac{\gamma}{(\tilde{\nu} - \tilde{\nu}_{jk})^2 + \gamma^2}. \tag{1.12}$$

Usually, the natural broadening is smaller than pressure broadening, then we can write

$$g_L(\tilde{\nu}-\tilde{\nu}_{jk}) = \frac{1}{\pi}\frac{\gamma}{(\tilde{\nu}-\tilde{\nu}_{jk}-\Delta\tilde{\nu})^2+\gamma^2}, \tag{1.13}$$

where $\Delta\tilde{\nu}$ represents the pressure shift of the line. At pressure P, if we can express the pressure shift as $\Delta\tilde{\nu} = \delta_0 P$ for a pure sample, where δ_0 is the self-induced pressure shift parameter with the unit of $\mathrm{cm}^{-1}\mathrm{atm}^{-1}$.

When both Doppler and collisional broadening must be considered (for example, in gases at moderate pressure), the resulting profile is obtained through convolution of the Gaussian and Lorentzian functions to yield the Voigt profile (the equations will be presented in Chapter 2) [67]. The Voigt Profile has its place in the spectroscopic community; however, it is not able to describe the physics of molecular interactions perfectly. Therefore, complex line profiles are needed to explain the effects such as:

- **Dicke Narrowing effect:** In moderate pressure ranges, where the collisions affect the velocities, the use of the Voigt profile is not adequate. Since the mean free path becomes equal to or less than the wavelength of the incident radiation, the resulting motion of the molecules is Brownian, and thus the diffusion of the gas becomes relevant. The line shape functions which can determine the narrowing parameter for a transition in Brownian motion are a) the Galatry profile or Soft collision model [30, 68]; this line shape assumes only small changes in the radiators velocity during collisions. b) The Rautian-Sobelman profile or Hard collision model [69] or Nelkin-Ghatak [70]: for this line shape, each collision erases any information about the radiators velocity. That, therefore, randomizes the velocities of the radiators and introduces a velocity-changing rate related to the diffusion coefficient which will be introduced in Chapter 4.

- **Speed Dependent effect:** For molecules, the mean speed obtained by Maxwellian distribution [2] is not enough to explain the collisional speed of the absorber and perturber molecules since the broadening and shifts of each transition vary with the speed of collisions. There are a couple of methods to implement speed dependent effect in line profiles [31, 32] which will be described in details in Chapter 2. The first one is using hypergeometric functions used in the analysis in Chapter 3. The second method is applying a quadratic model used in Chapter 4 and 5 of this thesis. The quadratic speed dependent model is faster in term of calculation and includes the dependence of relaxation rates on the absorber speed.

- **Line mixing effect:** The reason that line mixing effects happen, lies in the difference of rotational energy between the levels for a single vibrational band where the thermal energy is larger than the rotational energy difference. In this case, inelastic collisions occur, and as a result, the population transfers between the rotational levels [34, 71]. At the microscopic level, we can explain the dependence of the band's behaviour on collisions using a relaxation matrix. This information allows us to decrease the number of variables to obtain valid results, especially where the shape of the band changes with pressure. The relaxation matrix elements are related to the rates of inelastic collisions that transfer populations from one rotational level to another. The diagonal elements of W are the low-pressure broadening coefficients of the lines, while the off-diagonal ones describe the interference between two lines (see Chapter 4 for formulations of line mixing).

1.4.1 Line shape effects in the atmosphere

When looking at atmospheric spectra, measurements are made through a non-homogeneous medium, i.e., pressure, and temperature are changing with altitude. Breaking that atmosphere up into smaller intervals (about 1 km), one can assume those small intervals are homogeneous (just like a gas cell in the lab) and at each of those intervals, a spectrum can

---

[2] Maxwell-Boltzmann distribution shows different speeds for a gas at a given temperature

be computed for a set of atmospheric conditions that describe that particular interval. The final spectrum that can be seen is the addition of all the spectra from the different atmospheric levels.

Keeping this in mind, it is known that the pressure of the atmosphere decreases with altitude. Also assuming a simple Voigt, the spectral line shape is the convolution of pressure broadening and Doppler broadening. Hence, when closer to the ground, pressure broadening will be the most important, making the spectral line broader contributing more absorption in the wings of the spectral line of the solar absorption spectrum. While higher in the atmosphere Doppler broadening is more important and since it is a narrower line shape, it contributes more absorption in the line center.

1.5 Standard databases

Planetary and atmospheric remote sensing measurements entirely depend on the availability of reference spectroscopic information for the target species measured in the laboratory. Such mandatory information indeed exists and is gathered in the standard spectroscopic databases (for example, the ATMOS database [72], GEISA Gestion et Etude des Informations Spectroscopiques Atmospheriques [4] and HITRAN HIgh resolution TRANsmission database [1]).

Depending on the spectral range and the involved species, the nature of the reference spectroscopic data stored in these databases differs. Generally, for small to medium-sized molecules (such as ozone and carbon dioxide, where individual lines are observable), the reference information consists of parameters describing the profile of the lines.

The model spectrum of the species can be calculated by using these lists of line parameters in various absorption path length and pressure conditions. For bigger molecules, such as chlorofluorocarbons (CFCs), individual lines are not resolved in atmospheric spectra, and the spectroscopic reference information exists as absorption cross-section spectra measured in physical conditions similar to the atmospheric conditions.

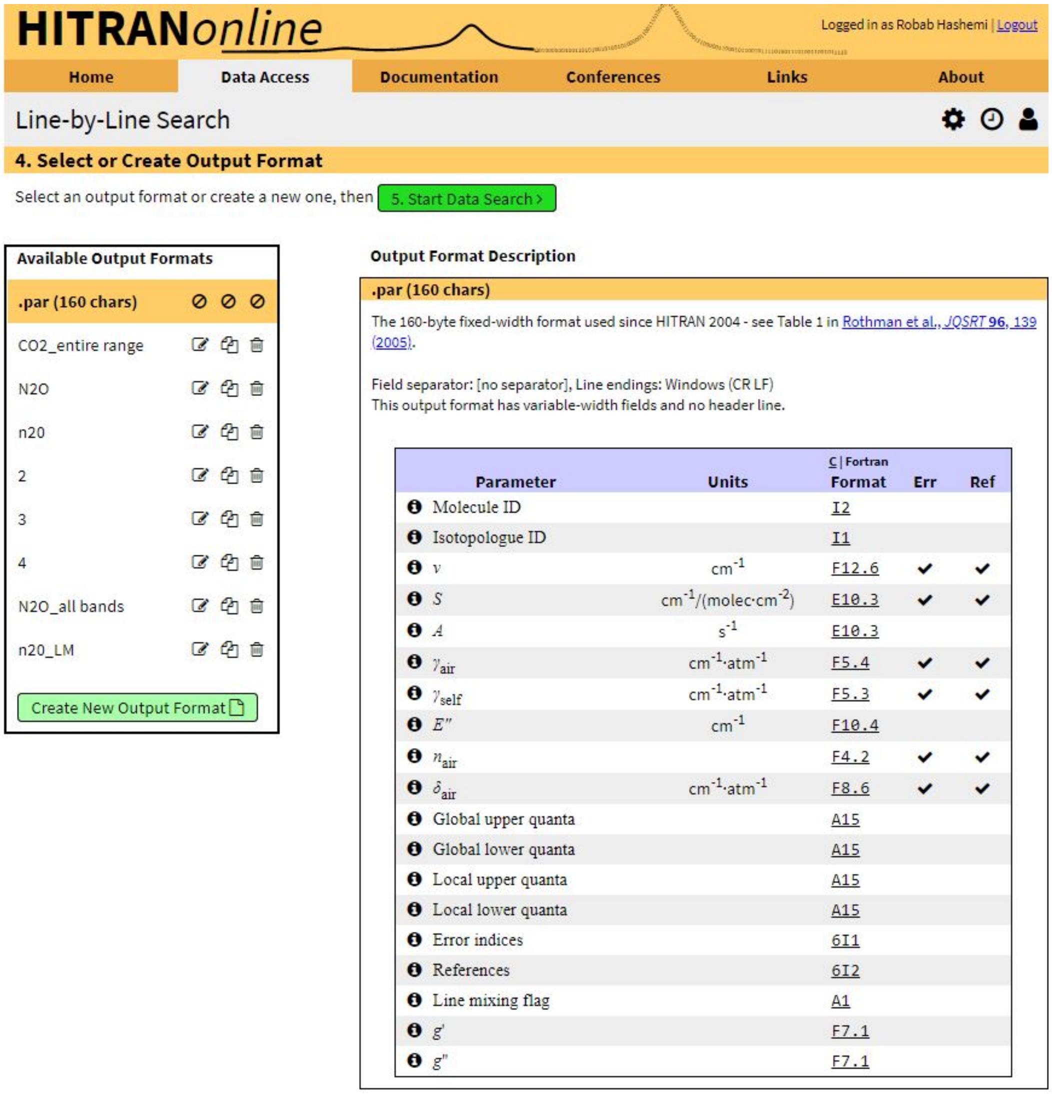

The 160-byte fixed-width format used since HITRAN 2004 - see Table 1 in Rothman et al., *JQSRT* **96**, 139 (2005).

Field separator: [no separator], Line endings: Windows (CR LF)
This output format has variable-width fields and no header line.

Parameter	Units	C | Fortran Format	Err	Ref
Molecule ID		I2		
Isotopologue ID		I1		
ν	cm^{-1}	F12.6	✓	✓
S	cm^{-1}/(molec·cm^{-2})	E10.3	✓	✓
A	s^{-1}	E10.3		
γ_{air}	cm^{-1}·atm^{-1}	F5.4	✓	✓
γ_{self}	cm^{-1}·atm^{-1}	F5.3	✓	✓
E''	cm^{-1}	F10.4		
n_{air}		F4.2	✓	✓
δ_{air}	cm^{-1}·atm^{-1}	F8.6	✓	✓
Global upper quanta		A15		
Global lower quanta		A15		
Local upper quanta		A15		
Local lower quanta		A15		
Error indices		6I1		
References		6I2		
Line mixing flag		A1		
g'		F7.1		
g''		F7.1		

Figure 1.2: Screenshot of HITRAN online website [3] presenting the line by line spectroscopic parameters in current HITRAN database. The table includes mol as molecular species identification number (ID), iso as the isotopologue number, ν_{ij} wavenumber in cm^{-1}, intensity, S_{ij} in cm^{-1}/(moleculecm^{-2}), A_{ij} as Einstein coefficient in s^{-1}, self- and air-broadening (γ_{self} and γ_{air}) in cm$^{-1}/atm$, lower state energy (E'') in cm^{-1} (as explained in section 2.1, the wavenumber is directly proportional to energy and in HITRAN it is presented with cm^{-1} unit), the temperature dependence of the air-broadening (n_{air}), and shift parameter (δ_{air}) in cm$^{-1}/atm$ and the lower and upper state statistical weights (g'' and g'). For more information see Ref. [1].

Individual line parameters include the position, the intensity, the self and airbroadened widths, the temperature dependence of the airbroadened width, the self- and air-pressure shift of the line position. A large amount of such data are currently available. For example, the HITRAN database includes parameters for 4.5 million lines belonging to 47 molecules. This database contains the required parameters for simulating the light emittance and transmittance in a gaseous environment, such as Earth's atmosphere. The parameters in HITRAN are presented in Figure 3.1. With HITRAN online, spectroscopists can select the required transition data by building a query, and they can select different molecules in various wavenumber ranges. Also, it allows choosing between different isotopologues, and the user can create the desired output file [73, 74].

Still, the reference database may contain some outdated information and sometimes the information may be inaccurate. These deficiencies may originate from measurement complexities and incorrect measurement approaches resulting in errors. Also, for some spectral ranges, there are no available measurements. One objective of the thesis is to try filling in those gaps for spectroscopic parameters. The work in this thesis relies on high-resolution Fourier transform infrared spectroscopy and laser spectroscopy as methods of measuring spectral line parameters. I devoted my research to:

- Collecting the required laboratory data with high resolution and high signal to noise ratio
- Testing different line profiles for simulating the spectra as accurately as possible
- Retrieving the parameters such as speed dependence, narrowing, and line mixing to feed the databases with more accurate new sets of parameters

1.6 The primary use of spectroscopic line shape studies

The spectroscopic results of laboratory line shape studies enable accurate modelling of infrared radiative transfer in the atmosphere of Earth and other planets. The radiative transfer explains that when an electromagnetic beam radiates through the atmosphere, it might:

- lose energy due to absorption
- gain energy due to emission
- get scattered

For simplistic cases, the radiative transfer equation has specific solutions; however, more complex numerical models are required to solve the radiative transfer equation for realistic instances. The atmospheric scientists are working on the radiative transfer equation [75–78] to improve the retrieval algorithms and go beyond the straight-forward line profiles and interpret the observed spectra of radiances regarding variables like temperature, humidity, gas concentrations (or pressure), clouds, and surface characteristics. The objective is to reduce the difference between the radiance spectra collected by the instrument and the calculations made by radiative transfer models to estimate the atmospheric concentrations, temperature, and pressure profiles more accurately.

1.6.1 How are the spectroscopic line shape parameters used in radiative transfer codes?

The radiative transfer equation is

$$\frac{dI(\nu,s)}{ds} = -\alpha(\nu,s)I(\nu,s) + \alpha(\nu,s)B(\nu,T(s)), \tag{1.14}$$

where I is the spectral radiance, shows the power in a given direction, per unit area, per unit solid angle, and per unit frequency (ν), B is the Planck function that describes the wavelength and temperature dependence of black body radiation, and s represents the distance along the path which radiation travels. The above equation can be solved in several steps; first, the absorption coefficient should be calculated, and then the radiative transfer equation should be integrated. The third problem is related to the computing the Jacobians. However, the objective of the present thesis is not solving the radiative transfer equation, but to show where the line shape parameters are needed [78, 79].

The absorption coefficient, α, can be formulated using

$$\begin{aligned}\alpha(\nu, p, T, x_1, ..., x_N) = \Sigma_{i=1}^{N} \frac{p x_i}{k_B T} \Sigma_{j=1}^{M} S_{ij} g(\tilde{\nu}_{ij}, \nu, p, T, x_1, ..., x_N) \\ + C_1(\nu, p, T, x_1, ..., x_N) + ... + C_L(\nu, p, T, x_1, ..., x_N)\end{aligned} . \tag{1.15}$$

As can be seen the absorption coefficient $\alpha(\nu, ...$ depends on the frequency ν, temperature T, pressure p, and volume mixing ratios of different gases ($x_1, ..., x_N$), Variable N with index i shows the different gas species and M with index j the spectral lines of each gas. The constant k_B introduces the Boltzmann constant. The product of the line intensity (S_{ij}) and line shape function $g(\tilde{\nu}_{ij}, ...)$ in the second summation shows the spectral lines contribution. The terms C_1 to C_L are functions of temperature, pressure, frequency, and gas volume mixing ratios. This equation illustrates, where the line shape profiles appear in the calculation of atmospheric profiles.

Typically, the signal measured by optical sensors cannot be translated into atmospheric parameters directly in a straightforward way. The inversion process should be applied which consists of adjusting the gas concentration so that the modelled spectrum best fits the measured one. The best fit is usually obtained by searching for the minimum of a cost function. In least-squares fits, the cost function is

$$M(x) = [y - F(x)]^T S_y^{-1} [y - F(x)] + [x - x_a]^T R [x - x_a], \tag{1.16}$$

where x is the variable of interest to retrieve (e.g. the vector of concentrations of the gas at different altitudes), y is the observation. S_y^{-1} is the error covariance matrix of the observations and $F(x)$ is the radiative transfer model. The second part of the cost function ($[x - x_a]^T R [x - x_a]$) is a term added in case of ill-conditioned inversions, i.e. in circum-

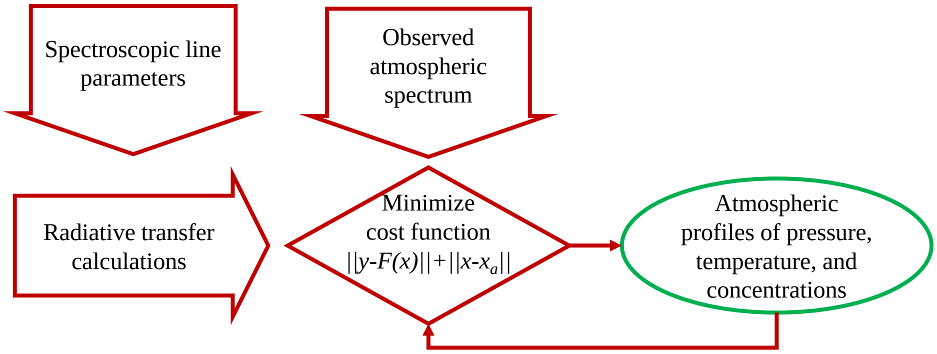

Figure 1.3: A flowchart illustrating how atmospheric profiles such as concentration or temperature can be obtained using spectroscopic parameters and radiative transfer models. The spectroscopic line parameters are entered in the radiative transfer codes. By comparing the observation atmospheric spectra to the radiative transfer models and minimizing the difference (the cost function as introduced in Eq. (1.16)), the atmospheric concentration and temperature and pressure profiles can be obtained.

stances in which $F(x)$ depends weakly on one or more components of the retrieval vector x. The term R introduces an inverse model and x_a is a priori profile [78, 79]. Figure 1.3 summarizes the procedure of obtaining atmospheric vertical profiles.

There are several retrieval algorithms, which are fast and reliable. One is Automatized Atmospheric Absorption Atlas known as 4A [80], which is based on a line-by-line radiative transfer model and has good spectral coverage. In this program, employing different line shape effects, better results can be obtained for the absorption.

Another example is Non-linear Optimal Estimator for MultivariatE Spectral analysis (NEMESIS) for analysis of measurement on Saturn and Titan composite infrared spectrometer (on board the NASA Cassini spacecraft) [78]. NEMESIS can be used to simulate observations of other planets as well. The moderate resolution atmospheric radiance and transmittance model (MODTRAN) [81] and the fast atmospheric signature CODE known as FASCODE [82] are two successful algorithms used by the spectroscopic community.

1.6.2 Evaluation of line parameters

A proper method of modelling atmospheric spectra is to take into account the individual absorption spectral lines in the range of frequencies of the measured spectrum, and compute them over the range of pressures and temperatures measured by the instrument line-of-sight.

The quality of spectroscopic line parameters is an important factor for retrieval and it should be evaluated; there are several publications on the influence of updated parameters in estimating the temperatures, pressures, and concentrations obtained with remote sensing data. The study performed by Frankenberg et al. [83] revealed the over-estimation error associated with CH_4 concentration recorded by the SCanning Imaging Absorption SpectroMeter for Atmospheric CHartographY (SCIAMACHY) instrument. This error was due to inaccurate line shape parameters used for the H_2O molecule. In other research, Alvarado et al. [84] assessed the parameters obtained for H_2O, CH_4, and N_2O. They found that using the updated line parameters for CH_4 gives much smaller mean bias in the obtained CH_4 from observation. Furthermore, the authors used updated line parameters for N_2O and they observed substantial error reduction in the retrieved profile for N_2O. Armante et al. [85] offered a strategy to evaluate spectroscopic parameters by using Spectroscopic Parameters and Radiative Transfer Evaluation (SPARTE) chain. The SPARTE chain is based on the comparison of forward radiative transfer simulations and observations of spectra made from various instruments.

Updating and evaluating the spectroscopic databases is important in the simulation of atmospheric spectra. In Figure 1.4, the fit is shown for ozone retrievals using two recent updates of GEISA database in 2011 and 2015. Clearly, GEISA 2015 has done a better job of matching the observations, and the residuals are reduced by a factor of three when using the more accurate values (resulting into 6 % improvement in the model) [86].

1.7 Thesis outline

Chapter 2 is devoted to the required background theoretical information on the molecular spectroscopy focusing on rotational and vibrational spectroscopy. The topics include the fundamentals of vibrational and rotational spectroscopy to help to describe the observations of electromagnetic radiation in the infrared spectral region.

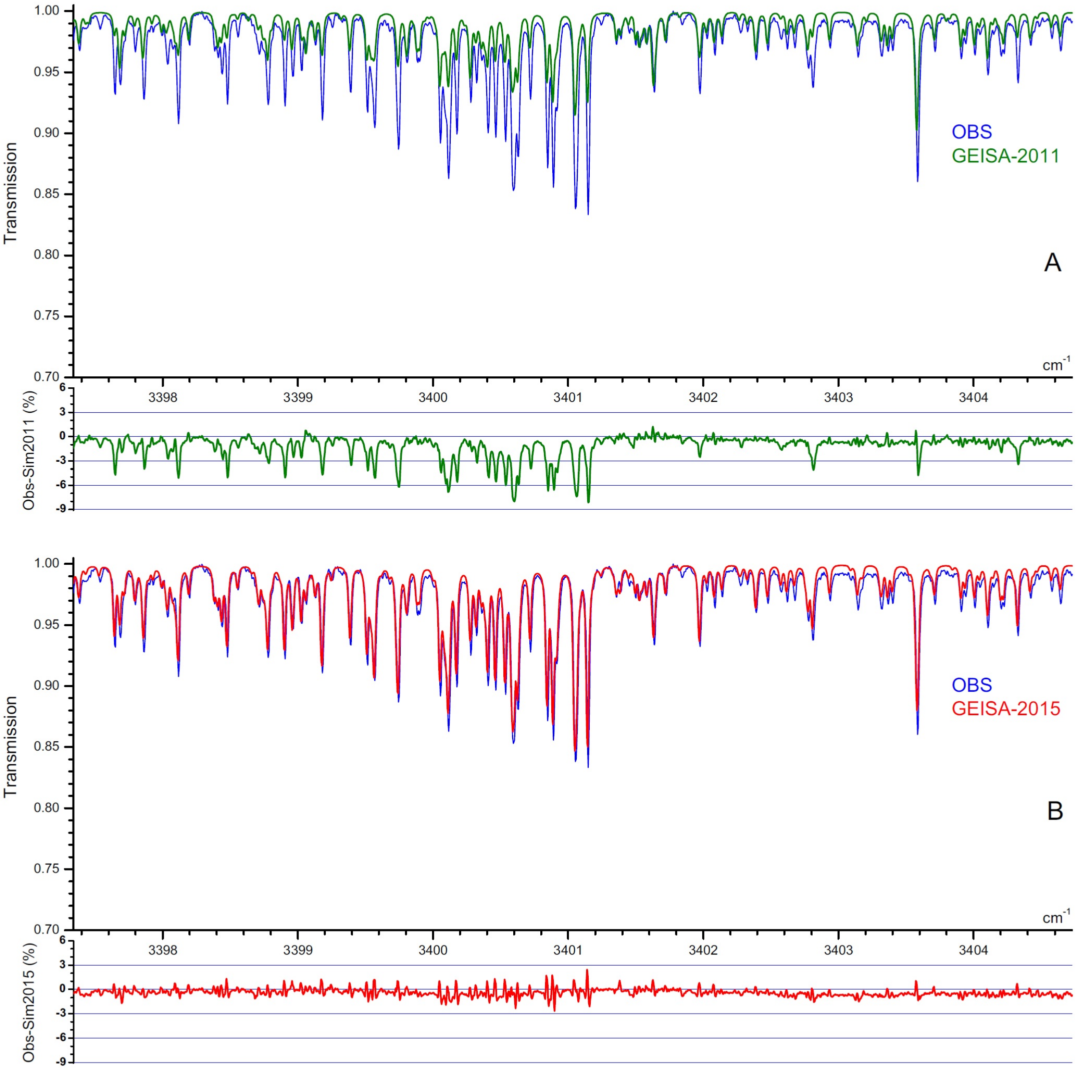

Figure 1.4: Simulation of ozone absorption using GEISA-2011 (upper panel) and GEISA-2015 (lower panel) near 3400 cm^{-1}. The figure is reprinted from Journal of Molecular Spectroscopy, N. Jacquinet-Husson, R. Armante, N.A. Scott, A. Chdin, L. Crpeau, C. Boutammine et al., Volume 327, September 2016, Pages 31-72. With permission from Elsevier [4].

In Chapter 3, the study I performed to check the accuracy of our measurement setup is described. I used acetylene gas, and calculated the Boltzmann constant with a technique called 'Doppler thermometry' which is reprinted from Journal of Chemical Physics.

In the next two chapters, I have described the two experiments that have been conducted on atmospheric trace gases carbon monoxide and methane, which are reprinted papers from two different journals. In each one of these chapters, the motivations have been described separately. A literature review is done for each study to show why the research was needed.

Chapter 4 describes a project to measure of laboratory spectra of CO mixed with CO_2 in the $2-0$ band to obtain the required spectroscopic parameters for planetary research. These result will be included in databases to be used in concentration calculations by astrophysicists.

Chapter 5 presents the spectroscopic study of methane. I used the spectra recorded by a Fourier transform spectrometer (FTS) at the Jet Propulsion Laboratory, Pasadena, California to collect the line parameters for methane. The current values for $\nu_3 + \nu_4$ band of methane in the HITRAN database are based on semi-empirical calculations. Therefore, this study is required to improve values for this band. Also, the speed dependent and line mixing coefficients are measured for methane. The self and air-broadened half -width, self and air-pressure-induced shift are retrieved.

Finally, in Chapter 6, the impact of my research is stated and the conclusions with a summary of ideas for the thesis is presented. Potential improvements for future projects are discussed. The references and Appendix are presented as last sections of the document.

Chapter 2

Background theoretical information on the absorption spectroscopy

Because of the importance of trace gases in the dynamic of planetary atmosphere, the molecules of concern for this thesis are the trace gases such as acetylene (C_2H_2), carbon monoxide (CO), and methane (CH_4). In order to perform spectral line shape study of these molecules, concepts of rotational and vibrational spectroscopy need to be explained. The absorption spectra of acetylene in the $\nu_1 + \nu_3$, the $2-0$ band of carbon monoxide, and $\nu_3 + \nu_4$ for methane emerge as a result of their interaction with IR light. Therefore, I will discuss the theoretical principles of the absorption spectrum. The properties of electromagnetic radiation and the fundamentals of rotational-vibrational spectroscopy will be reviewed. I will present rotational and vibrational spectroscopy individually since the transitions of the above-mentioned molecules happen because of both rotation and vibration of the molecules. Also, I will address selection rules, and will provide definitions of the band and branches. For interpreting spectra, the line shape models used in this thesis include the Voigt, Rautian and speed dependence Voigt models. The book by Peter F. Bernath: Spectra of Atoms of Molecules [2] was used as the primary resource to write this chapter.

2.1 Properties of electromagnetic radiation

To understand the physics of spectroscopy, several terms related to electromagnetic radiation need to be defined. Electromagnetic radiation (EM) exists as Oscillation of electric and magnetic fields.

The EM field, with electric and magnetic fields perpendicular to each other as its components, travels with the speed of light in a direction perpendicular to both electric and magnetic fields. As shown in Figure 2.1, if the electric field is along $+y$ axis and magnetic field along $+z$ axis, the EM field propagates along $+x$ axis obeying the right hand rule (if one points the right hand fingers in the direction of the electric field propagation, by bending the fingers in the magnetic field direction, the thumb finger shows the direction of wave propagation).

EM radiation is a periodic wave and can be characterized by properties such as its amplitude (maximum displacement, A), wavelength (the distance of one full cycle of the oscillation, λ), and frequency (the number of cycles per second, ν). The following equation expresses the relation between wavelength and frequency,

$$c = \lambda\nu, \tag{2.1}$$

with c as the speed of light, λ referring to wavelength, and ν as frequency. The frequency is related to the energy of photons by this relationship: $E = h\nu = hc/\lambda$, where E is energy, h is Planck's constant. This means that light particles, can only deposit discrete amount of energy. Therefore light can behave like a wave and particle. Since EM radiation travels at the speed of light, each wavelength corresponds to a given frequency [2].

The Schrödinger equation expresses how a quantum state of a molecule changes with time. Solving Schrödinger's equation produces the wave functions and energy eigenvalues. The time-dependent part of Schrödinger's equation is

$$i\hbar\frac{\partial}{\partial t}\Psi(r,t) = \hat{H}\Psi(r,t), \tag{2.2}$$

where Ψ presents the wave function of the system and $\hat{H}$ is the Hamiltonian operator including kinetic energy and potential energy. The term $\hbar = h/2\pi$ is the reduced Plank constant. The time-independent Schrödinger equation is shown by the following equation:

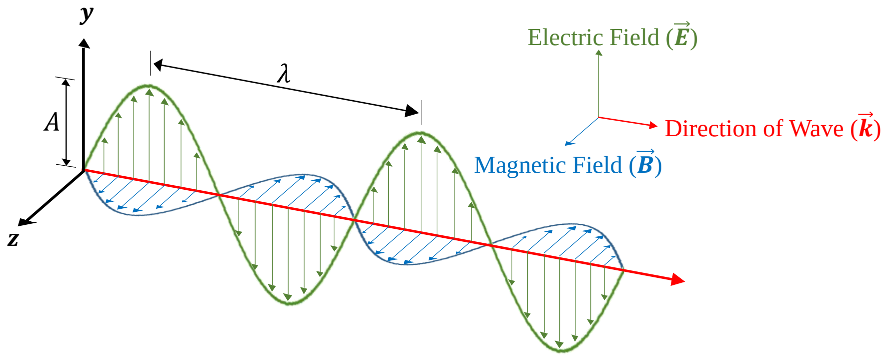

Figure 2.1: Propagation of electromagnetic wave in the x direction while the electric field is in the y direction and the magnetic one in the z direction. A is the amplitude and λ is the wavelength. This figure is reproduced based on the Figure 2.1 of the book by M. Hollas, Modern Spectroscopy [5].

$E\Psi = \hat{H}\Psi$, where E corresponds to the energy of the state Ψ. Using the Born-Oppenheimer approximation, one is able to split the motion of the quantum system into motions of nuclei and electrons, because of their mass difference. The separation of nuclei and electrons motion and writing the wavefunction as a product of the nuclear and electronic states makes the analysis of the nuclear motion easier. One can define the energy of the split system by the electronic, vibrational, and rotational energy components associated with the motion of such a system. Then by solving Schrödinger equation, we can obtain the allowed energies for a system.

The electronic levels are linked to the distribution of the electrons; the vibrational levels are linked to the vibration of the molecule, and the rotational levels are associated with the rotation of the molecule. The spacing of electronic levels is the largest and rotational levels have the smallest frequencies. Therefore, high energy ultra-violet or visible light is required in order for the molecule to have changes in the electronic states. In Figure 2.2, the energy states for a diatomic molecule are presented, where considering the approximation, the molecule vibrates similar to a simple harmonic oscillator. For having the vibrational transitions, a change in the dipole moment is needed and will be explained later in this chapter (for homo-nuclear diatomic molecules like N_2, there is no change in transition dipole moment). In this thesis, only the rotational-vibrational transitions are described

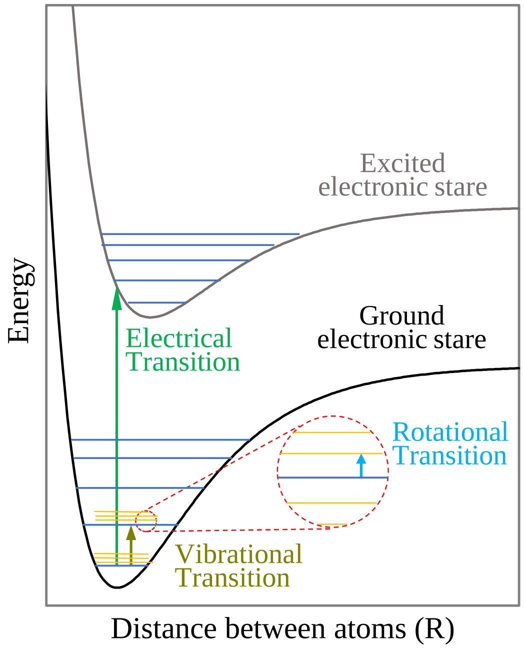

Figure 2.2: This figure shows the energy states for a diatomic molecule. The curves present the electronic levels, the vibrational levels are presented by the blue lines, and the rotational ones are shown by the red lines. For an electronic state, the lowest value of the potential curve shows the electronic energy. This figure is reproduced based on Figure 9.9 of the book by P. Bernath, Spectra of Atoms and Molecules, [2].

Table 2.1: Number of normal modes for molecules [2]. There are 3 coordinates for each N atom, then the total coordinate number is 3N coordinates (3N degrees of freedom for translation, rotation and vibration). For a linear molecule, the rotation about its molecular axis is not observable.

Molecule	Non-Linear	Linear
Translational	3	3
Rotational	3	2
Vibrational	3N-6	3N-5
Total	3N	3N

because of the absorption of infrared radiation by greenhouse gases and causing vibrational and rotational motion for these molecules.

2.2 Vibrational-rotational spectroscopy

To know about the rotational-vibrational structure of a molecule, it is necessary to learn about the energy of vibrational and rotational states.

2.2.1 Vibrational motion

Normally, one can define the vibration of molecules employing a limited set of what is termed ”normal modes”. These normal modes match with distinct vibrational motions which are independent of the others. One or a combination of normal modes can be used to describe a vibration. The various type of motion with specific symmetry can describe the normal modes (a powerful tool to learn about the normal modes symmetry is group theory). The number of atoms in a molecule determines the number of normal modes. The wavefunction that describes the vibrational nuclear motion, for a linear molecule, is product of $3N-5$ normal modes where N is the number of atoms, and for the nonlinear molecules, it is $3N-6$ as shown in Table 2.1. The energy of such a system can be obtained by summing the energy for individual normal modes.

A diatomic molecule has only one vibrational mode; the energy of each vibrational levels, can be shown as [87]

$$E_V = \omega(v + 1/2) + \chi(v + 1/2)^2 + ..., \tag{2.3}$$

with ω as the harmonic frequency of the vibrational mode, χ is its first anharmonicity correction, and v is the quantum number of the vibration mode. E_V for a polyatomic molecule is the sum of the energy for the excited vibrational normal modes, [87].

$$E_V = \Sigma_i \omega_i (v_i + d_i/2) + \Sigma_i \Sigma_{j>i} x_{ij} (v_i + d_i/2)(v_j + d_j/2) + ..., \tag{2.4}$$

where the indices i and j refer to the normal modes, and the degeneracy of mode i is shown by d_i. We can define the vibrational levels using the the quantum numbers associated with all the normal modes of the molecule ($v_1 v_2 ... v_{3N-6}$).

Then, for the transition between two vibrational states, the energy can be obtained,

$$\Delta E_V = E_V(v'_1 v'_2 ... v'_{3N-6}) - E_V(v''_1 v''_2 ... v''_{3N-6}). \tag{2.5}$$

The $'$ and $''$ refer to the upper and lower energy states respectively. Vibrational transitions correspond to changes in the vibrational quantum numbers (Δv_i). Where if $\Delta v_i = 1$, we will have a fundamental band, and a band would be an overtone if $\Delta v_i > 1$. Sometimes, more than one quantum number changes for a band (combination bands). When the lower energy level is the vibrational ground state, bands are distinguished using the term $\Sigma_i \Delta v_i \nu_i$. Transitions between two excited states are called a ”hot band”, which is identified by $\Sigma_i \Delta v'_i \nu'_i - \Sigma_i \Delta v''_i \nu''_i$.

For a vibrational mode to be infrared-active, there must be a change in dipole moment. The dipole moment is a vector defined by the summation over the multiplication of the charge of particles with their position vector.

2.2.2 Rotational motion

In addition to vibrational motion, molecules can rotate and have internal energy levels of rotation. The energy of a rotational state, E_R, for a simple linear molecule is [87]

$$E_R = BJ(J+1) - DJ^2(J+1)^2, \tag{2.6}$$

with

$$B(cm^{-1}) = h/8\pi^2 cI_m. \tag{2.7}$$

The constant D shows the centrifugal distortion, and J is the quantum number associated with the total angular momentum of the molecule. In the equation of rotational constant B, I_m is the moment of inertia of the molecule.

One can now determine the energy of the rotational transition (ΔE_R) which is defined by the energy difference between the two rotational states assumed in the transition,

$$E_R = E_R(J') - E_R(J''). \tag{2.8}$$

Note that transitions associated with rotations are linked to a variation of the quantum number J (ΔJ).

Similar to vibrations, the features of the rotational structure are determined by the symmetry of the molecular rotors categorized into several classes such as linear molecules, spherical top molecules, symmetric and asymmetric top molecules [2]. To distinguish these classes, one compelling mathematical tool is group theory where molecules are classified with similar symmetry into the same point group (symmetry elements of a molecule forms a point group with at least one point unmoved). Samples of symmetry operations are the inversion, rotation, and reflection. When there is an inversion, each point moves through the center of the molecule to a position opposite the original point. In the rotation operation, the molecule remains symmetric after rotating around a principal axis (C_n), where n defines the angle of the rotation ($= 2\pi/n$). A reflection operation is one in which the molecule looks unchanged across a mirror plane, (σ).

2.2.3 Rotational-Vibrational motion

Infrared radiation causes vibrational transitions in molecules. The excitation of a vibration and rotations simultaneously leads to Rotational-Vibrational spectra. Then, each of the vibrational states include some rotational levels with a specific energy. Therefore, it can be said the vibrational transitions correspond to transitions between rotational states of two separate levels of vibration. The energy of a rotational state can be calculated for a single vibrational level and it is derived by the summation of their energy,

$$E_{VR} = E_V(v_1 v_2 ... v_{3N-6}) + E_R(J). \tag{2.9}$$

The rotation-vibration energy for a transition is obtained by the difference between the energy of the two vibration-rotation levels,

$$E_{VR} = E_V(v'_1 v'_2 ... v'_{3N-6}) + E_R(J') - E_V(v''_1 v''_2 ... v''_{3N-6}) - E_R(J''). \tag{2.10}$$

Here, E_{VR} is relevant to the frequency of the transition. The transitions are associated with a frequency that defines the line position in the spectrum. The rotational constant varies with the vibrational states because B is related to the potential energy and as internuclear separation, r, increases, the rotational constant decreases and it can be measured by a method called combination differences (between the lines which share a common upper or lower level).

The rotational-vibrational transitions produce a particular structure in the spectrum. Note that a band refers to a transition from one set of vibrational modes to another and the branches can be defined within a band based on the change in rotational value J. The vibrational band is indeed divided into different branches. Transitions associated with a change

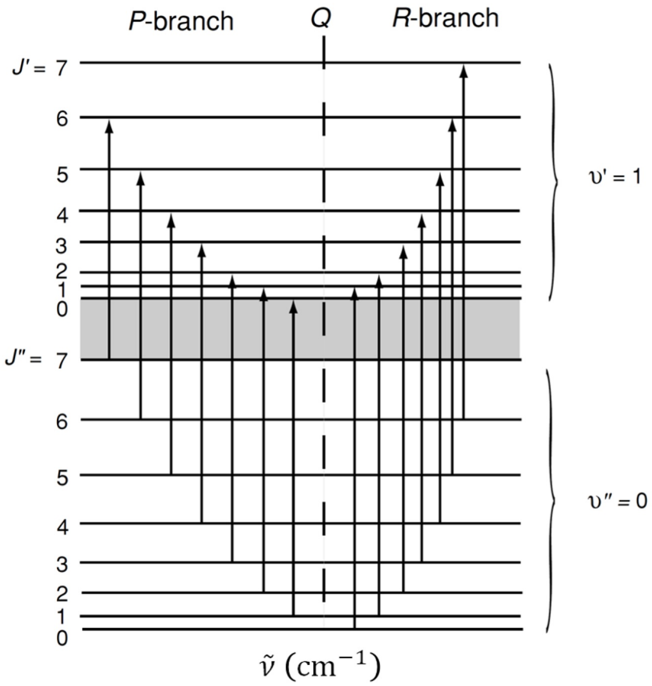

Figure 2.3: Rotation-vibration transitions. Transitions associated to a $\Delta J = 1$. define the R-branch of the vibrational band and $\Delta J = -1$ called the P-branch. The Q-branch may be present where $\Delta J = 0$. The figure is taken from Liou, K. N. An Introduction to Atmospheric Radiation. Academic Press (Elsevier Science). [6]

$\Delta J = +1$ define the R-branch, which evolves from the band center towards the higher energies. Transitions associated to a change $\Delta J = -1$ define the P-branch, which evolves in the opposite direction. Then the spectral lines are distinguished as $R(J'')$ or $P(J'')$ as presented in Figure 2.3. A third branch, the Q-branch may be present in the vibrational band and corresponds to $\Delta J = 0$.

To sum up, the ro-vibrational spectra reveal information on the properties of molecules obeying both the rotational and vibrational selection rules. Based on the selection rules the spectral shape can be defined. Three branches may appear in the spectra (P, Q, and R) corresponding to variations in the vibrational quantum number J. The ro-vibrational bands can be classified into perpendicular and parallel bands. For the first class, the dipole moment change is perpendicular to the molecular axis and changes the vibrational angular momentum. The key here is to distinguish the proper point groups because molecules with similar symmetry can be categorized into the same point group and simplify the classification.

2.2.4 Overview of the structure of the molecules under investigation

The first molecule in the present study is C_2H_2, which is a linear molecule from $D_{\mathrm{inf}h}$ point group. From Table 2.1 the molecule has seven normal modes. However, only five of the modes are IR active (the IR active modes are important for the sake of infrared spectroscopy in this study). The five IR active modes of C_2H_2 are presented in Figure 2.4: (1) ν_1 as symmetric $C-H$ stretching, (2) ν_2 as symmetric $C-C$ stretching, (3) ν_3 as asymmetric $C-H$ stretching, (4) ν_4 as symmetric bending, and (5) ν_5 as asymmetric bending. Furthermore, there are bands called combination bands which are the addition of a couple of normal modes [5].

The second molecule under the investigation is CO, as a diatomic molecule having a linear structure it only has one normal mode shown in Figure 2.5. This asymmetric molecule belongs to the $C_{\mathrm{inf}v}$ point group. The first transition of CO from ground stated (shown by $v = 0$) to the first excited state ($v = 1$) refers to fundamental band and from

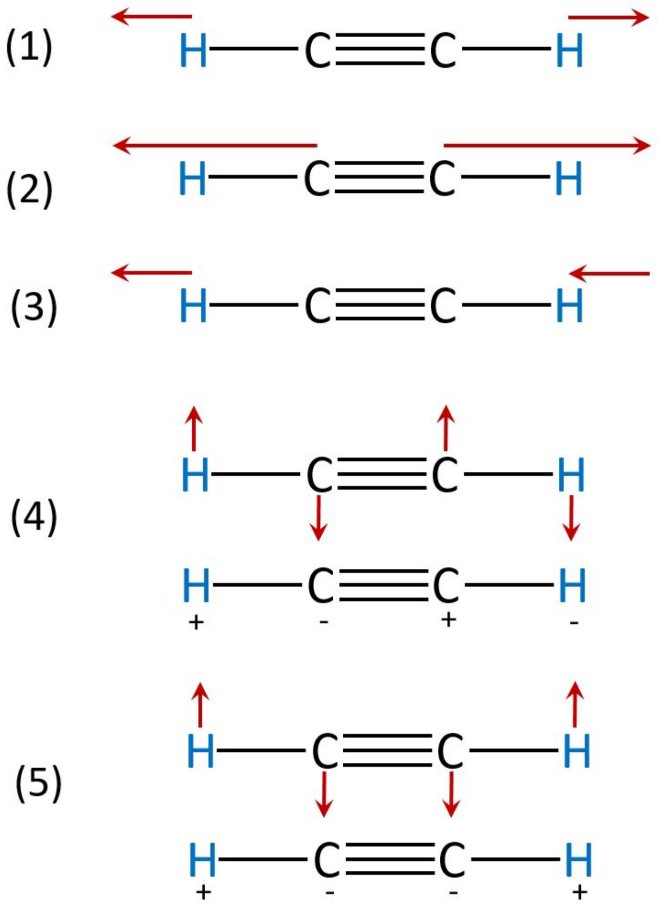

Figure 2.4: The five IR active modes of C_2H_2: (1) ν_1 as symmetric $C-H$ stretching, (2) ν_2 as symmetric $C-C$ stretching, (3) ν_3 as asymmetric $C-H$ stretching, (4) ν_4 as symmetric bending, and (5) ν_5 as asymmetric bending.

Figure 2.5: The IR active mode of CO molecule.

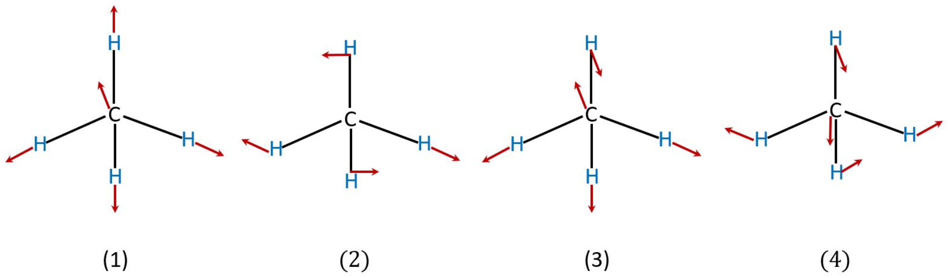

Figure 2.6: The normal modes of vibration for CH_4 molecule. (1) ν_1 as symmetric $C-H$ stretching, referred to $A1$ symmetry, (2) the double degenerate ν_2 as symmetric bending referred to E symmetry, (3) two triply-degenerate ν_3 as asymmetric $C-H$ stretching, (4) ν_4 as asymmetric bending $F2$ species. The ν_3 and ν_4 modes are IR active.

ground state to the second excited state ($v = 2$) is called the first overtone transition (where the excited mode occurs for the vibrational levels above $v = 1$) as the focus of my study. The most likely transitions are the fundamental ones, and then the lower overtone transitions.

The third molecule of interest is CH_4, containing five atoms and belonging to T_d symmetry group with nine normal vibrational modes. Out of methane normal modes, there are five bending and four stretching modes. These normal modes are attributed to different symmetry species such as A class, E, $F1$ and $F2$ species representing the following vibrational motions: ν_1 as symmetric $C-H$ stretching, referred to $A1$ symmetry, the double degenerate ν_2 as symmetric bending referred to E symmetry, two triply-degenerate ν_3 as asymmetric $C-H$ stretching, ν_4 as asymmetric bending $F2$ species. Among these modes ν_3 and ν_4 are IR active. My studied band is a combination band of $\nu_3 + \nu_4$ which is a strong vibrational band.

2.3 Theoretical line shape models used in the thesis

In section 1.3, the normalized line profile function is introduced as $g(\tilde{\nu}-\tilde{\nu}_{jk})$ and the simpler line shape profiles were described. Here, more details are provided. The spectral line shape is given by the following function,

$$\alpha(\tilde{\nu}-\tilde{\nu}_0) = S\left(\frac{g(x,y)}{\sigma\sqrt{\pi}}\right), \tag{2.11}$$

where $S = S_0PL$ with S_0 being the line strength, P the partial pressure of the gas and L the absorption path-length. The term $g(x,y)$ is the spectral line shape of choice. The unitless parameters x and y are defined as

$$x = \left(\frac{\tilde{\nu}-\tilde{\nu}_0-\delta}{\sigma}\right). \tag{2.12}$$

In Eq. (2.12) $\tilde{\nu}_0$ is the angular frequency of the molecular line center, δ is the collisional shift, and $\sigma = \tilde{\nu}_0\sqrt{\frac{2k_BT}{Mc^2}}$ is the calculated Doppler half width at e^{-1} intensity ($\gamma_D = \sqrt{(ln2)}\sigma$. In this equation M is the molecular mass. The parameter y can be defined as

$$y = \frac{\gamma}{\sigma}, \tag{2.13}$$

where γ is the line width considering all contributions to line broadening.

The collisional broadening and shifting slightly depend on the molecular speed. Taking this dependence into account, the line shape profile becomes the speed dependent Voigt (SDV) profile. Following the formalism developed by Berman, Ward and Pickett, the SDV expression becomes [31, 32, 88]

$$I_{SDV} = \frac{1}{\pi}Re\left[\int_{-\infty}^{+\infty}\frac{f_M(\overrightarrow{v})}{\left(\gamma(v)-i(\omega-\delta(v)-\overrightarrow{K}.\overrightarrow{v}\right)}d^3\overrightarrow{v}\right], \tag{2.14}$$

where $f_M(\overrightarrow{v})$ is the Maxwell-Boltzmann distribution of molecular velocities with $\overrightarrow{K}$ as the wave vector. By using the Kummer confluent hypergeometric function, $F_1(a,b,z)$, the collisional broadening and shifting can be written as

$$\gamma(v) = \frac{\gamma}{2^{m/2}} {}_1F_1\left(-\frac{m}{2}, \frac{3}{2}, -\left(\frac{v}{v_{MPS}}\right)^2\right). \tag{2.15}$$

$$\delta(v) = \frac{\delta}{2^{n/2}} {}_1F_1\left(-\frac{n}{2}, \frac{3}{2}, -\left(\frac{v}{v_{MPS}}\right)^2\right). \tag{2.16}$$

In Eq. (2.15) and (2.16) m and n are parameters related to the intermolecular potential which is approximated by an inverse power form, namely $V(r) = r^{-q}$ with $m = (q-3)/(q-1)$, $n = -3/(q-1)$. Here v_{MPS} is the most probable speed of the emitter molecules and it can be obtained using Eq. (2.17)

$$v_{MPS} = \left(\frac{2k_BT}{M}\right)^{1/2}. \tag{2.17}$$

Having used the dimensionless parameters x and y which have already been defined, the SDV profile in Eq. (2.14) becomes as the following equation [31],

$$I_{SDV} = \frac{1}{2\sqrt{\pi}}\left\{1 - \frac{4}{\pi}\int_0^{+\infty} tan^{-1}\left[\frac{x(u)^2 + y(u)^2 - u^2}{2uy(u)}\right] e^{-u^2} u\, du\right\}. \tag{2.18}$$

In the 2.18 parameter u is $u = \frac{v}{v_{MPS}}$ and the value for term tan^{-1} is $tan^{-1} \in [-\pi/2, \pi/2]$.

The speed dependent Voigt profile can also be implemented using a quadratic model. The quadratic form is faster in term of calculation and includes the dependence of relaxation rates Γ on the absorber speed, v_a.

$$\gamma(v_a) = \gamma_0 + \gamma_2[(\frac{v_a}{v_{a0}})^2 - \frac{3}{2}]. \tag{2.19}$$

Using the definition of $\gamma(v_a)$, the speed dependent Voigt profile is obtained. In these equations the parameter $\gamma_0 =< \gamma(v_a) >$ is the mean relaxation rate and γ_2 corresponds to speed dependence of the relaxation rate.

Then the quadratic speed dependent profile will be as

$$g_{qSDV}(t) = \frac{exp[-i\omega_0 t - (\gamma_0 - 3\gamma_2/2)t]}{(1+\gamma_2 t)^{1.5}} exp[-\frac{(kv_{a0}t)^2}{4(1+\gamma_2 t)}], \tag{2.20}$$

where ω_0 is the rest angular frequency (collisionless), and $k = \omega_0/c$. I developed a code using MATLAB to implement the hypergeometric speed dependent Voigt profile for simulating the spectra.

The narrowing coefficients β^0 measured using the RP (Rautian-Sobelman) line shape model [69]. The RP profile can be formulated as

$$g_R(x,y,z) = ARe[\frac{F(x,y+z)}{1-\sqrt{\pi}zF(x,y+z)}], \tag{2.21}$$

with the same x, y, and A parameters defined for the Voigt profile, plus the parameter z which is defined as $z = \frac{ln2\sqrt{\beta_C}}{\gamma_D}$. Here β_C, (in cm^{-1}) introduces the average effect of collisions on Doppler broadening. To be able to judge whether the hard or soft collision models are properly simulating the spectra, besides β_C, the dynamical friction parameter β_{diff} (in cm^{-1}atm^{-1}) of the Brownian motion need to be obtained (the formula for β_{diff} will be presented in Chapter 4).

With the definitions provided in this chapter, the foremost objective of studying molecular spectra is to define the line positions and to determine the structure of the molecules. With molecular symmetries, the rotational constants are obtained and then the vibrational frequencies can be measured. There are some techniques to measure rotational-vibrational spectra of molecules such as laser spectroscopy and Fourier transform spectroscopy. These techniques are described in the following chapters, and the example experiments are provided analyzed using different line shapes.

Chapter 3

Laser spectroscopy of acetylene molecule for Doppler thermometry and measurements of the Boltzmann constant

This chapter is reprinted from the Journal of Chemical Physics, 141(21): 214201, Hashemi R, Povey C, et al. 2014, Doppler Thermometry of Acetylene for Accurate Measurements of the Boltzmann Constant, with the permission of AIP Publishing [89]. [3] This line shape study of acetylene is a good fit for this thesis since it enables finding the major sources of error in spectroscopic experimental measurements and understanding where improvements can be made. Furthermore, the proposed method in this study is an interesting strategy; we use the physical concepts of line shape to determine previously measured precise values (such as the Boltzmann constant). My contributions to this project were:

- Helping Dr. Povey (former group member) to record the spectra. I was responsible for starting and ending each measurement, Dr. Povey produced essential advice when difficulties arose.
- Pre-processing the data and creating the transmission spectra, with the help of H. Naseri and the summer students in our lab (M. Derksen and J. Garber).
- Developing code using MATLAB software to do the calculations and simulations.
- Preparing the results and writing the manuscript.

---

[3] The copyright permission can be found in Appendix A, Section A.2.

3.1 Introduction

The objective of this study is the retrieval of the Boltzmann constant (k_B) with high precision in order to figure out to what extent the experimental procedure is reliable. The accepted value for the k_B published by the Committee on Data for Science and Technology (CODATA) is $1.3806488 \times 10^{-23}$ JK^{-1} with a relative uncertainty of 9.1×10^{-7} [90]. This value was determined by measurements of the ideal gas constant, R [90]). The Boltzmann constant can be defined as $k_B = R/N_A$ where R is the ideal gas constant (obtained accurately using the measurement of speed of sound in argon), and N_A is Avogadro number relating the atomic mass unit to kilogram (6.022140857(74)10^{23} mol^{1}). Thus, k_B can be calculated based on an accurate determination of R.

Another method of measuring k_B is laser spectroscopy using the Doppler-width thermometry approach, which was used in this study. Different experimental groups have attempted this alternate method, and the calculated relative uncertainty in its value on order of 10^{-4} and 10^{-5}, [91–95]. It is desirable to improve the known value of k_B to have relative accuracy higher than already achieved 9.1×10^{-7}. To acquire such high accuracy, a significant improvement to the experimental design is required.

The experiment is based on measuring ro-vibrational absorption features of C_2H_2 gas inside temperature and pressure controlled cell maintained at thermal equilibrium. The Doppler width dominates the full width at half-maximum of the absorption line due to the molecular velocity distribution along the laser beam at low gas pressure.

The Doppler width of a spectral absorption line recorded in a cell is related to the equilibrium temperature and Boltzmann constant as it is shown in Eq. (3.1)

$$k_B = \left(\frac{\gamma_D}{\tilde{\nu}}\right)^2 \left(\frac{Mc^2}{2\ln(2)T}\right), \tag{3.1}$$

where γ_D is the Doppler broadening, M is the mass of the gas particle, speed of light is presented with c, T is temperature, and $\tilde{\nu}$ is the line position.

Several research groups have carried out spectroscopic measurements to obtain k_B. Lemarchand et al. [96, 97] have studied laser absorption spectroscopy in the mid-IR and determined a value of $1.38080(20) \times 10^{23}$ JK^{-1} for k_B, which agreed within total systematic uncertainty about 2.3×10^{-6} to the accepted CODATA value which is a remarkable result. Casa et al. [92] have studied spectra of carbon dioxide transitions and have achieved an relative error of 1.6×10^{-4} in their reported value for k_B of $1.38058(13) \times 10^{-23}$ JK^{-1}. Yamada et al. [93] have determined k_B using the Doppler width of acetylene transitions and reported a value for the k_B equal to $1.3940(17) \times 10^{-23}$ JK^{-1}. This group mentioned that in their determination of the Doppler width of a ro-vibrational absorption line using a comb-locked diode laser the lack of accuracy in temperature measurement is the main contributor to the error. Truong et al. [98] have measured k_B to be $1.38104(59) \times 10^{-23}$ JK^{-1}. The relative deviation of their result from CODATA value was 2.7×10^{-4}.

The common profiles used by the authors to analyze the spectra recorded at very low pressure were the Voigt profile (VP) [29] and the Gaussian profile. The influence of Dicke narrowing [30] on the accuracy of Doppler width measurements has been considered in several studies. Lemarchand et al. [96] have employed NH_3 spectra using the VP and Galatry (soft collisions) [68] models, and they obtained k_B with uncertainty as low as 3.7×10^{-5}. Recently, Castrillo et al. [99] have found the relative uncertainty of k_B to be 2.4×10^{-5} by using a line shape study of H_2O and considering both the Speed Dependent Voigt (SDV) model [31, 32, 88] and the newly introduced partially correlated Speed Dependent Hard Collision (pcSDHC) profile [33, 100, 101].

In this study, a 3-channel tunable diode laser spectrometer with a temperature and pressure-controlled cell was used to record spectra of the $P(25)$ line of acetylene. From these spectra, the Doppler broadening of the $P(25)$ transition was measured, and k_B was retrieved using the SDV line shape model. The value of k_B was compared with previously published results and the amount reported in the CODATA database.

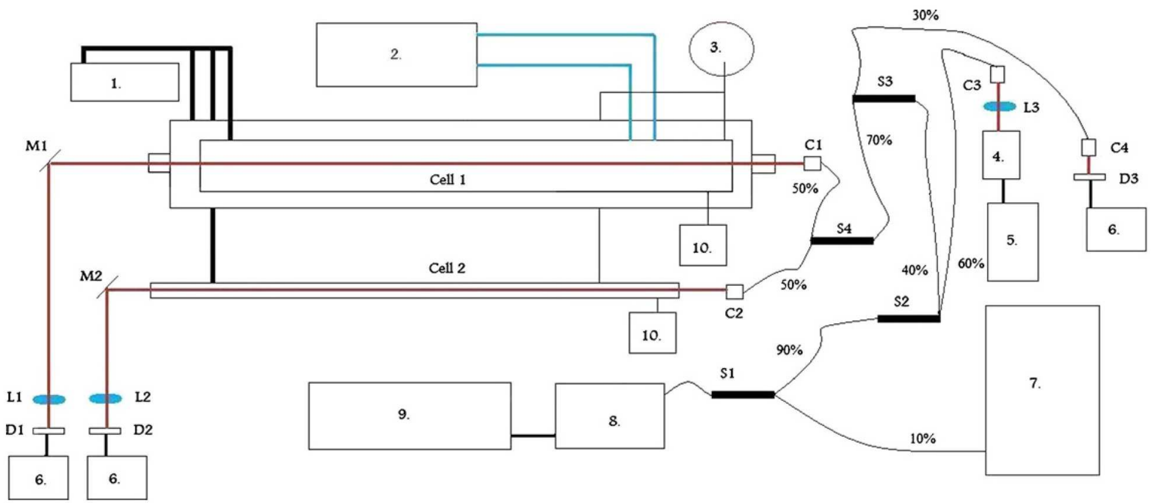

Figure 3.1: ”Reprinted figure from Journal of Molecular Spectroscopy, Chad Povey,Adriana Predoi-Cross,Daniel R. Hurtmans, Line shape study of acetylene transitions in the $\nu_1 + \nu_2 + \nu_4 + \nu_5$ band over a range of temperatures, 268, 177-188, 2011, with permission from Elsevier [7]. Spectrometer setup: Legend: 1 vacuum system; 2 cooling system NesLab ULT-80 Chiller; 3 gas sample; 4 and 5 Fabry Perot interferometer and controller; 6 detector pre-amplifiers and power supplies; 7 WA-1500 EXFO wavemeter; 8 and 9 velocity diode laser head and controller; 10 MKS Baratron pressure gauges; $L1$, $L2$ and $L3$ focusing lenses; $M1$ and $M2$ directing mirrors; $D1, D2$ and $D3$ InGaAs detectors; $C1-C4$ collimators; $S1-S4$ fiber splitters; The ticker black lines present vacuum lines. Blue lines show coolants and the red lines display laser path. Finally, the thin curved lines appear to be fiber optic cables.

3.2 Experimental procedure

The spectra analyzed in this study were recorded using a 3-channel tunable diode laser spectrometer designed for line shape studies of gases. It used a New Focus Velocity Laser System, tunable between 1500 nm to 1640 nm, with a high signal to noise ratio (> 2000) [7].

The instrument setup is presented in Figure 3.1. The first channel is a temperature and pressure controlled gas cell. The second channel incorporates a room-temperature reference gas cell. Both cells have the same path length of 1.54 m. The third channel records the background signal. An accurate line shape analysis can be performed by measuring the signals of the three channels simultaneously.

3.2.1 The three-channel laser spectrometer

The primary components of measuring spectra in the lab were: a light source; the tunable diode laser offering a wide range of tunability is used to interact with a sample. The New Focus Velocity diode laser used, employs a modified Littman-Metcalf laser cavity which provides mode-hop-free tuning of the wavelength (the laser is capable of scanning between the user-defined maximum and minimum wavelength range) [102]. The wavelength of the laser light can be measured using a combination of a Fabry Perot cavity and a WA-1500 wavemeter from EXFO. A second room-temperature gas cell was also available in the lab [102].

Several detectors were used for measuring the temperature, pressure, and the absorption of the light passing through the chamber. The optical design of the tunable diode laser spectrometer uses three InGaAs (indium gallium arsenide) photodiode detectors. The transmission was measured through the use of three InGaAs detectors. One of the detectors measures the incoming light from the gas cell, while the second one covers the incoming light from the reference cell, and the third detector measures the background power of the laser.

The entire experimental setup was controlled and monitored using LabVIEW software. To convert the raw data into transmission spectra, software developed in LabVIEW by Dr. Povey was used [102]. Creating transmission spectra from the recorded spectra was very challenging. Because each spectrum is unique (because of thermal differences in the detectors and diode laser), therefore, careful calculation of a transmission file must be made. The observations showed that the background channel signal was slightly different than the signal on the main channel. That's why the background was corrected as follows. The calculation of transmission was performed in three steps.

First, the spectral features were cut out of the raw spectrum followed by calculating the difference between the background spectrum and the measured spectrum. Next step was fitting the difference using a Chebyshev polynomial and recalculating the background correcting it with the polynomial. Note that the background signal was measured with the same type of detector with similar noise level to eliminate the mechanical noise in the recorded spectra. Finally, the signal file was divided by the corrected background to create the transmission spectra.

The double chamber spectrometer made it easier to do the line positions measurements simultaneously. Then to find out if any time delay or sampling issues existed to create considerable drift in the line positions, every spectrum was fitted individually for both the main and reference channels and the difference between the two channels was calculated. To correct for the inaccuracies in the wavemeter, the spectra were shifted using low-pressure spectra measured on channel 2.

3.2.2 Temperature and Pressure Measurement

To test the thermal stability and thermal gradient inside the cell, several experiments were performed. The temperature controlled absorption gas cell which was centred inside a vacuum jacket to diminish the thermal conductive/convective coupling to the outside cell. Heating and cooling were achieved by a temperature-controlled fluid (methanol or ethanol) which was in direct contact with the cell body.

The primary concern in the operation of the variable temperature cell was the temperature gradient along the length of the cell. Though it was not feasible to remove thermal gradients from the design of the absorption cell completely, improvements were made to minimize it. Platinum resistor thermometers were positioned on rods in different depths and distances and attached to the cell flanges. Several sensors were employed for taking temperature measurements and monitoring the temperature variability of the cell over its base length (the Neslab ULT-80 bath provides temperatures between -80 to +80 degree Celsius), and the thermometers were calibrated using the triple point of water.

The diagram of the temperature sensor setup is given in Figure 3.2. One of the flanges has three temperature ports, one pressure port, and a gas inlet port. The other flange has

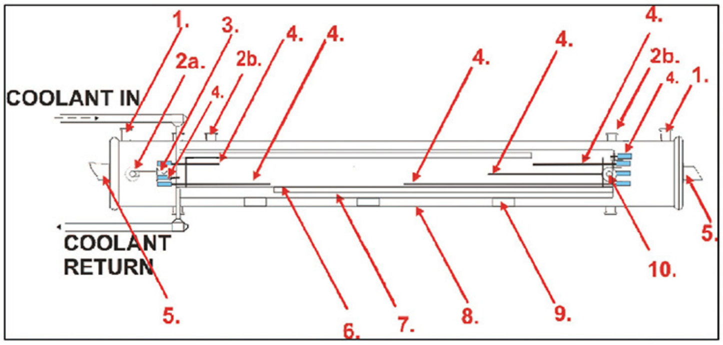

Figure 3.2: Side view of the temperature controlled cell. Legend: 1- vacuum port, 2a- gas inlet, 2b- vacuum field-through for platinum resistors, 3- vacuum valve, 4- temperature sensors using platinum resistors, 5- CaF_2 windows mounted at Brewster angle, 6- fins for directing the coolant through the coolant jacket, 7- coolant jacket, 8- outer cell body, 9- cell support, 10- valve for de-pressuring of the outer jacket.

four temperature ports and one gas outlet port. Inside the cell, for heating and cooling the gas, the temperature controlled cell was created using a Neslab ULT-80 thermal bath.

Based on the tests performed at room temperature, the averaged thermal stability in the gas cell was ±0.0052 K over the four hours of measurement as can be seen in Figure 3.3. I also checked the vertical and horizontal thermal gradient inside the cell and found that larger gradients were formed at the lower temperatures, but at room temperature, the thermal horizontal gradient between the ends was $1.6 \times 10^{-4}\ K/cm$. The measured vertical temperature gradient was $4.17 \times 10^{-5}\ K/cm$ which was smaller than the horizontal one.

The pressures of the gas samples were monitored using two MKS Baratron capacitance manometers with a full-scale reading of 10 Torr (for the temperature controlled gas cell) and 100 Torr (for the reference gas cell), and their accuracy is on the order of 10^{-5} Torr. There was only a negligible drift in the overall pressure with time as a result of local temperature instabilities in the laboratory.

The pure gas sample of acetylene was provided by Praxair with a quoted concentration of 99.99%. Using the spectrometer setup described in Section 3.2.1, the spectra for $P(25)$ transition in the $\nu_1 + \nu_3$ absorption band of C_2H_2 were recorded at an average temperature of 295.78 K. For this transition, the spectra were recorded at different pressures in the 0.25 Torr to 9 Torr range. The spectra were recorded four times for each pressure, and every

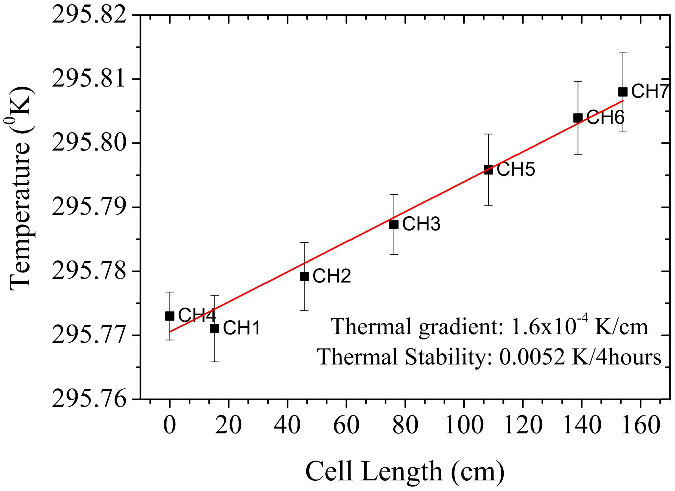

Figure 3.3: Thermal gradient and thermal stability for 7 thermometers in the inner cell for four hours.

spectrum is the average of 100 spectra.

3.2.3 Details on Spectrometer's functionality

To monitor and record the spectra, LabVIEW software was used which operates using a New Focus Velocity laser system. The interface of the laser virtual instrument in LabVIEW lets the user a) select the desired wavelength for scanning and b) select specific transitions to be scanned. For scanning, one can set the laser's Central wavelength to the preferred starting wavelength and measure the pressure and temperature. Then, the piezo voltage was ramped from -3 V up to 2.7 V corresponding to 30 GHz in a user set interval of about 0.001 V. The average and standard deviation of 100 data points for each of the detectors at every step was measured. When the piezo scan finished, the temperature and pressure were recorded over again, and then the process was repeated for a new central wavelength.

The spectrometer (introduced in this chapter) combines a Thorlabs SA200-14A Fabry Perot (FP) interferometer and a wavemeter to do the wavelength calibration. The FP cavity has a 1.5 GHz (0.05 cm^{-1}) free spectral range and has a high sensitivity. Two critical aspects in testing the FP cavity were examining the fringe spacing to confirm the Free

Spectral Range (FSR) of 0.05 cm^{-1}, and then verifying the measurements of line positions. To confirm the FP cavity's FSR size, the following experiment was performed.

For this test, the laser piezo was scanned from -2 to 2 V with 3 seconds between samples to read 3 wavelengths from the WA1500 EXFO wavemeter. The average value of the wavelengths for every laser piezo voltage was recorded and the standard deviation was calculated. After a complete laser piezo scan had been recorded, the wavenumbers associated with each peak were found and subtracted from each other to find the average FSR for that scan. The results of average spacing for five scans showed that the free spectral range for the FP cavity is 0.049616 ± 0.000381 cm^{-1}. This result confirmed the use of 0.05 cm^{-1} as the correct fringe spacing for any analysis completed with this system. When the wavelength scale has been set, a transmission file can be built. Chebyshev polynomial functions were used to correct the background of the spectral files. The frequency was measured directly by using our calibrated EXFO wavemeter.

The non-linearity of the piezo element was improved through the incorporation of an FP interferometer in combination with the wavemeter to determine the laser wavelength. This method enables us to record reliable wavelength scales. When a scan is completed over multiple FSRs, the wavelength of the laser at the first FP peak is recorded. Using this wavelength and the properties of the FP cavity, the wavelength of each peak recorded by the cavity can be obtained. For a complete scan of the piezo in the laser, almost 30 peaks were observed associated with the FSR of the FP cavity. From previous observations, it is found that, that the piezo non-linearity is approximately a cubic function. Therefore, these 30 peaks will allow for 29 separate sub-regions where the piezo will appear linear in the area between successive peaks.

The reproducibility of line-width in the measurement was also examined. To verify the uncertainty of the line-width measurement, 500 identical spectra were recorded to examine and determine the uncertainty in the line-width by overplotting them and checking the possible drifts. At a pressure of about 0.5 Torr, the average line-width at half maximum was found to be 0.0098371 cm^{-1} with an error of 0.41×10^{-6} cm^{-1} for the line center which shows the reproducibility of the recordings.

For the low pressure measurements, the spectra of the $\nu_1 + \nu_3$ band of acetylene were examined. This band was ideal for this experiment because it is a strong absorption band and perfect line positions are available in the literature [7, 103]. The difference between each of the retrieved line positions between the two channels was found to be about 1.65×10^{-5} cm^{-1} on average.

3.3 Spectroscopic Results and Error Analysis

Proper use of line shapes is required to measure the Doppler line width which is related to k_B. The Doppler width is because of the velocity distribution of the molecules in the gas cell. To obtain accurate modelling of the recorded high-resolution absorption line shapes and to obtain the Doppler width, different physical effects such as pressure broadening, pressure-induced shifting, and molecular speed dependent effects have to be taken into account.

I used the formalism presented by Eq. 2.18 in 2.3 to implement speed dependent Voigt profile for a single-spectrum simulation using MATLAB software. This program was used to fit the experimental data to the theoretical line shape.

The analysis of the recorded spectral files was accomplished by first creating a wavelength scale using the combined information obtained from the wavemeter and the positions of the Fabry Perot peaks. The transmission profiles were fitted with the SDV line shape model to obtain the residuals (Observation-Calculation) for each pressure. The software minimizes the differences between the experimental spectra and the calculated spectra by adjusting various line parameters through non-linear least squares. The improved quality of the residuals indicates a higher accuracy in the line shape parameters obtained.

In the analysis procedure, I fitted the line position, intensity, broadening and Doppler width while fixing the self-shifting values to the highly accurate values determined previ-

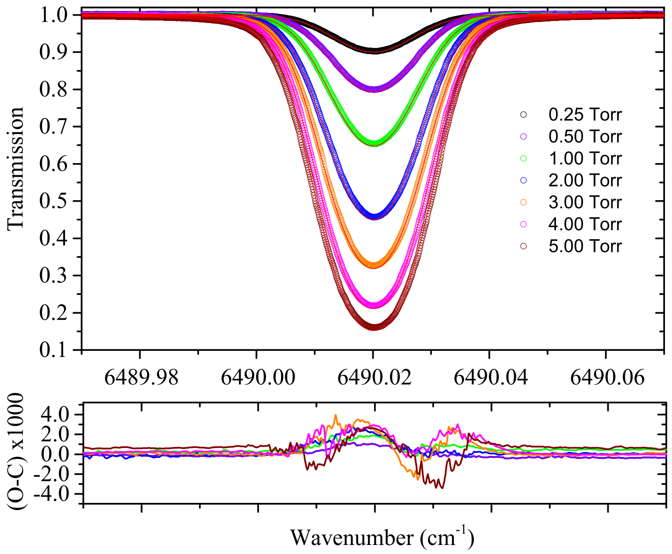

Figure 3.4: Sample plot of the transmission spectrum of the $P(25)$ line of C_2H_2 at pressures 0.25-5 Torr and 295.78 K. Residuals $(O-C)$ under these conditions resulting from least squares single-spectrum fittings of experimental data to SDV line shape model (bottom panel)

ously by former group member; Povey et al. [7]. Figure 3.4 shows the spectra of the $P(25)$ line fitted with the SDV model measured at 295.78 K and different pressures. The upper panel shows the observed data, and the lower panel shows the residuals plotted for several pressures. Each of the lower panels was plotted with the same vertical scale to make it easier to compare them.

Figure 3.4 presents the results of fitting the spectral profile in the pressure range of 0.25 to 5 Torr using the SDV profile. In the implementation of the SDV profile, the broadening and shift are assumed to depend on collisional speed, and on inverse power law expression for the intermolecular potential energy surface. I fitted with different values of the q parameter (four values were used, $q = 1,5,6,12$ to see the effect of different type of potentials. Mathematically, the potentials are type of measure functions, which can be assigned to different points. Then, integrating the measure functions, one can obtain the desired information needed (i.e., force). For example, $q = 6$ describes the dispersion energy and the $q = 12$ presents the short-range repulsion energy. The $q = 5$ is not a form of a well-known

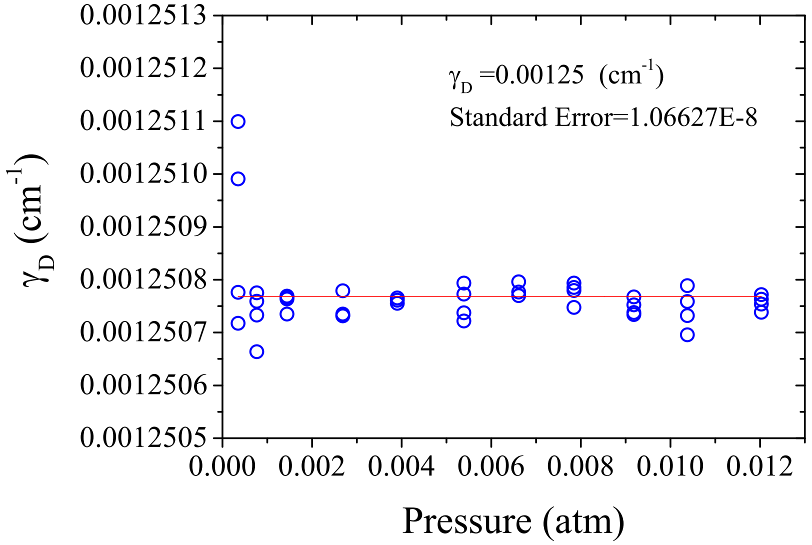

Figure 3.5: Plot of Doppler broadening values (for a single self-broadening value) across all pressures; the averaged value of Doppler width and the standard error is shown in this diagram.

potential, however, it is an approximation which was able to minimize the residuals with smaller RMS value). It is found that $q = 5$, is in agreement with the findings of Hashemi et al. [104].

The bottom panel in the Figure 3.4 shows that at lower pressures, SDV profile can simulate well the recorded spectra within the noise level. It can also be seen the '*w*' shape structure in the center of the residuals especially in pressures above 1 Torr. The collisions induce confinement of molecules by the surrounding molecules, which cause the Doppler contribution of the line shape becomes narrower [30]. To take into account this narrowing parameter a line shape model such as the partially Correlated Speed Dependent Hard Collision (pCSDHC) model [101] is required. To use such a sophisticated profile, high signal to noise is needed which was not achievable in our lab.

In the fitting procedure, both the self-broadening (γ_S) and Doppler broadening (γ_D) are related to the width of the line. Thus, they cannot be fitted simultaneously, as they are highly correlated. To determine a precise value for γ_S, I first calculated the standard deviation of all γ_D values across all pressures for γ_S values and plotted the results. Then fitted these points to a quadratic function and calculated the minimum based on the first derivative of the equation of best fit. The minimum value obtained, served to be the optimum γ_S value. For the obtained γ_S value, I fitted for γ_D and obtained a pressure dependence relationship for γ_D.

Hence, the Doppler width values can be plotted as a function of the gas pressure and, by doing a fit to a linear function, one can take the zero-order coefficient with its statistical uncertainty as a zero-pressure measurement of the Doppler width. This leads to the correct evaluation of the statistical uncertainty. It was found that the zero-order width is equal to 0.00125 cm^{-1} with error about 6.12×10^{-6} cm^{-1}.

The γ_D values were plotted in a diagram with the pressure in one axis. The γ_D value should be constant with pressure as it is only a function of physical constants. Therefore, the correct γ_S coefficient should allow for the retrieval of a constant, γ_D. Figure 3.5 illustrates this where γ_D remains constant as the pressure changes. After finding the ideal value for the self-broadening coefficient, I was able to refit the data and obtain new values for the γ_D. For example for the self-broadening value equal to 0.107 $\mathrm{cm}^{-1}\mathrm{atm}^{-1}$, I obtained the averaged $\gamma_D = 0.0012507$ cm^{-1} with a statistical error of 1.066×10^{-8} cm^{-1}.

The Boltzmann constant was obtained for each of the Doppler width values, and the mean value for k_B was found as shown in Figure 3.6. In this procedure, 44 spectra were used. Using these γ_D values, I calculated k_B using Eq. (3.1) to obtain the accurate values for k_B. It was obtained that in the low pressure the average value of k_B is 1.38066×10^{-23} JK^{-1} for SDV model.

3.3.1 Statistical and Systematic Error Analysis

Determining an accurate value for k_B requires better knowledge of different error sources. Considering Eq. (3.1), the uncertainty of the calculation for k_B is due to the uncertainties in measuring $\tilde{\nu}$, T and γ_D as can be seen in the Eq. (3.2). Moreover, the error resulted from

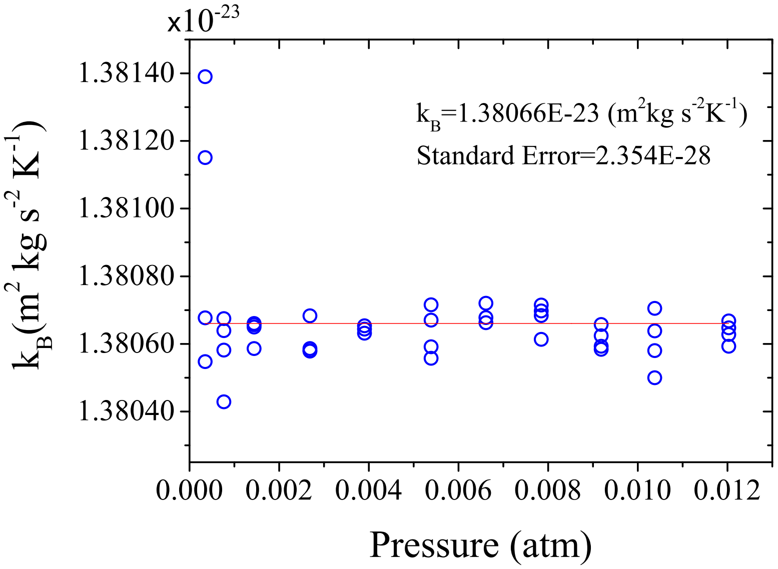

Figure 3.6: Plot of calculated Boltzmann constant values within its mean value and standard error across pressure. The graph shows how at the lowest pressure, because of precision limit of measuring device, the error of k$_B$ is larger.

implemented line shape model should be taken into account. The following expression is used to determine the error in k_B,

$$\frac{\delta_{k_B}}{k_B} = \sqrt{4\left(\frac{\delta_{\gamma_D}}{\gamma_D}\right)^2 + 4\left(\frac{\delta_{\tilde{\nu}}}{\tilde{\nu}}\right)^2 + \left(\frac{\delta_T}{T}\right)^2}. \tag{3.2}$$

To identify the statistical error in temperature, the standard deviation of the mean for temperature was calculated to be 0.005 K. The temperature stability of the inner cell was tested by recording data each 60 second over a time span of about 4 hours. The relative error contribution of temperature stability for room temperature was 1.75×10^{-5}. Also, the error due to the horizontal temperature gradient was considered, and it was obtained that the relative uncertainty was 8.33×10^{-5} for the whole inner chamber. Investigating the vertical temperature gradient resulted in relative error contribution to be 0.00014×10^{-5} which is smaller compared to the horizontal error along the cell. Therefore, the relative error due to the temperature measurement was 8.51×10^{-5}. The statistical errors of the line positions were determined similarly.

The relative uncertainties for the Doppler width (γ_D), position (ν) and temperature (T) which are the most significant error contributors were found to be 0.84×10^{-5}, 0.00038×10^{-5} and 8.51×10^{-5} for the average calculation respectively. Line-center frequency measurement showed that the relative error is 0.00025×10^{-5}. From these errors, the most significant contributor was due to the temperature measurement within this experiment. Using these values the relative error for k_B is 8.54×10^{-5} for SDV model.

Taking into account the different error budgets, the systematic error was also calculated in the measurement. First of all, the combined uncertainty of the temperature measurement and the resistance or voltage measurement can be expressed as an equivalent temperature uncertainty in millikelvin (mK). The uncertainty diversifies with temperature due to the variation of the sensor sensitivity. To read the temperature from the temperature sensor output, a resistance (R) had to be converted to a temperature (T) using a polynomial derive from calibration data. This process created another source of uncertainty on how well the polynomial represents the sensor calibration data. The absolute error was found to be 2.4 mK as the systematic error source of temperature measurement and leads the relative error contribution of 0.81×10^{-5}.

The error of frequency scale measurement that comes from frequency calibration from FP interferometer and EXFO wavemeter was in the order of 10^{-5} cm^{-1}. The wavemeter precision was in the order of 10^{-3} cm^{-1}. However, the calibration processes offer an error in line position about 10^{-5} cm^{-1} using the FP cavity, the wavemeter and channel 2 spectra, gives rise to 1.65×10^{-5} cm^{-1} error in the wavenumber (as it is explained before).

Furthermore, in fitting with the SDV profile, the influence of the type of interaction potential was considered in the analysis. Using $q = 5$ resulted in less error in the simulation of the spectra and its average relative error calculated to be 0.38×10^{-5}.

Based on all these error budgets, the relative error of k_B is 1.87×10^{-5} which is smaller than the obtained statistical error. Combining both types of error, the global error in the calculation of k_B was 8.74×10^{-5}. This error in the measurement was less than the errors reported in the findings of the previous studies by Casa et al. [92] and Djerroud et al. [94]. They have obtained this uncertainty to be 1.6×10^{-4} and 1.9×10^{-4} respectively (it is four times larger than the obtained result by Castrillo et al. [99], where they have obtained the relative uncertainty to be 2.4×10^{-5}).

For this study, accurate line shape parameters have been obtained using Speed Dependent Voigt profile to calculate the value for the Boltzmann constant 1.38066×10^{-23} JK^{-1} with the relative statistical uncertainty of 8.54×10^{-5} at low pressure for the SDV model. Also, the relative systematic error for k_B was 1.87×10^{-5}. Though this value is larger than the reported uncertainty by CODATA, the work is valuable to find out where most of the experimental error originated. The results will be provided in the last chapter. The next chapter is about the particular experiment conducted to do the precise line shape study of carbon monoxide mixed with carbon dioxide gas.

Chapter 4

CO_2 Pressure Broadening and Shift Coefficients for the $2-0$ Band of $^{12}C^{16}O$

The following chapter is reprinted from Journal of Molecular Spectroscopy, 326, 60-72; R Hashemi, A Predoi-Cross, J Vander Auwera et al. 2016, CO_2 Pressure Broadening and Shift Coefficients for the $2-0$ band of $^{12}C^{16}O$, with permission from Elsevier [64]. [4] I did this project as my internship at the University of Brussels in Belgium under the supervision of Dr. Vander Auwera. Discussing different possibilities for performing an experiment at ULB, I decided to work on $2-0$ Band of CO primarily for planetary research interest. I collected the data with help of Dr. Vander Auwera in the Service de Chimie Quantique et Photophysique. I also did data analysis, prepared the results and figures and wrote the manuscript. The theoretical calculations were done by Dr. Dudaryonok and Dr. Lavrentieva. Dr. Vandaele, a scientist from Belgian space agency, who also involved indirectly in this project and provided updates about the SOIR satellite data.

4.1 Introduction

Carbon monoxide (CO) exists in Venus's atmosphere [44], which was until recently probed by the Solar Occultation in the InfraRed (SOIR) instrument on board the ESA Venus Express spacecraft [105]. CO is also presents in the atmosphere of Mars [106], which is studied using the NOMAD instrument on board the ExoMars Trace Gas Orbiter [105]. Because the atmospheres of Venus and Mars are mostly composed of carbon dioxide [45, 107],

---

[4] The copyright permission can be found in Appendix A, Section A.2.

precise spectroscopic line shape parameters of CO perturbed by CO_2 are required to retrieve CO concentrations from SOIR or NOMAD spectra. Knowledge of temperature dependencies of these parameters is also needed since the temperature changes at the altitudes probed by these instruments. For example, the temperature varies in the Venus mesosphere from about 170 to 270 K for altitudes in the range 60-160 km probed by SOIR [108].

Probing carbon monoxide in the atmospheres of Venus and Mars using SOIR or NOMAD relies on the first overtone $(2-0)$ band of $^{12}C^{16}O$, located near 4260 cm^{-1} (2.3 μm) [105]. Table 4.1 summarizes studies carried out for various bands of the primary isotopologue of carbon monoxide, using a different line-shape function. This summary shows that only a few studies have been devoted to the $2-0$ band of $^{12}C^{16}O$ perturbed by CO_2 (CO_2 is the dominant gas in Venus's atmosphere, that's why studying it as a perturber gas is important).

In the context of the SOIR and NOMAD missions, the present work aimed to measure shape-specific parameters of absorption lines of the $2-0$ band of $^{12}C^{16}O$ perturbed by CO_2 and their dependence on temperature. These measurements were carried out by simultaneously fitting 21 spectra of CO/CO_2 mixtures recorded using Fourier transform spectroscopy. Three line shape models have been used to reproduce the observed spectra of carbon monoxide: the Voigt profile (VP) [67], the Rautian profile (RP) [69] to account for Dicke narrowing effects [30], and the quadratic Speed Dependent Voigt profile (qSDV) [119, 120] to account for the dependence of line shape parameters on the relative speed of the molecules.

CO_2 pressure-induced broadening and shift coefficients of the lines of $^{12}C^{16}O$ have been determined, together with the temperature dependence of these parameters. Also, line mixing (LM) coefficients have been measured using all three line shape profiles [71]. The retrieved parameters were then compared with CO_2 broadening and shift coefficients calculated using a semi-empirical method. The method used is based on the impact theory of broadening and includes correction factors, the parameters of which are determined by fit-

Table 4.1: Previous studies on different bands of $^{12}C^{16}O$. T is the temperature ("RT" = room temperature), and BP, GP, HC_vP, LRCG, LP, SDVP and VP represent the Benedict, the Galatry, an empirical Hard Collision and Speed Sependent Lorentz, the Ladenburg Reiche Curve of Growth, the Lorentz, the Speed Dependent Voigt and the Voigt profiles, respectively.

Author(s)	Band(s)	Perturber(s)	T / K	Line-shape
Varanasi, 1971 [109]	1 – 0 2 – 0	CO, N_2, CO_2	295	LRCG
Bouanich, 1972 [110]	2 – 0	He, Ne, Ar, Kr, Xe	300	–
Bouanich & Brodbeck, 1973 [111]	2 – 0	CO, N_2, O_2, HCl, NO, CO_2	299	–
Varanasi, 1975 [9]	1 – 0	CO_2 CO	200 – 300 100 – 300	LRCG
Varanasi and Sarangi, 1975 [112]	1 – 0	N_2	83 – 300	LRCG
Nakazawa and Tanaka, 1982 [11]	1 – 0	CO, N_2, O_2, CO_2	300	LP, BP
Bouanich, 1983 [113]	2 – 0	N_2, CO	133 – 298	LP
Bouanich, 1984 [114]	2 – 0	CO	85 – 298	LP
Bouanich *et al.*, 1996 [115]	2 – 0	CO He, Kr, O_2, N_2	296	LP
Predoi-Cross *et al.*, 2000 [13]	2 – 0	CO N_2	296 303	VP LP, HC_vP
Zou and Varanasi, 2002 [116]	1 – 0 2 – 0	CO, air	174-296	VP
Brault *et al.*, 2003 [14]	2 – 0	CO	297 – 301	VP, SDVP
Sung *et al.*, 2005 [10]	1 – 0 2 – 0 3 – 0	CO_2	201 – 300 298 298	VP
Colmont *et al.*, 2007 [117]	0 – 0	N_2, O_2, CO_2 He, Ne, Ar, Kr, Xe	RT	VP, GP, SDVP
Devi *et al.*, 2012-13 [12, 118]	2 – 0	CO, air	150-298	SDVP

ting the calculated broadening or shift coefficients to the experimental data. To compare the theoretical and experimental results, line-shape-specific parameters had to be measured for each temperature. Finally, the Exponential Power Gap (EPG) law has been used to obtain weak CO_2 line mixing coefficients and CO_2 broadening parameters at different temperatures.

4.2 Experimental details

High resolution absorption spectra of the $2-0$ band of carbon monoxide (Matheson, 99.9 % purity) mixed with carbon dioxide (Sigma Aldrich, 99.8 % purity) at total pressures ranging from 156 to 1212 hPa (117 to 909 Torr) and at 4 different temperatures between about 240 K and 283 K have been recorded using a Bruker IFS 120 which was upgraded to a 125 HR Fourier transform spectrometer. The instrument was fitted with a Tungsten source, an entrance aperture with diameter set to 1.00 or 1.15 mm, a CaF_2 beamsplitter, a band-pass filter limiting the transmission to the $3980-5100$ cm^{-1} range, and an InSb detector cryogenically cooled to 77 K. The temperatures, total pressures, CO mole fractions (χ), maximum optical path differences (δ_{max} which will be defined later in this section), and diameters of the entrance aperture of the spectrometer used for each measurement are listed in Table 4.2.

The review of Fourier transform spectrometery (FTS) is reduced to a brief overview of the features related to our research since there are reasonably reliable descriptions accessible in the literature [121–123]. The Bruker IFS125HR spectrometer is used here, which is a Michelson interferometer [124], and consists of a beamsplitter dividing a incident light beam into two parts. There are two reflecting mirrors; one fixed and the other one moving and sending back the beams to the beamsplitter. Therefore, the two beams travel two different paths, leading to constructive and destructive interference. The optical path difference is obtained using $\delta_{OP} = 2[x_2 - x_1]$ where x_1 and x_2 present the travelled distances from the beamsplitter to the fixed and moving mirrors.

The interferometer of the FTS at University of Brussels (ULB) includes the source compartment, the interferometer, the sample chamber, and the detectors. The incident light is focused on an iris (with varying size between 0.5 to 12 mm). It is then collimated into a beam with 7 cm diameter to be input of the Michelson interferometer. Upon exiting the interferometer, the beam then goes to the sample chamber and reaches to the detector. A schematic diagram of the FTS at ULB is shown in Figure 4.1.

A Fourier transform spectrometer can produce a cosine Fourier transform of the input beam (with spectral irradiance $B(\tilde{\nu})$) over different values of δ as optical path difference [121],

$$I'(\delta) = \int B(\tilde{\nu})[1 + cos(2\pi\tilde{\nu}\delta)]d\tilde{\nu}. \tag{4.1}$$

The modulated part is written as

$$I(\delta) = \int B(\tilde{\nu})cos(2\pi\tilde{\nu}\delta)d\tilde{\nu}, \tag{4.2}$$

where $I(\delta)$ is called the interferogram. If we obtain its Fourier transform,

$$\tilde{B}(\tilde{\nu}) = \int I(\delta)\exp(-2i\pi\tilde{\nu}\delta)d\delta. \tag{4.3}$$

Then the spectral distribution of radiation can be recovered. Regarding optical path

Table 4.2: Experimental conditions, temperature (T in Kelvin), total pressure P_{tot} (hPa), CO mole fraction (x), Maximum Optical Path Difference (MOPD in cm), diameter of the entrance aperture of the spectrometer (iris in mm).

#	T	P_{tot}	x	MOPD	iris
1	283.2 (10)	156.5 (8)	0.092	112.5	1.00
2	283.4 (10)	333 (2)	0.043	112.5	1.00
3	283.4 (10)	660 (3)	0.061	112.5	1.00
4	283.4 (10)	931 (5)	0.043	112.5	1.00
5	283.4 (10)	961 (5)	0.084	112.5	1.00
6	283.4 (10)	1198 (6)	0.067	112.5	1.00
7	270.0 (10)	165.9 (8)	0.081	112.5	1.00
8	270.0 (10)	334 (2)	0.040	112.5	1.00
9	270.0 (10)	331 (2)	0.118	112.5	1.00
10	270.0 (10)	653 (3)	0.060	112.5	1.00
11	270.0 (10)	938 (5)	0.092	112.5	1.00
12	270.0 (10)	1212 (6)	0.071	112.5	1.00
13	255.4 (15)	167.9 (8)	0.219	90.0	1.00
14	255.4 (15)	333 (2)	0.111	36.0	1.00
15	255.4 (15)	601 (3)	0.061	18.0	1.15
16	255.4 (15)	927 (5)	0.100	18.0	1.15
17	255.4 (15)	1199 (6)	0.078	18.0	1.15
18	240.5 (20)	333 (2)	0.106	36.0	1.15
19	240.5 (20)	667 (3)	0.053	18.0	1.15
20	240.5 (20)	665 (3)	0.129	18.0	1.15
21	240.5 (20)	934 (5)	0.092	18.0	1.15

Note the resolution is equal to $0.9/\delta_{max}$. The numbers between parentheses represent the absolute uncertainty in units of the last digit quoted. The uncertainty given for the sample pressure is conservatively estimated to be 0.5% of reading. The mole fractions χ are equal to ratio of the pressure of carbon monoxide, measured when filling the cell, to the total pressure. The measured temperature span only covers small range of temperature in Venus's atmosphere, that we were able to achieve in our lab.

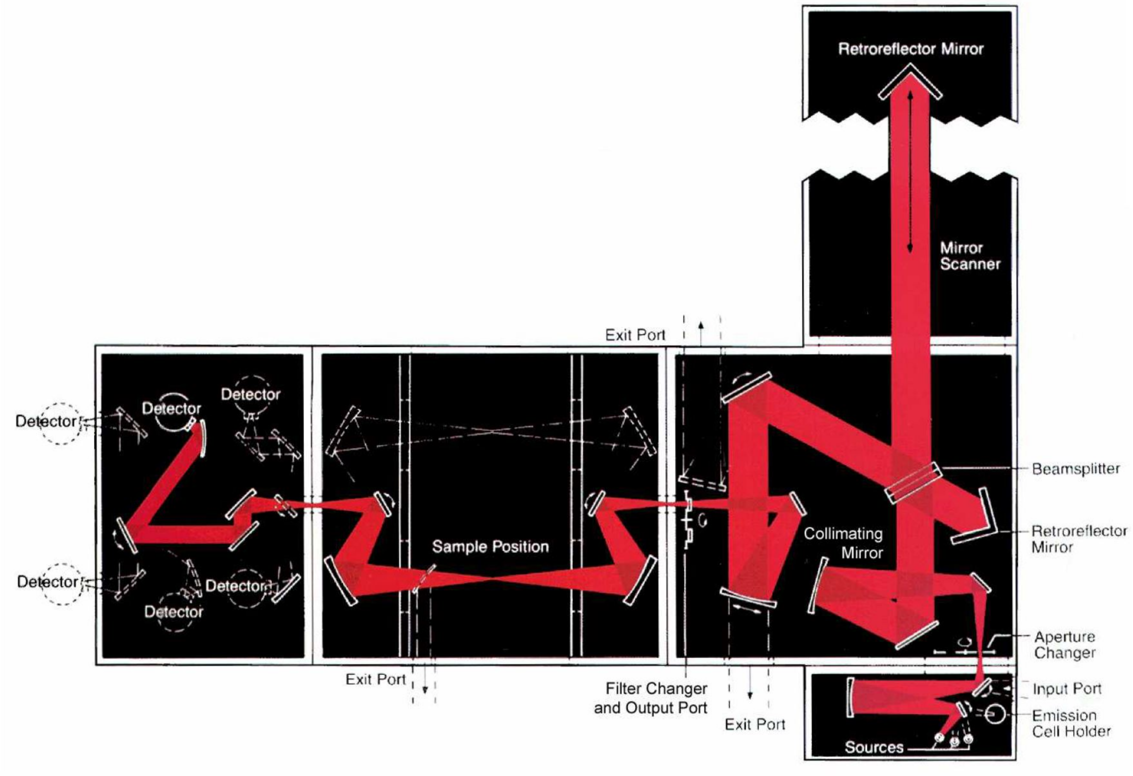

Figure 4.1: Different components of the FTS at ULB. This figure is taken from Ref. [8] created by Dr. Vander Auwera.

difference, this equation needs both the negative and positive sides up to $\delta_{max} = \infty$.

Because the continuous functions can be split into the summation of an even and an odd part,

$$I(\delta) = \frac{1}{2}[I(\delta) + I(-\delta)] + \frac{1}{2}[I(\delta) - I(-\delta)] = E(\delta) + O(\delta). \tag{4.4}$$

Then it can be written as

$$\tilde{B}(\tilde{\nu}) = 2\int E(\delta) cos(2\pi\tilde{\nu}\delta) d\delta - 2i \int O(\delta) sin(2\pi\tilde{\nu}\delta) d\delta. \tag{4.5}$$

The $\tilde{B}(\tilde{\nu})$ is real (and even) in case the interferogram is an even function and it is complex if not. If it is an even function for instance, the spectrum is then computed using the cosine Fourier transform,

$$\tilde{B}(\tilde{\nu}) = 2\int I(\delta) cos(2\pi\tilde{\nu}\delta) d\delta. \tag{4.6}$$

Theoretically, $\tilde{B(\tilde{\nu})}$ is indistinguishable with $B(\tilde{\nu})$. Nevertheless, there are a few experiential issues that cause $\tilde{B(\tilde{\nu})}$ be different from the true spectrum $B(\tilde{\nu})$. The truncation of the interferogram, the finite size of the source, phase errors, and optical misalignment are examples. FTS offers several advantages such as the quality of collected spectra and high signal to noise ratio, the speed of spectral recording, the high accuracy of the wavelength measurement, and data reproducibility. Refs [121–123] are suggested for more details.

The gas mixtures were directly prepared in a 19.7 (2) cm long double jacketed stainless steel cell, closed by CaF_2 windows and located inside the evacuated spectrometer. The temperature of the cell was stabilized using methanol circulating in the double cell wall and an external NESLAB, model ULT-80. It was measured using two thermocouples fixed on the outside cell wall, at each end of the cell. The gas pressures were measured using two absolute MKS Baratron gauges model 690A, of 10 and 1000 Torr full-scale ranges. A total of 21 spectra were recorded. Transmittances were generated for all the spectra using empty cell spectra recorded at a lower resolution.

The alignment of the interferometer was checked just before recording the spectra reported in this work. The wavenumber scale was confirmed to be the same, taking into account the changes of the point spacing resulting from the various maximum optical path differences used.

4.3 Analysis of the spectra

All the measurements performed in the present research involved the analysis of the entire $2-0$ band of $^{12}C^{16}O$ at once, in the range from 4157 to 4332 cm^{-1}. CO_2 broadening and shift coefficients of the P(22) to R(22) lines, together with the temperature dependence of these parameters and first-order line mixing coefficients [71], have been measured using a multi-spectrum fitting program developed in Brussels [125, 126]. The software adjusts a synthetic spectrum to each of any number of observed Fourier transform spectra, using a Levenberg-Marquardt least-squares fitting procedure. Each synthetic spectrum, interpo-

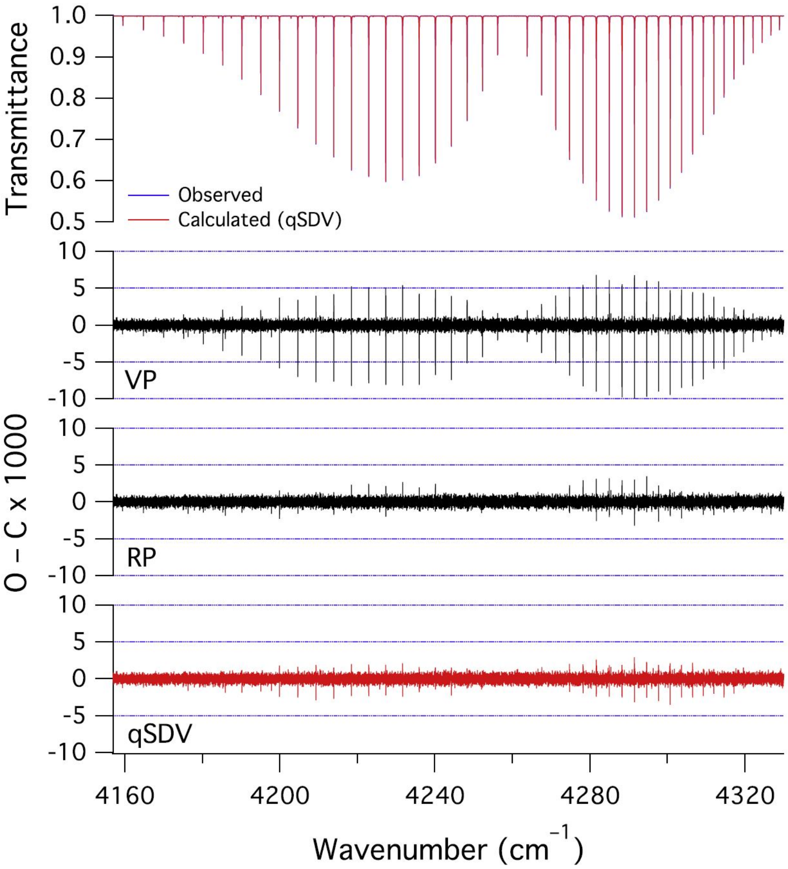

Figure 4.2: Transmittance spectrum of the $2-0$ band of $^{12}C^{16}O$ broadened by CO_2, observed [156.5 (8) hPa, No. 1 in Table 4.2] and best-fit calculated at the same conditions using the qSDV line shape model. The lower graphs present the residuals for the displayed spectrum of the multi-spectrum analysis of the 21 spectra listed in Table 4.2 with the VP, RP and qSDV line shape models.

lated 4 times with respect to the observed spectrum, is calculated as the convolution of a monochromatic transmission spectrum with an instrument line shape function, which includes the effects of the finite maximum optical path difference and of the finite size of the entrance aperture in the interferometer as fixed contributions [127]. In the present work, the Gaussian width of the line shape models used was always held fixed to the value calculated for the Doppler broadening. The pressure-induced widths b_L and shifts $\Delta\tilde{\nu}$ of the CO

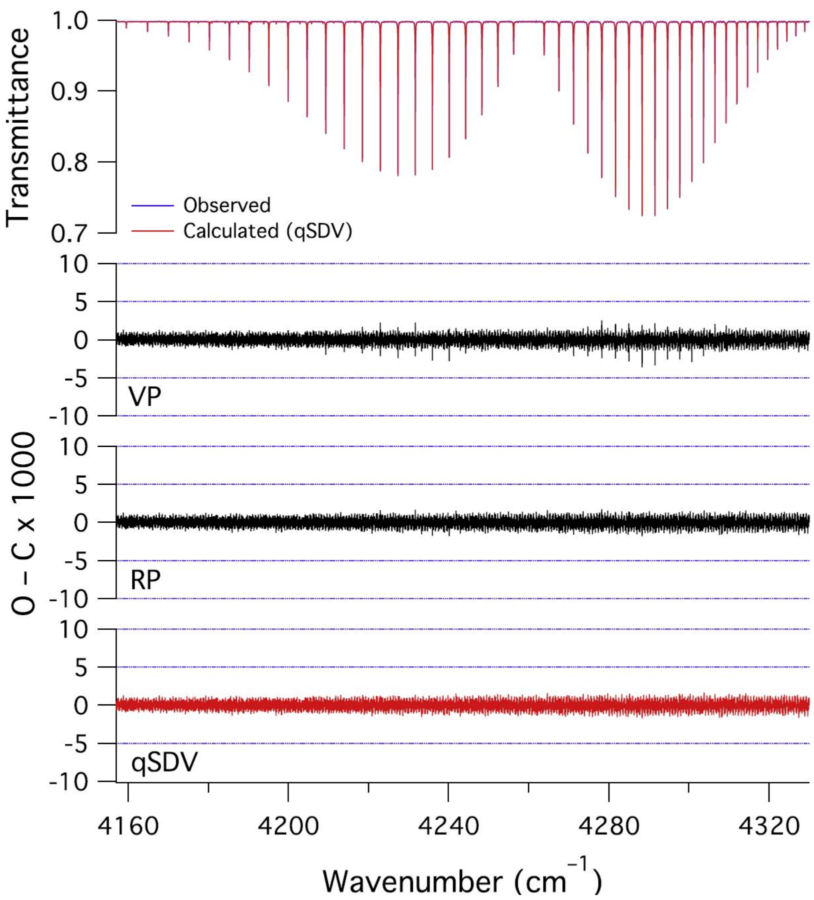

Figure 4.3: Same as Figure 4.2 for spectrum No. 8 in Table 4.2 [334 (2) hPa].

absorption lines were modelled using the following expressions,

$$b_L = P_{tot}\left[b_L^0(\mathrm{CO}-\mathrm{CO_2})(1-x)(T_0/T)^{n_1} + b_L^0(\mathrm{self})\,x\,(T_0/T)^{n_2}\right], \tag{4.7}$$

$$\Delta\tilde{\nu} = P_{tot}\left[d^0(\mathrm{CO}-\mathrm{CO_2})(1-x) + d^0(\mathrm{self})\,x\right], \tag{4.8}$$

$$d^0(T) = d^0(T_0) + d'(T-T_0), \tag{4.9}$$

where P_{tot} is the total sample pressure, $T_0 = 296$ K, x is the mole fraction of CO, and $b_L^0(\mathrm{CO}-\mathrm{CO_2})$, $b_L^0(\mathrm{self})$, $d^0(\mathrm{CO}-\mathrm{CO_2})$ and $d^0(\mathrm{self})$ are the CO_2 broadening, self broadening, CO_2 shift, and self shift coefficients of the CO lines, respectively. Parameters n_1 and n_2 are the temperature dependence exponents of the CO_2- and self-broadening coefficients of the CO lines, respectively, and d' quantifies the temperature dependence of the line shift

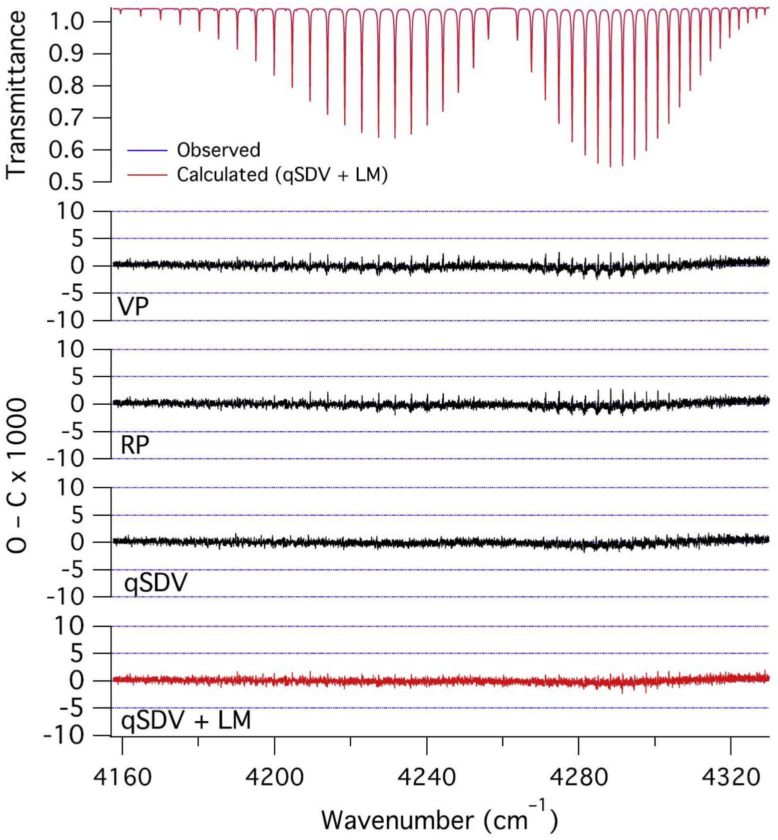

Figure 4.4: Transmittance spectrum of the $2-0$ band of $^{12}C^{16}O$ broadened by CO_2, observed [1199 (6) hPa, No. 17 in Table 4.2] and best-fit calculated at the same conditions using the qSDV line shape model with weak line mixing. The lower panels present the residuals for the displayed spectrum of the multi-spectrum analysis of the 21 spectra listed in Table 4.2 with the VP, RP and qSDV line shape models, and the qSDV line shape model with weak line mixing. The remaining residual shows the limit of fit quality and the knowledge on the temperature dependence of line mixing effect.

coefficients. Although the latter was not measured in the present work for the CO_2 shift coefficients of the $^{12}C^{16}O$ lines, the temperature dependence of the self shift coefficients of these lines was set to available literature information.

The positions and intensities of the $^{12}C^{16}O$ lines were fixed to the values available in HITRAN [128] (note that they are actually from Farrenq *et al.* [129] and Devi *et al.* [118], respectively). The self-broadening and self-shift coefficients were fixed to the values reported by Brault *et al.* [14] (Table 7), while their temperature dependencies were set to the values of Devi *et al.* [118]. Initial values of the CO_2 broadening and shift coefficients were taken from Sung and Varanasi [10]. Lines not measured by these authors were given the approximate initial values of 0.06 $\mathrm{cm^{-1}atm^{-1}}$ and -0.005 $\mathrm{cm^{-1}atm^{-1}}$, respectively, estimated from the results reported by Sung and Varanasi [10].

To properly model the $2-0$ band of $^{12}C^{16}O$ at higher pressure, first-order line mixing [71] was included for the P- and R-branch lines, according to (see for example [130]). The first-order line mixing approach is appropriate for moderate line overlapping cases as of this study,

$$g_k^{LM} = \mathrm{Re}(g_k) + Y_k \,\mathrm{Im}(g_k), \tag{4.10}$$

where g_k^{LM} represents the profile of line k affected by line mixing, and $\mathrm{Re}(g_k)$ and $\mathrm{Im}(g_k)$ are the real and imaginary parts of the normalized line shape function, respectively. The quantity $Y_k^0 = Y_k/P$ is the so-called first-order line mixing coefficient [see Eq. (4.20) in section 4.5].

Absorption lines of the $2-0$ band of $^{13}C^{16}O$ were also observed in the spectra. Their parameters were taken from HITRAN [128]. Because of the weakness of the corresponding absorption, the CO_2-related line shape parameters were assumed to be equal to the corresponding coefficients provided for air as the perturber gas in HITRAN. To correctly model the $^{13}C^{16}O$ absorption, it was found necessary to fit the corresponding line intensities. Because some of the $^{13}C^{16}O$ lines are overlapped by stronger lines of the main isotopologue, we used the same strategy as recently done for weak hot bands of CO_2 [126]. It involved adjusting the intensities of all the lines of the $2-0$ band of $^{13}C^{16}O$ simultaneously through fitting of the square of the transition dipole moment of that band (see Eqs. 2 and 3 of [126]). The initial values of the parameters involved in that latter quantity, i.e., the square of the rotationless transition dipole moment and HermanWallis coefficients, were determined by fitting the line intensities available in HITRAN [128].

The temperature dependence of the line intensities was accounted for using the lower level energies available in HITRAN [128], and partition functions calculated using the program `TIPS` [131] (June 2011 version) provided with HITRAN. In addition to the parameters describing the CO_2 pressure induced effects on the shape of $^{12}C^{16}O$ lines, the measurements performed required adjusting the following parameters. The baseline in each spectrum was modelled with a polynomial expansion, involving 1 to 3 fitted parameters. The mole fraction of carbon monoxide in each spectrum was adjusted. Although the line positions were fixed to literature values ($\tilde{\nu}_{lit}$), they were matched to all the spectra by application of the expression $\tilde{\nu}_m = \tilde{\nu}_{lit}\ (1 + C)$, where $\tilde{\nu}_m$ are the line positions matched to all the spectra and the factor C was fitted. This solution was preferred to over fitting the individual line positions because low-pressure spectra were not available.

To compare the results of the multi-spectrum analysis of the 21 spectra listed in Table 4.2 with the VP, RP and qSDV line shape models without first-order line mixing, Figures 4.2 to 4.4 present the residuals obtained for 3 spectra corresponding to the lowest total pressure achieved in this work, an intermediate and a high total pressure, respectively. The residuals presented in Figure 4.2 show that, at low pressure, the observed line shapes are narrower than the VP (although not apparent on the figure, the residuals exhibit the characteristic 'w'-shape). The residuals obtained for the RP and qSDV do however not allow discriminating between these 2 line shape models. Figure 4.3 shows that similar results are obtained at intermediate total pressures, even though the signatures in the residuals are significantly smaller. At high pressure, Figure 4.4 shows that the qSDV line shape model, with or without first-order line mixing, best reproduces the observed line profiles.

4.4 Results of the measurements

4.4.1 CO_2 broadening and shift coefficients

The CO_2 pressure broadening coefficients measured in the present work for $^{12}C^{16}O$ are gathered in Table 4.3 (see Appendix A for the complete list of lines and results). They are depicted and compared with previous studies in Figure 4.5. The broadening coefficients decrease with increasing $|m|$ (throughout the article, $m = -J''$ and $J'' + 1$ for $P-$ and $R-$ branch lines, respectively) and the values retrieved with the qSDV model are slightly larger than obtained with the VP line shape model, as expected. The reason for this discrepancy lies in the narrower absorption line shape obtained with speed-dependent effects compared to the Voigt profile. As a result, the absorption peak is higher and hence higher broadening values are obtained for the qSDV profile.

Table 4.3: CO_2 broadening coefficients at 296 K and their temperature dependence measured for the $2-0$ band of $^{12}C^{16}O$ by multi-spectrum fitting 21 FTS spectra using the VP, RP and qSDV profiles

	$b_L^0(CO - CO_2)$ ($cm^{-1}atm^{-1}$)			n_1		
Line	VP (unc)	RP (unc)	qSDV (unc)	VP (unc)	RP (unc)	qSDV (unc)
P(22)	0.05820 (41)	0.05506 (36)	0.06041 (44)	0.648 (66)	0.711 (63)	0.704 (55)
P(21)	0.05693 (27)	0.05502 (24)	0.05755 (28)	0.753 (43)	0.803 (41)	0.761 (38)
P(20)	0.05845 (19)	0.05747 (17)	0.05979 (21)	0.694 (29)	0.740 (27)	0.712 (25)
P(19)	0.05975 (14)	0.05904 (13)	0.06133 (15)	0.713 (21)	0.764 (19)	0.725 (18)
P(18)	0.06029 (10)	0.05990 (9)	0.06183 (11)	0.710 (15)	0.745 (14)	0.722 (13)
P(17)	0.06154 (8)	0.06137 (7)	0.06296 (9)	0.694 (11)	0.728 (10)	0.704 (10)
P(16)	0.06223 (6)	0.06226 (6)	0.06358 (7)	0.710 (8)	0.739 (8)	0.717 (7)
P(15)	0.06300 (5)	0.06336 (5)	0.06419 (5)	0.729 (7)	0.746 (6)	0.730 (6)

$'unc'$ are the statistical uncertainties (1σ) estimated by the least squares fitting procedure.

The present results are in excellent agreement with the CO_2 broadening coefficients reported by Sung and Varanasi [10], with improved uncertainties. The measured CO_2 broadening values with qSDV line shape are larger than the ones measured with VP and RP line shapes. The speed dependent effects result in narrower line shapes compared to those found by using the Voigt and Rautian profiles. Then the absorption peak would be higher and results in higher broadening values. The temperature dependence of the CO_2 broadening coefficients measured in this work using the 3 line shape models is presented in Figure 4.6 and listed in Table 4.3. Interestingly, the present measurements exhibit an intensity dependence, similar to the three line shape models. This dependence may also be seen in the measurements reported for the fundamental band by Sung and Varanasi [10]. The results reported by Nakazawa and Tanaka [11] for the *R* branch of the fundamental band do exhibit a minimum for the same *m* value as in the present work, but not at higher *J*. The present results are improved by at least one order of magnitude compared to previous

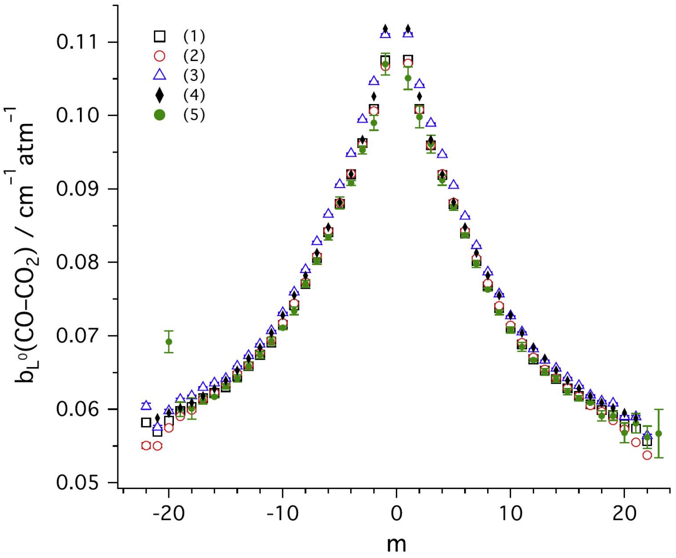

Figure 4.5: CO_2 broadening coefficients for the $2-0$ band of $^{12}C^{16}O$ at 296 K measured in this work with the VP (1), RP (2) and qSDV (3) line shape models, and in previous studies (4: at 299 K [9]; 5: at 298 K using a VP [10]). The error bars associated with the present measurements represent the uncertainty of measurement (1σ), estimated by the least squares fitting algorithm. The measured CO_2 broadening values with qSDV line shape are larger than the ones measured with VP and RP line shapes.

studies.

The measured CO_2 shift coefficients are gathered in Table 4.4 and are compared with previous results in Figure 4.7. The three sets of measurements are more precise (by a factor of 5) than the ones reported by Sung and Varanasi [10]. The reason may lie in the systematic discrepancies among the experimental conditions such as the temperature measurements and the used line shape in the modelling (i.e., Sung and Varanasi [10], have used the Voigt profile in modelling the observed spectra).

To allow comparisons with the theoretical calculations, the CO_2 broadening and shift coefficients were also measured using the qSDV line shape model including first-order line mixing, separately at each of the four temperatures. The results of these measurements are reported in Tables 4.5, 4.6 and 4.11 (see Appendix A for the complete list of lines and results).

4.4.2 Speed dependence of CO_2-broadening coefficients and first-order line mixing

The speed dependence of the CO_2-broadening coefficients and the first-order line mixing coefficients obtained in this work using the qSDV profile are listed in Table 4.7. Based on these results, the speed-dependent parameter depends on angular momentum as the line broadening parameter is *J* dependent, so is the speed-dependent parameter. Broadening and speed dependence is linked to the collisions, and the impact of collisions change when the angular momentum is changing.

The former parameters, divided by the corresponding CO_2-broadening coefficients, are compared in Figure 4.8 with the speed dependence coefficients reported by Devi et al. [12] for pure CO and a CO-air mixture (the speed dependence was assumed to be independent of the perturber gas in that work). The rotational dependence of both sets of coefficients agrees very well, the values in the present work are about 50% larger because of the effect of the mass of the different broadener used in the study by Devi et al. [12] (the discrepancy in results for different molecular systems is due to having different mass, moment of inertia, and absorber-perturber intermolecular potentials).

Table 4.4: CO_2 line shift coefficients for the $2-0$ band of $^{12}C^{16}O$ measured by multi-spectrum fitting 21 FTS spectra using the VP, RP and qSDV profiles

Line		$d^0(CO - CO_2)$ ($cm^{-1}atm^{-1}$)		
	$\tilde{\nu}$ (cm^{-1})	VP (unc)	RP (unc)	SDV (unc)
P(22)	4159.5595	−0.00748 (25)	−0.00735 (22)	−0.00750 (21)
P(21)	4164.8408	−0.00676(16)	−0.00659 (15)	−0.00673 (14)
P(20)	4170.0551	−0.00637 (11)	−0.00628 (10)	−0.00627 (10)
P(19)	4175.2024	−0.00685 (8)	−0.00675 (8)	−0.00673 (7)
P(18)	4180.2825	−0.00701 (6)	−0.00694 (6)	−0.00687 (5)
P(17)	4185.2952	−0.00698 (5)	−0.00692 (4)	−0.00688 (4)
P(16)	4190.2404	−0.00669 (4)	−0.00663 (3)	−0.00657 (3)
P(15)	4195.1180	−0.00633 (3)	−0.00630 (3)	−0.00624 (3)

’unc’ are the statistical uncertainties (1σ) estimated by the least squares fitting procedure.

The first-order line mixing coefficients determined for the 3 line shape models are presented and compared with previous studies [12–14] in Figure 4.9. Even though the obtained values are small, taking the line mixing effects into account was vital as they affect the measured CO_2 shift coefficients. All the reported Y_k^0 coefficients follow a similar rotational dependence and agree quite well. The measurements reported for a CO-air mixture [12] and pure CO [12, 14] agree very well, even though weak line mixing coefficients for different perturbers are not expected to be the same. The measurements for CO-N_2 by Predoi-Cross et al. [13] tend to be systematically lower. The present results (for CO-CO_2) in the P branch are in better agreement (with improved uncertainty) with Brault et al. [14] and Devi et al. [12] than with Predoi-Cross et al. [13], while the opposite is observed for the *R* branch. These observations may be an indication of the difficulties to retrieve first-order line mixing coefficients from measured spectra.

Table 4.5: CO_2 broadening coefficients measured for the $2-0$ band of $^{12}C^{16}O$ using the qSDV profile by multispectrum fitting all the spectra recorded at each temperature

	$b_L^0(CO - CO_2)$ $(cm^{-1}atm^{-1})$			
Line	283.4	270.0	255.4	240.5
P(22)	0.0603 (150)	0.0609 (100)	0.0586 (120)	0.0626 (130)
P(21)	0.0571 (22)	0.0580 (30)	0.0596 (73)	0.0545 (190)
P(20)	0.0604 (20)	0.0589 (22)	0.0596 (49)	0.0618 (160)
P(19)	0.0607 (12)	0.0616 (17)	0.0621 (37)	0.0605 (75)
P(18)	0.0621 (10)	0.0615 (12)	0.0612 (26)	0.0628 (64)
P(17)	0.0629 (6)	0.0626 (9)	0.0631 (20)	0.0630 (42)
P(16)	0.0633 (6)	0.0635 (7)	0.0636 (16)	0.0634 (33)
P(15)	0.0639 (4)	0.0643 (5)	0.0640 (13)	0.0640 (26)

'unc' are the statistical uncertainties (1σ) estimated by the least squares fitting procedure.

4.4.3 Narrowing parameters and Mass diffusion coefficient

The narrowing coefficients β^0 measured using the RP (Rautian-Sobelman) line shape model are also listed in Table 4.7 and presented in Figure 4.10. Displayed in Figure 4.10, is the dynamic friction coefficient β^0_{diff}, deduced from the relation [132, 133],

$$\beta^0_{\text{diff}} = \frac{k_B T}{2\pi c\, m_1 D_{12}}, \tag{4.11}$$

where k_B is the Boltzmann constant, T is the temperature, c is the velocity of light, m_1 is the mass of the active molecule, and D_{12} is the mass diffusion coefficient of $CO-CO_2$ binary system. The latter was estimated at 296 K and 1 atm using the expression [133, 134]

$$D_{12} = \frac{\varepsilon_D k_B^{3/2}}{\sqrt{\pi}\sigma_{12}^2 \Omega_{12}^{(1,1)}(T_{12}^*)} \sqrt{T^3 \frac{M_1+M_2}{2M_1M_2}}, \tag{4.12}$$

where $\varepsilon_D = 3/8$ [134], M_1 and M_2 are the molecular weights of CO and CO_2, $\Omega_{12}^{(1,1)}(T_{12}^*)$ is a dimensionless reduced collision integral function of the reduced temperature, $T_{12}^* = k_B T/\varepsilon_{12}$; σ_{12} and ε_{12} are scaling parameters for the spherical part of the interaction potential. Using ε_{12}/k_B=155.2 K and $\varepsilon_{12} = 3.711 \times 10^{-8}$ cm, we obtained $D_{12} = 0.103$ and 0.140 $cm^{-2}s^{-1}$, at the lowest (240.5 K) and highest (283.4 K) temperatures achieved experimentally, leading to $\beta^0_{diff} = 0.0368$ and 0.0320 $cm^{-1}atm^{-1}$ respectively. Note that, as already indicated, measurements with the RP line shape model were carried out assuming that the narrowing coefficient β^0 was independent of temperature. As also observed for example for self-broadened O_2 [135], the measured narrowing coefficients presented in Figure 4.10 seem to indicate that the narrowing effect induced by velocity changing collisions decreases with increasing m. Technically, for the higher J values, the narrowing parameter should be larger than the ones for the lower Js. Because as the J values increases, the molecule rotates faster and as a result narrowing effect should be more. However, as Figure 4.10 shows, most of the larger measured narrowing parameters are associated with lower Js and except few values at high J, the measured narrowing coefficients are larger than the theoretical β^0_{diff}, which indicates that the broadening coefficients may be affected by speed dependence [135] and that the RP line shape model is probably not appropriate. The obtained results

Experiments and theoretical calculations are complimentary for determining the line shape parameters. Theoretical calculations of line shape parameters for some cases are complicated to be performed directly in the line-by-line simulations. Typically, the experimentalists measure some of the lines in the lab and provide the results to the theoreticians to be used in modelling and calculation of line lists.

4.5 Theoretical calculations of CO_2-broadened and CO_2-shift coefficients

To calculate the CO_2 broadening and shift coefficients of rovibrational lines of carbon monoxide, two known approaches were used: a technique [136] that incorporates correction factors the parameters of which being determined by fitting calculated broadening or shift coefficients to experimental data, and the Exponential Power Gap (EPG) law.

Table 4.6: CO_2 shift coefficients measured for the $2-0$ band of $^{12}C^{16}O$ using the qSDV profile by multi-spectrum fitting all the spectra recorded at each temperature

Line		$d_0(T)(\mathrm{CO}-\mathrm{CO_2})$ ($\mathrm{cm^{-1}atm^{-1}}$)			
	$\tilde{\nu}$ ($\mathrm{cm^{-1}}$)	283.4	270.0	255.4	240.5
P(22)	4159.5595	−0.00749 (28)	−0.00716 (34)	−0.00881 (64)	−0.00721 (130)
P(21)	4164.8408	−0.00635 (19)	−0.00686 (23)	−0.00758 (43)	−0.00751 (74)
P(20)	4170.0551	−0.00605 (14)	−0.00622 (16)	−0.00708 (29)	−0.00661 (52)
P(19)	4175.2024	−0.00644 (10)	−0.00675 (11)	−0.00745 (21)	−0.00725 (36)
P(18)	4180.2825	−0.00662 (8)	−0.00667 (8)	−0.00769 (15)	−0.00795 (25)
P(17)	4185.2952	−0.00668 (6)	−0.00686 (6)	−0.00722 (11)	−0.00770 (18)
P(16)	4190.2404	−0.00640 (5)	−0.00650 (5)	−0.00696 (9)	−0.00721 (14)
P(15)	4195.1180	−0.00598 (4)	−0.00616 (4)	−0.00688 (7)	−0.00671 (11)

’unc’ are the statistical uncertainties (1σ) estimated by the least squares fitting procedure.

4.5.1 Calculations of CO_2 broadening and CO_2 shift coefficients with the straight-line trajectory approximation

To calculate the CO_2 broadening and shift coefficients of rovibrational lines of carbon monoxide, a technique is used [136] that is performed in the framework of the binary impact approximation. The well-known general assumptions of the theory are the following:

Table 4.7: Speed dependence of the broadening (SDB) coefficients and weak line mixing (LM) parameters, and narrowing parameters (in $cm^{-1}atm^{-1}$) measured for the $2-0$ band of $^{12}C^{16}O$ by multi-spectrum fitting 21 FTS spectra with the qSDV and RP models, respectively

Line		qSDV		RP
	$\tilde{\nu}$ (cm^{-1})	SDB	LM	Narrowing
P(22)	4159.5595	0.0112 (56)	−0.0086 (26)	0.028 (11)
P(21)	4164.8408	0.00351 (58)	0.0009 (17)	0.007 (5)
P(20)	4170.0551	0.00751 (32)	−0.0002 (12)	0.027 (5)
P(19)	4175.2024	0.00849 (23)	−0.0010 (8)	0.046 (5)
P(18)	4180.2825	0.00843 (17)	0.0013 (6)	0.034 (3)
P(17)	4185.2952	0.00800 (13)	0.0047 (4)	0.043 (3)
P(16)	4190.2404	0.00776 (11)	0.0018 (3)	0.043 (2)
P(15)	4195.1180	0.00696 (9)	−0.0030 (3)	0.043 (2)

’unc’ are the statistical uncertainties (1σ) estimated by the least squares fitting procedure.

the collisions are considered to be binary, the duration of a collision is less than the time between collisions of molecules, colliding particles are assumed to follow classical, prescribed paths, and no line mixing effects occur. In this case, the general equations for the CO_2-broadened halfwidth γ_{if} and CO_2-broadened shift δ_{if} of the transition $i \to f$ can be written as

$$\gamma_{if} = A(i,f) + \sum_{i'} D^2(ii'|l)P_l(\omega_{ii'}) + \sum_{f'} D^2(ff'|l)P_l(\omega_{ff'}), \tag{4.13}$$

$$\delta_{if} = B(i,f) + \sum_{i'} D^2(ii'|l)P_l(\omega_{ii'}) + \sum_{f'} D^2(ff'|l)P_l(\omega_{ff'}). \tag{4.14}$$

Here,

$$A(i,f) = n/c \sum_{2} \rho(2) \int_0^\infty v dv b_0^2(v,2,i,f), \tag{4.15}$$

is a term derived from the Anderson theory [137, 138] and due to integral cut-off, where n and $\rho(p)$ are the density and p-level rotational populations of the perturbing molecules, v

is the relative molecular velocity, and $b_0(v,p)$ is the cut-off parameter. In Eq. 4.14, the first term

$$B(i,f) = n/c(\alpha_f - \alpha_i)\sum_2 \rho(2)\int_0^\infty v dv b_0^{-3}(v,2), \tag{4.16}$$

is the contribution of the isotropic part of the potential. Here, α_f and α_i are the polarizabilities of molecules in the upper and lower vibrational states, respectively. The sums in Eqs. 4.13 and 4.14 include the transitions of different tensor rank ℓ (for dipole $\ell = 1$, quadrupole $\ell = 2$ and other $\ell = \ldots$) and can be represented as products of two different factors $D^2(ii'|l)$ and $P_l(\omega)$, where

$$P_l(\omega) = n/c\sum_p \rho(p)\sum_{l'p'} A_{ll'}D^2(pp'|l')F_{ll'}\left(\frac{2\pi c b_0(p,i,f)}{v}(\omega+\omega_{pp'})\right), \tag{4.17}$$

is the efficiency function for the scattering channel $i \to i'$, $f \to f'$. The efficiency function can be represented in the form of

$$P_l(\omega) = P_l^A(\omega)C_l(\omega), \tag{4.18}$$

where $P_l^A(\omega)$ is the efficiency function calculated in the Anderson approximation [137, 138]. The factor $C_l(\omega)$ represents the corrections for different factors ignored in the Anderson theory, and can be determined by fitting to experimental data. It was found that the correction factor in the case of CO-CO$_2$ calculations is sufficient as a J-dependent function,

$$C_l(\omega_{ii'}) = \frac{c_1}{c_2\sqrt{J_i}+1}\left(1+\frac{c_3}{1+c_4(J_i-c_5)^2}\right), \tag{4.19}$$

where $c_1 - c_5$ are the fitting parameters. The calculations were performed with $c_1 = 1.9$, $c_2 = 0.25$, $c_3 = -2.7\times10^{-4}T + 0.165$, $c_4 = 0.05$ and $c_5 = 10$ for CO$_2$ broadening coefficients, and $c_1 = 2.5$, $c_2 = 1.0$, $c_3 = 0$, $c_4 = 0$ and $c_5 = 0$ for CO$_2$ shift coefficients. It was found that such a modification of the impact theory allowed us to reproduce correctly the measured CO$_2$ broadening and CO$_2$ shift coefficients.

The calculated values take into account the contributions due to dipole-quadrupole and quadrupole-quadrupole interactions, as well as the induction and dispersion terms in the expansion of intermolecular potential. The CO molecular constants, i.e., the dipole moment, the components of quadrupole moment and the dipole polarizability, were taken from [139]. The rotational constants of the ground and excited vibrational levels were taken from [140], and the spectroscopic parameters for the carbon dioxide molecule were taken from [141]. For the line shift calculation, we used one more adjusted parameter in the upper vibrational level, i.e., the effective dipole polarizability $\alpha_f = \alpha_f^0[1 + c_\alpha\sqrt{J}]$ where the required values $\alpha_f^0 = -2.5 \times 10^{-4}T + 2.039$ and $c_\alpha = 5.4 \times 10^{-6}T + 0.0002$ were obtained from the fit to the experimental data.

The results for CO$_2$ broadening and CO$_2$ shift coefficients can be found in Tables 4.8 and 4.9, respectively (see supplementary file for the complete list of lines and results). Comparison of the theoretical CO$_2$ broadening coefficients with the parameters measured at different temperatures (listed in Table 4.5) shows that, for the lower temperatures, the differences between the calculated and experimental values are considerable. The best agreement is obtained for 296 K and 283.4 K, as Figure 4.11 shows. Similarly, theoretical CO$_2$ shift coefficients have been compared to the parameters measured at each temperature (listed in Table 4.6, where the complete list of lines and results are provided in the supplementary file). Figure 4.12 compares coefficients measured at two temperatures and calculated at the same temperatures and 296 K. The rotational dependence of the CO$_2$ shift coefficients observed in the P branch is rather well reproduced by the calculations, while the agreement is worse for the R branch. The temperature dependence of the CO$_2$ broadening coefficients were also determined. The calculated temperature dependence exponents n_1 are compared with the experimental values in Figure 4.6. Note that I could not obtain a reliable temperature dependence of the CO$_2$ shift coefficients, because the temperature span was too small.

4.5.2 Semi-empirical calculations of CO_2 broadening and CO_2 line mixing coefficients

The CO_2 broadening coefficients and weak CO_2 line mixing coefficients of the $^{12}C^{16}O$ lines have been calculated using a semi-empirical method known as the Exponential Power Gap law (EPG). Both the CO_2 broadening coefficients and associated CO_2 line mixing coefficients can be approximated using elements of the relaxation matrix that provides information on the physical state and collisional transfer between pairs of energy levels of the CO molecules perturbed by carbon dioxide molecules. The amplitude of the line mixing component is directly proportional to the pressure.

The weak line mixing effects are quantified as an asymmetry added to the qSDV lineshape used to retrieve the experimental CO_2-broadened coefficients. If we take into account the collisional energy transfer between two energy levels labelled j and k, we can write

$$Y_k^0(T) = 2\sum_{j\neq k} \frac{d_j}{d_k} \frac{W_{jk}}{\tilde{\nu}_k - \tilde{\nu}_j}, \tag{4.20}$$

where $Y_k^0(T)$ is the weak CO_2 line mixing coefficient of the transition of interest, d_k and d_j are components of the dipole moment, W_{jk} are off-diagonal elements of the relaxation matrix, $\tilde{\nu}_j$ and $\tilde{\nu}_k$ are line positions in cm^{-1}. In the relaxation matrix formalism, the CO_2 broadening coefficients are the real parts of the diagonal elements of the relaxation matrix. The off-diagonal elements are directly related to the collisional transfer rates κ_{jk}, as $W_{jk} = -\beta\kappa_{jk}$ where $\beta = 0.55$. The value of $\beta = 0.55$ has been determined as the value that offers the lowest standard deviation between calculated and experimentally retrieved line mixing coefficients. Presented in Figure 4.13, is the experimental line mixing coefficients extrapolated to 296 K along with the calculated line mixing coefficients for a few β values. The detailed balanced relation connects the rate of transfer from state k to j to the rate of transfer from j to k

$$\rho_k\kappa_{jk} = \rho_j\kappa_{kj}, \tag{4.21}$$

where ρ_k is the population of the rotational level k. The Exponential Power Gap (EPG) law provides an expression for the collisional transfer rates from the lower rotational level k to a higher rotational level j as

$$\kappa_{jk} = a(T)\left[\frac{|\Delta E_{jk}|}{B_0}\right]^{-b} exp\left(\frac{-c|\Delta E_{jk}|}{k_B T}\right). \tag{4.22}$$

with ΔE_{jk} as the energy gap between the two rotational levels in cm^{-1}, B_0 as the rotational constant in the lower energy level, and a, b, and c as the parameters to be optimized using nonlinear least squares. Assuming that the collisional rates are the same in the upper and lower vibrational levels, the diagonal elements of the relaxation matrix can be written as

$$W_{kk} = 1/2\left[\sum_j \kappa_{jk}\right]_{upper} + 1/2\left[\sum_j \kappa_{jk}\right]_{lower}. \tag{4.23}$$

Table 4.8: Theoretical CO_2 broadening coefficients for the $2-0$ band of $^{12}C^{16}O$ at different temperatures and resulting temperature dependence exponent n_1

Line		b_L^0(CO – CO$_2$) (cm^{-1}atm^{-1})					
	$\tilde{\nu}$ (cm^{-1})	296	283.4	270.0	255.4	240.5	n_1
P(22)	4159.5595	0.05740	0.05924	0.06137	0.06391	0.06677	0.727
P(21)	4164.8408	0.05774	0.05960	0.06173	0.06428	0.06716	0.728
P(20)	4170.0551	0.05814	0.06000	0.06215	0.06471	0.06761	0.725
P(19)	4175.2024	0.05860	0.06047	0.06263	0.06521	0.06812	0.724
P(18)	4180.2825	0.05915	0.06103	0.06320	0.06579	0.06872	0.721
P(17)	4185.2952	0.05983	0.06171	0.06389	0.06649	0.06944	0.715
P(16)	4190.2404	0.06066	0.06255	0.06474	0.06736	0.07033	0.709
P(15)	4195.1180	0.06172	0.06363	0.06582	0.06846	0.07145	0.702

The CO_2 line mixing coefficients retrieved using the qSDV profile from spectra recorded at each of the four temperatures of the present work are presented in Figure 4.14 and Table 4.11 (the complete list of lines and results can be found in the supplementary file). The

Table 4.9: Theoretical CO_2 shift parameters for the $2-0$ band of CO at different temperatures

Line		$d_0(T)$ ($cm^{-1}atm^{-1}$)				
	$\tilde{\nu}$ (cm^{-1})	296	283.4	270.0	255.4	240.5
P(22)	4159.5595	−0.00697	−0.00719	−0.00744	−0.00771	−0.00798
P(21)	4164.8408	−0.00683	−0.00707	−0.00732	−0.00760	−0.00789
P(20)	4170.0551	−0.00670	−0.00694	−0.00720	−0.00749	−0.00780
P(19)	4175.2024	−0.00655	−0.00680	−0.00708	−0.00738	−0.00770
P(18)	4180.2825	−0.00640	−0.00666	−0.00694	−0.00726	−0.00759
P(17)	4185.2952	−0.00625	−0.00651	−0.00680	−0.00713	−0.00746
P(16)	4190.2404	−0.00608	−0.00635	−0.00665	−0.00698	−0.00732
P(15)	4195.1180	−0.00589	−0.00617	−0.00646	−0.00679	−0.00716

temperature dependence of the line mixing coefficients is minimal if any. Nevertheless, the empirical fit parameters a, b and c (Eq. 4.22) were determined from analysis of the collisional rates inferred from these measured line mixing coefficients. The values obtained are listed in Table 4.10. The parameter a changes with temperature and we quantify this temperature dependence as $a(T) = a_0(T_0/T)^{n_3}$ for each of the R- and P-branches. Both the a_0 and n_3 values are presented in the last two columns of our Table 4.10. It can be observed that b is nearly constant and c is slowly increasing with temperature.

Similarly, the CO_2 broadening coefficients were calculated using the EPG method. These calculated values are listed in Table 4.12 (the complete list of lines and results can be found in the Appendix A), and overlaid with the theoretical and experimental coefficients in Figure 4.11. As can be seen, there is a good agreement between the semi-empirical calculation and observed broadening coefficients for the stronger lines. The results will be presented later on in Chapter 6 of the dissertation. A similar study was performed to improve the line shape of methane spectra which will be discussed in chapter 5.

Table 4.10: Adjustable EPG parameters for $^{12}C^{16}O$ at different temperatures.

T(K)		a	Error	b	Error	c	Error	a_o	n_3
240	P	0.05812	3.78×10^{-8}	0.44096	1.54×10^{-7}	1.06991	2.54×10^{-7}	0.04707	1.0067
255	P	0.05471	3.71×10^{-9}	0.43934	1.6×10^{-8}	1.07336	2.81×10^{-8}	0.04707	1.0067
270	P	0.05164	3.64×10^{-9}	0.43795	1.67×10^{-8}	1.07669	3.09×10^{-8}	0.04707	1.0067
283	P	0.04923	1.13×10^{-9}	0.43686	5.43×10^{-9}	1.07963	1.06×10^{-8}	0.04707	1.0067
296	P	0.04708	6.30×10^{-6}	0.43596	4.21×10^{-5}	1.08235	3.30×10^{-5}	0.04707	1.0067
240	R	0.06259	3.86×10^{-9}	0.45623	1.43×10^{-8}	1.05517	2.04×10^{-8}	0.05064	1.0095
255	R	0.0589	3.63×10^{-7}	0.45457	1.43×10^{-6}	1.05844	2.17×10^{-6}	0.05064	1.0095
270	R	0.0556	1.18×10^{-9}	0.45315	4.9×10^{-9}	1.06164	7.93×10^{-9}	0.05064	1.0095
283	R	0.05276	6.39×10^{-6}	0.45037	3.8×10^{-5}	1.06617	2.77×10^{-5}	0.05064	1.0095
296	R	0.05078	1.14×10^{-7}	0.45188	5.19×10^{-7}	1.06629	9.25×10^{-7}	0.05064	1.0095

Table 4.11: CO_2 weak line mixing coefficients Y_k^0 (atm^{-1}) for the $2-0$ band of $^{12}C^{16}O$ measured using the qSDV profile by multi-spectrum fitting all the spectra recorded at each temperature, and corresponding values calculated using the EPG law

	240.5 K		255.4 K		270.0 K		283.4 K	
Line	qSDV	EPG	qSDV	EPG	qSDV	EPG	qSDV	EPG
P(22)	−0.0673	0.004	0.0066	0.004	−0.0055	0.0039	−0.0105	0.0039
P(21)	−0.0005	0.004	0.0153	0.004	−0.0053	0.0039	0.003	0.0039
P(20)	0.0053	0.0041	−0.0094	0.004	0.0008	0.004	0000	0.0039
P(19)	−0.011	0.0041	0.0054	0.004	−0.0016	0.004	−0.0014	0.0039
P(18)	0.0014	0.0041	−0.0015	0.0041	0.0017	0.004	0.001	0.0039
P(17)	0.0125	0.0041	0.0006	0.0041	0.0037	0.004	0.0057	0.0039
P(16)	0.0022	0.0041	0.0007	0.004	0.001	0.0039	0.0028	0.0038
P(15)	−0.0072	0.0041	−0.0014	0.004	−0.0038	0.0039	−0.0024	0.0038

Table 4.12: CO_2 broadening coefficients for the $2-0$ band of $^{12}C^{16}O$ calculated using EPG calculations at four different temperatures.

Line	240 K	255 K	270 K	285 K	296 K
P(22)	0.065146	0.062536	0.060092	0.058150	0.056358
P(21)	0.066075	0.063431	0.060955	0.058988	0.057171
P(20)	0.067023	0.064345	0.061837	0.059846	0.058006
P(19)	0.067996	0.065285	0.062746	0.060729	0.058866
P(18)	0.069001	0.066257	0.063687	0.061645	0.059759
P(17)	0.070048	0.067271	0.064669	0.062603	0.060693
P(16)	0.071148	0.068338	0.065704	0.063613	0.061679
P(15)	0.072317	0.069473	0.066806	0.064688	0.062730

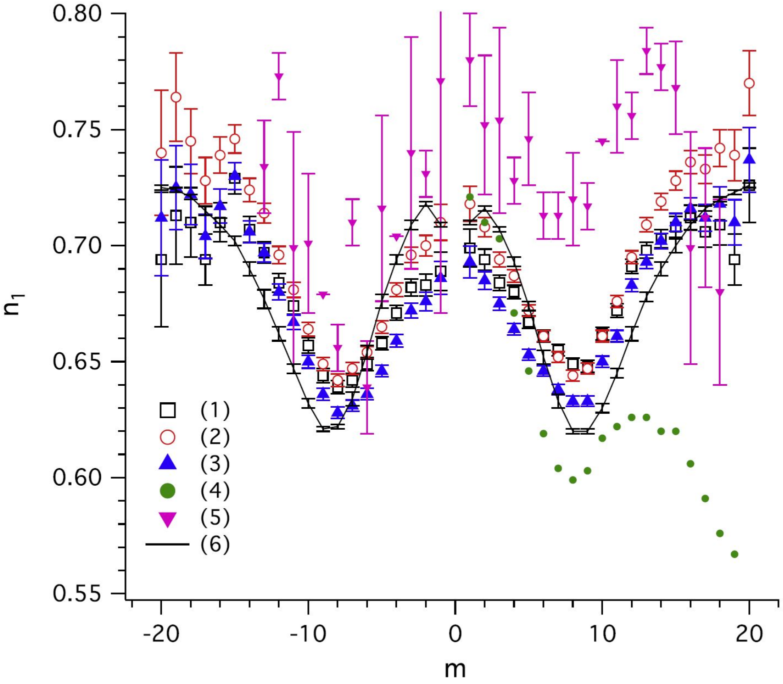

Figure 4.6: Temperature dependence exponent of the CO_2 broadening coefficients for the $2-0$ band of $^{12}C^{16}O$ measured in this work with the VP (1), RP (2) and qSDV (3) line shape models. The error bars associated with these measurements represent the uncertainty of measurement (1σ), estimated by the least squares fitting algorithm. Measurements reported for the fundamental band of $^{12}C^{16}O$ by Nakazawa and Tanaka using the Lorentz profile [11] (4) and by Sung and Varanasi [10] using the VP (5), and values calculated using a semi-classical method are also shown. The measured temperature dependence of CO_2 broadening coefficients are improved at least by one order of magnitude using qSDV line shape. The graph also shows how the rotational dependence of n changes with the intensity of the transitions. The reason the present results are more precise, is that the values reported in Ref. [10] are retrieved based on only three temperature measurement and analyzed using the Voigt profile. For Ref. [11], only *R* branch line were measured and analyzed using the Lorentzian profile.

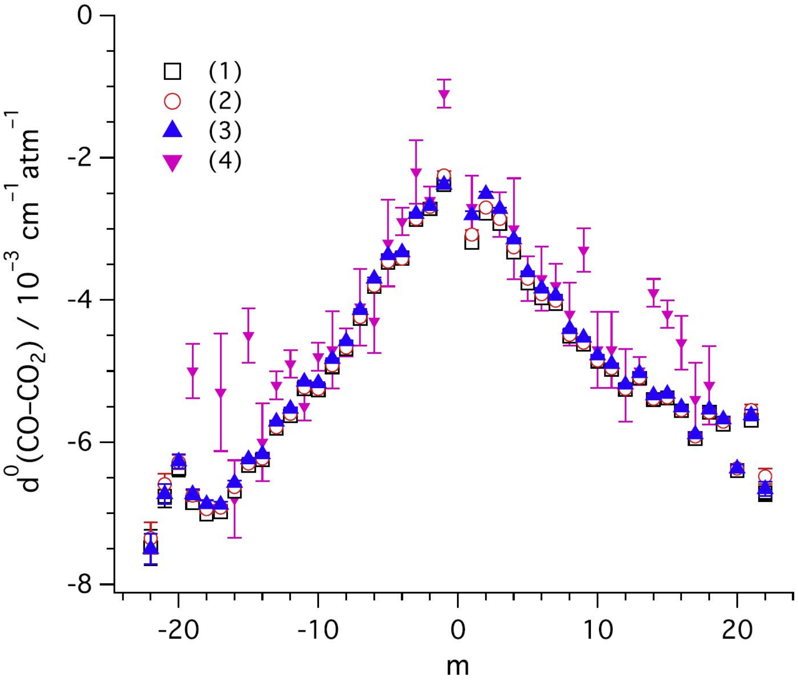

Figure 4.7: CO_2 shift coefficients for the $2-0$ band of $^{12}C^{16}O$ at 296 K measured in this work with the VP (1), RP (2) and qSDV (3) line shape models, and reported at 298 K by Sung and Varanasi [10] (4). The error bars associated with the present measurements represent the uncertainty of measurement (1σ), estimated by the least squares fitting algorithm. The present results show improved uncertainty compared to Ref. [10].

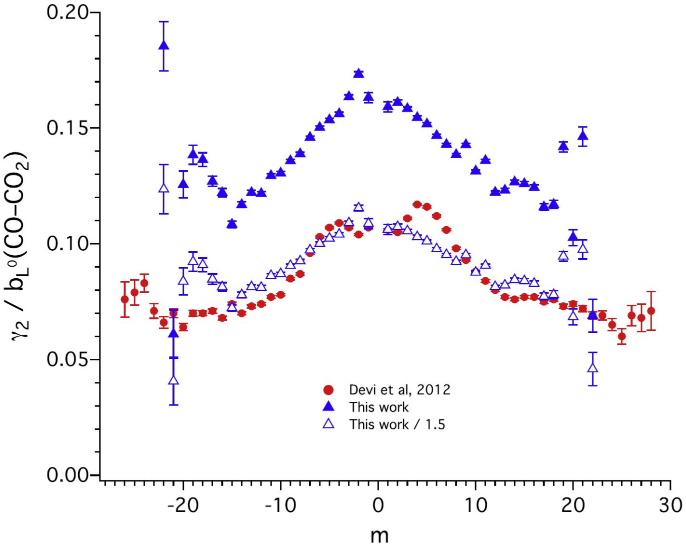

Figure 4.8: Relative quadratic speed dependence of the CO_2 broadening coefficients measured in this work for the 20 band of $^{12}C^{16}O$ with the qSDV line shape model,and measurements reported by Devi et al. [12] for pure CO and a CO-air mixture (the speed dependence was assumed to be independent of the perturber gas in that work). The present measurements divided by 1.5 are also shown to indicate the effect of molecular mass of the perturber gas. The error bars associated with the present measurements represent the uncertainty of measurement (1σ), estimated by the least squares fitting algorithm.

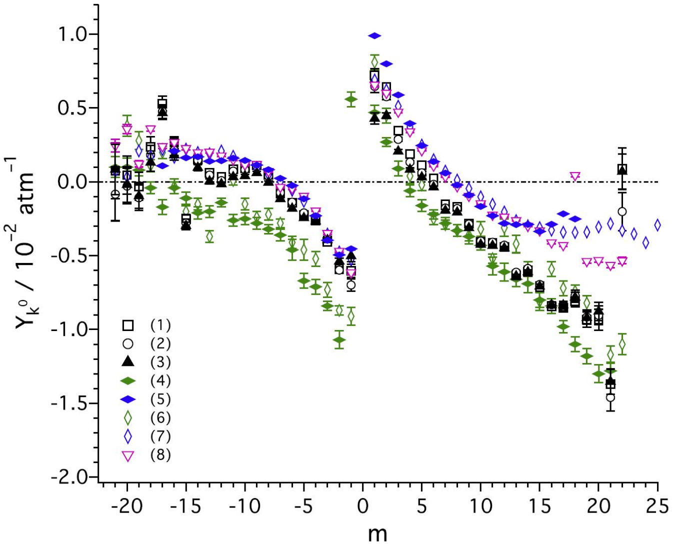

Figure 4.9: Weak line mixing coefficients for the $2-0$ band of $^{12}C^{16}O$ measured in the present work with the VP (1), RP (2) and qSDV (3) line shape models. The error bars associated with these measurements represent the uncertainty of measurement (1σ), estimated by the least squares fitting algorithm. Measurements reported in the literature for CO-N_2 [13] (4) and CO-air [12] (5) mixtures, and pure CO (6: [13], 7: [12], 8: [14]) are also presented. This graph shows that qSDV (3) has smoother rotational dependence compared to other results with improved precision.

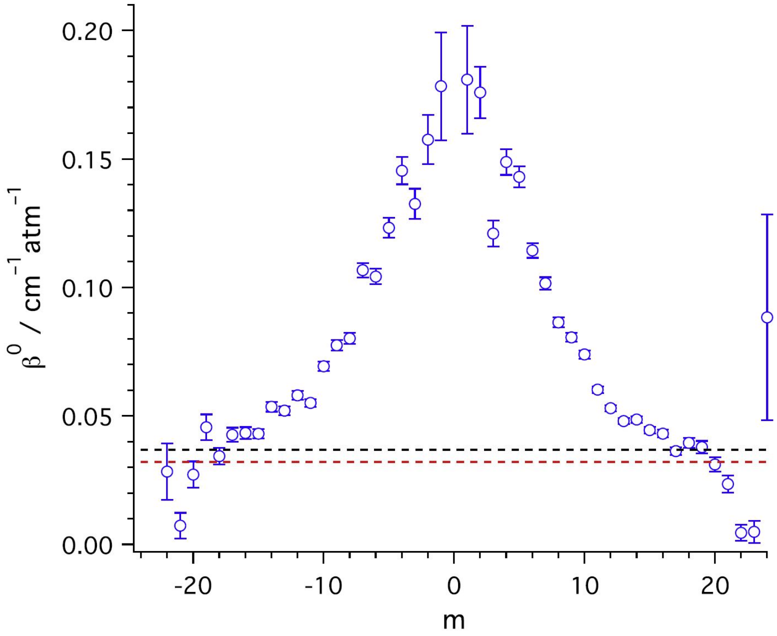

Figure 4.10: CO_2 narrowing coefficients for the $2-0$ band of $^{12}C^{16}O$ measured using the Rautian and Sobelman (RP) line shape model. The error bars represent the uncertainty of measurement (1σ), estimated by the least squares fitting algorithm. The dynamic friction coefficient β^0_{diff} estimated at the lowest (240.5 K) and highest (283.4 K) experimental temperatures are also shown as black and red dashed lines, respectively. Most of the measured narrowing values are larger than the calculated dynamic friction coefficient.

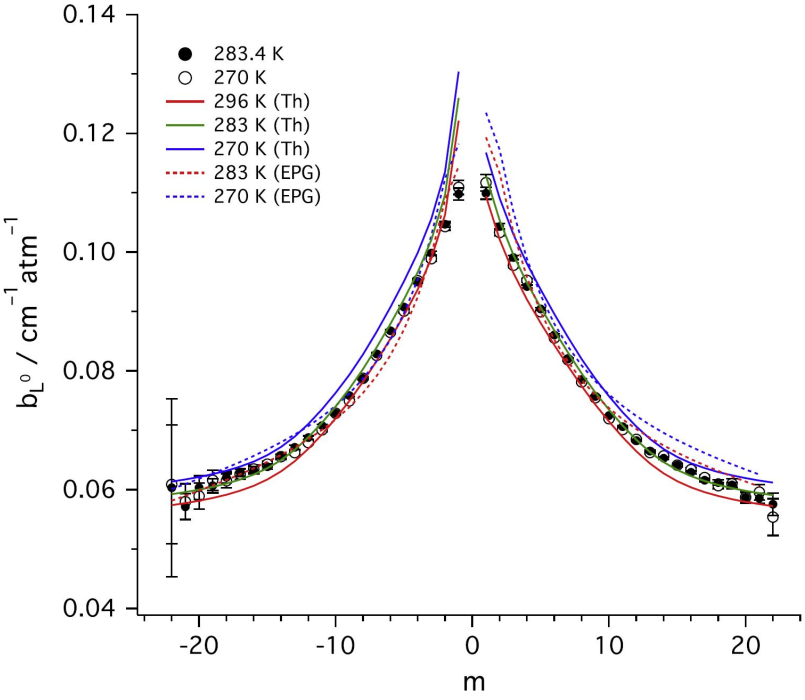

Figure 4.11: Comparison of CO_2 broadening coefficients measured at 2 temperatures in the $2-0$ band of $^{12}C^{16}O$ with semi-classical calculations and EPG calculation. The results are in excellent agreement proving the validity of the experimental results.

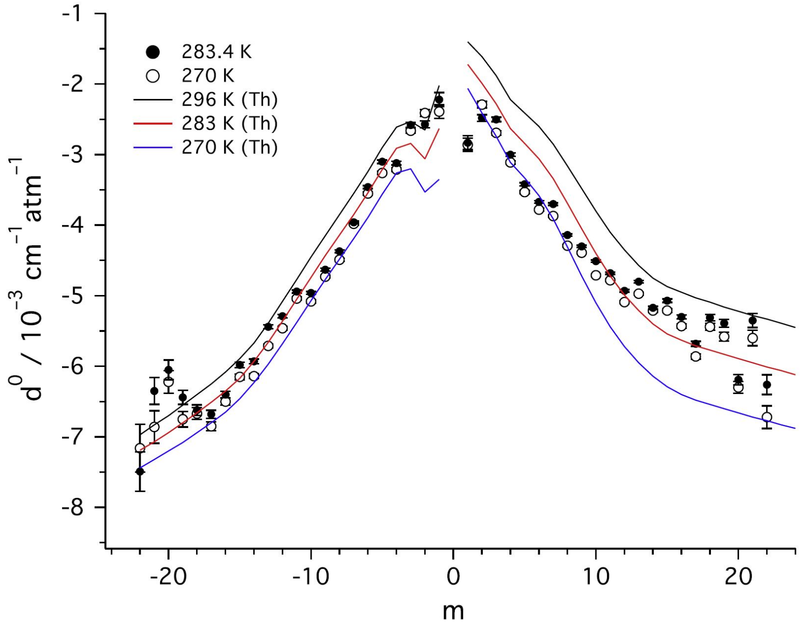

Figure 4.12: Same as Figure 4.11 for the CO_2 shift coefficients. The calculated shift coefficients shown by dash lines are in agreement with the measured shift values in the *P* branch, proving the reliability of the experimental results. For the *R* branch, the agreement is better for 283 K.

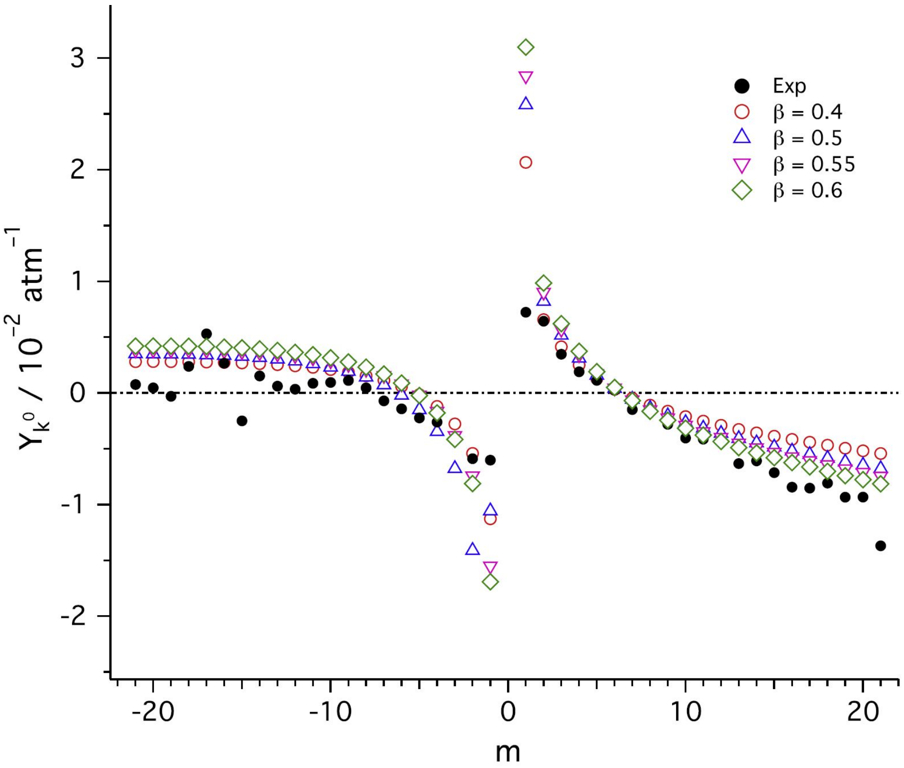

Figure 4.13: Weak line mixing coefficients measured at 296 K in the $2-0$ band of $^{12}C^{16}O$ and calculated using the EPG law with different values of β. The value $\beta = 0.55$ was determined as the value offers the lowest standard deviation between calculated and experimentally retrieved line mixing coefficients.

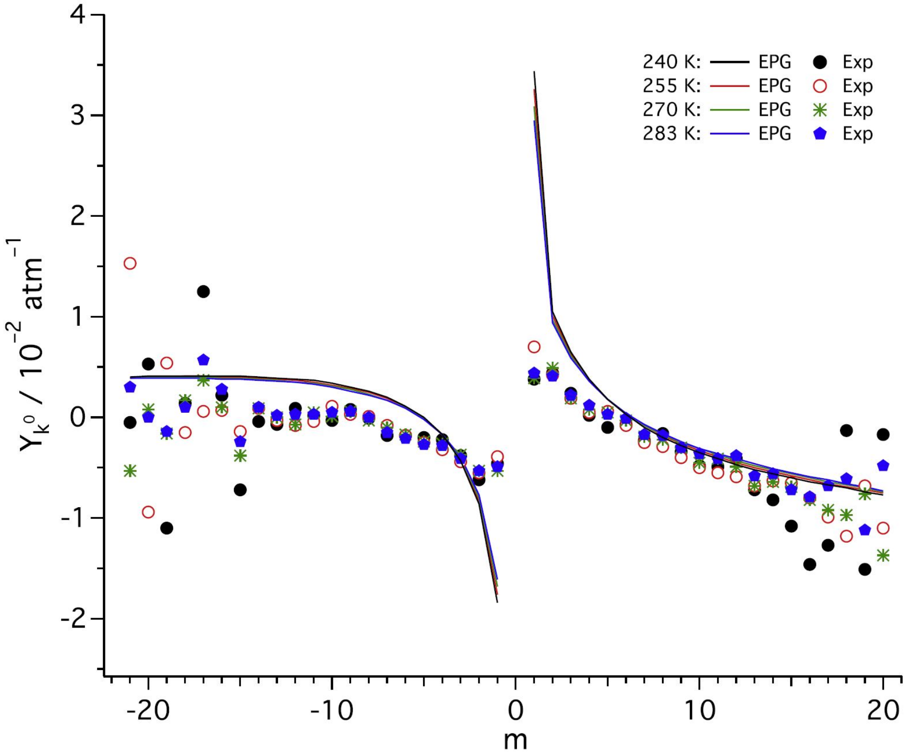

Figure 4.14: Weak line mixing coefficients in the $2-0$ band of $^{12}C^{16}O$, measured and calculated using the EPG law with $\beta = 0.55$ at the same temperatures. The solid lines presents the EPG calculation. The behaviour of the lines near $|m = 1|$ can be explained by looking at the Eq. (4.22), where it is sensitive to ΔE_{jk} value.

Chapter 5

Spectroscopic line parameters of $^{12}CH_4$ for atmospheric composition retrievals in the 4300-4500 cm^{-1} region

The chapter is reprinted from Journal of Quantitative Spectroscopy and Radiative Transfer, 186, 106117; Hashemi R, Predoi-Cross A, Nikitin A.V, et al. 2017, Spectroscopic line parameters of CH_4 for atmospheric composition retrievals in the 4300-4500 cm^{-1} region [142], with permission from Elsevier. [5] In this research, the precise line shape study of methane is performed. To do this project, the experimental data were recorded by Dr. Smith (at NASA Langley), Dr. Devi (at College of William and Mary) and, Dr. Sung (at the Jet Propulsion Laboratory, JPL) in the 4100-4500 cm^{-1} region. Of the several bands in the recorded region, I suggested working on the $\nu_3 + \nu_4$ band located in the 4300-4500 cm^{-1} region. I calibrated the spectra in the pre-processing stage and analyzed the data. Then, I prepared the tables and figures of results and wrote the manuscript. A section of this project for the theoretical calculation of parameters was done by and Dr. Nikitin and Tyuterev from Tomsk University.

5.1 Introduction

The aim of this study is to further our knowledge of Earth's carbon cycle through spectroscopic remote sensing of methane ($^{12}CH_4$). The yearly increase rate of methane in the Earth's atmosphere is about 1%, while the information on the increase sources is limited.

---

[5] The copyright permission can be found in Appendix A, Section A.2.

Studying the strength of different sources and their distribution by using remote sensing techniques, can help in enhancing knowledge on the sources.

The management of sinks and emissions of this long-lived gas relies on having accurate laboratory measurements to interpret atmospheric spectra [143, 144].

These laboratory spectroscopic results will be helpful to achieve vertical profiles of methane. Vertical profile information arises from the spectral line shape study, where the wing segments of the lines provide knowledge of the atmospheric elements closer to the surface, and the central segment of the line is impacted more by gas at higher elevations [145]. When looking at atmospheric spectra, we are measuring through a non-homogeneous medium (i.e., pressure, temperature, etc are changing with altitude). By breaking that atmosphere up into small intervals, we can assume those small intervals are homogeneous (like a gas cell in the lab) and at each of those intervals we can compute a spectrum for a set of atmospheric conditions that describe that particular interval. The final spectrum that we see is the addition of all the spectrum's from the different atmospheric levels.

We know that pressure of the atmosphere decreases with altitude. We also know that (assuming a simple Voigt) the spectral line shape is the convolution of pressure broadening and Doppler broadening. Hence, when closer to the ground pressure broadening will be the most important, making the spectral line broader contributing more absorption in the wings of the spectral line of the solar absorption spectrum. While higher in the atmosphere Doppler broadening is more important and since it is a narrower line shape it contributes more absorption in the line center. To the best of our knowledge, the wings of the spectral line are susceptible to line mixing and the line center is influenced predominantly by speed dependent effects. Therefore, these advanced parameters must be examined in retrieval algorithms to achieve vertical profiles more accurately.

Obtaining information on the temperature dependence of CH_4-CH_4 and CH_4-air-broadened half-widths and shifts are needed for the interpretation of spectra that are recorded by instruments on spacecraft, balloons, and ground-based platforms. A laboratory spectroscopic study of CH_4 in the 4300 to 4500 cm^{-1} (2.22 to 2.33 μm) spectral region over the range of terrestrial atmospheric temperatures was performed.

Previous published studies in the 1.6 to 7.5 μm region have provided line parameters (CH_4-CH_4 and CH_4-air-broadened half-widths and shifts and their temperature dependences exponents) for a large number of transitions of the three most abundant methane isotopologues [146–174].

The temperature dependencies of the CH_4-air-broadened half-widths coefficients have been previously determined for the strongest transitions [15, 16]. Similarly, relaxation matrix element coefficients have been measured in the P- and R-branch in the octad region [15, 16]. However, some dense spectral regions, such as Q-branches and several weaker lines have not been analyzed thoroughly.

In this study, the CH_4-CH_4 and CH_4-air-broadened half-width and pressure-shift coefficients, along with their temperature dependencies for methane transitions in the $\nu_3 + \nu_4$ band were measured. The off-diagonal relaxation matrix element coefficients and quadratic speed dependence were taken into account for several transitions. Theoretical calculations were also performed to obtain line positions and intensities.

5.2 Experiment

High-resolution spectra of 99.99% ^{12}C-enriched samples of pure methane and dilute mixtures in dry air at temperatures between 148 K and room temperature were used in this study. The signal to noise ratio was above 2000. A total of 14 spectra were recorded by Dr. Smith, Dr. Sung and Dr. Devi at a resolution of 0.005 cm^{-1} using the Bruker IFS 125 HR Fourier transform spectrometer (FTS) located at JPL. The coolable absorption cell has an optical path of 20.38 cm and has been built to fit inside the sample compartment of the Bruker FT spectrometer [175, 176].

The spectrometer setup consisted of a Globar source, a CaF_2 beam-splitter and a liquid-N_2 cooled InSb detector. The diameter of the aperture was set to 1 mm. It took nearly 20

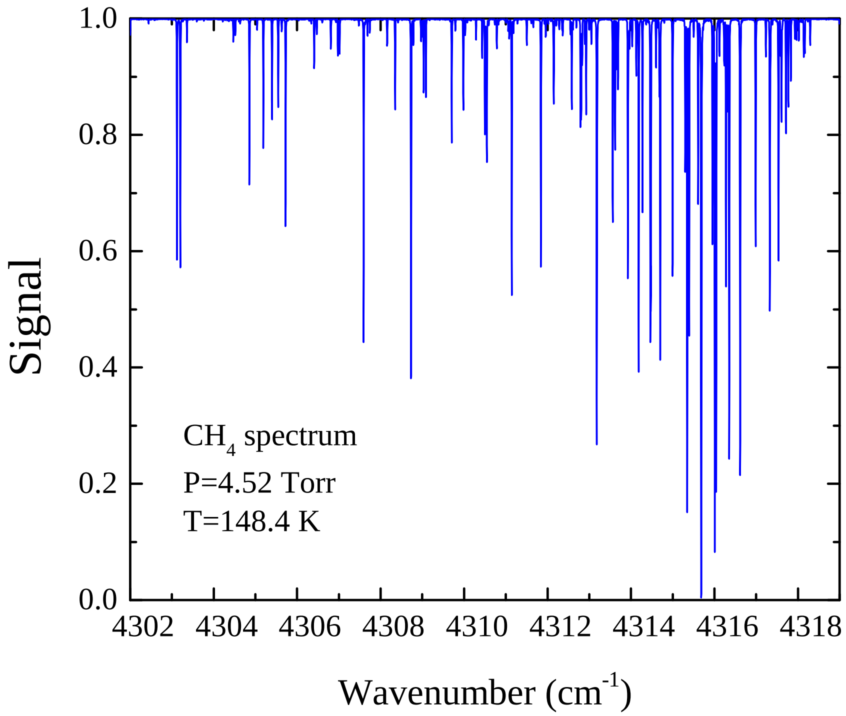

Figure 5.1: A experimental normalized transmitted spectrum in the spectral region of the $\nu_3 + \nu_4$ band of methane recorded at P=4.52 Torr and T=148.4 K (spectrum number 7 in the Table 5.1). This example spectrum shows different transitions in short wavenumber region for methane.

minutes for the sample mixtures in the cell to reach equilibrium and for the pressure and temperature to stabilize. Sample pressures were controlled using periodically calibrated Baratron gauges of the appropriate range. For wavenumber calibration purpose, the water vapour transitions of the ν_3 band appearing within the filter bandpass of 3750-5200 cm^{-1} were used because of the presence of residual trace amounts of H_2O and CO_2 in the evacuated FT spectrometer. For more details see Ref. [177]

Of the 14 spectra, eight spectra were recorded with pure methane samples and 6 of the spectra were obtained with dilute mixtures of the $^{12}CH_4$ in dry air. The experimental gas conditions are listed in Table 5.1.

In Figure 5.1, an example of experimental spectrum is presented.

Table 5.1: Experimental conditions of spectra used in this study. VMR is the volume mixing ratio, P is the pressure in Torr and T is the temperature in K.

#	Gas sample	VMR	P (Torr)	T (K)
1	$^{12}CH_4$	1.00	385.00	298.4
2	$^{12}CH_4$	1.00	22.20	250.0
3	$^{12}CH_4$	1.00	121.51	250.0
4	$^{12}CH_4$	1.00	9.90	200.0
5	$^{12}CH_4$	1.00	43.95	200.0
6	$^{12}CH_4$	1.00	169.00	200.0
7	$^{12}CH_4$	1.00	4.52	148.4
8	$^{12}CH_4$	1.00	149.06	148.5
9	$^{12}CH_4$+air	0.055	112.60	250.0
10	$^{12}CH_4$+air	0.057	254.58	250.0
11	$^{12}CH_4$+air	0.073	148.49	200.0
12	$^{12}CH_4$+air	0.074	299.95	200.0
13	$^{12}CH_4$+air	0.096	95.06	148.4
14	$^{12}CH_4$+air	0.043	225.37	148.4

5.3 Analysis of the spectra

The analysis of spectra was performed in the spectral interval of 4300-4500 cm^{-1} of the $\nu_3+\nu_4$ band. A multispectrum fitting program [178] was used to retrieve the spectroscopic parameters by fitting short spectral intervals to cover the entire band. The program fits the line parameters such as the position, the intensity, and the width for each of the spectral lines. It is an iterative procedure for minimizing the sum of the squares of the differences between the simulated spectrum and the observed spectrum. To take into account the spectral distortions, parameters such as the background level (100 % transmission level) and instrumental line shape should be considered as part of the least squares solution. In the fitting procedure, by fitting each specific intervals from all 14 spectra simultaneously, one value was derived for each of the fitted parameters. Detailed explanations can be found in Ref. [178].

The spectral line parameters to initiate the least-squares fittings were taken from the

HITRAN database [179]. A multispectrum fitting software was used to analyze the set of spectra using the qSDV and VP profiles [67, 180]. Line mixing was included for selected transitions using the off-diagonal relaxation matrix elements formalism [181].

The speed dependence line profile is related to molecular collision velocity; hence the Lorentz width can be described as a function of velocity as it is explained in Refs. [170, 182],

$$b_L^0 = b_L^0(v_m)\left(1 + S\left[\left(\frac{v}{v_p}\right)^2 - c\right]\right), \tag{5.1}$$

where v is the speed of the molecular collision, v_m is the mean speed of the molecular collision, v_p is the most probable speed of the collision, and S is the speed dependence parameter (SD) reported in this study. c is a constant and its value is taken to be 1.5 so that the Lorentz width will be the same when $S = 0$ as that usually used in the Lorentz equation when speed dependence is neglected.

Short spectral intervals (2-5 cm^{-1}) were fitted at a time. I added the spectra one by one starting from the ones recorded at the lowest pressure until all 14 spectra were included in the fits. The reason the spectra were added one by one is that, I was able to fit for each spectra and find the best initial line parameters to start the multispectrum fit. The line positions and intensities, the Lorentz CH_4-CH_4 and CH_4-air-broadened half-width and shift coefficients, and their temperature dependencies were retrieved. The initial value for the speed dependence parameter was fixed to an average value I found in HITRAN [179]. The background also was fitted to a first order Chebyshev polynomial. The speed dependence parameter was measured for the strong and medium strength transitions.

The multispectrum fitting software optimizes the statistical errors and retrieves precise line parameters for all the transitions in the entire band of study. In Figure 5.2, the top panel shows all the experimental spectra, and in the bottom panels, the weighted residuals multiplied by 1000 (Observed-Calculated) are presented. Each spectrum was given a weight (maximum of 1) depending on their S/N ratio. Most of the spectra had a high S/N ratio, and hence the weight of 1.0 was given.

5.4 Calculated line list for methane transitions in the octad range

Several studies have been devoted to theoretical predictions [183–185] of methane line positions and intensities in the octad range. Four normal mode frequencies of CH_4 exhibit an approximate relation of stretching and bending frequencies with $\nu_1 \approx \nu_3 \approx 2\nu_2 \approx 2\nu_4$ resulting in vibrational levels being grouped into polyads with levels of nearby energies. In terms of this resonant polyad structure, the spectral interval considered in this work corresponds to strong bands of the methane octad. The analysis of methane spectra is a complicated problem due to high degeneracies and quasi-degeneracies of ro-vibrational levels and numerous accidental perturbations [186, 187].

Physically meaningful values of resonance coupling parameters can be quite accurately obtained from molecular *ab initio* potential energy surface (PES) calculations using high-order contact transformations (CT) [188] of the full nuclear motion Hamiltonian [189]. This enabled reducing the number of adjustable parameters and avoiding strong correlations among them. The resulting mixed effective polyad model [188] that used information obtained from first principles of quantum chemistry calculations have shown a more robust behaviour with respect to the convergence of the least squares fit.

As an initial step, a full set of ro-vibrational terms in the Effective Hamiltonian (EH) were accurately derived from the PES of Nikitin et al. [190] using the MOL-CT program suite [188]. At the second step, some of the diagonal parameters are relaxed through the empirical optimization. These are the parameters that are well determined in the least squares fit experimental data of Hilico et al. [191], Albert et al. [192], Daumont et al. [193] and Brown et al. [194]. The MIRS computational code [195] was used for the fit.

General characteristics of the calculated list were as follows. Over 10000 line positions (including those of lower polyads) have been included in the EH fit using an extrapolation polyad scheme that resulted in a RMS deviation of 0.002 cm^{-1}. About 3500 line intensities

Table 5.2: Sample table for the results obtained by theoretical calculations. $\tilde{\nu}$ is wavenumber in cm^{-1}, I is the intensity in HITRAN units cm^{-1}/(molecule cm^{-2}) at $T = 296$ K, C is vibration-rotation Td symmetry type and n is polyad vibration-rotation ranking number.

$\tilde{\nu}$	Intensity	J lower state	C	n	J upper state	C	n
4300.0493	7.65×10^{-22}	3	F1	1	3	F2	22
4300.3643	1.71×10^{-21}	3	A2	1	2	A1	8
4305.1870	2.29×10^{-22}	2	F2	1	2	F1	16
4305.5436	7.37×10^{-22}	8	A1	1	8	A2	20
4324.9324	1.38×10^{-21}	1	F1	1	1	F2	11
4329.0086	6.79×10^{-22}	2	E	1	2	E	14
4330.1071	1.12×10^{-21}	2	F2	1	2	F1	19
4330.6318	1.04×10^{-22}	3	F2	1	3	F1	28
4330.9139	5.51×10^{-22}	2	E	1	2	E	15

belonging to 24 sub-bands in the total octad range (3500-4800 cm^{-1}) have been fitted with the overall RMS deviation of 7%. Errors in strong lines intensities ($5 \times 10^{-21} - 2 \times 10^{-22}$ cm^{-1}/(molecule cm^{-2})) were in the 2-3% range and in the medium size lines (10^{-22} – 10^{-23} cm^{-1}/(molecule cm^{-2})) in the range $\approx 5\%$ that roughly corresponded to experimental uncertainties.

The final calculations and details of the method are described in [196]. Table 5.2 presents a sample of the line list. The entire list is available in the supplemental file in Table A.10.

5.5 Measured line shape parameters

The retrieved line positions were calibrated on an absolute scale using positions of ν_3 of water vapour line positions as described in Ref. [197]. The comparison of some of the line parameters with HITRAN [179] is shown in Figure 5.3. The existing values in HITRAN are reported based on a semi-empirical calculation of other bands in the octad region [15, 16]. Therefore, the differences obtained for line positions and line intensities make sense, and the present results are considered good substitutions of the older existent values in

HITRAN. The reason why the current measurements are reliable lies in the vibrational dependence of line parameters that cannot be neglected for achieving high accuracies.

The line positions and intensities have been measured and compared to our theoretically calculated values and the values in the databases. These parameters are plotted in Figure 5.4. These comparisons of positions and intensities suggest that the present results agree well with HITRAN and GEISA [4] databases. For line positions, the agreement is on the order of 10^{-4} cm^{-1}. To obtain the differences, the values are subtracted from observed results (i.e., $cal - obs$). For the intensities, the percentage difference were obtained (i.e., $\frac{(cal-obs)}{obs} \times 100$) and it is less than 4% for most of the cases compared to HITRAN [179] and GEISA [4] databases.

A sample of the measured line parameters for the transitions in the $\nu_3 + \nu_4$ band is shown in Table 5.3. The entire table is presented in the supplemental file attached to this document as Appendix A. For each transition listed, the upper and lower rotational assignment, line position, line intensity, Lorentz CH_4-CH_4 and CH_4-air-broadened half-width coefficients, temperature dependence for CH_4-CH_4 and CH_4-air-broadened half-width coefficients and their uncertainties are reported. Included in Table 5.4 are the CH_4-CH_4 and CH_4-air-pressure-shift coefficients and the temperature dependencies of CH_4-CH_4 and CH_4-air-shift coefficients and their uncertainties. The speed dependence parameter and its uncertainty were included in this table. (The entire list is available in Table A.12 in the Appendix A.)

Table 5.4: Measured CH_4-air-shift coefficients, CH_4-CH_4- shift coefficients in cm^{-1} and speed dependence parameters (SD) of methane obtained by multispectrum fitting using qSDV profile and the temperature dependencies of CH_4-air-shift coefficients (T.d.a.s) and CH_4-CH_4-shift coefficients (T.d.s.s). Both T.d.a.s and T.d.s.s are multiplied by factor of 10^5 in this table. Note that US shows upper state and LS presents lower state.

LS	US	CH_4-air-shift	CH_4-CH_4-shift	T.d.a.s	T.d.s.s	SD
3F1 1	3F2 22	−0.0079(2)	−0.0107(1)	4.132(2)	9.552(9)	0.044(2)
3A2 1	2A1 8	−0.0071(2)	−0.0091(1)	1.876(1)	7.638(10)	0.064(2)

3F1 1	3F2 23	−0.0075(2)	−0.0110(2)	4.038(2)	8.859(13)	0.069(2)
3F2 1	3F1 25	−0.0069(2)	−0.0091(2)	3.903(2)	9.720(15)	0.070(3)
1F1 1	1F2 11	−0.0070(1)	−0.0096(1)	3.820(1)	8.396(6)	0.069(1)
2E 1	2E 14	−0.0070(2)	−0.0087(1)	3.459(2)	8.885(7)	0.076(2)
2F2 1	2F1 19	−0.0067(1)	−0.0092(1)	2.852(1)	7.293(6)	0.081(1)
2F2 1	2F1 19	−0.0066(2)	−0.0098(1)	2.545(2)	6.700(9)	0.071(2)
3F1 1	3F2 27	−0.0071(3)	−0.0106(1)	4.021(3)	7.951(12)	0.066(3)
3F2 1	3F1 29	−0.0073(2)	−0.0097(1)	1.947(2)	6.987(11)	0.075(2)

The measured pressure broadening and pressure shift parameters for the transitions in the 4300-4500 cm^1 region are plotted Figures 5.5 and 5.6 as a function of m ($m = -J''$, J'' and $J''+1$, for the P, Q and R branches, respectively). The present values of the Lorentz width and pressure-shift coefficients have been compared to the previous room temperature measurements [198, 199] and it can be concluded that the present results are in very good agreement (in terms of their behaviour with quanta m) with the measured results from Refs. [198, 199]. The measured air- and self- half width coefficients decrease for larger quantum numbers. In Figures 5.5 and 5.6 these results are plotted.

Figure 5.5 shows that the Lorentz CH$_4$-CH$_4$-broadened half-widths were larger than the CH$_4$-air-broadened half-widths measured for the same transitions. The reason lies in the mass ratio of the perturber and absorber gas; where the mass of perturber molecule is smaller, the broadening of line is larger. Also, it is found that the measured CH$_4$-CH$_4$-shift coefficients are slightly larger in magnitude than CH$_4$-air-shift coefficients measured for the same transitions. The results are also compared with published results in Refs. [15, 16] for the ν_4 and ν_2 bands. Figure 5.7 shows that the CH$_4$-air-broadening and temperature dependencies of CH$_4$-air-broadening coefficients in the present study are larger than the results obtained for the ν_4 band and smaller than the corresponding results in the ν_2 band

Table 5.3: Measured wavenumber ($\tilde{\nu}$) in cm^{-1}, intensities in cm^{-1}/(molecule cm^{-2}), CH_4-air-broadened half-width coefficients (air-b) and CH_4-CH_4-broadened half-width coefficients (self-b) of methane in $\mathrm{cm}^{-1}\mathrm{atm}^{-1}$ obtained by multispectrum fitting using qSDV profile and their temperature dependencies (n_1) and n_2 respectively. Note that US shows upper state and LS presents lower state.

LS	US	$\tilde{\nu}$	Int. $\times 10^{-22}$	air-b	self-b	n_1	n_2
3F1 1	3F2 22	4300.052054	7.4380(2)	0.0651(2)	0.0821(1)	0.899(3)	0.813(2)
3A2 1	2A1 8	4300.367139	16.858(5)	0.0670(1)	0.0844(1)	0.883(2)	0.815(2)
1F1 1	1F2 11	4324.935011	13.462(3)	0.0617(1)	0.0807(4)	0.867(3)	0.783(1)
2E 1	2E 14	4329.010901	6.3530(2)	0.0648(1)	0.0824(1)	0.875(2)	0.810(2)
2F2 1	2F1 19	4330.110245	10.892(2)	0.0639(1)	0.0811(1)	0.879(4)	0.801(1)
2F2 1	2F1 19	4330.110259	10.858(4)	0.0634(1)	0.0815(1)	0.890(4)	0.791(2)
2E 1	2E 15	4330.916544	5.3680(2)	0.0666(2)	0.0839(1)	0.910(1)	0.830(2)
3F2 1	3F1 29	4332.661710	4.7620(1)	0.0663(3)	0.0833(1)	0.860(1)	0.850(3)

of methane. Note that each of the points in this figure is averaged for several $P-$, $Q-$ and $R-$ branch lines over the $|m|$ value.

The temperature dependencies of CH_4-CH_4 and CH_4-air-broadened half-width coefficients are plotted in Figure 5.8. A power law model was used to obtain the temperature dependencies of CH_4-CH_4 and CH_4-air-broadened half-width coefficients (shown by Eq. (4.7)). In the top panel, the temperature dependencies exponents for CH_4-CH_4-broadened half-width coefficients are shown and in the bottom panel shows the results of temperature dependence of the air-width. The temperature dependence exponents for the CH_4-CH_4-broadened half-width coefficients were slightly lower than the temperature dependence exponent for CH_4-air-broadened half-width coefficients.

Temperature dependencies of CH_4-CH_4 and CH_4-air-pressure-shift coefficients are plotted in Figure 5.9. In this case, a linear model (Eq. (4.9)) was used to calculate the temperature dependence of CH_4-CH_4 and CH_4-air-shift coefficients (with units of cm^{-1} atm^{-1} K^{-1}). As can be seen, the temperature dependence exponents of CH_4-CH_4-shift coefficients are higher than those for air-shift parameters for the same reason that was mentioned for the self- and air- half-width coefficients. For both CH_4-CH_4- and CH_4-air-broadening, the temperature dependencies of the shifts are mostly positive.

The Voigt profile is not able to fit the spectra within the experimental noise levels at higher pressures. Furthermore, at high pressures, some intervals include pairs of transitions with line mixing. To remedy the fault, line mixing for both CH_4-CH_4 and CH_4-air- broadening was modelled using the off-diagonal relaxation matrix formalism [181]. The results are presented in Table 5.5. The off-diagonal coefficients reported in Table 5.5 is chosen to be W_{jk}, where j denotes the spectral line with the more significant lower state energy, i.e., the larger E''. The temperature dependence of line mixing were not determined for the measured transitions. I fixed the temperature dependence of both off-diagonal coefficient elements to an average value of 0.8 [179], resulted in smaller residuals. Figure 5.10 shows the graph of the CH_4-air- and CH_4-CH_4- broadening coefficients. (The line parameters measured by Voigt profile can be found in the supplemental file.)

Table 5.5: Measured off-diagonal relaxation matrix coefficients elements of methane obtained by multispectrum fitting using qSDV profile. The units are the same as for the broadening coefficients.

Identification	Line mixing pairs	Wavenumber	CH_4-CH_4-bro.	CH_4-air-bro.
Q(7)	7F2 ← 7F1	4315.9529	0.01041(12)	0.00502(9)
	7F1 ← 7F2	4316.2335		
Q(14)	14F2 ← 14F1	4301.0252	0.00572(8)	0.04046(22)
	14F1 ← 14F2	4301.0758		
Q(10)	10F1 ← 10F2	4304.5201	0.00335(5)	0.00232(6)
	10F2 ← 10F1	4304.9658		
Q(3)	3F2 ← 3F1	4303.1202	0.00184(3)	0.00275(10)
	3F1 ← 3F2	4303.1993		
Q(11)	11F2 ← 11F1	4309.8862	0.03052(34)	0.01599(25)
	11F1 ← 11F2	4309.9593		

Q(12)	12F1 ← 12F2	4305.5770	0.03552(15)	0.04048(10)
	12F2 ← 12F1	4306.1222		
Q(7)	7F2 ← 7F1	4308.3480	0.01557(14)	0.00142(2)
	7F1 ← 7F2	4308.9931		
Q(6)	6F2 ← 6F1	4310.2885	0.00799(6)	0.01262(11)
	6F1 ← 6F2	4310.5247		
R(9)	9F2 ← 8F1	4311.2963	0.03475(21)	0.03842(18)
	9F1 ← 8F2	4311.2615		
Q(12)	12F1 ← 12F2	4312.8945	0.05142(34)	0.04617(28)
	12F2 ← 12F1	4312.9909		
Q(9)	9F1 ← 9F2	4313.0702	0.00452(4)	0.00814(7)
	9F2 ← 9F1	4313.1003		
Q(6)	6F2 ← 6F1	4313.5633	0.00831(5)	0.00801(4)
	6F1 ← 6F2	4313.9262		
Q(3)	3F2 ← 3F1	4332.0556	0.00244(1)	0.00405(3)
	3F1 ← 3F2	4332.6617		
R(12)	12F1 ← 11F2	4334.6284	0.04988(12)	0.00765(5)
	12F2 ← 11F1	4334.8528		
Q(4)	4F2 ← 4F1	4335.4462	0.00338(6)	0.00384(8)
	4F1 ← 4F2	4335.9395		
R(4)	4F1 ← 3F2	4336.4328	0.00297(1)	0.00029(1)
	4F2 ← 3F1	4336.4554		
Q(4)	4F1 ← 4F2	4339.1155	0.00238(2)	0.00265(5)
	4F2 ← 4F1	4339.3148		
R(6)	6F1 ← 5F2	4345.6286	0.00562(4)	0.00207(3)
	6F2 ← 5F1	4345.8555		

R(5)	5F1 ← 4F2	4347.2279		0.03190(19)
	5F2 ← 4F1	4347.4451		
P(10)	9F1 ← 10F2	4348.8625	0.03748(17)	0.05300(25)
	9F2 ← 10F1	4349.0847		
R(7)	7F1 ← 6F2	4349.9837	0.00916(4)	0.00788(8)
	7F2 ← 6F1	4350.0760		
R(8)	8F1 ← 7F2	4354.0281	0.00999(8)	0.00635(7)
	8F2 ← 7F1	4354.3298		
Q(11)	11F1 ← 11F2	4354.5254	0.02665(12)	0.03613(17)
	11F2 ← 11F1	4354.8744		
R(10)	10F2 ← 9F1	4355.4112	0.07300(60)	0.01701(49)
	10F1 ← 9F2	4356.1034		
Q(9)	9F2 ← 9F1	4356.6425	0.03653(32)	0.05600(26)
	9F1 ← 9F2	4357.0117		
R(4)	4F2 ← 3F1	4356.8961	0.01023(16)	0.00668(24)
	4F1 ← 3F2	4357.2511		
R(9)	9F2 ← 8F1	4358.1561	0.02040(13)	0.02508(21)
	9F1 ← 8F2	4359.0025		
Q(13)	13F1 ← 13F2	4359.3724	0.03387(15)	0.00875(7)
	13F2 ← 13F1	4359.4715		
P(8)	7F1 ← 8F2	4363.1162	0.00342(1)	0.00435(6)
	7F2 ← 8F1	4363.2974		
R(11)	11A1 ← 10A2	4366.1335	0.00263(8)	0.00430(7)
	11A2 ← 10A1	4366.7579		
R(10)	10F2 ← 9F1	4456.2596	0.04111(12)	0.04843(18)
	10F1 ← 9F2	4456.6824		

P(8)	7F1 ← 8F2	4459.4667	0.00146(4)	0.00437(6)
	7F2 ← 8F1	4459.4939		
P(4)	3F1 ← 4F2	4494.4075	0.00825(5)	0.00025(1)
	3F2 ← 4F1	4494.8964		
R(9)	9F1 ← 8F2	4496.3316	0.00816(4)	0.02924(16)
	9F2 ← 8F1	4496.8113		
R(8)	8F1 ← 7F2	4498.2368	0.00174(1)	0.00556(4)
	8F2 ← 7F1	4498.8457		
R(13)	13F1 ← 12F2	4499.3494	0.06500(11)	0.00540(4)
	13F2 ← 12F1	4499.9996		

The finding of this part of research will be addressed at the last section in the conclusions chapter.

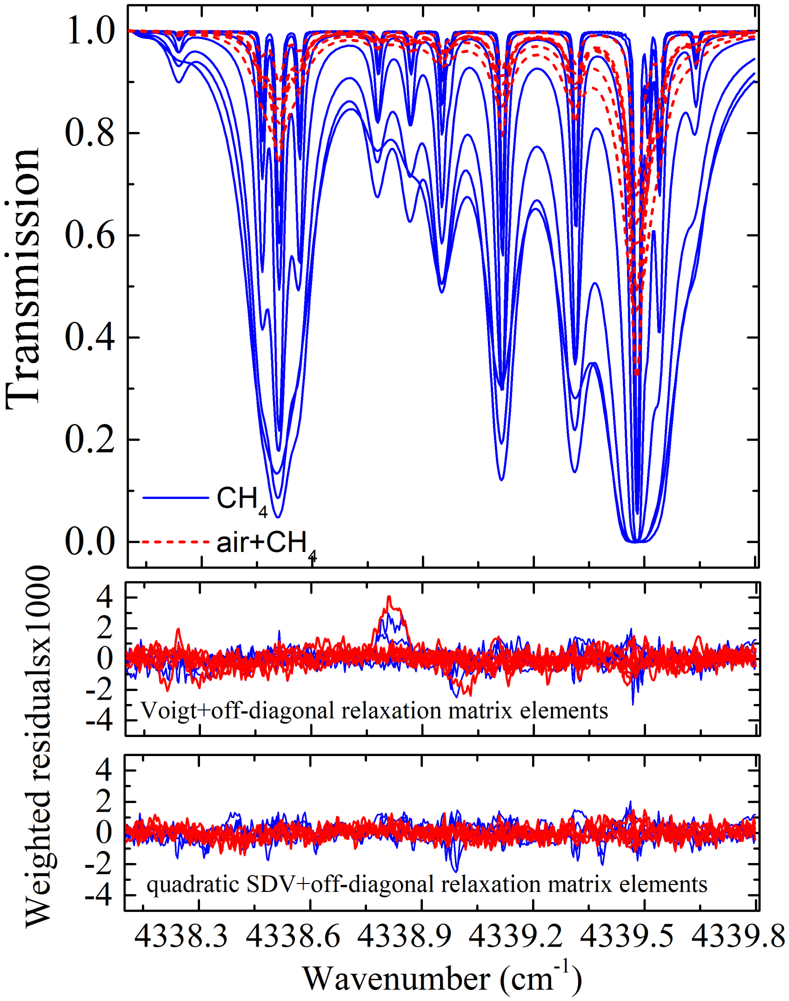

Figure 5.2: An example of a multispectrum fitted interval of the $\nu_3 + \nu_4$ band of pure methane and methane broadened by air (see Table 5.1). The upper panel shows the observed spectra at different pressures and temperatures (each of the blue lines present the spectra of pure methane and red ones present the methane spectra mixed with air). The bottom panels show the residuals of VP and qSDV profile considering line mixing.

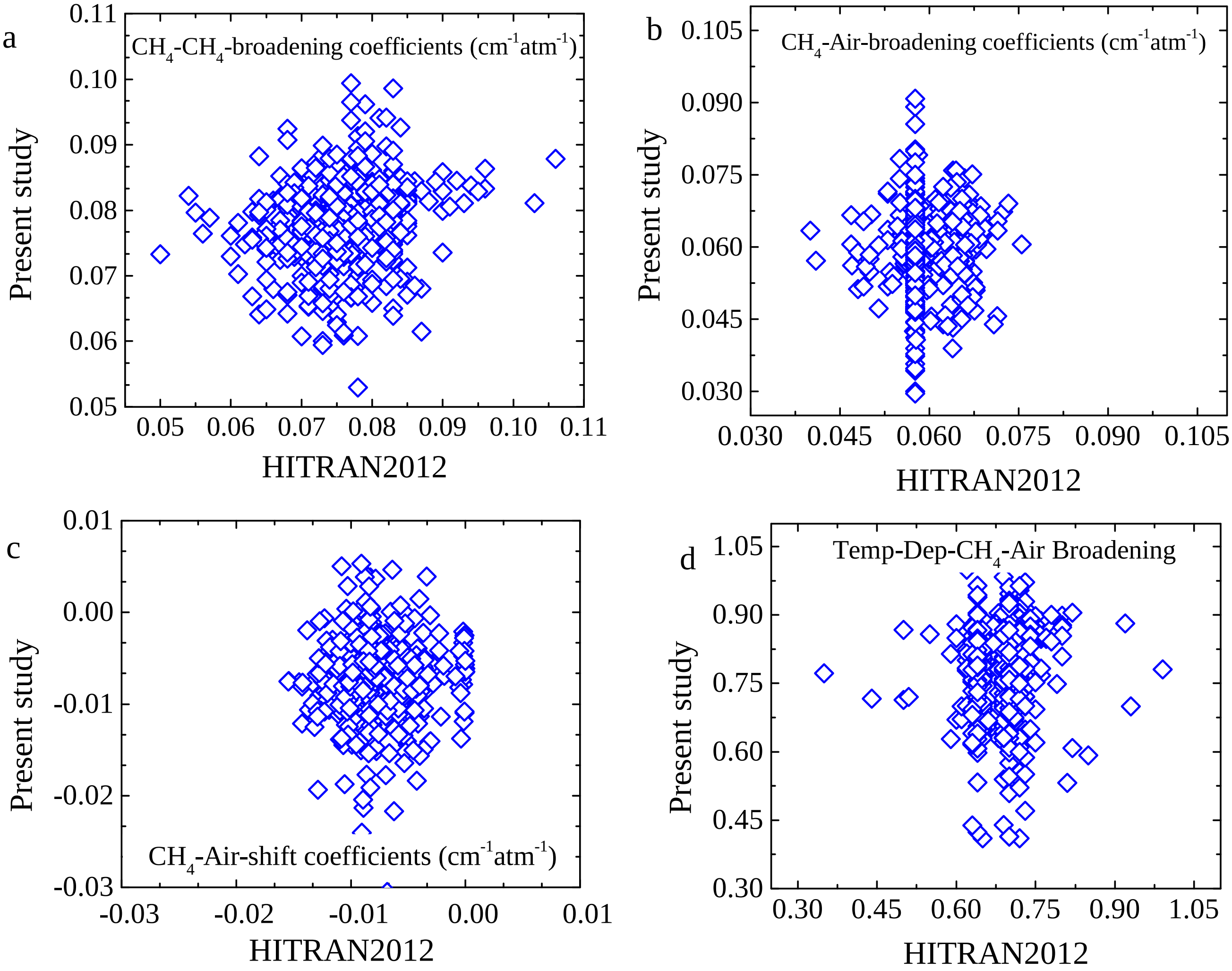

Figure 5.3: Comparison of measured line parameters for transitions in the $\nu_3+\nu_4$ band of methane with HITRAN. The broadening and shift coefficients are in cm^{-1} atm^{-1} at 296 K. The obtained discrepancy between the values can be explained by the difference in the retrieval approaches; in HITRAN the semi-empirical method employed is based on older measured parameters in the octad region for different bands. The top panels (a) and (b) compare the measured self and air- broadening coefficients with the values in HITRAN2012. Clearly, the present measured values are different than HITRAN, as if they were identical, they would have lined up on a straight $y = x$ line. Similarly, panel (c) and (d) represents air- shift coefficients, and temperature dependence of air-broadening compared to HITRAN database. As can be seen there are multiple values for each point which is as a results of the polyad quantum numbers.

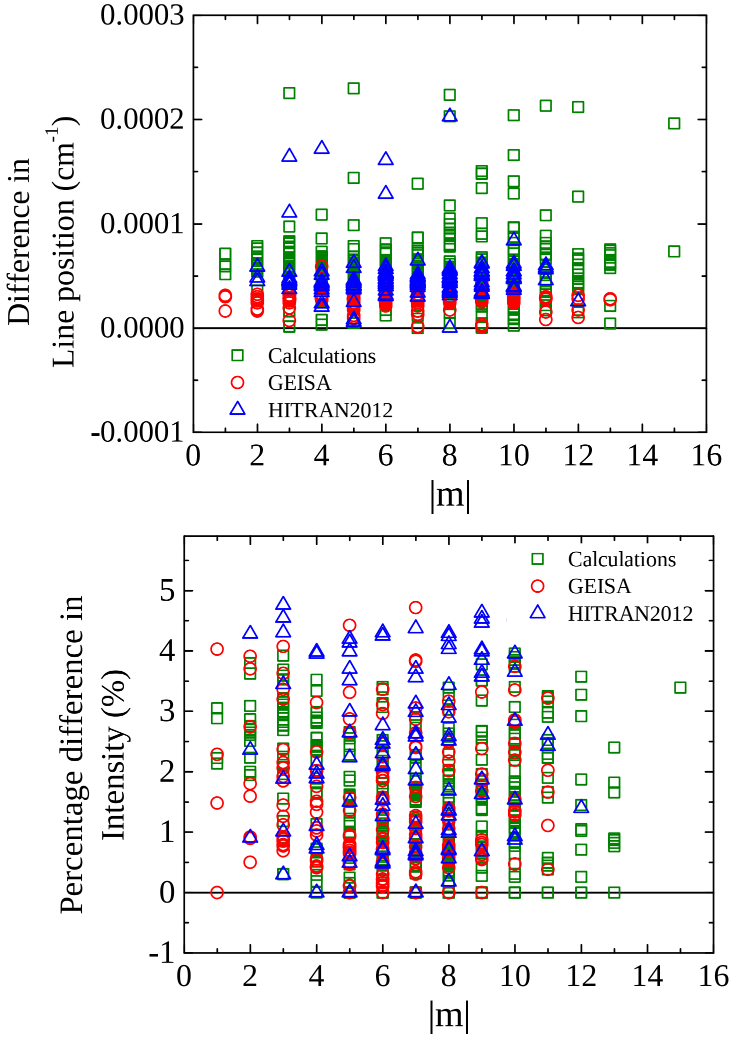

Figure 5.4: Comparison of measured line positions and intensities of $\nu_3 + \nu_4$ band of methane with HITRAN, GEISA databases and theoretical calculations for both P and R branches (shown with $|m|$). As can be seen there are several values for each $|m|$ numbers (based on Table 5.2 information). These multiple points for each $|m|$, results from the polyad quantum number and different symmetry species (A, F, and E). Polyad quantum number accounts for higher-order terms in the potential energy expansion due to the anharmonic vibrations of methane molecule.

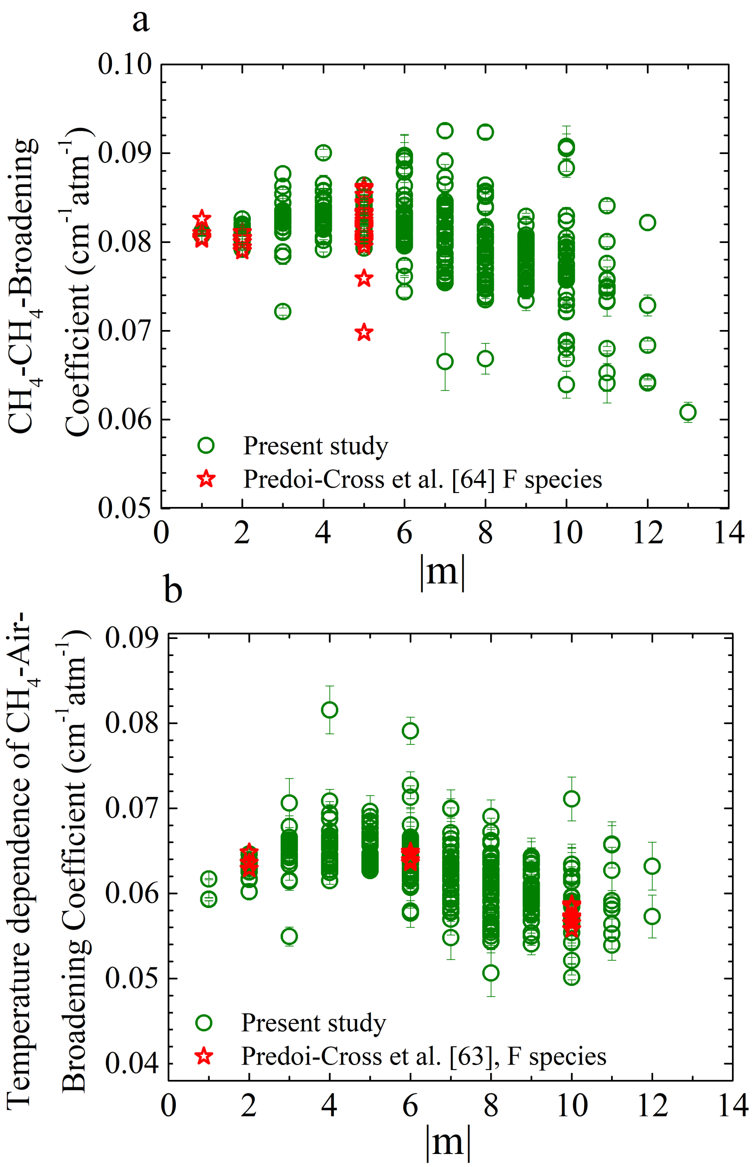

Figure 5.5: CH_4-CH_4 and CH_4-air- broadening coefficients of the $\nu_3 + \nu_4$ band of methane compared with previous studies and their rotational dependence (the same explanation for multiple values for each $|m|$ as Figure 5.4.)

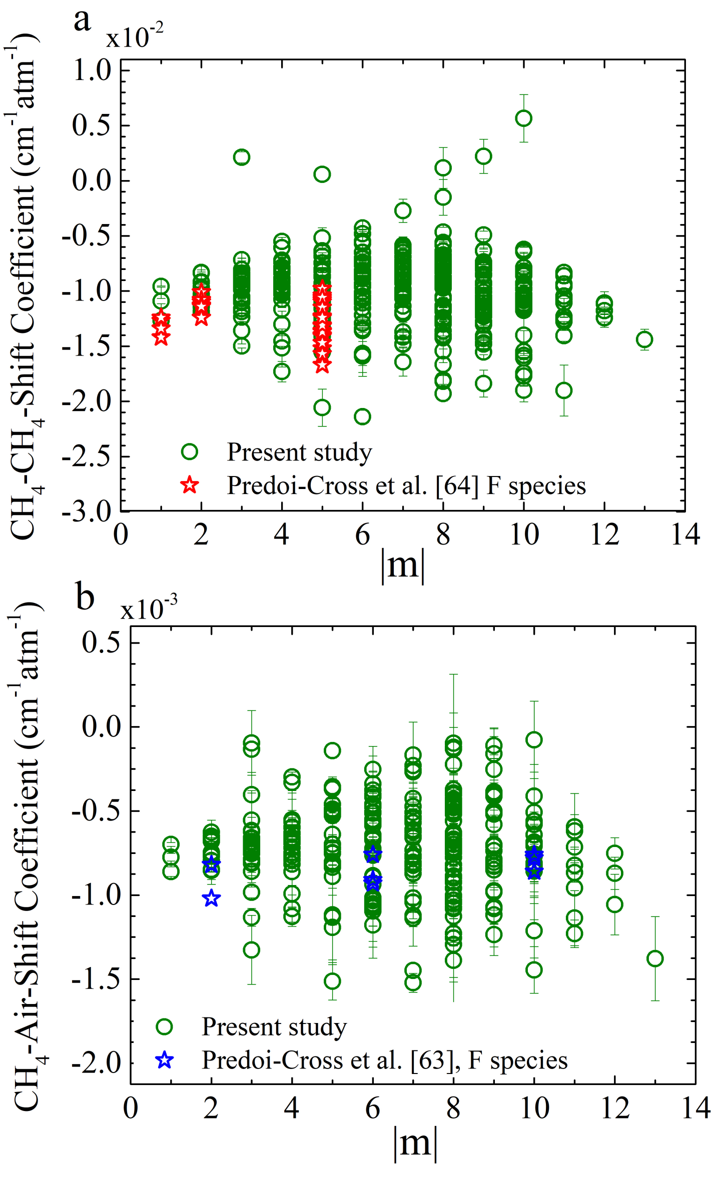

Figure 5.6: CH_4-CH_4 and CH_4-air- induced shift coefficients of the $\nu_3 + \nu_4$ band of methane compared with previous studies.

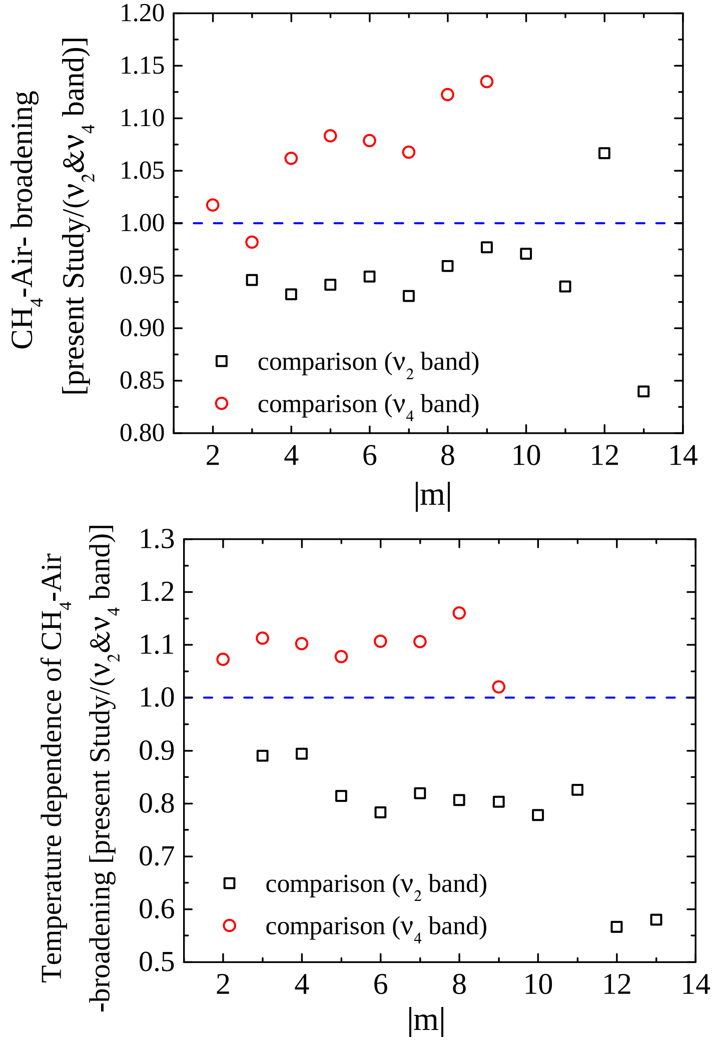

Figure 5.7: Comparison of obtained air- broadening coefficients and temperature dependencies of air- broadening coefficients in the $\nu_3 + \nu_4$ band of methane with published results of ν_2 and ν_4 band (present study/$\nu_2\nu_4$) [15, 16]. We note that each of these data points representing the average of several transition over $|m|$ value. The present measured air-broadening values are larger than ν_4 band ans smaller than ν_2 band values, stating that there is a vibrational dependence for the air- broadening of methane. The bottom panel presents the same type of comparison for the temperature dependence of air- broadening coefficient.

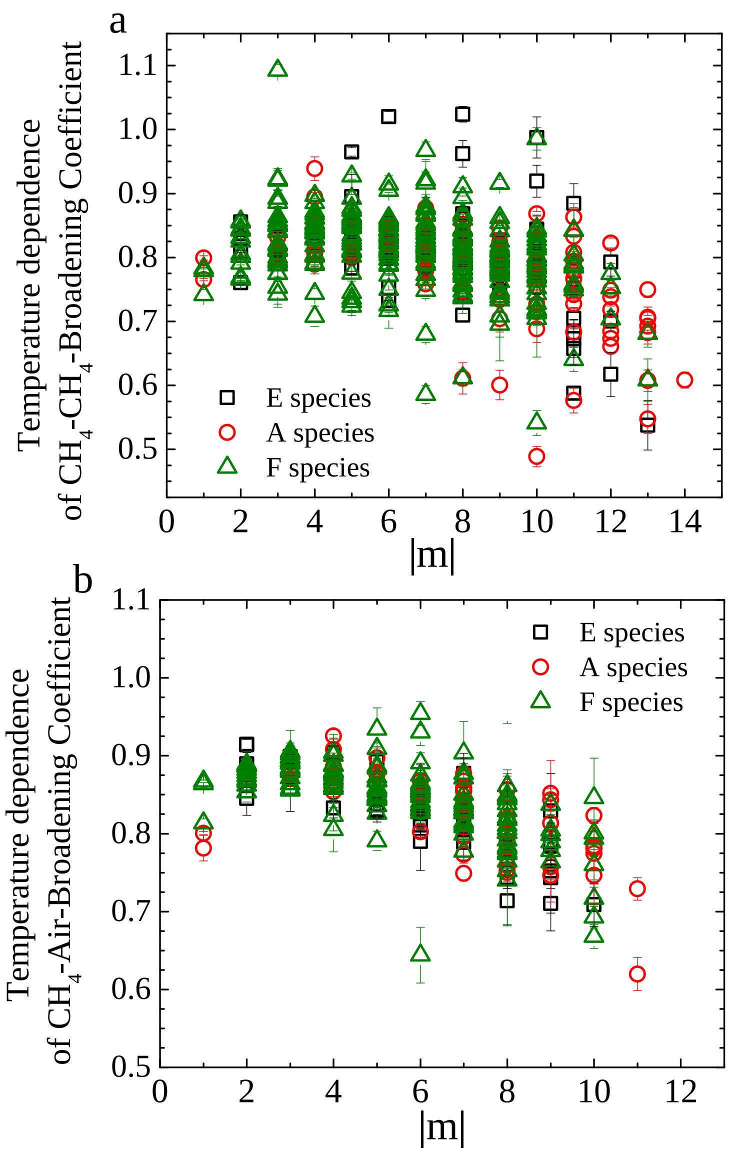

Figure 5.8: Temperature dependence of CH_4-CH_4 and CH_4-air-broadened half-width coefficients in the $\nu_3 + \nu_4$ band of methane for *A*, *E*, and *F* symmetry species. A rotational dependence trend can be seen in both panels for the temperature dependence of self and air-broadening coefficients.

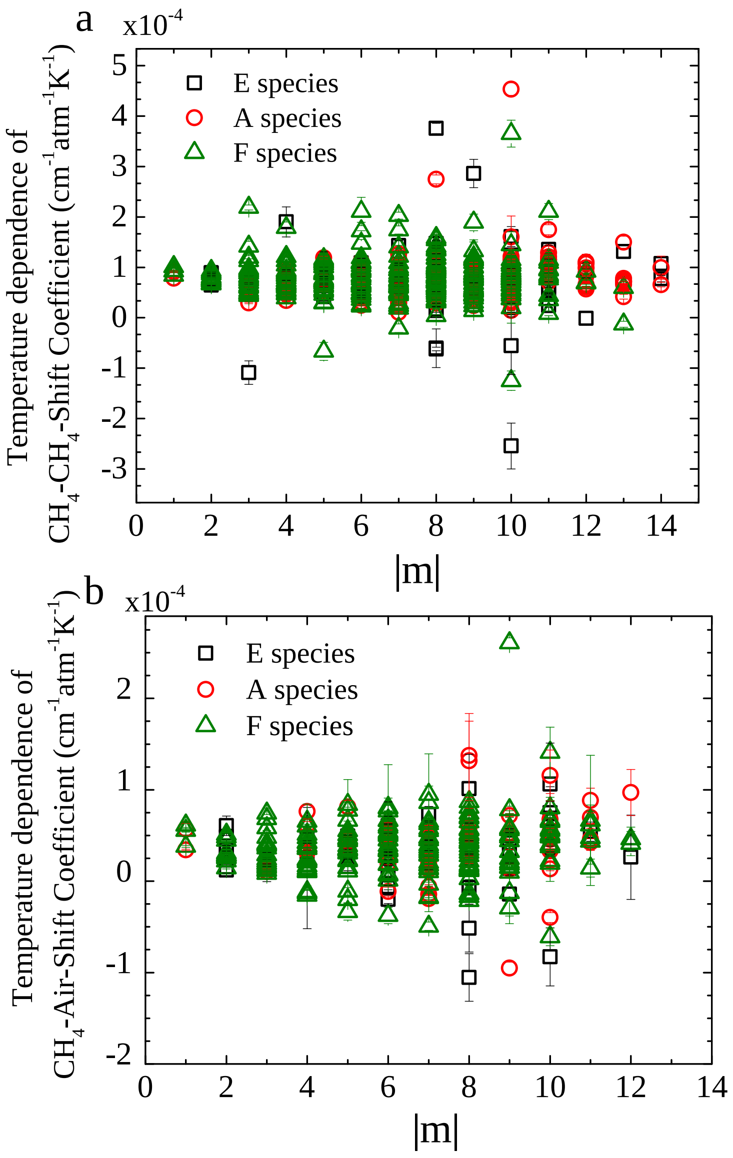

Figure 5.9: Temperature dependence exponents of CH_4-CH_4 and CH_4-air-shift coefficients in the $\nu_3 + \nu_4$ band of methane for *A*, *E*, and *F* symmetry species.

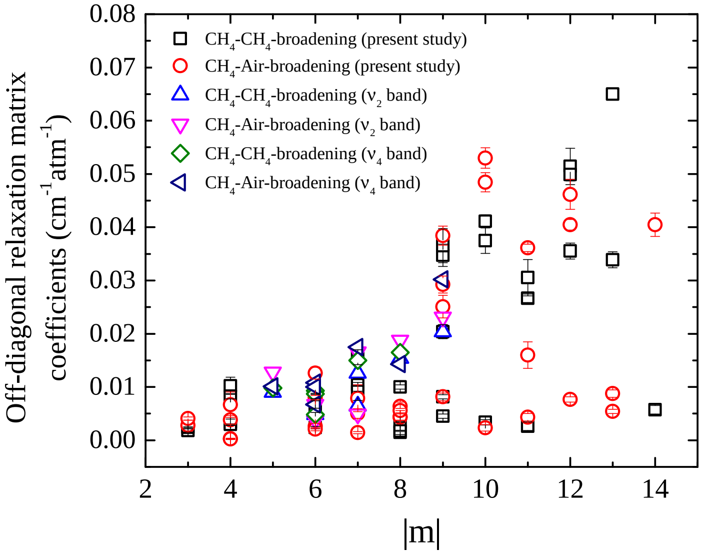

Figure 5.10: Off-diagonal relaxation matrix coefficients elements in the $\nu_3 + \nu_4$ band of methane compared to Refs. [15, 16]. The graph shows that there is a rotational dependence for the line mixing coefficients. The comparison with other band results, presents that how most of the values are overlapped, indicating that there is not strong vibrational dependence for the line mixing coefficients.

Chapter 6

Conclusions

Collecting information on the shape of a spectral line and measuring the line shape parameters contribute to understanding the underlying mechanism controlling the absorption and emission of radiation in planetary atmospheres. There is immense interest in specific spectroscopic parameters that are used in the simulation of high-resolution observations recorded by satellites to circumvent systematic errors in concentration calculation due to using incorrect line shape parameters. The error on concentration retrieval results in difficulties in obtaining valid information on climate change and on variation of the sources and sinks of the atmospheric greenhouse gases.

To avoid the errors due to using inaccurate line shape parameters, recording laboratory spectra with high resolution and signal to noise ratio is necessary. Several remote sensing missions will profit from these line shape investigations. Example satellite missions include GOSAT, and ACE.

Line shape coefficients, such as line positions, intensities, pressure broadening, pressure shifts, speed dependence and line mixing are needed. With these parameters, remote sensing spectra can be simulated, and the concentration of different species existing in the probed atmospheres can be determined. The simulation produced by using least squares fitting of the calculated model to the observed spectra.

6.1 Summary

The first part of the thesis was on the calculation of the Boltzmann constant with high accuracy based on the spectral line shape study of acetylene recorded using a tunable diode laser. This method is an alternative creative method of obtaining precise values to find out where most of the experimental errors originate (the error sources will be discussed later in this chapter). In this investigation, it was intended to collect the line shape parameters using the speed dependent Voigt profile to calculate absorption coefficients. The next focus of the thesis was the investigation of line parameters for two atmospheric trace gases (CO and CH_4 molecules) using different line shape models including the effects of line mixing. High-resolution spectra under a variety of laboratory conditions were recorded. The EPG formalism was employed to get off-diagonal relaxation matrix elements (line mixing coefficients). For acetylene, I did not apply the line mixing effect because of the low pressure of the spectra.

The most recent HITRAN database is HITRAN 2016, and part of the present research has contributed to this database by adding more validated laboratory results. The task also involves creating semi-empirical models for interpolating and extrapolating these data to complete the database beyond the existing measured parameters. These data will be invaluable for modelling and interpreting spectra of planetary atmospheres.

6.2 The results and findings

This document introduces a useful approach to use more advanced line shape parameters in spectroscopic communities, by using a line profile which is capable of simulating the observed absorption spectra with high accuracy, at a low computational cost. Throughout the thesis, it was shown that by using the speed dependent Voigt profile in the analysis of experimental spectra, more precise values for line parameters were obtained. Therefore, for the future spectroscopic databases, this model including line mixing can replace the Voigt profile. Calculating the experimental spectra based on the line-by-line method is a challenging task since most often the spectra are collected in a wide range of pressures and temperatures (based on the atmospheric conditions). The multispectrum technique is used in the present thesis to fit the spectra simultaneously and includes the correlations among the different parameters.

The laboratory spectroscopy of atmospheric trace gases acetylene, carbon monoxide, and methane have been described, and a line shape study is used to explain the acquired spectra. The proposed gases are of interest for planetary researchers to obtain information on the gas quantity.

6.2.1 Acetylene study

The purpose of this study was Doppler thermometry of acetylene for measuring the Boltzmann constant. In any experiments, two sorts of errors may affect the residual obtained for each atmospheric spectra. The first type is random error often emerging from instrumental noise. The second type of error is the systematic error related to the line shape parameters where they enter in radiative transfer codes. The most accurate spectroscopic parameters help atmospheric scientists avoid under/overestimation of concentration calculation. Therefore, for reducing these type of errors, laboratory spectra with higher resolution are needed to retrieve the spectroscopic parameters. Following is a test performed on acetylene gas to understand the experimental error sources.

The spectra were recorded at room temperature and low gas pressures to complete Doppler thermometry. The reason why acetylene was used for this experiment is because previously several experiments on this gas were performed in our lab and I had prior knowledge about the experimental procedure. Besides, it is a linear molecule, and its spectra were easy to analyze. Room temperature was a good choice to conduct experiments since the thermal stability was achievable faster and more dependably. It was crucial to do the measurement in low pressure to avoid line center shifts and drifts. Line shape parameters have been obtained by examining the commonly used Voigt profile, and speed dependent Voigt profiles. Using the Voigt function was not adequate for calculating the Boltzmann constant as the calculated error value was too large. The calculated value for the Boltzmann constant using Doppler thermometry in the test using speed dependent Voigt model was 1.38066×10^{-23} JK^{-1} with relative statistical uncertainty of 8.54×10^{-5} at low pressure. The relative systematic error for k_B was 1.87×10^{-5}.

The conclusion for the first part of this study was that the signal to noise ratio requires the use of a more robust line shape model. In this experiment with the average signal to noise ratio (S/N=2000), the SDV model outperformed the Voigt profile resulting in higher accuracy (which was almost one order of magnitude higher). However, the signal to noise ratio was not high enough to allow us to distinguish the difference between different asymmetric components (because the fit error can not be lower than noise level). Therefore, this more advanced partially correlated speed dependent hard collision (pcSDHC) model did not result in any better performance.

Utilizing error analysis, the most significant uncertainty in this analysis was due to the temperature measurement, and the second most significant uncertainty was due to the line shape model that was used. The relative uncertainties for the Doppler width (γ_D), line position (ν) and temperature (T) 0.84×10^{-5}, 0.00038×10^{-5} and 8.51×10^{-5}, respectively. It is found that for temperature measurements, the thermal gradient was the most substantial error contributor. The uncertainty in the modelling of collisional effects was limited by the knowledge on the fitting parameters such as self-broadening, Doppler width, and parameter q as the type of potential and thus parameters m and n in the implementing the SDV model.

This experiment was a good examination case to estimate the accuracy of the experimental setup and the spectrometer. Based on the relative systematic error in the measurement of k_B (1.87×10^{-5}), it can be concluded that the first step in improving the accuracy was to re-calibrate and improve the thermometers and be careful in temperature stability (i.e., keeping the room temperature stable during the experiment) for spectroscopic experiments. For getting a more improved result, there are methods such as designing smaller sample cell and better measurement devices and detectors for recording accurate line positions.

The wide range of experimentalists who perform similar measurements can benefit from the result of this project. Knowing where are the major sources of errors, they can make adjustments to obtain more exact data measurement.

6.2.2 Carbon monoxide study

In the second phase of this dissertation, completed at the University of Brussels (ULB), a detailed analysis of high-resolution Fourier transform spectra of CO mixed with CO_2 at total pressures up to 1212 hPa were carried out using a multispectrum least squares fitting technique. The necessity of this research was studying the CO-CO_2 interaction on Venus's atmosphere. The qSDV profile with weak line mixing adequately modelled the observed molecular line shapes, to within the noise level.

The CO_2 broadening and shift coefficients for transitions in the $2-0$ band of $^{12}C^{16}O$, up to $J''=22$ were measured. The temperature dependence of the broadening parameters, as well as the weak line mixing coefficients, were obtained. The data tables provided in chapter 4 were outstanding results since they have been used to populate the HITRAN database as the most accurate results measured so far and will appear in the next update of the HITRAN2020 paper. Following improvements were achieved:

- The broadening values were improved by 1-2 % over the existing HITRAN values.
- The pressure shift coefficients obtained had higher precision and three to five times higher accuracy compared to the existing shift coefficient values on the database (see Figure 4.7).
- As is shown in Table 4.3, temperature dependencies of the broadening parameters obtained with an accuracy of 10^{-5}, resulting in one order of magnitude improvement to the existing values.

- More importantly, the speed dependent and line mixing parameters are added and have been used to populate all the bands of CO.

For the temperature dependencies of the broadening parameters, an interesting trend was found. The temperature dependencies had an inverse relation with intensity, and the lower intensity lines had stronger temperature dependence.

Moreover, semi-empirical calculations were performed to obtain CO_2 broadening and CO_2 shift parameters. Comparison with the corresponding observed coefficients revealed that the calculated values are comparable at 296 K. Also, the weak CO_2 line mixing coefficients were collected using the EPG method. It is found that the temperature dependency is small for line mixing and CO_2-shift coefficients mostly because of the small temperature span used. The remaining residual structure in the modelling of this spectra is because we neglected the temperature dependence of line mixing.

The line intensities in this study did not vary noticeably when various line profiles were used (VP profile was 2 to 3 % less than the qSDV function). The narrowing and speed dependent effects result in narrower line shapes compared to those found by using the Voigt profile. Then the absorption peak would be higher and will lead to higher broadening values. An impressive finding of this study was that there is a rotational dependence for speed dependent parameter, therefore, for both P and R branches, we can extrapolate the results to get the values for higher quantum numbers. Furthermore, the graph of results for the speed dependence parameter showed the reduction of speed-dependent effect with perturber gas mass.

Using the qSDV line shape for CO-CO_2 represented an improvement in the computation accuracy compared to previous studies, affirming that this profile can advance concentration retrievals from satellite data meeting the threshold limit (the CO detection limit for SOIR instrument is 15 part per billion).

A study plan for the future will be to find out if there is a vibrational dependence between different bands. If for the existing experimental results, we find a trend, then we can predict the values for more bands without doing further experiments. This will be advantageous where we cannot comfortably experiment (e.g., weaker bands or higher temperatures not achievable in the lab).

6.2.3 Methane study:

The last part of my thesis was dedicated to line shape study of methane. The $\nu_3+\nu_4$ band of methane is an important band and had never been modelled using advanced line parameters for high-resolution spectroscopy. The existing line parameters in the HITRAN database are from a semi-empirical calculation of other bands in the octad region and should be revised in order to obtain accurate methane concentration. Therefore, the nature of this study was to determine the accurate line shape parameters such as CH_4-CH_4 and CH_4-air-broadened half-width, CH_4-CH_4 and CH_4-air-shift parameters and line mixing coefficients. The temperature dependence of CH_4-CH_4 and CH_4-air-broadened half-width, CH_4-CH_4 and CH_4-air-shift parameters in the $\nu_3+\nu_4$ band of methane were also needed.

Comparison of intensities and line positions of a selected number of strong transitions showed good agreement between the present work, HITRAN, GEISA databases and theoretical calculation. A difference of about 5% was expected since the existing values are reported based on the semi-empirical calculations in HITRAN. The findings of this research are expected to be included in the database after validation.

Comparisons of the present results and HITRAN2012 values showed that the average deviation of line intensities was between 1 to 4% for methane. This improvement is capable of providing accuracy conditions for the satellite missions for Earth's atmospheric research. The desired accuracy for GOSAT is 0.4%, and it means achieving 8 part per billion uncertainty in concentration measurements. The improved results obtained for the present study, are able to decrease the standard deviation of the concentrations at least five times by taking into account the right values for pressure-induced shift coefficient.

Comparisons of the line positions with HITRAN, the absolute differences were found to be in the order of 10^{-3} cm^{-1} to 10^{-4} cm^{-1}. This discrepancy was about five percent for most of the lines. Even this much variation in radiative transfer calculations is non-negligible and should be taken into account.

The determined temperature dependence for CH_4-CH_4 and CH_4-air-broadening were often close, and for several transitions, the temperature dependence exponents for self-broadened half-width coefficients were slightly higher compared with those to air-broadened half-width coefficients. Similarly, the temperature dependence for CH_4-CH_4-shift coefficients that were more significant corresponded with those for CH_4-air-shift coefficients.

The quadratic speed dependent Voigt profile including line mixing through the off-diagonal relaxation matrix elements formalism showed better residuals. Fitting the spectra in a limited wavenumber range each time, the line mixing parameters were determined for several mixed pairs of transitions. The difference between CH_4-CH_4 and CH_4-air-line mixing coefficients was small. It is hoped that the performed measurement presented in the thesis will encourage the implementation of better quantum mechanical models for methane line shapes.

6.3 Closing remarks

Laboratory spectroscopic studies help to improve estimating of atmospheric compositions mole fractions leading to enhanced capability for understanding environmental concerns. Better uncertainties of atmospheric retrievals can be gained by removing the sources of systematic errors in calculations, by adding spectral line parameters. Accordingly, advanced molecular line shapes should be examined.

To assess atmospheric spectra with high accuracy, the individual absorption spectral lines can be computed in the frequency range of the measured spectrum, in a variety of pressures and temperatures gauged by the instrument line-of-sight. In the line by line model, the lines are taken from the HITRAN. For every frequency, the line-by-line calculation is made to obtain the participation of each spectral line for a particular molecule.

The evaluation of existing spectroscopic databases and their updates with the latest spectroscopic data requires an open-ended practice. In particular, the validation of the spectroscopic parameters in the most extended range of temperature, pressure, and absorber amounts appropriate to the specifications of existing or future instruments are essential to fully exploit their observing capabilities.

The results of this laboratory study discussed the broad aims of the Atmospheric Composition Laboratory Research Program to advance the observation and knowledge of terrestrial atmospheric and planetary formation [194] and to provide an improved measurements of the environment.

6.4 Publications

- Predoi-Cross A, Hashemi R, Devi V, Naseri H, Smith M A H, Analysis of Fourier transform spectra of N_2O in the ν_3 band for atmospheric composition retrievals, Canadian Journal of Physics 96, 454-464, (2018).

- Hashemi R, Dudaryonok A S, Lavrentieva N N, Vandaele A C, Vander Auwera J, Nikitin A V, Tyuterev Vl G, Sung K, Smith M A H, Devi V, Predoi-Cross A, Fourier Transform Spectroscopy of two trace gases namely Methane and Carbon monoxide for planetary and atmospheric research application, Journal of Physics, (Feb 2017).

- Hashemi R, Predoi-Cross A, Nikitin A V, Tyuterev V G, Sung K, Smith M A H, Devi V, Spectroscopic line parameters of CH_4 for atmospheric composition retrievals in the 4300-4500 cm^{-1} region, Journal of Quantitative Spectroscopy and Radiative Transfer, 186, 106117, (2017).

- Hashemi R, Predoi-Cross A, Vander Awera J et al., CO_2 Pressure Broadening and Shift Coefficients for the $2-0$ Band of CO, Journal of Molecular Spectroscopy, 326, 60-72, (2016).

- Hashemi R, Povey C, Predoi-Cross A et al., Doppler Thermometry of Acetylene for Accurate Measurements of the Boltzmann Constant, Journal of Chemical Physics, 141(21): 214201, (2014).
- Hashemi R, Rozario H, Povey C, Predoi-Cross A, Line-shape models testing on six acetylene transitions in the $\nu_1 + \nu_3$ band broadened by N_2, Journal of Quantitative Spectroscopy and Radiative Transfer, 140, 58-66, (2014).
- Hashemi R, Rozario H, Ibrahim A, Predoi-Cross A, Line Shape Study of the Carbon Dioxide Laser Band I Canadian Journal of Physics, 91(11): 924-936, (2013).

Non-refereed publications

- Karns J, Matt W, Kochanov R V, Gordon I E, Rothman L S, Tan Y, Hashemi R, Kanbur S, Tenbergen B, HITRAN Application Programming Interface and Efficient Spectroscopic Tools (HAPIEST), 15th Biennial HITRAN Conference united with 14th ASA conference, Cambridge, MA, USA, (2018).
- Sowiski1 M, Bielska K, Wjtewicz S, Domysawska J, Hashemi R, Morzyski P, Wciso P, Cygan A, Predoi-Cross A, Ciuryo R, Lisak D, Oxygen Spectra in O_2-N_2 Mixture Measured with FS-CRDS, IMAMPC 2017 conference, (2017).
- Hashemi R, Predoi- Cross A et al., Multispectrum analysis of methane in the $\nu_1 + \nu_4$ bands and temperature dependencies of self- and air-broadened line parameters, The 24th Colloquium on High-Resolution Molecular Spectroscopy, HRMS 2015, Dijon, France, (2015).
- Hashemi R, Vander Awera J et al., CO_2- Broadening and shift parameters of CO in the atmosphere of Venus, The 24th Colloquium on High-Resolution Molecular Spectroscopy, HRMS 2015, Dijon, France, (2015).

- Hashemi R, Predoi- Cross A et al., High-Resolution Spectroscopy of Methane for Climate Change Research Applicationsin The International Summer School SPECATMOS on the Spectroscopy and Physico-Chemistry of Planetary Atmospheres, Frjus, France, (2015).
- Hashemi R, Predoi-Cros A, Self- and air-broadened line shape parameters of methane in the 2.3 microns range, Congrs de l'ACP at University of Alberta, (2015).
- Hashemi R, Rozario H, Buldyreva J, Mellau G, Predoi-Cross A, Spectroscopic study of acetylene and hydrogen cyanide, French-German summer school, Corsica, France, (2014).
- Hashemi R, Rozario H, Povey C, Garber J, Derksen M, Predoi-Cross A, Recent line-shape and Doppler thermometry studies involving transitions in the $\nu_1 + \nu_3$ band of acetylene, Proceedings of the HITRAN Conference, Cambridge, MA, USA, (2014).
- Hashemi R, Rozario H, Povey C, Garber J, Derksen M, Predoi-Cross A, Recent line-shape studies involving transitions in the $\nu_1 + \nu_3$ band of acetylene, Proceedings of the Line-shape study Conference, Bologna, Italy, (2014).

Bibliography

[1] I.E. Gordon, L.S. Rothman, C. Hill, R.V. Kochanov, Y. Tan, P.F. Bernath, M. Birk, V. Boudon, A. Campargue, K.V. Chance, B.J. Drouin, J.-M. Flaud, R.R. Gamache, J.T. Hodges, D. Jacquemart, V.I. Perevalov, A. Perrin, K.P. Shine, M.-A.H. Smith, J. Tennyson, G.C. Toon, H. Tran, V.G. Tyuterev, A. Barbe, A.G. Csszr, V.M. Devi, T. Furtenbacher, J.J. Harrison, J.-M. Hartmann, A. Jolly, T.J. Johnson, T. Karman, I. Kleiner, A.A. Kyuberis, J. Loos, O.M. Lyulin, S.T. Massie, S.N. Mikhailenko, N. Moazzen-Ahmadi, H.S.P. Mller, O.V. Naumenko, A.V. Nikitin, O.L. Polyansky, M. Rey, M. Rotger, S.W. Sharpe, K. Sung, E. Starikova, S.A. Tashkun, J. Vander Auwera, G. Wagner, J. Wilzewski, P. Wciso, S. Yu, and E.J. Zak. The hitran2016 molecular spectroscopic database. *Journal of Quantitative Spectroscopy and Radiative Transfer*, 203:3 – 69, 2017. ISSN 0022-4073. doi: https://doi.org/10.1016/j.jqsrt.2017.06.038. URL `http://www.sciencedirect.com/science/article/pii/S0022407317301073`. HITRAN2016 Special Issue.

[2] P.F. Bernath. *Spectra of Atoms and Molecules*. Oxford University Press, 2005. ISBN 9780195346459. URL `https://books.google.ca/books?id=pW3uok6nITMC`.

[3] URL `http://hitran.org/`.

[4] N. Jacquinet-Husson, L. Crepeau, R. Armante, C. Boutammine, A. Chdin, N.A. Scott, C. Crevoisier, V. Capelle, C. Boone, N. Poulet-Crovisier, A. Barbe, A. Campargue, D. Chris Benner, Y. Benilan, B. Bzard, V. Boudon, L.R. Brown, L.H. Coudert, A. Coustenis, V. Dana, V.M. Devi, S. Fally, A. Fayt, J.-M. Flaud, A. Goldman, M. Herman, G.J. Harris, D. Jacquemart, A. Jolly, I. Kleiner, A. Kleinbhl, F. Kwabia-Tchana, N. Lavrentieva, N. Lacome, Li-Hong Xu, O.M. Lyulin, J.-Y. Mandin, A. Maki, S. Mikhailenko, C.E. Miller, T. Mishina, N. Moazzen-Ahmadi, H.S.P. Mller, A. Nikitin, J. Orphal, V. Perevalov, A. Perrin, D.T. Petkie, A. Predoi-Cross, C.P. Rinsland, J.J. Remedios, M. Rotger, M.A.H. Smith, K. Sung, S. Tashkun, J. Tennyson, R.A. Toth, A.-C. Vandaele, and J. Vander Auwera. The 2009 edition of the geisa spectroscopic database. *Journal of Quantitative Spectroscopy and Radiative Transfer*, 112(15):2395 – 2445, 2011. ISSN 0022-4073. doi: https://doi.org/10.1016/j.jqsrt.2011.06.004. URL `http://www.sciencedirect.com/science/article/pii/S0022407311002160`.

[5] Edward W. Castner. Modern spectroscopy, 4th edition (j. michael hollas). *Journal of Chemical Education*, 82(1):43, 2005. doi: 10.1021/ed082p43.1. URL `https://doi.org/10.1021/ed082p43.1`.

[6] K.N. Liou. *An Introduction to Atmospheric Radiation*. International Geophysics.

Elsevier Science, 2002. ISBN 9780080491677. URL `https://books.google.ca/books?id=mQ1DiDpX34UC`.

[7] Chad Povey, Adriana Predoi-Cross, and Daniel R Hurtmans. Line shape study of acetylene transitions in the <i> ν </i> < sub> 1</sub> +<i> ν </i> ₂ +<i> ν </i> < sub> 4</sub>+<i> ν </i> ₅ band over a range of temperatures. *Journal of Molecular Spectroscopy*, 268(1):177–188, 2011.

[8] Jean Vander Auwera. *Quantitative high resolution Fourier transform infrared spectroscopy*. PhD thesis, Universite Libre de Bruxelles, 2004.

[9] Prasad Varanasi. Measurement of line widths of co of planetary interest at low temperatures. *Journal of Quantitative Spectroscopy and Radiative Transfer*, 15(2):191 – 196, 1975. ISSN 0022-4073. doi: https://doi.org/10.1016/0022-4073(75)90017-5. URL `http://www.sciencedirect.com/science/article/pii/0022407375900175`.

[10] Keeyoon Sung and Prasad Varanasi. Co_2-broadened half-widths and co_2-induced line shifts of co relevant to the atmospheric spectra of venus and mars. *Journal of Quantitative Spectroscopy and Radiative Transfer*, 91(3):319 – 332, 2005. ISSN 0022-4073. doi: https://doi.org/10.1016/j.jqsrt.2004.05.063. URL `http://www.sciencedirect.com/science/article/pii/S0022407304002225`.

[11] T. Nakazawa and M. Tanaka. *J. Quant. Spectrosc. Radiat. Transf.*, 28:471–480, 1982.

[12] V. Malathy Devi, D. Chris Benner, M.A.H. Smith, A.W. Mantz, K. Sung, L.R. Brown, and A. Predoi-Cross. Spectral line parameters including temperature dependences of self- and air-broadening in the 2-0 band of co at 2.3μm. *Journal of Quantitative Spectroscopy and Radiative Transfer*, 113(11):1013 – 1033, 2012. ISSN 0022-4073. doi: https://doi.org/10.1016/j.jqsrt.2012.02.010. URL `http://www.sciencedirect.com/science/article/pii/S0022407312000696`. Three Leaders in Spectroscopy.

[13] Predoi-Cross A, Bouanich J. P, Chris Benner D, May A. D, and Drummond J. R. Broadening, shifting, and line asymmetries in the 2-0 band of co and con_2: Experimental results and theoretical calculations. *The Journal of Chemical Physics*, 113: 158, 2000. doi: https://doi.org/10.1063/1.481783. URL `https://aip.scitation.org/doi/10.1063/1.481783#Metrics-content`.

[14] J.W Brault, L.R Brown, C Chackerian, R Freedman, A Predoi-Cross, and A.S Pine. Self-broadened co line shapes in the 2-0 band. *Journal of Molecular Spectroscopy*, 222(2):220 – 239, 2003. ISSN 0022-2852. doi: https://doi.org/10.1016/j.jms.2003.07.002. URL `http://www.sciencedirect.com/science/article/pii/S0022285203002327`.

[15] M.A.H. Smith, D. Chris Benner, A. Predoi-Cross, and V. Malathy Devi. A multispectrum analysis of the ν_4 band of $^{13}ch_4$: Widths, shifts, and line mixing coefficients. *Journal of Quantitative Spectroscopy and Radiative Transfer*,

112(6):952 – 968, 2011. ISSN 0022-4073. doi: https://doi.org/10.1016/j.jqsrt.2010.11.017. URL `http://www.sciencedirect.com/science/article/pii/S0022407310004401`.

[16] M.A.H. Smith, D. Chris Benner, A. Predoi-Cross, and V. Malathy Devi. Air- and self-broadened half widths, pressure-induced shifts, and line mixing in the 2 band of 12ch4. *Journal of Quantitative Spectroscopy and Radiative Transfer*, 133:217 – 234, 2014. ISSN 0022-4073. doi: https://doi.org/10.1016/j.jqsrt.2013.08.004. URL `http://www.sciencedirect.com/science/article/pii/S0022407313003233`.

[17] R.K. Pachauri and L.A. Meyer. Ipcc, 2014: Climate change 2014: Synthesis report. contribution of working groups i, ii and iii to the fifth assessment report of the intergovernmental panel on climate change. *IPCC, Geneva, Switzerland*, page 151, 2014. URL `https://link.aps.org/doi/10.1103/PhysRev.89.472`.

[18] URL `http://www.ipcc.ch/report/ar5/index.shtml`.

[19] J. Hansen, R. Ruedy, M. Sato, and K. Lo. Global surface temperature change. *Rev. Geophys.*, 48:RG4004, 2010. doi: 10.1029%2F2010RG000345.

[20] P. F. Levelt, E. Hilsenrath, G. W. Leppelmeier, G. H. J. van den Oord, P. K. Bhartia, J. Tamminen, J. F. de Haan, and J. P. Veefkind. Science objectives of the ozone monitoring instrument. *IEEE Transactions on Geoscience and Remote Sensing*, 44 (5):1199–1208, May 2006. ISSN 0196-2892. doi: 10.1109/TGRS.2006.872336.

[21] H. Bovensmann, J. P. Burrows, M. Buchwitz, J. Frerick, S. Nol, V. V. Rozanov, K. V. Chance, and A. P. H. Goede. Sciamachy: Mission objectives and measurement modes. *Journal of the Atmospheric Sciences*, 56(2):127–150, 1999. doi: 10.1175/1520-0469(1999)056⟨0127:SMOAMM⟩2.0.CO;2. URL `https://doi.org/10.1175/1520-0469(1999)056<0127:SMOAMM>2.0.CO;2`.

[22] Reinhard Beer, Thomas A. Glavich, and David M. Rider. Tropospheric emission spectrometer for the earth observing system's aura satellite. *Appl. Opt.*, 40(15): 2356–2367, May 2001. doi: 10.1364/AO.40.002356. URL `http://ao.osa.org/abstract.cfm?URI=ao-40-15-2356`.

[23] P. F. Bernath. The Atmospheric Chemistry Experiment (ACE). , 186:3–16, January 2017. doi: 10.1016/j.jqsrt.2016.04.006.

[24] M. Alexe, P. Bergamaschi, A. Segers, R. Detmers, A. Butz, O. Hasekamp, S. Guerlet, R. Parker, H. Boesch, C. Frankenberg, R. A. Scheepmaker, E. Dlugokencky, C. Sweeney, S. C. Wofsy, and E. A. Kort. Inverse modelling of ch$_4$ emissions for 20102011 using different satellite retrieval products from gosat and sciamachy. *Atmospheric Chemistry and Physics*, 15(1):113–133, 2015. doi: 10.5194/acp-15-113-2015. URL `https://www.atmos-chem-phys.net/15/113/2015/`.

[25] C. Frankenberg, R. Pollock, R. A. M. Lee, R. Rosenberg, J.-F. Blavier, D. Crisp, C. W. O'Dell, G. B. Osterman, C. Roehl, P. O. Wennberg, and D. Wunch. The orbiting carbon observatory (oco-2): spectrometer performance evaluation using prelaunch direct sun measurements. *Atmospheric Measurement Techniques*, 8(1):301–313, 2015. doi: 10.5194/amt-8-301-2015. URL `https://www.atmos-meas-tech.net/8/301/2015/`.

[26] J. Houghton. *The Physics of Atmospheres*. Cambridge University Press, 2002. ISBN 9780521011228. URL `https://books.google.ca/books?id=K9wGHim2DXwC`.

[27] URL `http://www.ndsc.ws/`.

[28] C. Camy-Peyret, P. Jeseck, Y. Té, S. Payan, and J. Evrard. IASI balloon: a nadir looking Fourier transform spectrometer operating in thermal emission for atmospheric sounding. In B. Warmbein, editor, *European Rocket and Balloon Programmes and Related Research*, volume 471 of *ESA Special Publication*, pages 245–250, August 2001.

[29] W. Voigt. ber das gesetz intensittsverteilung innerhalb der linien eines gas spektrams. *Sitzber. Bayr Akad. Mnchen Ber.*, 603, 1912.

[30] R. H. Dicke. The effect of collisions upon the doppler width of spectral lines. *Phys. Rev.*, 89:472–473, Jan 1953. doi: 10.1103/PhysRev.89.472. URL `https://link.aps.org/doi/10.1103/PhysRev.89.472`.

[31] Paul R. Berman. Speed-dependent collisional width and shift parameters in spectral profiles. *Journal of Quantitative Spectroscopy and Radiative Transfer*, 12(9):1331 – 1342, 1972. ISSN 0022-4073. doi: https://doi.org/10.1016/0022-4073(72)90189-6. URL `http://www.sciencedirect.com/science/article/pii/0022407372901896`.

[32] Herbert M. Pickett. Effects of velocity averaging on the shapes of absorption lines. *The Journal of Chemical Physics*, 73(12):6090–6094, 1980. doi: 10.1063/1.440145. URL `https://doi.org/10.1063/1.440145`.

[33] A. S. Pine. Line shape asymmetries in arbroadened hf(v=10) in the dickenarrowing regime. *The Journal of Chemical Physics*, 101(5):3444–3452, 1994. doi: 10.1063/1.467529. URL `https://doi.org/10.1063/1.467529`.

[34] David P. Edwards and L. Larrabee Strow. Spectral line shape considerations for limb temperature sounders. *Journal of Geophysical Research: Atmospheres*, 96(D11):20859–20868. doi: 10.1029/91JD02293. URL `https://agupubs.onlinelibrary.wiley.com/doi/abs/10.1029/91JD02293`.

[35] Piotr Wciso, Agata Cygan, Daniel Lisak, and Roman Ciuryo. Line-shapes analysis with ultra-high accuracy. *Journal of Physics: Conference Series*, 548(1):012022, 2014. URL `http://stacks.iop.org/1742-6596/548/i=1/a=012022`.

[36] J.M. Hollas. *High Resolution Spectroscopy*. Elsevier Science, 2013. ISBN 9781483100906. URL `https://books.google.ca/books?id=Pbn8BAAAQBAJ`.

[37] A.G. Reule. Errors in spectrophotometry and calibration procedures to avoid them. *Journal of Research of the National Bureau of Standards*, 80A(4):609, 1976. URL `https://nvlpubs.nist.gov/nistpubs/jres/80A/jresv80An4p609_A1b.pdf`.

[38] C. Bliefert and R Perraud. *Chimie de lenvironnement - Air, eau, sols, dchets*. De Boeck, 2009.

[39] URL `https://sos.noaa.gov/datasets/carbon-monoxide-2008-2011/`.

[40] URL `https://earthobservatory.nasa.gov/features/EnergyBalance/page4.php`.

[41] R.K. Pachauri and A. Reisinger. *Climate Change 2007: Synthesis Report*. Intergovernmental Panel on Climate Change, 2007. ISBN 92-9169-122-4. URL `https://www.ipcc.ch/publications_and_data/publications_ipcc_fourth_assessment_report_synthesis_report.htm`.

[42] B. N. Duncan and J. A. Logan. Model analysis of the factors regulating the trends and variability of carbon monoxide between 1988 and 1997. *Atmospheric Chemistry and Physics*, 8(24):7389–7403, 2008. doi: 10.5194/acp-8-7389-2008. URL `https://www.atmos-chem-phys.net/8/7389/2008/`.

[43] B. N. Duncan, J. A. Logan, I. Bey, I. A. Megretskaia, R. M. Yantosca, P. C. Novelli, N. B. Jones, and C. P. Rinsland. Global budget of co, 19881997: Source estimates and validation with a global model. *Journal of Geophysical Research: Atmospheres*, 112(D22). doi: 10.1029/2007JD008459. URL `https://agupubs.onlinelibrary.wiley.com/doi/abs/10.1029/2007JD008459`.

[44] Jean-Loup Bertaux, Ann-Carine Vandaele, Oleg Korablev, E. Villard, A. Fedorova, D. Fussen, E. Quémerais, D. Belyaev, A. Mahieux, F. Montmessin, C. Muller, E. Neefs, D. Nevejans, V. Wilquet, J. P. Dubois, A. Hauchecorne, A. Stepanov, I. Vinogradov, A. Rodin, the SPICAV/SOIR team, M. Cabane, E. Chassefière, J. Y. Chaufray, E. Dimarellis, F. Leblanc, F. Lefèvre, P. Rannou, E. Van Ransbeeck, L. Zasova, F. Forget, S. Lebonnois, D. Titov, S. Rafkin, G. Durry, J. C. Gérard, and B. Sandel. A warm layer in venus' cryosphere and high-altitude measurements of hf, hcl, h_2o and hdo. *Nature*, 450:646 EP –, Nov 2007. URL `http://dx.doi.org/10.1038/nature05974`.

[45] A.P. Vinogradov, Y.A. Surkov, B.M. Andreichikov, O.M. Kalinkina, and I.M. Grechischeva. The chemical composition of the atmosphere of venus. *Planetary atmospheres*, 40:3–16, 1971. doi: https://doi.org/10.1007/978-94-010-3063-2_1.

[46] W. P. Chu, E. W. Chiou, J. C. Larsen, L. W. Thomason, D. Rind, J. J. Buglia, S. Oltmans, M. P. McCormick, and L. M. McMaster. Algorithms and sensitivity analyses for stratospheric aerosol and gas experiment ii water vapor retrieval. *Journal of Geophysical Research: Atmospheres*, 98(D3):4857–4866. doi:

10.1029/92JD01628. URL https://agupubs.onlinelibrary.wiley.com/doi/abs/10.1029/92JD01628.

[47] Athena Coustenis, Alberto Negro, Alberto Salama, Bernhard Schulz, Emmanuel Lellouch, Pascal Rannou, Pierre Drossart, Thrse Encrenaz, Bernard Schmitt, Vincent Boudon, and Andrei Nikitin. Titan's 3-micron spectral region from iso high-resolution spectroscopy. *Icarus*, 180(1):176 – 185, 2006. ISSN 0019-1035. doi: https://doi.org/10.1016/j.icarus.2005.08.007. URL http://www.sciencedirect.com/science/article/pii/S0019103505002873.

[48] Vittorio Formisano, Sushil Atreya, Thérèse Encrenaz, Nikolai Ignatiev, and Marco Giuranna. Detection of methane in the atmosphere of mars. *Science*, 306(5702):1758–1761, 2004. ISSN 0036-8075. doi: 10.1126/science.1101732. URL http://science.sciencemag.org/content/306/5702/1758.

[49] A. Coradini, G. Filacchione, F. Capaccioni, P. Cerroni, A. Adriani, R.H. Brown, Y. Langevin, and B. Gondet. Cassini/vims-v at jupiter: Radiometric calibration test and data results. *Planetary and Space Science*, 52(7):661 – 670, 2004. ISSN 0032-0633. doi: https://doi.org/10.1016/j.pss.2003.11.005. URL http://www.sciencedirect.com/science/article/pii/S0032063303002356.

[50] P.G.J. Irwin, K. Sihra, N. Bowles, F.W. Taylor, and S.B. Calcutt. Methane absorption in the atmosphere of jupiter from 1800 to 9500 cm^1 and implications for vertical cloud structure. *Icarus*, 176(2):255 – 271, 2005. ISSN 0019-1035. doi: https://doi.org/10.1016/j.icarus.2005.02.004. URL http://www.sciencedirect.com/science/article/pii/S0019103505000564.

[51] D. J. Jacob, A. J. Turner, J. D. Maasakkers, J. Sheng, K. Sun, X. Liu, K. Chance, I. Aben, J. McKeever, and C. Frankenberg. Satellite observations of atmospheric methane and their value for quantifying methane emissions. *Atmospheric Chemistry and Physics*, 16(22):14371–14396, 2016. doi: 10.5194/acp-16-14371-2016. URL https://www.atmos-chem-phys.net/16/14371/2016/.

[52] E. J. Dlugokencky, L. Bruhwiler, J. W. C. White, L. K. Emmons, P. C. Novelli, S. A. Montzka, K. A. Masarie, P. M. Lang, A. M. Crotwell, J. B. Miller, and L. V. Gatti. Observational constraints on recent increases in the atmospheric ch$_4$ burden. *Geophysical Research Letters*, 36(18). doi: 10.1029/2009GL039780. URL https://agupubs.onlinelibrary.wiley.com/doi/abs/10.1029/2009GL039780.

[53] P. Bergamaschi, S. Houweling, A. Segers, M. Krol, C. Frankenberg, R. A. Scheepmaker, E. Dlugokencky, S. C. Wofsy, E. A. Kort, C. Sweeney, T. Schuck, C. Brenninkmeijer, H. Chen, V. Beck, and C. Gerbig. Atmospheric ch$_4$ in the first decade of the 21st century: Inverse modeling analysis using sciamachy satellite retrievals and noaa surface measurements. *Journal of Geophysical Research: Atmospheres*, 118(13):7350–7369. doi: 10.1002/jgrd.50480. URL https://agupubs.onlinelibrary.wiley.com/doi/abs/10.1002/jgrd.50480.

[54] . URL http://www.gosat.nies.go.jp/en/.

[55] . URL `http://www.gosat-2.nies.go.jp/`.

[56] A.V. Nikitin, O.M. Lyulin, S.N. Mikhailenko, V.I. Perevalov, N.N. Filippov, I.M. Grigoriev, I. Morino, Y. Yoshida, and T. Matsunaga. Gosat-2014 methane spectral line list. *Journal of Quantitative Spectroscopy and Radiative Transfer*, 154:63 – 71, 2015. ISSN 0022-4073. doi: https://doi.org/10.1016/j.jqsrt.2014.12.003. URL `http://www.sciencedirect.com/science/article/pii/S0022407314004750`.

[57] Annmarie Eldering, Chris Dell, Paul O. Wennberg, David Crisp, Michael R. Gunson, C Viatte, Charles Avis, Amy Braverman, Richard Castao, Albert Chang, Lars Chapsky, Cecilia Cheng, Brian Connor, Lan Dang, Gary Doran, Bonnie Fisher, Christian Frankenberg, D Fu, Robert Granat, and Jan Yoshimizu. The orbiting carbon observatory-2: First 18 months of science data products. 10:1–30, 09 2016.

[58] . URL `http://oco.jpl.nasa.gov/`.

[59] . URL `http://oco.jpl.nasa.gov/`.

[60] D. Chris Benner, V. Malathy Devi, Keeyoon Sung, Linda R. Brown, Charles E. Miller, Vivienne H. Payne, Brian J. Drouin, Shanshan Yu, Timothy J. Crawford, Arlan W. Mantz, Mary Ann H. Smith, and Robert R. Gamache. Line parameters including temperature dependences of air- and self-broadened line shapes of co_2: 2.06 μm region. *Journal of Molecular Spectroscopy*, 326:21 – 47, 2016. ISSN 0022-2852. doi: https://doi.org/10.1016/j.jms.2016.02.012. URL `http://www.sciencedirect.com/science/article/pii/S0022285216300261`. New Visions of Spectroscopic Databases, Volume I.

[61] A. C. Vandaele, M. De Mazière, R. Drummond, A. Mahieux, E. Neefs, V. Wilquet, O. Korablev, A. Fedorova, D. Belyaev, F. Montmessin, and J.-L. Bertaux. Composition of the Venus mesosphere measured by Solar Occultation at Infrared on board Venus Express. *Journal of Geophysical Research (Planets)*, 113:E00B23, December 2008. doi: 10.1029/2008JE003140.

[62] A. Seiff, J. T. Schofield, A. J. Kliore, F. W. Taylor, S. S. Limaye, H. E. Revercomb, L. A. Sromovsky, V. V. Kerzhanovich, V. I. Moroz, and M. Y. Marov. Models of the structure of the atmosphere of Venus from the surface to 100 kilometers altitude. *Advances in Space Research*, 5:3–58, 1985. doi: 10.1016/0273-1177(85)90197-8.

[63] URL `http://venus.aeronomie.be/en/soir/instrument.htm`.

[64] R. Hashemi, A. Predoi-Cross, A.S. Dudaryonok, N.N. Lavrentieva, A.C. Vandaele, and J. Vander Auwera. Co_2 pressure broadening and shift coefficients for the 20 band of co. *Journal of Molecular Spectroscopy*, 326:60 – 72, 2016. ISSN 0022-2852. doi: https://doi.org/10.1016/j.jms.2016.02.014. URL `http://www.sciencedirect.com/science/article/pii/S0022285216300285`. New Visions of Spectroscopic Databases, Volume I.

[65] R Hashemi, A S Dudaryonok, N N Lavrentieva, A C Vandaele, J Vander Auwera, AV Nikitin, VI G Tyuterev, K Sung, M A H Smith, V M Devi, and A Predoi-Cross. Fourier transform spectroscopy of two trace gases namely methane and carbon monoxide for planetary and atmospheric research application. *Journal of Physics: Conference Series*, 810(1):012008, 2017. URL `http://stacks.iop.org/1742-6596/810/i=1/a=012008`.

[66] Demtroder. W. *Laser Spectroscopy*. 3. Springer-Verlag Berlin Heidelberg, 2008. ISBN 978-3-540-73418-5.

[67] Woldemar Voigt. ber das gesetz der intensittsverteilurg innerhalb der linien eines gasspektrnms. *Sitzungsberichte der mathematisch-physikalischen Klassen der K. B. Akademie der Wissenschaften zu Mnchen*, page 603, 1912. URL `https://www.zobodat.at/pdf/Sitz-Ber-Akad-Muenchen-math-Kl_1912_0001.pdf`.

[68] Louis Galatry. Simultaneous effect of doppler and foreign gas broadening on spectral lines. *Phys. Rev.*, 122:1218–1223, May 1961. doi: 10.1103/PhysRev.122.1218. URL `https://link.aps.org/doi/10.1103/PhysRev.122.1218`.

[69] Sergei G Rautian and Igor I Sobel'man. The effect of collisions on the doppler broadening of spectral lines. *Soviet Physics Uspekhi*, 9(5):701, 1967. URL `http://stacks.iop.org/0038-5670/9/i=5/a=R04`.

[70] Mark Nelkin and Ajoy Ghatak. Simple binary collision model for van hove's $G_s(r,t)$. *Phys. Rev.*, 135:A4–A9, Jul 1964. doi: 10.1103/PhysRev.135.A4. URL `https://link.aps.org/doi/10.1103/PhysRev.135.A4`.

[71] P. Rosenkranz. Shape of the 5 mm oxygen band in the atmosphere. *IEEE Transactions on Antennas and Propagation*, 23(4):498–506, July 1975. ISSN 0018-926X. doi: 10.1109/TAP.1975.1141119.

[72] L. R. Brown, M. R. Gunson, R. A. Toth, F. W. Irion, C. P. Rinsland, and A. Goldman. 1995 atmospheric trace molecule spectroscopy (atmos) linelist. *Appl. Opt.*, 35(16): 2828–2848, Jun 1996. doi: 10.1364/AO.35.002828. URL `http://ao.osa.org/abstract.cfm?URI=ao-35-16-2828`.

[73] R.V. Kochanov, I.E. Gordon, L.S. Rothman, P. Wciso, C. Hill, and J.S. Wilzewski. Hitran application programming interface (hapi): A comprehensive approach to working with spectroscopic data. *Journal of Quantitative Spectroscopy and Radiative Transfer*, 177:15 – 30, 2016. ISSN 0022-4073. doi: https://doi.org/10.1016/j.jqsrt.2016.03.005. URL `http://www.sciencedirect.com/science/article/pii/S0022407315302466`. XVIIIth Symposium on High Resolution Molecular Spectroscopy (HighRus-2015), Tomsk, Russia.

[74] Christian Hill, Iouli E. Gordon, Laurence S. Rothman, and Jonathan Tennyson. A new relational database structure and online interface for the hitran database. *Journal of Quantitative Spectroscopy and Radiative Transfer*, 130:51 – 61, 2013. ISSN 0022-4073. doi: https://doi.org/10.1016/j.jqsrt.2013.04.027. URL `http:`

//www.sciencedirect.com/science/article/pii/S0022407313001751. HITRAN2012 special issue.

[75] *FRONT MATTER*, pages i–xvi. doi: 10.1142/9789812813718_fmatter. URL https://www.worldscientific.com/doi/abs/10.1142/9789812813718_fmatter.

[76] Christian von Savigny. Introduction to measurement techniques in environmental physics. *Lecture*, 2006.

[77] Massimo Carlotti. Global-fit approach to the analysis of limb-scanning atmospheric measurements. *Appl. Opt.*, 27(15):3250–3254, Aug 1988. doi: 10.1364/AO.27.003250. URL http://ao.osa.org/abstract.cfm?URI=ao-27-15-3250.

[78] P.G.J. Irwin, N.A. Teanby, R. de Kok, L.N. Fletcher, C.J.A. Howett, C.C.C. Tsang, C.F. Wilson, S.B. Calcutt, C.A. Nixon, and P.D. Parrish. The nemesis planetary atmosphere radiative transfer and retrieval tool. *Journal of Quantitative Spectroscopy and Radiative Transfer*, 109(6):1136 – 1150, 2008. ISSN 0022-4073. doi: https://doi.org/10.1016/j.jqsrt.2007.11.006. URL http://www.sciencedirect.com/science/article/pii/S0022407307003378. Spectroscopy and Radiative Transfer in Planetary Atmospheres.

[79] Clive D Rodgers. *Inverse Methods for Atmospheric Sounding*. WORLD SCIENTIFIC, 2000. doi: 10.1142/3171. URL https://www.worldscientific.com/doi/abs/10.1142/3171.

[80] URL http://ara.abct.lmd.polytechnique.fr/index.php?page=4a.

[81] A. Berk, L.S. Bernstein, G.P. Anderson, P.K. Acharya, D.C. Robertson, J.H. Chetwynd, and S.M. Adler-Golden. Modtran cloud and multiple scattering upgrades with application to aviris. *Remote Sensing of Environment*, 65(3):367 – 375, 1998. ISSN 0034-4257. doi: https://doi.org/10.1016/S0034-4257(98)00045-5. URL http://www.sciencedirect.com/science/article/pii/S0034425798000455.

[82] Gail P. Anderson James H. Chetwynd S. Miller Junfeng Wang Hilary E. Snell, Jean-Luc Moncet. Fascode for the environment (fase), 1995. URL https://doi.org/10.1117/12.211917.

[83] Christian Frankenberg, Peter Bergamaschi, Andre Butz, Sander Houweling, Jan Fokke Meirink, Justus Notholt, Anna Katinka Petersen, Hans Schrijver, Thorsten Warneke, and Ilse Aben. Tropical methane emissions: A revised view from sciamachy onboard envisat. *Geophysical Research Letters*, 35(15), 8 2008. ISSN 0094-8276. doi: 10.1029/2008GL034300.

[84] M. J. Alvarado, V. H. Payne, K. E. Cady-Pereira, J. D. Hegarty, S. S. Kulawik, K. J. Wecht, J. R. Worden, J. V. Pittman, and S. C. Wofsy. Impacts of updated spectroscopy on thermal infrared retrievals of methane evaluated with hippo data. *Atmospheric Measurement Techniques*, 8(2):965–985, 2015. doi: 10.5194/amt-8-965-2015. URL https://www.atmos-meas-tech.net/8/965/2015/.

[85] Raymond Armante, Noelle Scott, Cyril Crevoisier, Virginie Capelle, Laurent Crepeau, Nicole Jacquinet, and Alain Chdin. Evaluation of spectroscopic databases through radiative transfer simulations compared to observations. application to the validation of geisa 2015 with iasi and tccon. *Journal of Molecular Spectroscopy*, 327:180 – 192, 2016. ISSN 0022-2852. doi: https://doi.org/10.1016/j.jms.2016.04.004. URL `http://www.sciencedirect.com/science/article/pii/S002228521630056X`. New Visions of Spectroscopic Databases, Volume II.

[86] N. Jacquinet-Husson, R. Armante, N.A. Scott, A. Chdin, L. Crpeau, C. Boutammine, A. Bouhdaoui, C. Crevoisier, V. Capelle, C. Boonne, N. Poulet-Crovisier, A. Barbe, D. Chris Benner, V. Boudon, L.R. Brown, J. Buldyreva, A. Campargue, L.H. Coudert, V.M. Devi, M.J. Down, B.J. Drouin, A. Fayt, C. Fittschen, J.-M. Flaud, R.R. Gamache, J.J. Harrison, C. Hill, . Hodnebrog, S.-M. Hu, D. Jacquemart, A. Jolly, E. Jimnez, N.N. Lavrentieva, A.-W. Liu, L. Lodi, O.M. Lyulin, S.T. Massie, S. Mikhailenko, H.S.P. Mller, O.V. Naumenko, A. Nikitin, C.J. Nielsen, J. Orphal, V.I. Perevalov, A. Perrin, E. Polovtseva, A. Predoi-Cross, M. Rotger, A.A. Ruth, S.S. Yu, K. Sung, S.A. Tashkun, J. Tennyson, Vl.G. Tyuterev, J. Vander Auwera, B.A. Voronin, and A. Makie. The 2015 edition of the geisa spectroscopic database. *Journal of Molecular Spectroscopy*, 327:31 – 72, 2016. ISSN 0022-2852. doi: https://doi.org/10.1016/j.jms.2016.06.007. URL `http://www.sciencedirect.com/science/article/pii/S0022285216301011`. New Visions of Spectroscopic Databases, Volume II.

[87] W. Demtröder. *Atoms, Molecules and Photons: An Introduction to Atomic-, Molecular- and Quantum-physics ; with 43 Tables*. Advanced texts in physics. Springer, 2006. ISBN 9783540206316. URL `https://books.google.ca/books?id=Eehsvr8jVpAC`.

[88] J. Ward, J. Cooper, and Earl W. Smith. Correlation effects in the theory of combined doppler and pressure broadeningi. classical theory. *Journal of Quantitative Spectroscopy and Radiative Transfer*, 14(7):555 – 590, 1974. ISSN 0022-4073. doi: https://doi.org/10.1016/0022-4073(74)90036-3. URL `http://www.sciencedirect.com/science/article/pii/0022407374900363`.

[89] R. Hashemi, C. Povey, M. Derksen, H. Naseri, J. Garber, and A. Predoi-Cross. Doppler broadening thermometry of acetylene and accurate measurement of the boltzmann constant. *The Journal of Chemical Physics*, 141(21):214201, 2014. doi: 10.1063/1.4902076. URL `https://doi.org/10.1063/1.4902076`.

[90] Peter J. Mohr, Barry N. Taylor, and David B. Newell. Codata recommended values of the fundamental physical constants: 2010. *Journal of Physical and Chemical Reference Data*, 41(4):043109, 2012. doi: 10.1063/1.4724320. URL `https://doi.org/10.1063/1.4724320`.

[91] Christophe Daussy, Mickael Guinet, Anne Amy-Klein, Khelifa Djerroud, Yves Hermier, Stephan Briaudeau, Ch J Bordé, and Christian Chardonnet. Direct determina-

tion of the boltzmann constant by an optical method. *Physical review letters*, 98(25): 250801, 2007.

[92] G Casa, A Castrillo, G Galzerano, R Wehr, A Merlone, D Di Serafino, P Laporta, and L Gianfrani. Primary gas thermometry by means of laser-absorption spectroscopy: determination of the boltzmann constant. *Physical review letters*, 100(20):200801, 2008.

[93] Koichi M.T. Yamada, Atsushi Onae, Feng-Lei Hong, Hajime Inaba, and Tadao Shimizu. Precise determination of the doppler width of a rovibrational absorption line using a comb-locked diode laser. *Comptes Rendus Physique*, 10 (9):907 – 915, 2009. ISSN 1631-0705. doi: https://doi.org/10.1016/j.crhy.2009.10.011. URL `http://www.sciencedirect.com/science/article/pii/S1631070509001571`. Experimental determination of Boltzmann's constant.

[94] Khelifa Djerroud, Cyril Lemarchand, Alexandre Gauguet, Christophe Daussy, Stephan Briaudeau, Benot Darqui, Olivier Lopez, Anne Amy-Klein, Christian Chardonnet, and Christian J. Bord. Measurement of the boltzmann constant by the doppler broadening technique at a 3.8105 accuracy level. *Comptes Rendus Physique*, 10(9):883 – 893, 2009. ISSN 1631-0705. doi: https://doi.org/10.1016/j.crhy.2009.10.020. URL `http://www.sciencedirect.com/science/article/pii/S1631070509001820`. Experimental determination of Boltzmann's constant.

[95] L. Moretti, A. Castrillo, E. Fasci, M. D. De Vizia, G. Casa, G. Galzerano, A. Merlone, P. Laporta, and L Gianfrani. Determination of the boltzmann constant by means of precision measurements of (h_2o)-o-18 line shapes at 1.39 μ m. *Physical Review Letters*, 111(6):907–915, 2013.

[96] Cyril Lemarchand, Meriam Triki, Benoît Darquié, Ch J Bordé, Christian Chardonnet, and Christophe Daussy. Progress towards an accurate determination of the boltzmann constant by doppler spectroscopy. *New Journal of Physics*, 13(7):073028, 2011.

[97] C. Lemarchand, S. Mejri, P. L. T. Sow, M. Triki, S. K. Tokunaga, S. Briaudeau, C. Chardonnet, B. Darquie, and C. Daussy. A revised uncertainty budget for measuring the boltzmann constant using the doppler broadening technique on ammonia. *Metrologia*, 50(6):623, 2013.

[98] Gar-Wing Truong, Eric F May, Thomas M Stace, and André N Luiten. Quantitative atomic spectroscopy for primary thermometry. *Physical Review A*, 83(3):033805, 2011.

[99] A. Castrillo, L. Moretti, E. Fasci, M.D. De Vizia, G. Casa, and L. Gianfrani. The boltzmann constant from the shape of a molecular spectral line. *Journal of Molecular Spectroscopy*, 300:131 – 138, 2014. ISSN 0022-2852. doi: https://doi.org/10.1016/j.jms.2014.04.001. URL `http://www.sciencedirect.com/science/article/pii/S0022285214000861`. Spectroscopic Tests of Fundamental Physics.

[100] AS Pine. Asymmetries and correlations in speed-dependent dicke-narrowed line shapes of argon-broadened HF. *Journal of Quantitative Spectroscopy and Radiative Transfer*, 62(4):397–423, 1999.

[101] H. Tran, N.H. Ngo, and J.-M. Hartmann. Efficient computation of some speed-dependent isolated line profiles. *Journal of Quantitative Spectroscopy and Radiative Transfer*, 129(0):199 – 203, 2013. ISSN 0022-4073. doi: http://dx.doi.org/10.1016/j.jqsrt.2013.06.015.

[102] Chad Povey. *High Resolution Spectroscopy and Applications*. PhD thesis, University of Lethbridge, 2013.

[103] Alan A Madej, A John Alcock, Andrzej Czajkowski, John E Bernard, and Sergei Chepurov. Accurate absolute reference frequencies from 1511 to 1545 nm of the $\nu 1+\nu 3$ band of ¹² C2H2 determined with laser frequency comb interval measurements. *JOSA B*, 23(10):2200–2208, 2006.

[104] Robab Hashemi, Hoimonti Rozario, Chad Povey, and Adriana Predoi-Cross. Line-shape models testing on six acetylene transitions in the $\nu_1+\nu_3$ band broadened by n_2. *Journal of Quantitative Spectroscopy and Radiative Transfer*, 140:58 – 66, 2014. ISSN 0022-4073. doi: https://doi.org/10.1016/j.jqsrt.2014.02.013. URL `http://www.sciencedirect.com/science/article/pii/S0022407314000703`.

[105] A. C. Vandaele, E. Neefs, R. Drummond, I. R. Thomas, F. Daerden, J.-J. Lopez-Moreno, J. Rodriguez, M. R. Patel, G. Bellucci, M. Allen, F. Altieri, D. Bolsée, T. Clancy, S. Delanoye, C. Depiesse, E. Cloutis, A. Fedorova, V. Formisano, B. Funke, D. Fussen, A. Geminale, J.-C. Gérard, M. Giuranna, N. Ignatiev, J. Kaminski, O. Karatekin, F. Lefèvre, M. López-Puertas, M. López-Valverde, A. Mahieux, J. McConnell, M. Mumma, L. Neary, E. Renotte, B. Ristic, S. Robert, M. Smith, S. Trokhimovsky, J. Vander Auwera, G. Villanueva, J. Whiteway, V. Wilquet, and M. Wolff. Science objectives and performances of NOMAD, a spectrometer suite for the ExoMars TGO mission. *planss*, 119:233–249, December 2015. doi: 10.1016/j.pss.2015.10.003.

[106] Vladimir A. Krasnopolsky. Observations of the co dayglow at 4.7μm on mars: Variations of temperature and co mixing ratio at 50km. *Icarus*, 228(Complete):189–196, 2014. doi: 10.1016/j.icarus.2013.10.008.

[107] Geronimo L. Villanueva, Michael J. Mumma, Robert E. Novak, and Tilak Hewagama. Identification of a new band system of isotopic co_2 near 3.3 μm: Implications for remote sensing of biomarker gases on mars. *Icarus*, 195(1):34 – 44, 2008. ISSN 0019-1035. doi: https://doi.org/10.1016/j.icarus.2007.11.014. URL `http://www.sciencedirect.com/science/article/pii/S0019103507005842`.

[108] A. Seiff, J. T. Schofield, A. J. Kliore, F. W. Taylor, S. S. Limaye, H. E. Revercomb, L. A. Sromovsky, V. V. Kerzhanovich, V. I. Moroz, and M. Y. Marov. Models of the structure of the atmosphere of Venus from the surface to 100 kilometers altitude. *Advances in Space Research*, 5:3–58, 1985. doi: 10.1016/0273-1177(85)90197-8.

[109] P. Varanasi. Line-width measurements on co in an atmosphere of co_2. *Journal of Quantitative Spectroscopy and Radiative Transfer*, 11(3):249 – 253, 1971. ISSN 0022-4073. doi: https://doi.org/10.1016/0022-4073(71)90011-2. URL `http://www.sciencedirect.com/science/article/pii/0022407371900112`.

[110] Jean-Pierre Bouanich. Determination experimentale des largeurs et des deplacements des raies de la bande 0-2 de co pertube par les gaz rares (he, ne, ar, kr, xe). *Journal of Quantitative Spectroscopy and Radiative Transfer*, 12(12):1609 – 1615, 1972. ISSN 0022-4073. doi: https://doi.org/10.1016/0022-4073(72)90102-1. URL `http://www.sciencedirect.com/science/article/pii/0022407372901021`.

[111] J.P. Bouanich and C. Brodbeck. Vibration-rotation matrix elements for diatomic molecules; vibration-rotation interaction functions fvv (m) for co. *Journal of Quantitative Spectroscopy and Radiative Transfer*, 16(2):153 – 163, 1976. ISSN 0022-4073. doi: https://doi.org/10.1016/0022-4073(76)90097-2. URL `http://www.sciencedirect.com/science/article/pii/0022407376900972`.

[112] P. Varanasi and S. Sarangi. Measurements of intensities and nitrogen-broadened linewidths in the co fundamental at low temperatures. *J. Quant. Spectrosc. Radiat. Transf.*, 15:473–482, 1975.

[113] J.-P. Bouanich, R. Farrenq, and C. Brodbeck. Direct measurements of n2 broadened linewidths in the co fundamental at low temperatures. *Canadian Journal of Physics*, 61(2):192–197, 1983. doi: 10.1139/p83-026. URL `https://doi.org/10.1139/p83-026`.

[114] J.-P. Bouanich. On the temperature dependence of self-broadening in the first overtone band of co. *Journal of Quantitative Spectroscopy and Radiative Transfer*, 31(6):561 – 567, 1984. ISSN 0022-4073. doi: https://doi.org/10.1016/0022-4073(84)90061-X. URL `http://www.sciencedirect.com/science/article/pii/002240738490061X`.

[115] J.-P. Bouanich, D. Bermejo, J.L. Domenech, R.Z. Martinez, and J. Santos. Pressure-induced lineshifts in the 2-0 band of co self-perturbed and perturbed by he, kr, o_2, and n_2. *Journal of Molecular Spectroscopy*, 179(1):22 – 31, 1996. ISSN 0022-2852. doi: https://doi.org/10.1006/jmsp.1996.0180. URL `http://www.sciencedirect.com/science/article/pii/S0022285296901800`.

[116] Qunjun Zou and Prasad Varanasi. New laboratory data on the spectral line parameters in the 1-0 and 2-0 bands of co relevant to atmospheric remote sensing. *Journal of Quantitative Spectroscopy and Radiative Transfer*, 75(1):63 – 92, 2002. ISSN 0022-4073. doi: https://doi.org/10.1016/S0022-4073(02)00007-9. URL `http://www.sciencedirect.com/science/article/pii/S0022407302000079`.

[117] Jean-Marcel Colmont, Linh Nguyen, Franois Rohart, and Georges Wlodarczak. Lineshape analysis of the $j = 3 - 2$ and $j = 5 - 4$ rotational transitions of room temperature co broadened by n_2, o_2, co_2 and noble gases. *Journal of Molecular*

Spectroscopy, 246(1):86 – 97, 2007. ISSN 0022-2852. doi: https://doi.org/10.1016/j.jms.2007.08.003. URL `http://www.sciencedirect.com/science/article/pii/S0022285207002172`.

[118] V. Malathy Devi, D. Chris Benner, M.A.H. Smith, A.W. Mantz, K. Sung, L.R. Brown, and A. Predoi-Cross. Erratum to spectral line parameters including temperature dependences of self- and air-broadening in the 2-0 band of co at 2.3μm [j quant spectrosc radiat transfer 2012;113:101333]. *Journal of Quantitative Spectroscopy and Radiative Transfer*, 116:199 – 200, 2013. ISSN 0022-4073. doi: https://doi.org/10.1016/j.jqsrt.2012.11.020. URL `http://www.sciencedirect.com/science/article/pii/S0022407312005262`.

[119] Franois Rohart, Heinrich Mder, and HansWerner Nicolaisen. Speed dependence of rotational relaxation induced by foreign gas collisions: Studies on ch$_3$f by millimeter wave coherent transients. *The Journal of Chemical Physics*, 101(8):6475–6486, 1994. doi: 10.1063/1.468342. URL `https://doi.org/10.1063/1.468342`.

[120] H. Tran, C. Boulet, S. Stefani, M. Snels, and G. Piccioni. Measurements and modelling of high pressure pure co2 spectra from 750 to 8500cm^1. icentral and wing regions of the allowed vibrational bands. *Journal of Quantitative Spectroscopy and Radiative Transfer*, 112(6):925 – 936, 2011. ISSN 0022-4073. doi: https://doi.org/10.1016/j.jqsrt.2010.11.021. URL `http://www.sciencedirect.com/science/article/pii/S0022407310004449`.

[121] ROBERT JOHN BELL. Chapter one - fourier transform spectroscopy. In ROBERT JOHN BELL, editor, *Introductory Fourier Transform Spectroscopy*, pages 1 – 15. Academic Press, 1972. ISBN 978-0-12-085150-8. doi: https://doi.org/10.1016/B978-0-12-085150-8.50006-1. URL `http://www.sciencedirect.com/science/article/pii/B9780120851508500061`.

[122] R. J. Bell. *Fourier Transform Spectrometry*. Academic Press, 2001.

[123] P.R. Griffiths, J.A. De Haseth, and J.D. Winefordner. *Fourier Transform Infrared Spectrometry*. Chemical Analysis: A Series of Monographs on Analytical Chemistry and Its Applications. Wiley, 2007. ISBN 9780470106297. URL `https://books.google.ca/books?id=C_c0GVe8MX0C`.

[124] J. Connes. *Rev. Opt. Thor. Instrum.*, 40:45–79, 1961.

[125] M. Tudorie, T. Fldes, A.C. Vandaele, and J. Vander Auwera. Co$_2$ pressure broadening and shift coefficients for the 1-0 band of hcl and dcl. *Journal of Quantitative Spectroscopy and Radiative Transfer*, 113(11):1092 – 1101, 2012. ISSN 0022-4073. doi: https://doi.org/10.1016/j.jqsrt.2012.01.025. URL `http://www.sciencedirect.com/science/article/pii/S0022407312000519`. Three Leaders in Spectroscopy.

[126] L. Daneshvar, T. Fldes, J. Buldyreva, and J. Vander Auwera. Infrared absorption by pure co$_2$ near 3340cm^1: Measurements and analysis of collisional coefficients

and line-mixing effects at subatmospheric pressures. *Journal of Quantitative Spectroscopy and Radiative Transfer*, 149:258 – 274, 2014. ISSN 0022-4073. doi: https://doi.org/10.1016/j.jqsrt.2014.08.007. URL `http://www.sciencedirect.com/science/article/pii/S0022407314003513`.

[127] Ulf Litzn. Book review: Fourier transform spectrometry. by sumner p. davis, mark c. abrams, and james w. brault. *ChemPhysChem*, 3(8):719–720. doi: 10.1002/1439-7641(20020816)3:8⟨719::AID-CPHC719⟩3.0.CO;2-S. URL `https://onlinelibrary.wiley.com/doi/abs/10.1002/1439-7641%2820020816%293%3A8%3C719%3A%3AAID-CPHC719%3E3.0.CO%3B2-S`.

[128] L.S. Rothman, I.E. Gordon, Y. Babikov, A. Barbe, D. Chris Benner, P.F. Bernath, M. Birk, L. Bizzocchi, V. Boudon, L.R. Brown, A. Campargue, K. Chance, E.A. Cohen, L.H. Coudert, V.M. Devi, B.J. Drouin, A. Fayt, J.-M. Flaud, R.R. Gamache, J.J. Harrison, J.-M. Hartmann, C. Hill, J.T. Hodges, D. Jacquemart, A. Jolly, J. Lamouroux, R.J. Le Roy, G. Li, D.A. Long, O.M. Lyulin, C.J. Mackie, S.T. Massie, S. Mikhailenko, H.S.P. Mller, O.V. Naumenko, A.V. Nikitin, J. Orphal, V. Perevalov, A. Perrin, E.R. Polovtseva, C. Richard, M.A.H. Smith, E. Starikova, K. Sung, S. Tashkun, J. Tennyson, G.C. Toon, Vl.G. Tyuterev, and G. Wagner. The hitran2012 molecular spectroscopic database. *Journal of Quantitative Spectroscopy and Radiative Transfer*, 130:4 – 50, 2013. ISSN 0022-4073. doi: https://doi.org/10.1016/j.jqsrt.2013.07.002. URL `http://www.sciencedirect.com/science/article/pii/S0022407313002859`. HITRAN2012 special issue.

[129] Herv Herbin, Robert Farrenq, Guy Guelachvili, Bernard Pinchemel, and Nathalie Picqu. Perturbation analysis in the $c4\delta x4\phi$ rovibronic transitions of ticl at 3μm. *Journal of Molecular Spectroscopy*, 226(1):103 – 111, 2004. ISSN 0022-2852. doi: https://doi.org/10.1016/j.jms.2004.03.015. URL `http://www.sciencedirect.com/science/article/pii/S0022285204001158`.

[130] Bruce Gentry and L. Larrabee Strow. Line mixing in a n2broadened co$_2$ q branch observed with a tunable diode laser. *The Journal of Chemical Physics*, 86(10):5722–5730, 1987. doi: 10.1063/1.452770. URL `https://doi.org/10.1063/1.452770`.

[131] J. Fischer, R.R. Gamache, A. Goldman, L.S. Rothman, and A. Perrin. Total internal partition sums for molecular species in the 2000 edition of the hitran database. *Journal of Quantitative Spectroscopy and Radiative Transfer*, 82(1):401 – 412, 2003. ISSN 0022-4073. doi: https://doi.org/10.1016/S0022-4073(03)00166-3. URL `http://www.sciencedirect.com/science/article/pii/S0022407303001663`. The HITRAN Molecular Spectroscopic Database: Edition of 2000 Including Updates of 2001.

[132] A. Henry, D. Hurtmans, M. Margottin-Maclou, and A. Valentin. Confinement narrowing and absorber speed dependent broadening effects on co lines in the fundamental band perturbed by xe, ar, ne, he and n$_2$. *Journal of Quantitative Spectroscopy and Radiative Transfer*, 56(5):647 – 671, 1996. ISSN 0022-4073. doi: https:

//doi.org/10.1016/S0022-4073(96)00118-5. URL `http://www.sciencedirect.com/science/article/pii/S0022407396001185`.

[133] F. Thibault, A.W. Mantz, C. Claveau, A. Henry, A. Valentin, and D. Hurtmans. Broadening of the r(0) and p(2) lines in the co fundamental by helium atoms from 300k down to 12k: Measurements and comparison with close-coupling calculations. *Journal of Molecular Spectroscopy*, 246(1):118 – 125, 2007. ISSN 0022-2852. doi: https://doi.org/10.1016/j.jms.2007.09.001. URL `http://www.sciencedirect.com/science/article/pii/S0022285207002226`.

[134] J.O. Hirschfelder, C.F. Curtiss, R.B. Bird, and University of Wisconsin. Theoretical Chemistry Laboratory. *Molecular theory of gases and liquids*. Structure of matter series. Wiley, 1954. ISBN 9780471400653. URL `https://books.google.ca/books?id=HQtRAAAAMAAJ`.

[135] A. Cygan, D. Lisak, P. Masowski, K. Bielska, S. Wjtewicz, J. Domysawska, H. Abe, J. T. Hodges, R. S. Trawiski, and R. Ciuryo. Frequencystabilized cavity ringdown spectroscopy with a pdh locked laser. *AIP Conference Proceedings*, 1290(1):204–208, 2010. doi: 10.1063/1.3517556. URL `https://aip.scitation.org/doi/abs/10.1063/1.3517556`.

[136] A. D. Bykov, N. N. Lavrentieva, and L. N. Sinitsa. Semi-empiric approach to the calculation of H_2O and CO_2 line broadening and shifting. *Molecular Physics*, 102: 1653–1658, 2004. doi: 10.1080/00268970410001725765.

[137] P. W. Anderson. Pressure broadening in the microwave and infra-red regions. *Phys. Rev.*, 76:647–661, Sep 1949. doi: 10.1103/PhysRev.76.647. URL `https://link.aps.org/doi/10.1103/PhysRev.76.647`.

[138] C.J. Tsao and B. Curnutte. Line-widths of pressure-broadened spectral lines. *Journal of Quantitative Spectroscopy and Radiative Transfer*, 2(1):41 – 91, 1962. ISSN 0022-4073. doi: https://doi.org/10.1016/0022-4073(62)90013-4. URL `http://www.sciencedirect.com/science/article/pii/0022407362900134`.

[139] Jeanna Buldyreva, Nina Lavrentieva, and Vitaly Starikov. *Collisional Line Broadening and Shifting of Atmospheric Gases*. IMPERIAL COLLEGE PRESS, 2010. doi: 10.1142/p731. URL `https://www.worldscientific.com/doi/abs/10.1142/p731`.

[140] A.W. Mantz, J.-P. Maillard, Won B. Roh, and K. Narahari Rao. Ground state molecular constants of co. *Journal of Molecular Spectroscopy*, 57(1):155 – 159, 1975. ISSN 0022-2852. doi: https://doi.org/10.1016/0022-2852(75)90049-1. URL `http://www.sciencedirect.com/science/article/pii/0022285275900491`.

[141] Robert R. Gamache, Anne L. Laraia, and Julien Lamouroux. Half-widths, their temperature dependence, and line shifts for the hdoco$_2$ collision system for applications to co$_2$-rich planetary atmospheres. *Icarus*, 213(2):720 – 730, 2011.

ISSN 0019-1035. doi: https://doi.org/10.1016/j.icarus.2011.03.021. URL http://www.sciencedirect.com/science/article/pii/S0019103511001126.

[142] R. Hashemi, A. Predoi-Cross, A.V. Nikitin, Vl.G. Tyuterev, K. Sung, M.A.H. Smith, and V. Malathy Devi. Spectroscopic line parameters of ch$_4$ for atmospheric composition retrievals in the 43004500 cm^1 region. *Journal of Quantitative Spectroscopy and Radiative Transfer*, 186:106 – 117, 2017. ISSN 0022-4073. doi: https://doi.org/10.1016/j.jqsrt.2016.03.024. URL http://www.sciencedirect.com/science/article/pii/S0022407315303319. Satellite Remote Sensing and Spectroscopy: Joint ACE-Odin Meeting, October 2015.

[143] D. H. Ehhalt and U. Schmidt. Sources and sinks of atmospheric methane. *pure and applied geophysics*, 116(2):452–464, Mar 1978. ISSN 1420-9136. doi: 10.1007/BF01636899. URL https://doi.org/10.1007/BF01636899.

[144] J. Bogner, K. Spokas, E. Burton, R. Sweeney, and V. Corona. Landfills as atmospheric methane sources and sinks. *Chemosphere*, 31(9):4119 – 4130, 1995. ISSN 0045-6535. doi: https://doi.org/10.1016/0045-6535(95)80012-A. URL http://www.sciencedirect.com/science/article/pii/004565359580012A.

[145] J. Mendonca, K. Strong, G.C. Toon, D. Wunch, K. Sung, N.M. Deutscher, D.W.T. Griffith, and J.E. Franklin. Improving atmospheric co2 retrievals using line mixing and speed-dependence when fitting high-resolution ground-based solar spectra. *Journal of Molecular Spectroscopy*, 323:15 – 27, 2016. ISSN 0022-2852. doi: https://doi.org/10.1016/j.jms.2016.01.007. URL http://www.sciencedirect.com/science/article/pii/S002228521630008X. Atmospheric Spectroscopy.

[146] V Malathy Devi, B Fridovich, G.D Jones, and D.G.S Snyder. Strengths and lorentz broadening coefficients for spectral lines in the ν_3 and $\nu_2 + \nu_4$ bands of ch$_4$ and ch$_4$. *Journal of Molecular Spectroscopy*, 97(2):333 – 342, 1983. ISSN 0022-2852. doi: https://doi.org/10.1016/0022-2852(83)90271-0. URL http://www.sciencedirect.com/science/article/pii/0022285283902710.

[147] V.Malathy Devi, B. Fridovich, D.G.S. Snyder, G.D. Jones, and Palash P. Das. Tunable diode laser measurements of intensities and lorentz broadening coefficients of lines in the ν_2 band of ch$_4$. *Journal of Quantitative Spectroscopy and Radiative Transfer*, 29(1):45 – 47, 1983. ISSN 0022-4073. doi: https://doi.org/10.1016/0022-4073(83)90144-9. URL http://www.sciencedirect.com/science/article/pii/0022407383901449.

[148] V Malathy Devi, Curtis P. Rinsland, Michael J. Smith, and Drayton C. Benner. Measurements of ch$_4$ ν_4 band halfwidths using a tunable diode laser system and a fourier transform spectrometer. *Applied optics*, 24 17:2788–91, 1985.

[149] Devi VM, Rinsland CP, Smith MAH, and Benner DC. Tunable diode-laser measurements of widths of air-broadened and nitrogen-broadened lines in the ν_4 band of ^{12}ch$_4$. *Appl. Opt.*, 24:3321–3322, 1985.

[150] Devi VM, Rinsland CP, Benner DC, Smith MAH, and Thakur KB. Absolute intensities and self-broadened, n_2-broadened, and air-broadened lorentz half-widths for selected lines in the ν_3 band of $^{12}ch_3d$ from measurements with a tunable diode-laser spectrometer. *Appl. Opt.*, 25:1848–1853, 1986.

[151] Devi VM, Benner DC, Rinsland CP, Smith MAH, and Thakur KB. Diode-laser measurements of intensities and half-widths in the upsilon-6-band of $^{12}ch_3d$. *J. Mol. Spectrosc.*, 122:182–189, 1987.

[152] Devi VM, Rinsland CP, Smith MAH, and Benner DC. Air-broadened lorentz halfwidths and pressure-induced line shifts in the ν_4 band of $^{13}ch_4$. *Appl. Opt.*, 27: 2296–2308, 1988.

[153] Rinsland CP, Devi VM, Smith MAH, and Benner DC. Measurements of air-broadened and nitrogen-broadened lorentz width coefficients and pressure shift coefficients in the ν_4 and ν_2 bands of $^{12}ch_4$. *Appl. Opt.*, 27:631–651, 1988.

[154] Devi VM, Benner DC, Smith MAH, and Rinsland CP. Measurements of air-broadened, n_2-broadened, and o_2-broadened half-widths and pressure-induced line shifts in the ν_3 band of $^{13}ch_4$. *Appl. Opt.*, 30:287–304, 1991.

[155] Devi VM, Benner DC, Smith MAH, and Rinsland CP. Correction. *Appl. Opt.*, 30: 2928–2928, 1991.

[156] Smith MAH, Rinsland CP, Devi VM, and Benner DC. Temperature-dependence of broadening and shifts of methane lines in the ν_4 band. *Spectrochimica Acta*, 48A: 1257–1272, 1992.

[157] Benner DC, Devi VM, Smith MAH, and Rinsland CP. Air-broadening, n_2-broadening, and o_2-broadening and shift coefficients in the ν_3 spectral region of $^{12}ch_4$. *J. Quant. Spectrosc. Radiat. Transfer.*, 50:65–89, 1993.

[158] Benner DC, Devi VM, Smith MAH, and Rinsland CP. Devi vm, benner dc, smith mah, rinsland cp. measurements of air-broadening and pressure-shifting of methane lines in the 2.3 μm region. *J. Mol. Spectrosc.*, 157:95–111, 1993.

[159] Devi VM, Benner DC, Smith MAH, and Rinsland CP. Temperature-dependence of lorentz air-broadening and pressure-shift coefficients of $^{12}ch_4$ lines in the 2.3 μm spectral region. *J. Quant. Spectrosc. Radiat. Transfer*, 51:439–465, 1994.

[160] Devi VM, Benner DC, Smith MAH, Rinsland CP, and Brown LR. Measurements of air broadening, pressure shifting and off diagonal relaxation matrix coefficients in the ν_3 band of $^{12}ch_3d$. *J. Mol. Struct*, 517:455–475, 2000.

[161] Devi VM, Benner DC, Smith MAH, and Rinsland CP. Measurements of air-broadened width and air-induced shift coefficients and line mixing in the ν_6 band of $^{12}ch_3d$. *J. Quant. Spectrosc. Radiat. Transfer*, 68:1–41, 2001.

[162] Devi VM, Benner DC, Smith MAH, and Rinsland CP. Measurements of air broadened width and air induced shift coefficients and line mixing in the ν_5 band of ^{12}ch$_3$d. *J. Quant. Spectrosc. Radiat. Transfer*, 68:135–161, 2001.

[163] Devi VM, Benner DC, Smith MAH, Rinsland CP, and Brown LR. Multispectrum analysis of self- and nitrogen-broadening, pressure shifting and line mixing in the ν_3 parallel band of ^{12}ch$_3$d. *J. Quant. Spectrosc. Radiat. Transfer*, 73:603–640, 2002.

[164] Devi VM, Benner DC, Smith MAH, Rinsland CP, and Brown LR. Self- and n$_2$-broadening, pressure induced shift and line mixing in the ν_5 band of ^{12}ch$_3$d using a multispectrum fitting technique. *J. Quant. Spectrosc. Radiat. Transfer*, 74:1–41, 2002.

[165] A. Predoi-Cross, K. Hambrook, M. Brawley-Tremblay, J.-P. Bouanich, V. Malathy Devi, D. C. Benner, and L. R. Brown. Measurements and theoretical calculations of self-broadening and self-shift coefficients in the ν_2 band of CH $_3$D. *Journal of Molecular Spectroscopy*, 234:53–74, November 2005. doi: 10.1016/j.jms.2005.08.005.

[166] A. Predoi-Cross, L. R. Brown, V. M. Devi, M. Brawley-Tremblay, and D. C. Benner. Multispectrum analysis of ^{12}CH $_4$ from 4100 to 4635 cm $^{-1}$: 1. Self-broadening coefficients (widths and shifts). *Journal of Molecular Spectroscopy*, 232:231–246, August 2005. doi: 10.1016/j.jms.2005.04.007.

[167] Adriana Predoi-Cross, Kyle Hambrook, Shannon Brawley-Tremblay, Jean-Pierre Bouanich, V. Malathy Devi, and Mary Ann H. Smith. Room-temperature broadening and pressure-shift coefficients in the ν_2 band of ch$_3$do$_2$: Measurements and semi-classical calculations. *Journal of Molecular Spectroscopy*, 236(1):75 – 90, 2006. ISSN 0022-2852. doi: https://doi.org/10.1016/j.jms.2005.12.012. URL `http://www.sciencedirect.com/science/article/pii/S0022285205003097`.

[168] Adriana Predoi-Cross, Marco Brawley-Tremblay, Linda R. Brown, V. Malathy Devi, and D. Chris Benner. Multispectrum analysis of 12ch$_4$ from 4100 to 4635cm^1: Ii. air-broadening coefficients (widths and shifts). *Journal of Molecular Spectroscopy*, 236(2):201 – 215, 2006. ISSN 0022-2852. doi: https://doi.org/10.1016/j.jms.2006.01.013. URL `http://www.sciencedirect.com/science/article/pii/S0022285206000178`.

[169] Adriana Predoi-Cross, Anildev V. Unni, Henry Heung, V. Malathy Devi, D. Chris Benner, and Linda R. Brown. Line mixing effects in the $\nu_2 + \nu_3$ band of methane. *Journal of Molecular Spectroscopy*, 246(1):65 – 76, 2007. ISSN 0022-2852. doi: https://doi.org/10.1016/j.jms.2007.08.005. URL `http://www.sciencedirect.com/science/article/pii/S0022285207002159`.

[170] Smith MAH, Benner DC, Predoi-Cross A, and Devi VM. Multispectrum analysis of ^{12}ch$_4$ in the ν_4 band: I. air-broadened half widths, pressure-induced shifts, temperature dependences and line mixing. *J. Quant. Spectrosc. Radiat. Transfer*, 110: 639–653, 2009.

[171] Smith MAH, Benner DC, Predoi-Cross A, and Devi VM. Multispectrum analysis of ^{12}ch$_4$ in the ν_4 spectral region: Ii. self-broadened half widths, pressure-induced shifts, temperature dependences and line mixing. *J. Quant. Spectrosc. Radiat. Transfer*, 111:1152–1166, 2010.

[172] Sung K, Mantz AW, Smith MAH, Brown LR, Crawford TJ, Devi VM, and Benner DC. Cryogenic absorption cells operating inside a bruker ifs-125hr: First results for ^{13}ch$_4$ at 7 micron. *J. Mol. Spectrosc.*, 262:122–134, 2010.

[173] V. Malathy Devi, D. Chris Benner, Keeyoon Sung, Timothy J. Crawford, Shanshan Yu, Linda R. Brown, Mary Ann H. Smith, Arlan W. Mantz, Vincent Boudon, and Syed Ismail. Self- and air-broadened line shapes in the 2ν_3 p and r branches of ^{12}ch$_4$. *Journal of Molecular Spectroscopy*, 315:114 – 136, 2015. ISSN 0022-2852. doi: https://doi.org/10.1016/j.jms.2015.05.003. URL `http://www.sciencedirect.com/science/article/pii/S0022285215000934`. Spectroscopy with Synchrotron Radiation.

[174] VM. Devi, DC. Benner, K. Sung, LR. Brown, TJ. Crawford, MAH. Smith, AW. Mantz, and A. Predoi-Cross. Self- and air-broadened line shape parameters of 12ch4 : 4500-4620 cm^1. PII-13:23–25, 2014. URL `http://hdl.handle.net/2142/50833`.

[175] K. Sung, A. W. Mantz, M. A. H. Smith, L. R. Brown, T. J. Crawford, V. Malathy Devi, and D. C. Benner. Closed-cycle He-cooled Absorption Cells Designed For A Bruker Ifs-125hr: First Results Between 79 - 297 K. In *AAS/Division for Planetary Sciences Meeting Abstracts #42*, volume 42 of *Bulletin of the American Astronomical Society*, page 970, October 2010.

[176] K. Sung, A.W. Mantz, M.A.H. Smith, L.R. Brown, T.J. Crawford, V.M. Devi, and D.C. Benner. Cryogenic absorption cells operating inside a bruker ifs-125hr: First results for ^{13}ch$_4$ at 7μm. *Journal of Molecular Spectroscopy*, 262(2):122 – 134, 2010. ISSN 0022-2852. doi: https://doi.org/10.1016/j.jms.2010.05.004. URL `http://www.sciencedirect.com/science/article/pii/S0022285210001062`.

[177] Curtis P. Rinsland, V. Malathy Devi, Mary Ann H. Smith, and D. Chris Benner. Measurements of air-broadened and nitrogen-broadened lorentz width coefficients and pressure shift coefficients in the ν_4 and ν_2 bands of ^{12}ch$_4$. *Appl. Opt.*, 27(3): 631–651, Feb 1988. doi: 10.1364/AO.27.000631. URL `http://ao.osa.org/abstract.cfm?URI=ao-27-3-631`.

[178] D.Chris Benner, Curtis P. Rinsland, V.Malathy Devi, Mary Ann H. Smith, and David Atkins. A multispectrum nonlinear least squares fitting technique. *Journal of Quantitative Spectroscopy and Radiative Transfer*, 53(6):705 – 721, 1995. ISSN 0022-4073. doi: https://doi.org/10.1016/0022-4073(95)00015-D. URL `http://www.sciencedirect.com/science/article/pii/002240739500015D`.

[179] L.S. Rothman, I.E. Gordon, Y. Babikov, A. Barbe, D. Chris Benner, P.F. Bernath, M. Birk, L. Bizzocchi, V. Boudon, L.R. Brown, A. Campargue, K. Chance, E.A.

Cohen, L.H. Coudert, V.M. Devi, B.J. Drouin, A. Fayt, J.-M. Flaud, R.R. Gamache, J.J. Harrison, J.-M. Hartmann, C. Hill, J.T. Hodges, D. Jacquemart, A. Jolly, J. Lamouroux, R.J. Le Roy, G. Li, D.A. Long, O.M. Lyulin, C.J. Mackie, S.T. Massie, S. Mikhailenko, H.S.P. Mller, O.V. Naumenko, A.V. Nikitin, J. Orphal, V. Perevalov, A. Perrin, E.R. Polovtseva, C. Richard, M.A.H. Smith, E. Starikova, K. Sung, S. Tashkun, J. Tennyson, G.C. Toon, Vl.G. Tyuterev, and G. Wagner. The hitran2012 molecular spectroscopic database. *Journal of Quantitative Spectroscopy and Radiative Transfer*, 130:4 – 50, 2013. ISSN 0022-4073. doi: https://doi.org/10.1016/j.jqsrt.2013.07.002. URL `http://www.sciencedirect.com/science/article/pii/S0022407313002859`. HITRAN2012 special issue.

[180] V. Malathy Devi, D. Chris Benner, Mary Ann H. Smith, Arlan W. Mantz, Keeyoon Sung, and Linda R. Brown. Spectral line parameters including temperature dependences of air-broadening for the 2-0 bands of $^{13}c^{16}o$ and $^{12}c^{18}o$ at 2.3μm. *Journal of Molecular Spectroscopy*, 276-277:33 – 48, 2012. ISSN 0022-2852. doi: https://doi.org/10.1016/j.jms.2012.05.005. URL `http://www.sciencedirect.com/science/article/pii/S0022285212000872`.

[181] A. Lévy, N. Lacome, and C. Chackerian, Jr. Collisional line mixing. In K. N. Rao and A. Weber, editors, *Spectroscopy of the Earth's Atmosphere and Interstellar Medium*, pages 261–337, 1992.

[182] Adriana Predoi-Cross, Anildev V. Unni, Henry Heung, V. Malathy Devi, D. Chris Benner, and Linda R. Brown. Line mixing effects in the $\nu_2 + \nu_3$ band of methane. *Journal of Molecular Spectroscopy*, 246(1):65 – 76, 2007. ISSN 0022-2852. doi: https://doi.org/10.1016/j.jms.2007.08.005. URL `http://www.sciencedirect.com/science/article/pii/S0022285207002159`.

[183] A. V. Nikitin, M. Rey, and V. G. Tyuterev. New dipole moment surfaces of methane. *Chemical Physics Letters*, 565:5–11, April 2013. doi: 10.1016/j.cplett.2013.02.022.

[184] Michal Rey, Andrei V. Nikitin, and Vladimir G. Tyuterev. First principles intensity calculations of the methane rovibrational spectra in the infrared up to 9300 cm^1. *Phys. Chem. Chem. Phys.*, 15:10049–10061, 2013. doi: 10.1039/C3CP50275A. URL `http://dx.doi.org/10.1039/C3CP50275A`.

[185] M. Rey, A. V. Nikitin, and Vl. G. Tyuterev. Theoretical hot methane line lists up to t = 2000 k for astrophysical applications. *The Astrophysical Journal*, 789(1):2, 2014. URL `http://stacks.iop.org/0004-637X/789/i=1/a=2`.

[186] VlG. Tyuterev, JP. Champion, G. Pierre, and VI. Perevalov. Parameters of reduced hamiltonian and invariant parameters of interacting e and f_2 fundamentals of tetrahedral molecules: ν_2 and ν_4 bands of ch_4 and sih_4. *J. Mol. Spectrosc.*, 120:49–78, 1986.

[187] V.I. Perevalov, Vl.G. Tyuterev, and B.I. Zhilinskii. Reduced hamiltonian for 0100 and 0001 interacting states of tetrahedral xy_4 molecules: Calculated r2j2

and r2j3-type parameters for ν_2 and ν_4 bands of methane. *Journal of Molecular Spectroscopy*, 111(1):1 – 19, 1985. ISSN 0022-2852. doi: https://doi.org/10.1016/0022-2852(85)90062-1. URL `http://www.sciencedirect.com/science/article/pii/0022285285900621`.

[188] Vladimir Tyuterev, Sergei Tashkun, Michael Rey, Roman Kochanov, Andrei Nikitin, and Thibault Delahaye. Accurate spectroscopic models for methane polyads derived from a potential energy surface using high-order contact transformations. *The Journal of Physical Chemistry A*, 117(50):13779–13805, 2013. doi: 10.1021/jp408116j. URL `https://doi.org/10.1021/jp408116j`. PMID: 24131356.

[189] Michal Rey, Andrei V. Nikitin, and Vladimir G. Tyuterev. Complete nuclear motion hamiltonian in the irreducible normal mode tensor operator formalism for the methane molecule. *The Journal of Chemical Physics*, 136(24):244106, 2012. doi: 10.1063/1.4730030. URL `https://doi.org/10.1063/1.4730030`.

[190] Andrei V. Nikitin, Michael Rey, and Vladimir G. Tyuterev. Rotational and vibrational energy levels of methane calculated from a new potential energy surface. *Chemical Physics Letters*, 501(4):179 – 186, 2011. ISSN 0009-2614. doi: https://doi.org/10.1016/j.cplett.2010.11.008. URL `http://www.sciencedirect.com/science/article/pii/S0009261410014715`.

[191] J.-C. Hilico, O. Robert, M. Lote, S. Toumi, A.S. Pine, and L.R. Brown. Analysis of the interacting octad system of 12ch4. *Journal of Molecular Spectroscopy*, 208(1):1 – 13, 2001. ISSN 0022-2852. doi: https://doi.org/10.1006/jmsp.2001.8364. URL `http://www.sciencedirect.com/science/article/pii/S002228520198364X`.

[192] S. Albert, S. Bauerecker, V. Boudon, LR. Brown, JP. Champion, M. Loëte, A. Nikitin, and M. Quack. Global analysis of the high resolution infrared spectrum of methane $^{12}ch_4$ in the region from 0 to 4800 cm^{-1}. *Chemical Physics*, 356: 131–146, February 2009. doi: 10.1016/j.chemphys.2008.10.019.

[193] L. Daumont, A. V. Nikitin, X. Thomas, L. Régalia, P. Von der Heyden, V. G. Tyuterev, M. Rey, V. Boudon, C. Wenger, M. Loëte, and L. R. Brown. New assignments in the 2 μm transparency window of the $^{12}CH_4$ Octad band system. , 116: 101–109, February 2013. doi: 10.1016/j.jqsrt.2012.08.025.

[194] L.R. Brown, K. Sung, D.C. Benner, V.M. Devi, V. Boudon, T. Gabard, C. Wenger, A. Campargue, O. Leshchishina, S. Kassi, D. Mondelain, L. Wang, L. Daumont, L. Rgalia, M. Rey, X. Thomas, Vl. G. Tyuterev, O.M. Lyulin, A.V. Nikitin, H.M. Niederer, S. Albert, S. Bauerecker, M. Quack, J.J. OBrien, I.E. Gordon, L.S. Rothman, H. Sasada, A. Coustenis, M.A.H. Smith, T. Carrington, X.-G. Wang, A.W. Mantz, and P.T. Spickler. Methane line parameters in the hitran2012 database. *Journal of Quantitative Spectroscopy and Radiative Transfer*, 130:201 – 219, 2013. ISSN 0022-4073. doi: https://doi.org/10.1016/j.jqsrt.2013.06.020. URL `http://www.sciencedirect.com/science/article/pii/S0022407313002744`. HITRAN2012 special issue.

[195] A.V. Nikitin, M. Rey, J.P. Champion, and Vl.G. Tyuterev. Extension of the mirs computer package for the modeling of molecular spectra: From effective to full ab initio ro-vibrational hamiltonians in irreducible tensor form. *Journal of Quantitative Spectroscopy and Radiative Transfer*, 113(11):1034 – 1042, 2012. ISSN 0022-4073. doi: https://doi.org/10.1016/j.jqsrt.2012.01.027. URL `http://www.sciencedirect.com/science/article/pii/S0022407312000556`. Three Leaders in Spectroscopy.

[196] Tashkun SA Rey M Brown L Tyuterev VlG, Nikitin AV. in preparation. 2015.

[197] J.C. Hilico, M. Loete, and L.R. Brown. Line strengths of the 2 + 3 and 3 2 bands of methane (12ch4). *Journal of Molecular Spectroscopy*, 152(1):229 – 251, 1992. ISSN 0022-2852. doi: https://doi.org/10.1016/0022-2852(92)90134-A. URL `http://www.sciencedirect.com/science/article/pii/002228529290134A`.

[198] A. Predoi-Cross, M. Brawley-Tremblay, L. R. Brown, V. M. Devi, and D. C. Benner. Multispectrum analysis of $^{12}CH_4$ from 4100 to 4635 cm^{-1}: II. Air-broadening coefficients (widths and shifts). *Journal of Molecular Spectroscopy*, 236:201–215, April 2006. doi: 10.1016/j.jms.2006.01.013.

[199] A. Predoi-Cross, L. R. Brown, V. M. Devi, M. Brawley-Tremblay, and D. C. Benner. Multispectrum analysis of $^{12}CH_4$ from 4100 to 4635 cm^{-1}: 1. Self-broadening coefficients (widths and shifts). *Journal of Molecular Spectroscopy*, 232:231–246, August 2005. doi: 10.1016/j.jms.2005.04.007.

Appendix A

Appendix A including the tables for Chapters 4 and 5

A.1 The table of results for Chapters 4 and 5

Following tables present the complete list of measured and calculated line shape parameters for $2-0$ band of CO. Table A.1 contains CO_2 broadening coefficients at 296 K and their temperature dependence for CO followed by Table A.2 showing the measured results for CO_2 line shift coefficients for the $2-0$ band of $^{12}C^{16}O$. The next ones are Table A.3 and A.4 which include CO_2 broadening and shift coefficients measured for the $2-0$ band of $^{12}C^{16}O$ using the qSDV profile by multi-spectrum fitting all the spectra recorded at each temperature. Speed dependence of the broadening (SDB) coefficients and weak line mixing (LM) parameters, and narrowing parameters (in $cm^{-1}atm^{-1}$) measured for the $2-0$ band of $^{12}C^{16}O$ are presented in Table A.5. Theoretical CO_2 broadening coefficients for the $2-0$ band of $^{12}C^{16}O$ at different temperatures and resulting temperature dependence exponents are combined in Table A.6 followed by Table A.7 including Theoretical CO_2 shift parameters for the $2-0$ band of CO at different temperatures. Moreover, CO_2 weak line mixing coefficients Y_k^0 (atm^{-1}) for the $2-0$ band of $^{12}C^{16}O$ measured using the qSDV profile are gathered in Table 4.11. The last table for chapter 4 is Table A.9 presenting CO_2 broadening coefficients for the $2-0$ band of $^{12}C^{16}O$ calculated using EPG calculations.

Table A.1: CO_2 broadening coefficients at 296 K and their temperature dependence measured for the $2-0$ band of $^{12}C^{16}O$ by multi-spectrum fitting 21 FTS spectra using the VP, RP and qSDV profiles

	$b_L^0(CO-CO_2)$ ($cm^{-1}atm^{-1}$)			n_1		
Line	VP (unc)	RP (unc)	qSDV (unc)	VP (unc)	RP (unc)	qSDV (unc)
P(22)	0.05820 (41)	0.05506 (36)	0.06041 (44)	0.648 (66)	0.711 (63)	0.704 (55)
P(21)	0.05693 (27)	0.05502 (24)	0.05755 (28)	0.753 (43)	0.803 (41)	0.761 (38)
P(20)	0.05845 (19)	0.05747 (17)	0.05979 (21)	0.694 (29)	0.740 (27)	0.712 (25)
P(19)	0.05975 (14)	0.05904 (13)	0.06133 (15)	0.713 (21)	0.764 (19)	0.725 (18)
P(18)	0.06029 (10)	0.05990 (9)	0.06183 (11)	0.710 (15)	0.745 (14)	0.722 (13)
P(17)	0.06154 (8)	0.06137 (7)	0.06296 (9)	0.694 (11)	0.728 (10)	0.704 (10)
P(16)	0.06223 (6)	0.06226 (6)	0.06358 (7)	0.710 (8)	0.739 (8)	0.717 (7)
P(15)	0.06300 (5)	0.06336 (5)	0.06419 (5)	0.729 (7)	0.746 (6)	0.730 (6)

P(14)	0.06452 (4)	0.06487 (4)	0.06587 (5)	0.707 (6)	0.724 (5)	0.706 (5)
P(13)	0.06587 (4)	0.06601 (3)	0.06730 (4)	0.697 (5)	0.714 (4)	0.697 (4)
P(12)	0.06740 (3)	0.06767 (3)	0.06886 (4)	0.684 (4)	0.696 (4)	0.680 (3)
P(11)	0.06910 (3)	0.06941 (3)	0.07007 (3)	0.674 (4)	0.681 (3)	0.667 (3)
P(10)	0.07147 (3)	0.07175 (3)	0.07314 (3)	0.657 (3)	0.664 (3)	0.650 (3)
P(9)	0.07414 (3)	0.07442 (3)	0.07596 (3)	0.644 (3)	0.649 (3)	0.636 (3)
P(8)	0.07705 (3)	0.07731 (3)	0.07901 (3)	0.639 (3)	0.642 (3)	0.628 (3)
P(7)	0.08062 (3)	0.08088 (3)	0.08283 (3)	0.642 (3)	0.647 (3)	0.631 (3)
P(6)	0.08412 (3)	0.08432 (3)	0.08654 (3)	0.649 (3)	0.654 (3)	0.636 (3)
P(5)	0.08796 (3)	0.08812 (3)	0.09059 (4)	0.658 (3)	0.665 (3)	0.646 (3)
P(4)	0.09199 (4)	0.09206 (3)	0.09483 (4)	0.671 (3)	0.681 (3)	0.659 (3)
P(3)	0.09625 (4)	0.09607 (4)	0.09945 (5)	0.682 (4)	0.696 (3)	0.672 (3)
P(2)	0.1009 (6)	0.1006 (6)	0.1046 (7)	0.683 (5)	0.700 (4)	0.676 (4)
P(1)	0.1075 (12)	0.1067 (11)	0.1110 (13)	0.689 (8)	0.710 (8)	0.686 (7)
R(1)	0.1076 (11)	0.1071 (10)	0.1111 (13)	0.699 (8)	0.718 (8)	0.693 (7)
R(2)	0.1009 (6)	0.1008 (5)	0.1042 (7)	0.694 (5)	0.708 (4)	0.685 (4)
R(3)	0.09594 (4)	0.09597 (4)	0.09894 (5)	0.684 (3)	0.694 (3)	0.675 (3)
R(4)	0.09189 (3)	0.09205 (3)	0.09468 (4)	0.680 (3)	0.687 (3)	0.664 (3)
R(5)	0.08792 (3)	0.08815 (3)	0.09047 (3)	0.667 (3)	0.672 (3)	0.653 (2)
R(6)	0.08397 (3)	0.08428 (2)	0.08627 (3)	0.661 (3)	0.661 (2)	0.646 (2)
R(7)	0.08019 (2)	0.08055 (2)	0.08229(3)	0.655 (3)	0.652 (2)	0.638 (2)
R(8)	0.07676 (2)	0.07715 (2)	0.07869 (3)	0.649 (3)	0.644 (2)	0.633 (2)
R(9)	0.07378 (2)	0.07409 (2)	0.07570 (2)	0.648 (3)	0.647 (2)	0.633 (2)
R(10)	0.07107 (2)	0.07141 (2)	0.07272 (2)	0.662 (3)	0.661 (3)	0.650 (2)
R(11)	0.06883 (2)	0.06906 (2)	0.07052 (3)	0.672 (3)	0.676 (3)	0.661 (3)
R(12)	0.06680 (2)	0.06707 (2)	0.06823 (3)	0.691 (3)	0.695 (3)	0.683 (3)
R(13)	0.06526 (3)	0.06542 (2)	0.06667 (3)	0.698 (3)	0.709 (3)	0.693 (3)
R(14)	0.06413 (3)	0.06423 (3)	0.06559 (3)	0.703 (4)	0.719 (4)	0.702 (3)
R(15)	0.06287 (3)	0.06288 (3)	0.06430 (4)	0.708 (5)	0.728 (4)	0.710 (4)
R(16)	0.06184 (4)	0.06177 (4)	0.06323 (4)	0.712 (5)	0.736 (5)	0.716 (5)
R(17)	0.06069 (5)	0.06053 (4)	0.06194 (5)	0.706 (7)	0.733 (6)	0.712 (6)
R(18)	0.05988 (6)	0.05968 (5)	0.06111 (6)	0.709 (9)	0.742 (8)	0.718 (7)
R(19)	0.05922 (8)	0.05849 (7)	0.06082 (8)	0.694 (11)	0.739 (11)	0.710 (10)
R(20)	0.05796 (10)	0.05728 (9)	0.05902 (11)	0.726 (16)	0.770 (14)	0.737 (14)
R(21)	0.05735 (14)	0.05550 (13)	0.05898 (15)	0.669 (22)	0.728 (21)	0.693 (19)
R(22)	0.05565 (19)	0.05375 (17)	0.05642 (20)	0.665 (32)	0.708 (30)	0.665 (28)

’unc’ are the statistical uncertainties (1σ) estimated by the least squares fitting procedure.

Table A.2: CO_2 line shift coefficients for the $2-0$ band of $^{12}C^{16}O$ measured by multi-spectrum fitting 21 FTS spectra using the VP, RP and qSDV profiles

Line		d^0(CO – CO$_2$) (cm^{-1}atm^{-1})		
	$\tilde{\nu}$ (cm^{-1})	VP (unc)	RP (unc)	SDV (unc)
P(22)	4159.5595	−0.00748 (25)	−0.00735 (22)	−0.00750 (21)
P(21)	4164.8408	−0.00676(16)	−0.00659 (15)	−0.00673 (14)
P(20)	4170.0551	−0.00637 (11)	−0.00628 (10)	−0.00627 (10)
P(19)	4175.2024	−0.00685 (8)	−0.00675 (8)	−0.00673 (7)
P(18)	4180.2825	−0.00701 (6)	−0.00694 (6)	−0.00687 (5)
P(17)	4185.2952	−0.00698 (5)	−0.00692 (4)	−0.00688 (4)
P(16)	4190.2404	−0.00669 (4)	−0.00663 (3)	−0.00657 (3)
P(15)	4195.1180	−0.00633 (3)	−0.00630 (3)	−0.00624 (3)
P(14)	4199.9277	−0.00525 (2)	−0.00623 (2)	−0.00617 (2)
P(13)	4204.6695	−0.00581 (2)	−0.00579 (2)	−0.00571 (2)
P(12)	4209.3432	−0.00563 (2)	−0.00560 (2)	−0.00553 (2)
P(11)	4213.9486	−0.00525 (2)	−0.00523 (2)	−0.00515 (2)
P(10)	4218.4857	−0.00527 (2)	−0.00525 (1)	−0.00517 (1)
P(9)	4222.9542	−0.00494 (2)	−0.00492 (1)	−0.00483 (1)
P(8)	4227.3540	−0.00469 (2)	−0.00467 (1)	−0.00458 (1)
P(7)	4231.6850	−0.00426 (2)	−0.00424 (1)	−0.00414 (1)
P(6)	4235.9470	−0.00381 (2)	−0.00380 (2)	−0.00370 (1)
P(5)	4240.1399	−0.00347 (2)	−0.00346 (2)	−0.00337 (2)
P(4)	4244.2635	−0.00342 (2)	−0.00342 (2)	−0.00333 (2)
P(3)	4248.3176	−0.00287 (3)	−0.00286 (2)	−0.00279 (2)
P(2)	4252.3022	−0.00272 (4)	−0.00269 (3)	−0.00268 (3)
P(1)	4256.2171	−0.00238 (7)	−0.00225 (6)	−0.00238 (6)
R(1)	4263.8372	−0.00319 (7)	−0.00308 (6)	−0.00281 (6)
R(2)	4267.5421	−0.00278 (3)	−0.00270 (3)	−0.00251 (3)
R(3)	4271.1766	−0.00293 (2)	−0.00286 (2)	−0.00272 (2)
R(4)	4274.7407	−0.00333 (2)	−0.00326 (2)	−0.00315 (2)
R(5)	4278.2343	−0.00376 (2)	−0.00370 (1)	−0.00361 (1)
R(6)	4281.6570	−0.00397 (1)	−0.00392 (1)	−0.00384 (1)
R(7)	4285.0089	−0.00405 (1)	−0.00401 (1)	−0.00394 (1)
R(8)	4288.2898	−0.00451 (1)	−0.00449 (1)	−0.00441 (1)
R(9)	4291.4994	−0.00462 (1	−0.00460 (1)	−0.00453 (1)
R(10)	4294.6378	−0.00486 (1)	−0.00485 (1)	−0.00478 (1)
R(11)	4297.7046	−0.00498 (1)	−0.00496 (1)	−0.00490 (1)
R(12)	4300.6999	−0.00526 (1)	−0.00525 (1)	−0.00519 (1)
R(13)	4303.6233	−0.00510 (2)	−0.00509 (1)	−0.00503 (1)
R(14)	4306.4749	−0.00540 (2)	−0.00539 (2)	−0.00534 (2)
R(15)	4309.2544	−0.00538 (2)	−0.00537 (2)	−0.00532 (2)
R(16)	4311.9617	−0.00556 (2)	−0.00555 (2)	−0.00551 (2)
R(17)	4314.5966	−0.00595 (3)	−0.00592 (3)	−0.00589 (3)
R(18)	4317.1590	−0.00558 (4)	−0.00558 (3)	−0.00554 (3)
R(19)	4319.6488	−0.00575 (5)	−0.00571 (4)	−0.00568 (4)

R(20)	4322.0658	−0.00640 (6)	−0.00637 (6)	−0.00637 (5)
R(21)	4324.4098	−0.00569 (8)	−0.00555 (8)	−0.00562 (7)
R(22)	4326.6808	−0.00671 (12)	−0.00648 (11)	−0.00666 (10)

’unc’ are the statistical uncertainties (1σ) estimated by the least squares fitting procedure.

Table A.3: CO_2 broadening coefficients measured for the $2-0$ band of $^{12}C^{16}O$ using the qSDV profile by multi-spectrum fitting all the spectra recorded at each temperature

$b^0_L(CO-CO_2)$ $(cm^{-1}atm^{-1})$				
Line	283.4	270.0	255.4	240.5
P(22)	0.0603 (150)	0.0609 (100)	0.0586 (120)	0.0626 (130)
P(21)	0.0571 (22)	0.0580 (30)	0.0596 (73)	0.0545 (190)
P(20)	0.0604 (20)	0.0589 (22)	0.0596 (49)	0.0618 (160)
P(19)	0.0607 (12)	0.0616 (17)	0.0621 (37)	0.0605 (75)
P(18)	0.0621 (10)	0.0615 (12)	0.0612 (26)	0.0628 (64)
P(17)	0.0629 (6)	0.0626 (9)	0.0631 (20)	0.0630 (42)
P(16)	0.0633 (6)	0.0635 (7)	0.0636 (16)	0.0634 (33)
P(15)	0.0639 (4)	0.0643 (5)	0.0640 (13)	0.0640 (26)
P(14)	0.0656 (4)	0.0656 (4)	0.0650 (11)	0.0655 (22)
P(13)	0.0671 (3)	0.0663 (4)	0.0663 (8)	0.0672 (15)
P(12)	0.0688 (3)	0.0679 (3)	0.0680 (7)	0.0690 (13)
P(11)	0.0708 (2)	0.0701 (3)	0.0696 (7)	0.0707 (10)
P(10)	0.0729 (2)	0.0729 (3)	0.0718 (7)	0.0726 (9)
P(9)	0.0759 (2)	0.0750 (2)	0.0736 (5)	0.0765 (9)
P(8)	0.0787 (2)	0.0788 (2)	0.0778 (5)	0.0791 (9)
P(7)	0.0829 (2)	0.0826 (2)	0.0810 (5)	0.0829 (9)
P(6)	0.0868 (2)	0.0865 (3)	0.0843 (6)	0.0872 (8)
P(5)	0.0908 (2)	0.0901 (3)	0.0886 (6)	0.0908 (9)
P(4)	0.0951 (2)	0.0952 (3)	0.0939 (8)	0.0958 (11)
P(3)	0.0998 (3)	0.0989 (4)	0.0988 (9)	0.1004 (13)
P(2)	0.104 (5)7	0.1043 (6)	0.1033 (12)	0.1053 (19)
P(1)	0.1098 (10)	0.1109 (12)	0.1119 (29)	0.1101 (43)
R(1)	0.1099 (10)	0.1117 (14)	0.1108 (30)	0.1104 (41)
R(2)	0.1043 (5)	0.1033 (6)	0.1032 (13)	0.1050 (20)
R(3)	0.0991 (3)	0.0978 (4)	0.0983 (9)	0.0995 (14)
R(4)	0.0942 (2)	0.0953 (3)	0.0937 (7)	0.0943 (11)
R(5)	0.0904 (2)	0.0900 (2)	0.0890 (5)	0.0905 (8)
R(6)	0.0861 (2)	0.0856 (2)	0.0851 (5)	0.0860 (7)
R(7)	0.0820 (2)	0.0819 (2)	0.0810 (4)	0.0825 (6)
R(8)	0.0786 (2)	0.0781 (2)	0.0775 (4)	0.0780 (7)
R(9)	0.0757 (1)	0.0755 (2)	0.0733 (5)	0.0765 (7)

R(10)	0.0725 (2)	0.0720 (2)	0.0706 (4)	0.0712 (6)
R(11)	0.0706 (2)	0.0701 (2)	0.0683 (4)	0.0709 (7)
R(12)	0.0683 (2)	0.0685 (2)	0.0668 (5)	0.0685 (7)
R(13)	0.0665 (2)	0.0663 (2)	0.0651 (5)	0.0663 (9)
R(14)	0.0653 (2)	0.0657 (2)	0.0636 (6)	0.0658 (12)
R(15)	0.0641 (2)	0.0641 (3)	0.0632 (8)	0.0644 (13)
R(16)	0.0629 (2)	0.0634 (3)	0.0623 (9)	0.0634 (13)
R(17)	0.0616 (3)	0.0620 (4)	0.0620 (12)	0.0614 (22)
R(18)	0.0612 (5)	0.0607 (5)	0.0612 (14)	0.0611 (34)
R(19)	0.0608 (4)	0.0610 (8)	0.0596 (21)	0.0618 (30)
R(20)	0.0587 (9)	0.0587 (8)	0.0601 (25)	0.0582 (71)
R(21)	0.0586 (8)	0.0596 (13)	0.0582 (38)	0.0592 (44)
R(22)	0.0576 (19)	0.05554 (31)	0.0566 (49)	0.0589 (180)

’unc’ are the statistical uncertainties (1σ) estimated by the least squares fitting procedure.

Table A.4: CO_2 shift coefficients measured for the $2-0$ band of $^{12}C^{16}O$ using the qSDV profile by multi-spectrum fitting all the spectra recorded at each temperature

Line		$d_0(T)$(CO – CO_2) (cm^{-1}atm^{-1})			
	$\tilde{\nu}$ (cm^{-1})	283.4	270.0	255.4	240.5
P(22)	4159.5595	−0.00749 (28)	−0.00716 (34)	−0.00881 (64)	−0.00721 (130)
P(21)	4164.8408	−0.00635 (19)	−0.00686 (23)	−0.00758 (43)	−0.00751 (74)
P(20)	4170.0551	−0.00605 (14)	−0.00622 (16)	−0.00708 (29)	−0.00661 (52)
P(19)	4175.2024	−0.00644 (10)	−0.00675 (11)	−0.00745 (21)	−0.00725 (36)
P(18)	4180.2825	−0.00662 (8)	−0.00667 (8)	−0.00769 (15)	−0.00795 (25)
P(17)	4185.2952	−0.00668 (6)	−0.00686 (6)	−0.00722 (11)	−0.00770 (18)
P(16)	4190.2404	−0.00640 (5)	−0.00650 (5)	−0.00696 (9)	−0.00721 (14)
P(15)	4195.1180	−0.00598 (4)	−0.00616 (4)	−0.00688 (7)	−0.00671 (11)
P(14)	4199.9277	−0.00593 (3)	−0.00614 (3)	−0.00653 (6)	−0.00676 (9)
P(13)	4204.6695	−0.00544 (3)	−0.00571 (3)	−0.00612 (5)	−0.00616 (7)
P(12)	4209.3432	−0.00529 (2)	−0.00546 (3)	−0.00605 (4)	−0.00590 (6)
P(11)	4213.9486	−0.00494 (2)	−0.00504 (2)	−0.00563 (4)	−0.00557 (6)
P(10)	4218.4857	−0.00496 (2)	−0.00508 (2)	−0.00560 (4)	−0.00551 (5)
P(9)	4222.9542	−0.00463 (2)	−0.00473 (2)	−0.00534 (4)	−0.00510 (5)
P(8)	4227.3540	−0.00437 (2)	−0.00449 (2)	−0.00497 (4)	−0.00489 (5)
P(7)	4231.6850	−0.00396 (2)	−0.00398 (2)	−0.00462 (4)	−0.00450 (5)
P(6)	4235.9470	−0.00346 (2)	−0.00355 (2)	−0.00427 (4)	−0.00406 (5)
P(5)	4240.1399	−0.00310 (2)	−0.00326 (2)	−0.00397 (4)	−0.00353 (5)
P(4)	4244.2635	−0.00312 (3)	−0.00321 (3)	−0.00383 (5)	−0.00352 (6)
P(3)	4248.3176	−0.00258 (4)	−0.00266 (3)	−0.00328 (5)	−0.00297 (7)

P(2)	4252.3022	−0.00257 (5)	−0.00241 (5)	−0.00299 (7)	−0.00319 (10)
P(1)	4256.2171	−0.00222 (10)	−0.00239 (10)	−0.00245 (14)	−0.00273 (19)
R(1)	4263.8372	−0.00283 (10)	−0.00286 (9)	−0.00261 (13)	−0.00316 (19)
R(2)	4267.5421	−0.00248 (5)	−0.00229 (5)	−0.00297 (7)	−0.00254 (10)
R(3)	4271.1766	−0.00250 (3)	−0.00269 (3)	−0.00312 (5)	−0.00273 (7)
R(4)	4274.7407	−0.00300 (3)	−0.00311 (3)	−0.00338 (4)	−0.00330 (6)
R(5)	4278.2343	−0.00342 (2)	−0.00353 (2)	−0.00399 (4)	−0.00378 (5)
R(6)	4281.6570	−0.00367 (2)	−0.00378 (2)	−0.00409 (3)	−0.00417 (5)
R(7)	4285.0089	−0.00370 (2)	−0.00388 (2)	−0.00434 (3)	−0.00432 (4)
R(8)	4288.2898	−0.00414 (2)	−0.00429 (2)	−0.00498 (3)	−0.00488 (4)
R(9)	4291.4994	−0.00430 (2)	−0.00439 (2)	−0.00498 (3)	−0.00512 (4)
R(10)	4294.6378	−0.00451 (2)	−0.00471 (2)	−0.00528 (3)	−0.00521 (4)
R(11)	4297.7046	−0.00468 (2)	−0.00478 (2)	−0.00534 (3)	−0.00539 (4)
R(12)	4300.6999	−0.00493 (2)	−0.00509 (2)	−0.00574 (3)	−0.00568 (5)
R(13)	4303.6233	−0.00480 (2)	−0.00497 (2)	−0.00545 (4)	−0.00552 (5)
R(14)	4306.4749	−0.00518 (2)	−0.00521 (2)	−0.00579 (4)	−0.00576 (6)
R(15)	4309.2544	−0.00507 (2)	−0.00521 (3)	−0.00590 (5)	−0.00579 (7)
R(16)	4311.9617	−0.00530 (3)	−0.00543 (3)	−0.00604 (6)	−0.00587 (8)
R(17)	4314.5966	−0.00568 (4)	−0.00586 (4)	−0.00635 (7)	−0.00639 (11)
R(18)	4317.1590	−0.00531 (4)	−0.00544 (5)	−0.00620 (9)	−0.00620 (14)
R(19)	4319.6488	−0.00539 (6)	−0.00558 (6)	−0.00655 (11)	−0.00622 (19)
R(20)	4322.0658	−0.00619 (8)	−0.00630 (8)	−0.00694 (15)	−0.00732 (26)
R(21)	4324.4098	−0.00535 (10)	−0.00560 (11)	−0.00647 (21)	−0.00600 (38)
R(22)	4326.6808	−0.00626 (14)	−0.00672 (16)	−0.00775 (30)	−0.00734 (56)

’unc’ are the statistical uncertainties (1σ) estimated by the least squares fitting procedure.

Table A.5: Speed dependence of the broadening (SDB) coefficients and weak line mixing (LM) parameters, and narrowing parameters (in $cm^{-1}atm^{-1}$) measured for the $2-0$ band of $^{12}C^{16}O$ by multi-spectrum fitting 21 FTS spectra with the qSDV and RP models, respectively

Line		qSDV		RP
	$\tilde{\nu}$ (cm^{-1})	SDB	LM	Narrowing
P(22)	4159.5595	0.0112 (56)	−0.0086 (26)	0.028 (11)
P(21)	4164.8408	0.00351 (58)	0.0009 (17)	0.007 (5)
P(20)	4170.0551	0.00751 (32)	−0.0002 (12)	0.027 (5)
P(19)	4175.2024	0.00849 (23)	−0.0010 (8)	0.046 (5)
P(18)	4180.2825	0.00843 (17)	0.0013 (6)	0.034 (3)
P(17)	4185.2952	0.00800 (13)	0.0047 (4)	0.043 (3)
P(16)	4190.2404	0.00776 (11)	0.0018 (3)	0.043 (2)

P(15)	4195.1180	0.00696 (9)	−0.0030 (3)	0.043 (2)
P(14)	4199.9277	0.00770 (8)	0.0010 (2)	0.054 (2)
P(13)	4204.6695	0.00822 (6)	0.0000 (2)	0.052 (2)
P(12)	4209.3432	0.00838 (6)	−0.0001 (1)	0.058 (2)
P(11)	4213.9486	0.00907 (5)	0.0003 (1)	0.055 (2)
P(10)	4218.4857	0.00955 (5)	0.0004 (1)	0.069 (2)
P(9)	4222.9542	0.01032 (5)	0.0006 (1)	0.078 (2)
P(8)	4227.3540	0.01097 (5)	0.0000 (1)	0.080 (2)
P(7)	4231.6850	0.01209 (5)	−0.0012 (1)	0.107 (3)
P(6)	4235.9470	0.01300 (5)	−0.0018 (1)	0.104 (3)
P(5)	4240.1399	0.01391 (6)	−0.0024 (1)	0.123 (4)
P(4)	4244.2635	0.01481 (6)	−0.0027 (1)	0.145 (5)
P(3)	4248.3176	0.01626 (8)	−0.0039 (2)	0.133 (6)
P(2)	4252.3022	0.01812 (11)	−0.0054 (2)	0.158 (10)
P(1)	4256.2171	0.01811 (22)	−0.0050 (4)	0.178 (21)
R(1)	4263.8372	0.01769 (22)	0.0043 (4)	0.181 (21)
R(2)	4267.5421	0.01678 (11)	0.0045 (2)	0.176 (10)
R(3)	4271.1766	0.01567 (7)	0.0021 (1)	0.121 (5)
R(4)	4274.7407	0.01463 (6)	0.0008 (1)	0.149 (5)
R(5)	4278.2343	0.01373 (5)	0.0003 (1)	0.143 (4)
R(6)	4281.6570	0.01266 (5)	−0.0004 (1)	0.114 (3)
R(7)	4285.0089	0.01176 (4)	−0.0019 (1)	0.102 (2)
R(8)	4288.2898	0.01090 (4)	−0.0021 (1)	0.086 (2)
R(9)	4291.4994	0.01081 (4)	−0.0031 (1)	0.081 (2)
R(10)	4294.6378	0.00956 (4)	−0.0042 (1)	0.074 (2)
R(11)	4297.7046	0.00959 (4)	−0.0043 (1)	0.060 (1)
R(12)	4300.6999	0.00834 (4)	−0.0045 (1)	0.053 (1)
R(13)	4303.6233	0.00821 (5)	−0.0064 (1)	0.048 (1)
R(14)	4306.4749	0.00831 (5)	−0.0061 (1)	0.049 (1)
R(15)	4309.2544	0.00810 (6)	−0.0071 (2)	0.044 (1)
R(16)	4311.9617	0.00786 (7)	−0.0083 (2)	0.043 (2)
R(17)	4314.5966	0.00718 (8)	−0.0084 (3)	0.036 (2)
R(18)	4317.1590	0.00715 (10)	−0.0078 (3)	0.040 (2)
R(19)	4319.6488	0.00863 (12)	−0.0092 (5)	0.038 (2)
R(20)	4322.0658	0.00606 (19)	−0.0088 (6)	0.031 (3)
R(21)	4324.4098	0.00863 (22)	−0.0135 (9)	0.024 (3)
R(22)	4326.6808	0.00389 (39)	0.0007 (12)	0.005 (3)

’unc’ are the statistical uncertainties (1σ) estimated by the least squares fitting procedure.

Table A.6: Theoretical CO_2 broadening coefficients for the $2-0$ band of $^{12}C^{16}O$ at different temperatures and resulting temperature dependence exponent n_1

Line		$b_L^0(CO - CO_2)$ ($cm^{-1}atm^{-1}$)					
	$\tilde{\nu}$ (cm^{-1})	296	283.4	270.0	255.4	240.5	n_1
P(22)	4159.5595	0.05740	0.05924	0.06137	0.06391	0.06677	0.727
P(21)	4164.8408	0.05774	0.05960	0.06173	0.06428	0.06716	0.728
P(20)	4170.0551	0.05814	0.06000	0.06215	0.06471	0.06761	0.725
P(19)	4175.2024	0.05860	0.06047	0.06263	0.06521	0.06812	0.724
P(18)	4180.2825	0.05915	0.06103	0.06320	0.06579	0.06872	0.721
P(17)	4185.2952	0.05983	0.06171	0.06389	0.06649	0.06944	0.715
P(16)	4190.2404	0.06066	0.06255	0.06474	0.06736	0.07033	0.709
P(15)	4195.1180	0.06172	0.06363	0.06582	0.06846	0.07145	0.702
P(14)	4199.9277	0.06308	0.06499	0.06720	0.06986	0.07287	0.690
P(13)	4204.6695	0.06480	0.06672	0.06895	0.07162	0.07465	0.677
P(12)	4209.3432	0.06689	0.06883	0.07108	0.07377	0.07682	0.662
P(11)	4213.9486	0.06932	0.07129	0.07356	0.07627	0.07934	0.647
P(10)	4218.4857	0.07202	0.07402	0.07632	0.07906	0.08215	0.632
P(9)	4222.9542	0.07496	0.07701	0.07937	0.08216	0.08529	0.621
P(8)	4227.3540	0.07817	0.08032	0.08278	0.08568	0.08892	0.622
P(7)	4231.6850	0.08167	0.08397	0.08658	0.08966	0.09309	0.634
P(6)	4235.9470	0.08541	0.08789	0.09071	0.09404	0.09774	0.654
P(5)	4240.1399	0.08936	0.09204	0.09510	0.09871	0.10274	0.676
P(4)	4244.2635	0.09371	0.09659	0.09989	0.10380	0.10817	0.694
P(3)	4248.3176	0.09893	0.10204	0.10560	0.10983	0.11458	0.709
P(2)	4252.3022	0.10627	0.10965	0.11352	0.11813	0.12333	0.718
P(1)	4256.2171	0.12215	0.12598	0.13039	0.13562	0.14149	0.709
R(1)	4263.8372	0.10939	0.11283	0.11677	0.12146	0.12672	0.710
R(2)	4267.5421	0.10214	0.10538	0.10909	0.11351	0.11849	0.716
R(3)	4271.1766	0.09652	0.09954	0.10301	0.10712	0.11174	0.707
R(4)	4274.7407	0.09201	0.09484	0.09807	0.10189	0.10618	0.693
R(5)	4278.2343	0.08807	0.09070	0.09371	0.09726	0.10122	0.674
R(6)	4281.6570	0.08437	0.08681	0.08959	0.09287	0.09652	0.652
R(7)	4285.0089	0.08081	0.08308	0.08566	0.08870	0.09209	0.633
R(8)	4288.2898	0.07745	0.07957	0.08200	0.08487	0.08807	0.620
R(9)	4291.4994	0.07434	0.07637	0.07870	0.08147	0.08457	0.620
R(10)	4294.6378	0.07148	0.07346	0.07574	0.07845	0.08152	0.630
R(11)	4297.7046	0.06885	0.07080	0.07305	0.07573	0.07878	0.645
R(12)	4300.6999	0.06647	0.06840	0.07063	0.07330	0.07633	0.662
R(13)	4303.6233	0.06442	0.06634	0.06855	0.07120	0.07421	0.678
R(14)	4306.4749	0.06275	0.06465	0.06685	0.06949	0.07248	0.690
R(15)	4309.2544	0.06143	0.06332	0.06551	0.06813	0.07110	0.700
R(16)	4311.9617	0.06040	0.06229	0.06446	0.06707	0.07002	0.709
R(17)	4314.5966	0.05959	0.06147	0.06364	0.06623	0.06917	0.716

R(18)	4317.1590	0.05894	0.06081	0.06297	0.06555	0.06847	0.720
R(19)	4319.6488	0.05841	0.06027	0.06242	0.06499	0.06789	0.723
R(20)	4322.0658	0.05796	0.05982	0.06196	0.06451	0.06740	0.726
R(21)	4324.4098	0.05758	0.05942	0.06155	0.06410	0.06697	0.726
R(22)	4326.6808	0.05724	0.05908	0.06120	0.06373	0.06659	0.728

Table A.7: Theoretical CO_2 shift parameters for the $2-0$ band of CO at different temperatures

Line		$d_0(T)$ (cm^{-1}atm^{-1})				
	$\tilde{\nu}$ (cm^{-1})	296	283.4	270.0	255.4	240.5
P(22)	4159.5595	−0.00697	−0.00719	−0.00744	−0.00771	−0.00798
P(21)	4164.8408	−0.00683	−0.00707	−0.00732	−0.00760	−0.00789
P(20)	4170.0551	−0.00670	−0.00694	−0.00720	−0.00749	−0.00780
P(19)	4175.2024	−0.00655	−0.00680	−0.00708	−0.00738	−0.00770
P(18)	4180.2825	−0.00640	−0.00666	−0.00694	−0.00726	−0.00759
P(17)	4185.2952	−0.00625	−0.00651	−0.00680	−0.00713	−0.00746
P(16)	4190.2404	−0.00608	−0.00635	−0.00665	−0.00698	−0.00732
P(15)	4195.1180	−0.00589	−0.00617	−0.00646	−0.00679	−0.00716
P(14)	4199.9277	−0.00567	−0.00593	−0.00623	−0.00658	−0.00696
P(13)	4204.6695	−0.00539	−0.00566	−0.00597	−0.00633	−0.00674
P(12)	4209.3432	−0.00508	−0.00536	−0.00568	−0.00606	−0.00648
P(11)	4213.9486	−0.00477	−0.00505	−0.00538	−0.00576	−0.00620
P(10)	4218.4857	−0.00445	−0.00474	−0.00507	−0.00546	−0.00590
P(9)	4222.9542	−0.00415	−0.00443	−0.00477	−0.00516	−0.00561
P(8)	4227.3540	−0.00385	−0.00414	−0.00448	−0.00488	−0.00533
P(7)	4231.6850	−0.00355	−0.00385	−0.00419	−0.00460	−0.00506
P(6)	4235.9470	−0.00324	−0.00354	−0.00389	−0.00431	−0.00478
P(5)	4240.1399	−0.00290	−0.00321	−0.00356	−0.00398	−0.00446
P(4)	4244.2635	−0.00261	−0.00291	−0.00326	−0.00367	−0.00415
P(3)	4248.3176	−0.00253	−0.00284	−0.00320	−0.00363	−0.00411
P(2)	4252.3022	−0.00265	−0.00306	−0.00353	−0.00410	−0.00473
P(1)	4256.2171	−0.00202	−0.00263	−0.00335	−0.00422	−0.00523
R(1)	4263.8372	−0.00140	−0.00172	−0.00206	−0.00246	−0.00289
R(2)	4267.5421	−0.00161	−0.00199	−0.00241	−0.00291	−0.00345
R(3)	4271.1766	−0.00188	−0.00228	−0.00274	−0.00328	−0.00388
R(4)	4274.7407	−0.00222	−0.00263	−0.00311	−0.00367	−0.00429
R(5)	4278.2343	−0.00241	−0.00284	−0.00333	−0.00391	−0.00455
R(6)	4281.6570	−0.00260	−0.00306	−0.00358	−0.00420	−0.00490
R(7)	4285.0089	−0.00285	−0.00334	−0.00391	−0.00460	−0.00537
R(8)	4288.2898	−0.00316	−0.00369	−0.00431	−0.00505	−0.00589

R(9)	4291.4994	−0.00348	−0.00405	−0.00472	−0.00551	−0.00641
R(10)	4294.6378	−0.00380	−0.00440	−0.00510	−0.00593	−0.00687
R(11)	4297.7046	−0.00410	−0.00472	−0.00544	−0.00629	−0.00725
R(12)	4300.6999	−0.00435	−0.00499	−0.00572	−0.00659	−0.00756
R(13)	4303.6233	−0.00457	−0.00521	−0.00595	−0.00682	−0.00780
R(14)	4306.4749	−0.00475	−0.00540	−0.00614	−0.00701	−0.00798
R(15)	4309.2544	−0.00487	−0.00554	−0.00629	−0.00716	−0.00813
R(16)	4311.9617	−0.00495	−0.00563	−0.00640	−0.00728	−0.00824
R(17)	4314.5966	−0.00503	−0.00571	−0.00648	−0.00737	−0.00834
R(18)	4317.1590	−0.00509	−0.00577	−0.00654	−0.00744	−0.00841
R(19)	4319.6488	−0.00516	−0.00583	−0.00660	−0.00750	−0.00847
R(20)	4322.0658	−0.00522	−0.00589	−0.00666	−0.00756	−0.00853
R(21)	4324.4098	−0.00528	−0.00595	−0.00672	−0.00761	−0.00859
R(22)	4326.6808	−0.00533	−0.00601	−0.00677	−0.00767	−0.00864

Table A.8: CO_2 weak line mixing coefficients Y_k^0 (atm^{-1}) for the $2-0$ band of $^{12}C^{16}O$ measured using the qSDV profile by multi-spectrum fitting all the spectra recorded at each temperature, and corresponding values calculated using the EPG law

	240.5 K		255.4 K		270.0 K		283.4 K	
Line	qSDV	EPG	qSDV	EPG	qSDV	EPG	qSDV	EPG
P(22)	−0.0673	0.004	0.0066	0.004	−0.0055	0.0039	−0.0105	0.0039
P(21)	−0.0005	0.004	0.0153	0.004	−0.0053	0.0039	0.003	0.0039
P(20)	0.0053	0.0041	−0.0094	0.004	0.0008	0.004	0000	0.0039
P(19)	−0.011	0.0041	0.0054	0.004	−0.0016	0.004	−0.0014	0.0039
P(18)	0.0014	0.0041	−0.0015	0.0041	0.0017	0.004	0.001	0.0039
P(17)	0.0125	0.0041	0.0006	0.0041	0.0037	0.004	0.0057	0.0039
P(16)	0.0022	0.0041	0.0007	0.004	0.001	0.0039	0.0028	0.0038
P(15)	−0.0072	0.0041	−0.0014	0.004	−0.0038	0.0039	−0.0024	0.0038
P(14)	−0.0004	0.004	0.0009	0.0039	0.0009	0.0038	0.001	0.0037
P(13)	−0.0007	0.0039	−0.0003	0.0038	0	0.0037	0.0002	0.0036
P(12)	0.0009	0.0038	−0.0008	0.0037	−0.0007	0.0035	0.0003	0.0035
P(11)	0.0002	0.0037	−0.0004	0.0035	0.0005	0.0034	0.0003	0.0033
P(10)	−0.0003	0.0034	0.0011	0.0032	0.0001	0.0031	0.0005	0.003
P(9)	0.0008	0.003	0.0003	0.0029	0.0006	0.0028	0.0006	0.0026
P(8)	−0.0001	0.0026	0.0001	0.0025	−0.0003	0.0023	0000	0.0022
P(7)	−0.0018	0.002	−0.0008	0.0019	−0.001	0.0017	−0.0015	0.0017
P(6)	−0.0018	0.0011	−0.0018	0.001	−0.0017	0.001	−0.0021	0.0009
P(5)	−0.002	0000	−0.0025	−0.0001	−0.0024	−0.0001	−0.0027	−0.0002
P(4)	−0.0022	−0.0017	−0.0032	−0.0017	−0.0026	−0.0017	−0.0028	−0.0017

P(3)	−0.0038	−0.0043	−0.0044	−0.0041	−0.0037	−0.004	−0.0041	−0.0039
P(2)	−0.0062	−0.0086	−0.0055	−0.0083	−0.0053	−0.008	−0.0053	−0.0077
P(1)	−0.0046	−0.0184	−0.0039	−0.0176	−0.0053	−0.0168	−0.0049	−0.0161
R(1)	0.0038	0.0344	0.007	0.0326	0.0039	0.0309	0.0044	0.0295
R(2)	0.0044	0.0105	0.0042	0.0101	0.0049	0.0097	0.0041	0.0094
R(3)	0.0024	0.0065	0.0019	0.0063	0.0019	0.0061	0.0022	0.0059
R(4)	0.0002	0.0038	0.0005	0.0037	0.0008	0.0036	0.0012	0.0036
R(5)	−0.001	0.0018	0.0006	0.0018	0.0005	0.0018	0.0003	0.0018
R(6)	−0.0007	0.0003	−0.0008	0.0003	−0.0003	0.0004	−0.0001	0.0004
R(7)	−0.0023	−0.001	−0.0025	−0.0008	−0.0019	−0.0008	−0.0017	−0.0007
R(8)	−0.0016	−0.002	−0.0029	−0.0018	−0.0022	−0.0017	−0.0018	−0.0016
R(9)	−0.0034	−0.0028	−0.004	−0.0026	−0.003	−0.0025	−0.003	−0.0024
R(10)	−0.0048	−0.0035	−0.005	−0.0033	−0.0045	−0.0031	−0.0036	−0.0031
R(11)	−0.0049	−0.0041	−0.0055	−0.0039	−0.0041	−0.0037	−0.0041	−0.0036
R(12)	−0.0041	−0.0047	−0.0059	−0.0045	−0.0049	−0.0043	−0.0038	−0.0041
R(13)	−0.0072	−0.0052	−0.0068	−0.005	−0.0068	−0.0048	−0.0058	−0.0046
R(14)	−0.0082	−0.0056	−0.0063	−0.0054	−0.0064	−0.0052	−0.0056	−0.0051
R(15)	−0.0108	−0.006	−0.0065	−0.0058	−0.0069	−0.0056	−0.0072	−0.0055
R(16)	−0.0146	−0.0064	−0.008	−0.0062	−0.0082	−0.006	−0.0079	−0.0059
R(17)	−0.0127	−0.0067	−0.0099	−0.0066	−0.0092	−0.0064	−0.0068	−0.0062
R(18)	−0.0013	−0.007	−0.0118	−0.0069	−0.0097	−0.0067	−0.0061	−0.0066
R(19)	−0.0151	−0.0074	−0.0068	−0.0072	−0.0076	−0.007	−0.0112	−0.0069
R(20)	−0.0017	−0.0077	−0.011	−0.0075	−0.0137	−0.0074	−0.0048	−0.0073
R(21)	−0.0347	−0.008	−0.0076	−0.0078	−0.0103	−0.0077	−0.0162	−0.0076
R(22)	0.0198	−0.0083	−0.0098	−0.0082	0.0044	−0.008	−0.0023	−0.008

Table A.9: CO_2 broadening coefficients for the $2-0$ band of $^{12}C^{16}O$ calculated using EPG calculations

Line	240 K	255 K	270 K	285 K	296 K
P(22)	0.065146	0.062536	0.060092	0.05815	0.056358
P(21)	0.066075	0.063431	0.060955	0.058988	0.057171
P(20)	0.067023	0.064345	0.061837	0.059846	0.058006
P(19)	0.067996	0.065285	0.062746	0.060729	0.058866
P(18)	0.069001	0.066257	0.063687	0.061645	0.059759
P(17)	0.070048	0.067271	0.064669	0.062603	0.060693
P(16)	0.071148	0.068338	0.065704	0.063613	0.061679
P(15)	0.072317	0.069473	0.066806	0.064688	0.06273
P(14)	0.073574	0.070694	0.067992	0.065847	0.063863
P(13)	0.074942	0.072024	0.069285	0.067111	0.065098
P(12)	0.076454	0.073493	0.070713	0.068506	0.066462
P(11)	0.078148	0.075139	0.072313	0.070069	0.067989

P(10)	0.080078	0.077013	0.074132	0.071844	0.069724
P(9)	0.082313	0.079179	0.076233	0.073893	0.071723
P(8)	0.084945	0.081728	0.078699	0.076295	0.074063
P(7)	0.088105	0.084779	0.081647	0.07916	0.076851
P(6)	0.091972	0.088503	0.085235	0.082641	0.080231
P(5)	0.096806	0.093145	0.089696	0.086957	0.084414
P(4)	0.102997	0.099068	0.09537	0.092433	0.089708
P(3)	0.111115	0.106806	0.102758	0.099542	0.096564
P(2)	0.121759	0.116912	0.112372	0.108768	0.105438
P(1)	0.128186	0.123046	0.118233	0.114411	0.110882
R(1)	0.133988	0.128554	0.12347	0.119318	0.11575
R(2)	0.127164	0.122044	0.117251	0.113348	0.10997
R(3)	0.115622	0.11109	0.106835	0.103406	0.10034
R(4)	0.106848	0.102731	0.098859	0.095769	0.09293
R(5)	0.100169	0.096345	0.092745	0.089897	0.08722
R(6)	0.094958	0.091345	0.087943	0.085272	0.08271
R(7)	0.090795	0.087339	0.084084	0.081546	0.07908
R(8)	0.0874	0.084062	0.08092	0.078484	0.07608
R(9)	0.084579	0.081332	0.078278	0.075921	0.07357
R(10)	0.082195	0.07902	0.076036	0.073741	0.07143
R(11)	0.080147	0.077031	0.074103	0.07186	0.06959
R(12)	0.078362	0.075294	0.072414	0.070212	0.06797
R(13)	0.076784	0.073757	0.070918	0.06875	0.06654
R(14)	0.075369	0.072379	0.069575	0.067436	0.06525
R(15)	0.074085	0.071127	0.068354	0.06624	0.06408
R(16)	0.072904	0.069976	0.067232	0.065139	0.063
R(17)	0.071807	0.068907	0.06619	0.064116	0.06201
R(18)	0.070776	0.067903	0.065212	0.063155	0.06107
R(19)	0.069799	0.066952	0.064286	0.062244	0.06019
R(20)	0.068865	0.066043	0.063402	0.061374	0.05934
R(21)	0.067964	0.065168	0.062551	0.060537	0.05853
R(22)	0.067091	0.06432	0.061728	0.059726	0.05775

For $\nu_3 + \nu_4$ band of methane the complete list of tables are as follows: Table A.10 represents the results obtained by theoretical calculations. Next is Table A.11 that includes measured wavenumber in cm^{-1}, intensities in cm^{-1}/(molecule cm^{-2}), CH_4-air- broadened half- width coefficients and CH_4-CH_4- broadened half-width coefficients of methane in $\mathrm{cm}^{-1}\mathrm{atm}^{-1}$ obtained by multispectrum fitting using quadratic SDV profile and their temperature dependences (n_1) and n_2 respectively. Similarly, Table A.12 contains the measured CH_4-CH_4- and CH_4-air-shift coefficients in cm^{-1} and speed dependence parameters (SDV) of methane obtained by multispectrum fitting using quadratic SDV profile and the temperature dependences of CH_4-CH_4- and CH_4-air-shift coefficients. The last table (Table A.13) included as supplemental file presenting the results obtained by Voigt profile.

Table A.10: Sample table for the results obtained by theoretical calculations. $\tilde{\nu}$ is wavenumber in cm^{-1}, I is the intensity in HITRAN units cm^{-1}/(molecule cm^{-2}) at $T = 296$ K, C is vibration-rotation Td symmetry type and n is polyad vibration-rotation ranking number.

$\tilde{\nu}$	Intensity	J lower state	C	n	J upper state	C	n
4300.0493	7.65×10^{-22}	3	F1	1	3	F2	22
4300.3643	1.71×10^{-21}	3	A2	1	2	A1	8
4305.1870	2.29×10^{-22}	2	F2	1	2	F1	16
4305.5436	7.37×10^{-22}	8	A1	1	8	A2	20
4324.9324	1.38×10^{-21}	1	F1	1	1	F2	11
4329.0086	6.79×10^{-22}	2	E	1	2	E	14
4330.1071	1.12×10^{-21}	2	F2	1	2	F1	19
4330.6318	1.04×10^{-22}	3	F2	1	3	F1	28
4330.9139	5.51×10^{-22}	2	E	1	2	E	15
4331.2198	2.67×10^{-22}	2	F2	1	2	F1	20
4332.0532	3.52×10^{-22}	3	F1	1	3	F2	27
4332.6586	5.06×10^{-22}	3	F2	1	3	F1	29
4333.4374	1.32×10^{-21}	3	A2	1	3	A1	9
4333.6686	4.31×10^{-21}	0	A1	1	1	A2	5
4334.6313	3.37×10^{-22}	2	F2	1	3	F1	25
4334.9264	2.66×10^{-22}	3	F2	1	3	F1	30
4335.4241	1.49×10^{-21}	3	F1	1	3	F2	28
4335.8904	2.23×10^{-22}	4	E	1	4	E	25
4336.4926	3.57×10^{-22}	3	F2	1	3	F1	32
4336.9571	2.48×10^{-22}	5	F2	1	5	F1	47
4337.3179	2.03×10^{-22}	5	E	1	5	E	32
4337.4245	6.67×10^{-22}	3	A2	1	3	A1	10
4337.5484	1.14×10^{-21}	1	F1	1	2	F2	19
4339.1143	5.39×10^{-22}	4	F2	1	4	F1	39
4339.3144	4.58×10^{-22}	4	F1	1	4	F2	41
4339.4788	2.81×10^{-21}	4	A1	1	4	A2	12
4346.0979	6.43×10^{-22}	4	F2	1	5	F1	39
4346.3956	1.25×10^{-21}	5	F1	1	5	F2	50
4346.7338	6.42×10^{-22}	2	F2	1	3	F1	26
4347.3360	5.77×10^{-22}	6	A1	1	6	A2	19
4347.7331	1.29×10^{-21}	2	E	1	3	E	17
4348.1653	4.53×10^{-22}	7	A2	1	7	A1	21
4348.9378	2.62×10^{-21}	1	F1	1	2	F2	20
4350.4034	5.40×10^{-22}	6	A1	1	7	A2	17
4354.9975	1.13×10^{-21}	7	F1	1	7	F2	68
4355.8171	1.62×10^{-21}	3	A2	1	4	A1	12
4357.2485	7.86×10^{-22}	3	F2	1	4	F1	32

4357.5058	2.17×10^{-21}	3	F1	1	4	F2	35
4359.3168	1.46×10^{-21}	8	A1	1	8	A2	25
4359.5085	8.02×10^{-22}	8	F1	1	8	F2	81
4359.5764	5.49×10^{-22}	8	E	1	8	E	54
4371.1751	3.60×10^{-23}	7	A2	1	6	A1	26
4381.2134	1.70×10^{-22}	3	F1	1	4	F2	41
4381.5272	1.18×10^{-22}	6	F1	1	7	F2	54
4382.9364	7.19×10^{-22}	6	A2	1	7	A1	17
4384.8238	1.34×10^{-21}	6	A1	1	7	A2	20
4392.6477	1.67×10^{-21}	7	F1	1	8	F2	63
4394.7415	4.03×10^{-21}	4	A1	1	5	A2	17
4396.0255	1.27×10^{-21}	4	A1	1	5	A2	18
4398.2566	3.05×10^{-22}	7	F2	2	8	F1	63
4398.3607	9.94×10^{-22}	7	A2	1	8	A1	22
4400.0102	1.65×10^{-23}	8	E	2	9	E	45
4400.8689	3.32×10^{-22}	8	E	1	9	E	46
4407.5790	6.23×10^{-22}	5	E	1	6	E	38
4410.3159	4.92×10^{-22}	5	F1	1	6	F2	61
4414.5454	3.13×10^{-22}	6	F1	1	7	F2	62
4414.7645	3.40×10^{-22}	9	A2	1	10	A1	29
4427.8176	1.29×10^{-21}	7	F1	2	8	F2	75
4430.4188	9.71×10^{-22}	7	E	1	8	E	50
4430.7593	1.31×10^{-21}	7	F2	2	8	F1	72
4431.2749	1.79×10^{-21}	7	A2	1	8	A1	25
4432.6604	1.06×10^{-21}	7	F1	2	8	F2	76
4433.4198	4.17×10^{-22}	7	E	1	8	E	51
4433.6520	5.70×10^{-22}	7	F2	2	8	F1	73
4436.3926	1.40×10^{-21}	7	F2	1	8	F1	75
4455.7048	1.54×10^{-21}	9	A1	1	10	A2	29
4461.2106	7.30×10^{-22}	8	A1	1	7	A2	32
4461.3509	4.22×10^{-22}	8	F1	1	7	F2	91
4468.4597	6.56×10^{-22}	7	A2	1	6	A1	28
4468.9716	3.12×10^{-22}	7	F2	2	6	F1	78
4469.1655	2.46×10^{-22}	7	E	1	6	E	53
4469.3256	5.30×10^{-22}	7	F1	2	6	F2	80
4489.8954	4.04×10^{-22}	5	E	1	4	E	37
4489.9408	6.33×10^{-22}	5	F1	2	4	F2	56
4491.0758	6.36×10^{-22}	5	F2	1	4	F1	54
4491.1296	5.49×10^{-22}	5	F1	1	4	F2	57

Table A.11: Measured wavenumber ($\tilde{\nu}$) in cm^{-1}, intensities in cm^{-1}/(molecule cm^{-2}), CH$_4$-air-broadened half-width coefficients (air-b) and CH$_4$-CH$_4$-broadened half-width coefficients (self-b) of methane in cm^{-1}atm^{-1} obtained by multispectrum fitting using quadratic SDV profile and their temperature dependences (n_1) and n_2 respectively. Note that US shows upper state and LS presents lower state.

LS	US	$\tilde{\nu}$	Intensity	air-b	self-b	n_1	n_2
3F1 1	3F2 22	4300.052054	$7.4380(2)\times10^{-22}$	0.0651(2)	0.0821(1)	0.899(3)	0.813(2)
3A2 1	2A1 8	4300.367139	$1.6858(5)\times10^{-21}$	0.0670(1)	0.0844(1)	0.883(2)	0.815(2)
1F1 1	1F2 11	4324.935011	$1.3462(3)\times10^{-21}$	0.0617(1)	0.08072(4)	0.867(3)	0.783(1)
2E 1	2E 14	4329.010901	$6.3530(2)\times10^{-22}$	0.0648(1)	0.0824(1)	0.875(2)	0.810(2)
2F2 1	2F1 19	4330.110245	$1.0892(2)\times10^{-21}$	0.0639(1)	0.0811(1)	0.879(4)	0.801(1)
2F2 1	2F1 19	4330.110259	$1.0858(4)\times10^{-21}$	0.0634(1)	0.0815(1)	0.890(4)	0.791(2)
2E 1	2E 15	4330.916544	$5.368(2)\times10^{-22}$	0.0666(2)	0.0839(1)	0.910(1)	0.830(2)
3F2 1	3F1 29	4332.661710	$4.7620(1)\times10^{-22}$	0.0663(3)	0.0833(1)	0.860(1)	0.850(3)
3A2 1	3A1 9	4333.441604	$1.2507(5)\times10^{-21}$	0.0660(1)	0.0845(1)	0.885(3)	0.807(3)
0A1 1	1A2 5	4333.670822	$4.2194(10)\times10^{-21}$	0.0605(1)	0.0804(1)	0.802(5)	0.765(2)
2F2 1	3F1 25	4334.633837	$3.2500(1)\times10^{-22}$	0.0642(3)	0.0817(1)	0.860(1)	0.819(2)
3F2 1	3F1 30	4334.929742	$2.5210(1)\times10^{-22}$	0.0646(4)	0.0811(1)	0.880(1)	0.853(3)
3F1 1	3F2 28	4335.426543	$1.4540(3)\times10^{-21}$	0.0657(1)	0.0828(1)	0.897(3)	0.811(2)
4E 1	4E 25	4335.89168	$2.2840(1)\times10^{-22}$	0.0596(4)	0.0772(1)	0.830(1)	0.842(3)
3F2 1	3F1 32	4336.496244	$3.5400(2)\times10^{-22}$	0.0645(3)	0.0825(1)	0.910(1)	0.852(3)
3A2 1	3A1 10	4337.425156	$7.1490(2)\times10^{-22}$	0.0646(2)	0.0829(1)	0.866(3)	0.831(3)
1F1 1	2F2 19	4337.550831	$1.1089(4)\times10^{-21}$	0.0626(1)	0.0817(1)	0.866(2)	0.766(2)
4F2 1	4F1 39	4339.115494	$5.3850(2)\times10^{-22}$	0.0646(2)	0.0821(1)	0.860(1)	0.829(2)
4F1 1	4F2 41	4339.314783	$4.5840(2)\times10^{-22}$	0.0665(2)	0.0840(1)	0.880(1)	0.841(3)
4A1 1	4A2 12	4339.480862	$2.7354(8)\times10^{-21}$	0.0662(1)	0.0823(1)	0.889(2)	0.811(3)
4F2 1	5F1 39	4346.100102	$6.2730(3)\times10^{-22}$	0.0671(2)	0.0844(1)	0.870(1)	0.825(3)
5F1 1	5F2 50	4346.398219	$1.2700(3)\times10^{-21}$	0.0632(2)	0.0809(1)	0.859(3)	0.812(3)
2F2 1	3F1 26	4346.735927	$6.2210(3)\times10^{-22}$	0.0643(2)	0.0824(1)	0.890(1)	0.800(3)
2E 1	3E 17	4347.735476	$1.2565(5)\times10^{-21}$	0.0670(1)	0.0841(1)	0.899(4)	0.805(2)
1F1 1	2F2 20	4348.939398	$2.5536(7)\times10^{-21}$	0.0632(1)	0.0820(1)	0.876(3)	0.769(2)
6A1 1	7A2 17	4350.405466	$5.4020(2)\times10^{-22}$	0.0640(3)	0.0820(2)	0.840(1)	0.826(3)
7F1 1	7F2 68	4354.999355	$1.1464(3)\times10^{-21}$	0.0579(2)	0.0760(1)	0.780(1)	0.830(3)
3A2 1	4A1 12	4355.819081	$1.5861(6)\times10^{-21}$	0.068(1)	0.0849(2)	0.875(4)	0.806(3)
3F2 1	4F1 32	4357.251065	$7.6840(3)\times10^{-22}$	0.0664(3)	0.0839(2)	0.890(1)	0.789(3)
3F1 1	4F2 35	4357.50802	$2.1125(10)\times10^{-21}$	0.0664(1)	0.0817(1)	0.872(4)	0.804(3)
8A1 1	8A2 25	4359.318389	$1.4905(6)\times10^{-21}$	0.0543(2)	0.0734(1)	0.750(1)	0.804(3)
8E 1	8E 54	4359.578023	$5.5860(4)\times10^{-22}$	0.0554(4)	0.0744(2)	0.770(2)	0.797(4)
3A2 1	4A1 13	4371.178597	$6.474(3)\times10^{-22}$	0.0570(2)	0.0754(1)	0.850(1)	0.789(3)
3F1 1	4F2 41	4381.213706	$1.6590(1)\times10^{-22}$		0.0832(2)	0.880(2)	0.861(4)
6A2 1	7A1 17	4382.938826	$7.0560(3)\times10^{-22}$	0.0638(3)	0.0823(1)	0.840(1)	0.839(3)
6A1 1	7A2 20	4384.826943	$1.3219(5)\times10^{-21}$	0.0644(2)	0.0809(1)	0.854(5)	0.809(3)
4A1 1	5A2 18	4396.027323	$1.2532(3)\times10^{-21}$	0.0669(1)	0.0842(1)	0.876(3)	0.818(2)

7F2 1	8F1 63	4398.260444	$2.9470(3) \times 10^{-22}$	0.0613(5)	0.0788(2)	0.810(2)	0.815(3)
7A2 1	8A1 22	4398.364425	$9.6950(4) \times 10^{-22}$	0.0608(2)	0.0788(1)	0.820(1)	0.829(2)
8E 1	9E 45	4400.098489	$5.1180(4) \times 10^{-22}$	0.0597(5)	0.0797(2)	0.790(2)	0.805(3)
5E 1	6E 38	4407.581652	$6.2400(3) \times 10^{-22}$	0.0624(3)	0.0801(2)	0.840(1)	0.839(3)
6F1 1	7F2 62	4414.546128	$3.1170(2) \times 10^{-22}$	0.0609(4)	0.0787(1)	0.850(1)	0.825(3)
7F1 1	8F2 75	4427.818202	$1.2829(7) \times 10^{-21}$	0.0628(2)	0.0777(1)	0.840(1)	0.845(3)
7E 1	8E 50	4430.420020	$9.7180(5) \times 10^{-22}$	0.0559(2)	0.0721(1)	0.780(1)	0.828(3)
7F2 1	8F1 72	4430.760762	$1.3180(4) \times 10^{-21}$	0.0620(2)	0.0788(1)	0.820(1)	0.835(3)
7A2 1	8A1 25	4431.276913	$1.7962(7) \times 10^{-21}$	0.0588(1)	0.0769(1)	0.781(4)	0.809(3)
7F1 1	8F2 76	4432.662519	$1.0549(4) \times 10^{-21}$	0.0601(2)	0.0763(1)	0.820(1)	0.843(3)
7E 1	8E 51	4433.421696	$4.1700(4) \times 10^{-22}$	0.0509(3)	0.0676(2)	0.740(1)	0.789(4)
9A1 1	10A2 29	4455.706253	$1.5524(3) \times 10^{-21}$	0.0577(2)	0.0748(1)	0.780(1)	0.837(3)
8A1 1	7A2 32	4461.212937	$7.3380(4) \times 10^{-22}$	0.0535(3)	0.0726(1)	0.750(1)	0.837(3)
8F1 1	7F2 91	4461.353302	$4.2350(4) \times 10^{-22}$	0.0573(5)	0.0758(2)	0.770(2)	0.829(4)
7A2 1	6A1 28	4468.461306	$6.5880(4) \times 10^{-22}$	0.0582(3)	0.0774(1)	0.750(1)	0.819(3)
7F1 1	6F2 80	4469.326872	$5.3470(3) \times 10^{-22}$	0.0605(3)	0.0782(2)	0.830(1)	0.843(3)
5E 1	4E 37	4489.897238	$4.0380(2) \times 10^{-22}$	0.0565(2)	0.0757(1)	0.830(1)	0.809(3)
5F1 1	4F2 56	4489.942558	$6.3340(3) \times 10^{-22}$	0.0629(2)	0.0819(1)	0.850(1)	0.821(2)
5E 1	4E 37	4489.897217	$4.0330(2) \times 10^{-22}$	0.0564(3)	0.0756(1)	0.830(1)	0.805(3)
5F1 1	4F2 56	4489.942539	$6.3370(3) \times 10^{-22}$	0.0633(2)	0.0814(1)	0.840(1)	0.835(3)
5F2 1	4F1 54	4491.078175	$6.3650(2) \times 10^{-22}$	0.0646(2)	0.0831(1)	0.870(1)	0.809(3)
5F1 1	4F2 57	4491.132043	$5.4320(4) \times 10^{-22}$	0.0641(2)	0.0823(1)	0.830(1)	0.775(3)

Table A.12: Measured CH$_4$-air-shift coefficients, CH$_4$-CH$_4$- shift coefficients in cm^{-1} and speed dependence parameters (SD) of methane obtained by multispectrum fitting using quadratic SDV profile and the temperature dependences of CH$_4$-air-shift coefficients (T.d.a.s) and CH$_4$-CH$_4$-shift coefficients (T.d.s.s). Both T.d.a.s and T.d.s.s are multiplied by factor of 10^5 in this table. Note that US shows upper state and LS presents lower state.

LS	US	CH$_4$-air-shift	CH$_4$-CH$_4$-shift	T.d.a.s	T.d.s.s	SD
3F1 1	3F2 22	−0.0079(2)	−0.0107(1)	4.132(2)	9.552(9)	0.044(2)
3A2 1	2A1 8	−0.0071(2)	−0.0091(1)	1.876(1)	7.638(10)	0.064(2)
3F1 1	3F2 23	−0.0075(2)	−0.0110(2)	4.038(2)	8.859(13)	0.069(2)
3F2 1	3F1 25	−0.0069(2)	−0.0091(2)	3.903(2)	9.720(15)	0.070(3)
1F1 1	1F2 11	−0.0070(1)	−0.0096(1)	3.820(1)	8.396(6)	0.069(1)
2E 1	2E 14	−0.0070(2)	−0.0087(1)	3.459(2)	8.885(7)	0.076(2)
2F2 1	2F1 19	−0.0067(1)	−0.0092(1)	2.852(1)	7.293(6)	0.081(1)
2F2 1	2F1 19	−0.0066(2)	−0.0098(1)	2.545(2)	6.700(9)	0.071(2)
3F1 1	3F2 27	−0.0071(3)	−0.0106(1)	4.021(3)	7.951(12)	0.066(3)
3F2 1	3F1 29	−0.0073(2)	−0.0097(1)	1.947(2)	6.987(11)	0.075(2)
3A2 1	3A1 9	−0.0051(2)	−0.0070(1)	-0.571(2)	2.922(12)	0.066(2)
0A1 1	1A2 5	−0.0065(1)	−0.0109(1)	3.420(1)	9.122(15)	0.107(2)

3F2 1	3F1 30	−0.0071(3)	−0.0094(1)	1.229(2)	6.369(12)	0.045(3)
3F1 1	3F2 28	−0.0068(1)	−0.0096(1)	2.869(1)	6.027(12)	0.063(2)
3A2 1	3A1 10	−0.0066(2)	−0.0095(1)	1.540(2)	6.017(10)	0.070(2)
1F1 1	2F2 19	−0.0065(1)	−0.0092(1)	2.768(1)	7.245(11)	0.083(2)
4F2 1	4F1 39	−0.0066(2)	−0.0081(1)	0.508(2)	6.610(10)	0.076(2)
4F1 1	4F2 41	−0.0079(2)	−0.0101(1)	6.016(2)	10.432(14)	0.070(2)
4A1 1	4A2 12	−0.0070(1)	−0.0082(1)	3.676(1)	8.719(18)	0.067(2)
2F2 1	3F1 26	−0.0072(3)	−0.0095(1)	0.826(3)	6.292(13)	0.063(3)
2F2 1	3F1 27	−0.0066(3)	−0.0085(2)	1.171(3)	6.986(20)	0.061(3)
2E 1	3E 17	−0.0067(2)	−0.0092(1)	1.737(2)	6.082(10)	0.062(2)
1F1 1	2F2 20	−0.0063(1)	−0.0084(1)	1.440(1)	7.616(11)	0.073(2)
7A2 1	7A1 22	−0.0059(2)	−0.0088(1)	1.808(3)	5.661(15)	0.076(3)
6A2 1	7A1 16	−0.0078(3)	−0.0122(3)	5.287(3)	9.606(27)	0.086(5)
6A1 1	7A2 17	−0.0044(3)	−0.0064(2)	0.306(3)	2.802(14)	0.074(3)
6A2 1	6A1 22	−0.0056(1)	−0.0080(1)	1.914(1)	6.174(13)	0.089(2)
7F1 1	7F2 68	−0.0080(2)	−0.0114(1)	4.535(2)	7.476(12)	0.091(2)
3A2 1	4A1 12	−0.0045(2)	−0.0078(2)	-1.600(2)	3.381(16)	0.079(2)
3F2 1	4F1 32	−0.0063(3)	−0.0100(2)	1.650(2)	4.674(17)	0.061(3)
3F1 1	4F2 35	−0.0066(2)	−0.0084(1)	2.137(2)	6.414(14)	0.071(3)
8A1 1	8A2 25	−0.0083(2)	−0.0114(1)	5.911(2)	9.398(10)	0.090(2)
8F1 1	8F2 81	−0.0073(3)	−0.0107(1)	4.209(4)	7.933(13)	0.086(3)
2E 1	3E 18	−0.0061(3)	−0.0092(1)	2.896(2)	6.852(13)	0.083(3)
4A1 1	5A2 14	−0.0068(1)	−0.0088(2)	3.728(1)	6.454(24)	0.061(3)
2F2 1	3F1 32	−0.0062(2)	−0.0088(2)	0.835(2)	4.967(22)	0.071(3)
3F2 1	4F1 38	−0.0060(1)	−0.0082(1)	1.362(1)	5.364(17)	0.083(2)
3A2 1	4A1 15	−0.0056(1)	−0.0074(1)	-0.8070(1)	5.522(15)	0.090(2)
3F1 1	4F2 40	−0.0068(1)	−0.0088(1)	2.316(1)	8.513(13)	0.075(2)
6A1 1	7A2 20	−0.0051(2)	−0.0083(1)	-0.5970(2)	4.021(9)	0.088(2)
4F2 1	5F1 48	−0.0050(1)	−0.0082(1)	-0.7340(1)	2.906(13)	0.087(2)
7F1 1	8F2 63	−0.0075(2)	−0.0113(1)	5.064(2)	6.957(13)	0.090(3)
4E 1	5E 33	−0.0067(1)	−0.0101(2)	4.94(1)	6.289(22)	0.100(3)
4F1 1	5F2 46	−0.0070(1)	−0.0096(1)	3.865(1)	8.691(14)	0.069(2)
4A1 1	5A2 17	−0.0064(1)	−0.0093(1)	3.499(1)	5.275(14)	0.059(2)
4A1 1	5A2 18	−0.0084(2)	−0.0115(1)	5.032(2)	8.497(9)	0.067(2)
7A2 1	8A1 22	−0.0072(2)	−0.0103(1)	4.953(2)	7.458(9)	0.109(2)
8F1 1	9F2 68	−0.0083(3)	−0.0118(1)	4.426(4)	8.832(13)	0.085(3)
8A1 1	9A2 24	−0.0088(2)	−0.0129(2)	7.184(2)	10.006(17)	0.070(3)
5F1 1	6F2 57	−0.0047(2)	−0.0077(1)	-0.0920(2)	4.221(12)	0.087(3)
5E 1	6E 36	−0.0047(2)	−0.0070(1)	-0.713(2)	4.237(15)	0.096(3)
5F1 1	6F2 58	−0.0051(2)	−0.0043(1)	0.101(2)	4.747(12)	0.041(3)
5F2 1	6F1 56	−0.0076(1)	−0.0094(2)	4.562(1)	9.104(20)	0.101(2)
5F1 1	6F2 59	−0.0067(2)	−0.0093(1)	3.565(2)	6.498(12)	0.079(3)
6A1 1	7A2 23	−0.0038(1)	−0.0075(1)	-1.443(1)	2.922(10)	0.088(2)

6F1 1	7F2 64	−0.0043(2)	−0.0073(1)	-0.330(2)	2.465(11)	0.102(2)
6F2 1	7F1 66	−0.0051(2)	−0.0086(1)	1.341(2)	4.991(11)	0.091(2)
6A2 1	7A1 21	−0.0086(1)	−0.0114(2)	5.990(1)	11.715(19)	0.114(2)
6F2 1	7F1 68	−0.0066(2)	−0.0098(3)	3.967(2)	6.006(28)	0.083(3)
7E 1	8E 50	−0.0047(3)	−0.0079(1)	-0.679(3)	3.657(13)	0.093(2)
7F2 1	8F1 72	−0.0052(2)	−0.0082(1)	1.238(2)	4.294(12)	0.081(2)
7A2 1	8A1 25	−0.0062(2)	−0.0091(1)	2.334(2)	5.789(13)	0.096(2)
7F1 1	8F2 76	−0.0063(3)	−0.0094(1)	1.152(3)	4.787(13)	0.077(3)
7F1 1	8F2 78	−0.0072(3)	−0.0093(2)	5.202(3)	8.434(17)	0.103(3)
9A1 1	10A2 29	−0.0056(2)	−0.0072(1)	1.345(2)	6.097(10)	0.085(2)
9A2 1	10A1 33	−0.0058(2)	−0.0080(2)	3.328(2)	9.413(17)	0.074(3)
6A2 1	5A1 22	−0.0082(3)	−0.0124(2)	4.082(3)	8.518(20)	0.076(2)

Table A.13: Measured wavenumber ($\tilde{\nu}$) in cm^{-1}, intensities in cm^{-1}/(molecule cm^{-2}), CH_4-air- broadened half-width coefficients (air-b) and CH_4-CH_4- broadened half-width coefficients (self-b) of methane in $\text{cm}^{-1}\text{atm}^{-1}$ obtained by multispectrum fitting using Voigt profile and their temperature dependences (n_1) and n_2 respectively, CH_4-CH_4- and CH_4-air-shift coefficients and their temperature dependences (T.d.a.s and T.d.s.s).

LS	US	$\tilde{\nu}$	Intensity	air-b	self-b	n_1	n_2	air-s	self-s	T.d.a.s	T.ds.s.
3F1 1	3F2 22	4300.052055(4)	$7.4450(2) \times 10^{-22}$	0.0653(2)	0.0824(1)	0.899(4)	0.809(2)	−0.0079(2)	−0.0107(1)		9.557(9)
3F2 1	4F1 31	4356.029257(5)	$7.4980(5) \times 10^{-22}$	0.0666(2)	0.0835(2)	0.877(6)	0.832(5)	−0.0061(3)	−0.0095(2)	4.0750(3)	4.586(21)
7F2 2	7F1 57	4313.621103(9)	$7.507(6) \times 10^{-22}$	0.0615(4)	0.0812(2)	0.875(13)	0.803(7)	−0.0065(6)	−0.0067(2)	0.588(6)	14.01(31)
3F2 1	4F1 32	4357.251089(5)	$7.704(4) \times 10^{-22}$	0.0674(3)	0.0848(1)	0.879(7)	0.807(4)	−0.0069(4)	−0.0092(2)	6.449(4)	7.355(17)
3F1 1	3F2 25	4315.396042(6)	$7.7820(5) \times 10^{-22}$	0.0646(3)	0.0823(3)	0.889(7)	0.816(11)	−0.009(4)	−0.0124(3)	1.737(3)	9.301(41)
1F1 1	0F2 5	4308.730000(6)	$7.870(6) \times 10^{-22}$	0.0594(2)	0.0812(1)	0.814(5)	0.779(3)	−0.0085(3)	−0.0127(1)	5.026(3)	9.208(14)
2F2 1	3F1 27	4347.476020(4)	$7.9380(4) \times 10^{-22}$	0.0644(2)	0.0826(2)	0.892(6)	0.792(5)	−0.0067(3)	−0.0085(2)	6.196(3)	6.997(20)
6F2 2	6F1 58	4346.460646(6)	$8.0600(5) \times 10^{-22}$	0.063(3)	0.0816(2)	0.853(10)	0.797(6)	−0.0051(5)	−0.007(2)	1.106(5)	4.995(26)
7A2 1	8A1 23	4400.527496(9)	$8.1300(7) \times 10^{-22}$	0.0571(3)	0.0748(2)	0.819(11)	0.830(7)	−0.0072(4)	−0.0078(3)	0.774(5)	9.297(27)
9F2 1	10F1 95	4463.651062(8)	$8.1720(5) \times 10^{-22}$	0.0498(3)	0.0683(1)	0.695(13)	0.821(4)	−0.0077(4)	−0.0107(2)	4.654(5)	7.619(19)
8F1 1	8F2 81	4359.509977(8)	$8.2620(6) \times 10^{-22}$	0.0543(3)	0.0741(1)	0.752(11)	0.792(4)	−0.0073(4)	−0.0105(1)	3.929(4)	8.058(14)
9F2 1	10F1 75	4407.942762(13)	$8.5480(13) \times 10^{-22}$	0.0515(3)	0.0728(3)	0.798(17)	0.75(12)	−0.0065(5)	−0.0105(3)	4.213(6)	8.305(41)
9A1 1	9A2 26	4313.189654(22)	$8.6110(28) \times 10^{-22}$	0.0587(9)	0.0813(6)	0.786(38)	0.607(23)	−0.0083(10)	−0.0059(7)	4.365(12)	9.493(80)
5F1 1	5F2 38	4311.842668(6)	$8.6450(3) \times 10^{-22}$	0.0665(2)	0.0852(1)	0.909(7)	0.846(3)	−0.0084(4)	−0.0111(1)	1.592(4)	11.208(13)
8F2 2	9F1 83	4439.653032(11)	$8.8100(11) \times 10^{-22}$	0.0615(3)	0.0784(1)	0.833(13)	0.817(3)	−0.0042(5)	−0.0064(1)	7.700(5)	4.402(12)
10A2 1	11A1 26	4415.083816(18)	$8.8980(8) \times 10^{-22}$	0.0494(2)	0.0688(1)	0.730(14)	0.794(3)	−0.0078(3)	−0.012(1)	-0.036(4)	8.496(12)
9F1 1	10F2 76	4408.061597(9)	$8.9830(6) \times 10^{-22}$	0.049(3)	0.0688(2)	0.715(15)	0.786(5)	−0.0082(4)	−0.0112(2)	4.105(5)	8.797(17)
6F1 1	6F2 49	4313.563334(6)	$9.0550(3) \times 10^{-22}$	0.0624(3)	0.0809(2)	0.859(8)	0.789(5)	−0.0064(3)	−0.0095(2)	5.175(2)	6.267(20)
10A2 1	11A1 34	4476.934823(11)	$9.2480(11) \times 10^{-22}$	0.0498(4)	0.0693(2)	0.623(21)	0.768(6)	−0.0053(5)	−0.0083(3)	1.755(7)	12.819(28)
5F2 1	5F1 52	4347.199251(10)	$9.4050(25) \times 10^{-22}$	0.0658(8)	0.0804(3)	0.846(18)	0.839(8)	−0.0074(12)	−0.0103(3)	6.922(10)	5.980(39)
7A2 1	8A1 27	4437.234202(8)	$9.4940(4) \times 10^{-22}$	0.0604(3)	0.0800(1)	0.786(9)	0.803(3)	−0.0059(4)	−0.0090(1)	0.395(4)	3.998(11)
7A2 1	8A1 22	4398.364425(5)	$9.6930(4) \times 10^{-22}$	0.0608(2)	0.0787(1)	0.815(6)	0.829(2)	−0.0072(2)	−0.0103(1)	2.372(2)	7.437(9)
6F1 1	6F2 50	4316.988367(9)	$9.7040(11) \times 10^{-22}$	0.0579(6)	0.0752(4)	0.967(14)	0.889(8)	−0.0076(9)	−0.0136(5)	4.931(7)	4.561(31)
7E 1	8E 50	4430.420020(6)	$9.7190(4) \times 10^{-22}$	0.0559(2)	0.0721(1)	0.784(7)	0.828(3)	−0.0047(3)	−0.0079(1)	1.221(3)	3.658(13)
2E 1	3E 18	4362.530751(5)	$9.7540(4) \times 10^{-22}$	0.0600(2)	0.0776(1)	0.869(5)	0.783(3)	−0.0061(2)	−0.009(1)	-0.678(2)	6.985(11)
6E 1	6E 40	4350.534312(7)	$9.8440(9) \times 10^{-22}$	0.0614(3)	0.0807(2)	0.831(10)	0.810(6)	−0.0067(5)	−0.0088(2)	2.952(5)	8.474(27)
6E 1	6E 40	4350.534286(8)	$9.8980(11) \times 10^{-22}$	0.0623(4)	0.0820(2)	0.819(12)	0.816(6)	−0.0065(6)	−0.0088(3)	5.800(6)	9.134(32)
6A2 1	5A1 22	4481.082045(5)	$9.9850(5) \times 10^{-22}$	0.0604(2)	0.0787(1)	0.849(6)	0.817(4)	−0.0083(3)	−0.0125(2)	5.771(3)	8.462(20)
1F1 1	1F2 10	4316.355610(5)	$1.0439(6) \times 10^{-21}$	0.0598(2)	0.0808(3)	0.856(5)	0.742(9)	−0.0077(2)	−0.0111(3)	4.073(2)	10.043(32)
9A2 1	10A1 33	4456.318802(11)	$1.0468(4) \times 10^{-21}$	0.0574(2)	0.0744(1)	0.822(10)	0.874(4)	−0.0059(2)	−0.0076(2)	5.656(2)	9.843(17)
7F1 2	8F2 76	4432.662520(6)	$1.0550(4) \times 10^{-21}$	0.0601(2)	0.0763(1)	0.818(7)	0.843(3)	−0.0063(3)	−0.0094(1)	3.339(3)	4.778(13)
7F2 1	7F1 71	4355.243097(11)	$1.0586(22) \times 10^{-21}$	0.0583(4)	0.0764(2)	0.792(13)	0.828(5)	−0.0066(5)	−0.0093(2)	1.153(6)	6.579(26)
5F2 1	5F1 42	4314.477578(9)	$1.0620(7) \times 10^{-21}$	0.0623(5)	0.0813(7)	0.863(13)	0.872(17)	−0.0113(4)	−0.0165(8)	3.374(4)	8.784(86)
8F1 1	9F2 68	4400.408491(7)	$1.0670(5) \times 10^{-21}$	0.0566(2)	0.0752(1)	0.779(10)	0.813(4)	−0.0083(3)	−0.0117(1)	5.508(4)	8.916(13)
5F1 2	5F2 41	4317.328032(5)	$1.0793(6) \times 10^{-21}$	0.0639(3)	0.0826(2)	0.854(8)	0.744(5)	−0.0077(4)	−0.0093(2)	4.375(4)	7.579(21)
2F2 1	2F1 19	4330.110261(4)	$1.0857(4) \times 10^{-21}$	0.0634(1)	0.0815(1)	0.886(4)	0.790(2)	−0.0065(2)	−0.0099(1)	1.876(2)	6.652(10)
6A1 1	5A2 24	4479.597141(5)	$1.0867(9) \times 10^{-21}$	0.0596(1)	0.0770(1)	0.802(5)	0.833(3)	−0.0074(2)	−0.0101(1)	2.596(2)	9.779(12)
1F1 1	2F2 19	4337.550830(3)	$1.1093(3) \times 10^{-21}$	0.0625(1)	0.0817(1)	0.869(2)	0.763(2)	−0.0066(1)	−0.0096(1)	4.149(1)	6.909(9)
6E 1	7E 45	4422.715710(7)	$1.1213(8) \times 10^{-21}$	0.0578(2)	0.0758(3)	0.809(8)	0.831(8)	−0.0061(3)	−0.0106(3)	2.781(3)	6.536(33)
5F1 2	5F2 40	4314.464392(8)	$1.1319(7) \times 10^{-21}$	0.0665(6)	0.085(5)	0.788(12)	0.729(14)	−0.0019(4)		5.067(4)	9.873(76)
4F2 1	5F1 49	4393.917167(5)	$1.1377(5) \times 10^{-21}$	0.0634(2)	0.0801(2)	0.854(5)	0.893(6)	−0.005(2)	−0.0064(2)	1.360(2)	6.853(23)
7F1 1	7F2 68	4354.999361(5)	$1.1475(4) \times 10^{-21}$	0.0579(2)	0.0760(1)	0.777(6)	0.835(3)	−0.008(2)	−0.0119(1)	0.210(2)	7.022(10)
8F1 2	9F2 81	4443.327738(14)	$1.1598(26) \times 10^{-21}$	0.0603(5)	0.0765(3)	0.795(18)	0.866(7)	−0.0066(7)	−0.0076(4)	4.496(8)	4.731(39)

7F2 1	8F1 61	4392.745620(6)	$1.1631(5) \times 10^{-21}$	0.058(2)	0.0765(1)	0.802(7)	0.803(4)	−0.0067(3)	−0.0099(1)	-2.217(3)	7.255(14)
5F1 2	6F2 58	4407.266352(5)	$1.1964(5) \times 10^{-21}$	0.0634(2)	0.0765(1)	0.829(5)	0.818(3)	−0.005(3)	−0.0043(1)	3.863(2)	4.725(12)
6F2 2	6F1 48	4313.926137(6)	$1.2152(4) \times 10^{-21}$	0.0643(3)	0.0809(2)	0.851(9)	0.832(5)	−0.0075(3)	−0.0082(2)	0.116(3)	11.257(26)
3A2 1	3A1 9	4333.441604(4)	$1.2506(4) \times 10^{-21}$	0.066(1)	0.0845(1)	0.879(4)	0.807(3)	−0.0051(2)	−0.0070(1)	5.334(2)	2.922(12)
4A1 1	5A2 18	4396.027323(3)	$1.2532(3) \times 10^{-21}$	0.0669(1)	0.0842(1)	0.876(3)	0.818(2)	−0.0084(2)	−0.0115(1)	-0.567(2)	8.493(9)
2E 1	3E 17	4347.735477(3)	$1.2568(4) \times 10^{-21}$	0.067(1)	0.0841(1)	0.900(3)	0.803(3)	−0.0068(2)	−0.0092(1)	5.032(2)	6.064(11)
7A2 1	7A1 22	4349.823509(5)	$1.2606(6) \times 10^{-21}$	0.0588(2)	0.0784(1)	0.796(6)	0.782(4)	−0.0059(2)	−0.0086(1)	1.691(3)	5.724(15)
5F1 1	5F2 50	4346.398223(5)	$1.2700(7) \times 10^{-21}$	0.0632(1)	0.0809(1)	0.860(4)	0.811(3)	−0.0073(2)	−0.0099(1)	1.630(2)	6.926(14)
9A2 1	9A1 25	4316.315708(9)	$1.2712(11) \times 10^{-21}$	0.0605(3)	0.0793(4)	0.851(15)	0.752(16)	−0.0046(4)	−0.0075(4)	3.160(6)	6.786(50)
6F2 1	6F1 59	4350.721197(6)	$1.2720(10) \times 10^{-21}$	0.0612(2)	0.0797(2)	0.848(8)	0.820(7)	−0.0053(4)	−0.0086(3)	1.592(4)	7.429(40)
7F1 2	8F2 75	4427.818200(8)	$1.2807(6) \times 10^{-21}$	0.0623(2)	0.0774(1)	0.840(7)	0.844(3)	−0.0047(4)	−0.0079(2)	3.339(4)	3.310(18)
7F2 2	8F1 72	4430.760762(5)	$1.3181(4) \times 10^{-21}$	0.0621(2)	0.0788(1)	0.821(5)	0.836(3)	−0.0052(2)	−0.0082(1)	-0.547(2)	4.303(12)
6A1 1	7A2 20	4384.826942(4)	$1.3198(4) \times 10^{-21}$	0.064(1)	0.0806(1)	0.855(5)	0.809(3)	−0.0051(2)	−0.0083(1)	1.241(2)	4.059(9)
6E 1	7E 36	4384.339394(5)	$1.3411(8) \times 10^{-21}$	0.0583(2)	0.0773(3)	0.832(6)	0.784(10)	−0.0073(2)	−0.0101(3)	-0.582(2)	7.296(33)
7F1 2	7F2 56	4315.952843(21)	$1.3557(140) \times 10^{-21}$	0.0628(3)	0.0815(4)	0.873(9)	0.759(13)	−0.0053(3)	−0.0088(4)	4.229(4)	5.030(54)
5E 1	6E 36	4404.606131(5)	$1.3878(6) \times 10^{-21}$	0.0608(2)	0.0785(1)	0.852(5)	0.806(4)	−0.0046(3)	−0.0070(1)	-0.113(3)	4.166(16)
7F2 1	8F1 75	4436.393732(7)	$1.4046(7) \times 10^{-21}$	0.0564(2)	0.0755(2)	0.793(7)	0.820(5)	−0.0069(3)	−0.0091(2)	-0.459(3)	7.414(17)
5E 1	5E 28	4314.700239(6)	$1.4255(10) \times 10^{-21}$	0.0576(2)	0.0746(3)	0.837(7)	0.839(7)	−0.0073(3)	−0.0109(3)	3.503(3)	7.544(29)
7F1 1	8F2 78	4436.457066(7)	$1.4412(7) \times 10^{-21}$	0.0544(2)	0.0734(2)	0.778(7)	0.814(5)	−0.0072(3)	−0.0093(2)	2.882(3)	8.514(17)
3F1 1	3F2 28	4335.42654(3)	$1.4533(4) \times 10^{-21}$	0.0656(1)	0.0830(1)	0.899(3)	0.802(2)	−0.0069(2)	−0.0098(1)	5.200(2)	5.614(11)
8A1 1	8A2 25	4359.318391(6)	$1.4898(5) \times 10^{-21}$	0.0543(2)	0.0733(1)	0.753(7)	0.806(3)	−0.0083(2)	−0.0112(1)	2.688(2)	9.549(11)
9A1 1	10A2 29	4455.706253(5)	$1.5528(3) \times 10^{-21}$	0.0578(2)	0.0747(1)	0.779(7)	0.837(3)	−0.0055(2)	−0.0073(1)	5.846(2)	6.104(10)
4A1 1	4A2 11	4313.180747(6)	$1.5633(13) \times 10^{-21}$	0.0677(3)	0.0843(3)	0.927(7)	0.858(5)	−0.0112(5)	−0.0169(3)	1.544(4)	6.215(27)
7A2 1	7A1 18	4311.142327(7)	$1.5638(10) \times 10^{-21}$	0.0599(2)	0.0795(2)	0.835(6)	0.779(5)	−0.0041(3)	−0.0063(2)	6.071(3)	6.707(18)
3A2 1	4A1 12	4355.819082(4)	$1.5876(8) \times 10^{-21}$	0.0678(1)	0.0846(1)	0.888(3)	0.808(3)	−0.0051(2)	−0.0083(1)	1.432(2)	2.956(16)
6F1 1	7F2 64	4417.402208(5)	$1.5894(6) \times 10^{-21}$	0.0638(1)	0.0808(1)	0.843(4)	0.816(3)	−0.0043(2)	−0.0072(1)	-1.820(2)	2.462(11)
6F2 1	7F1 68	4422.679077(6)	$1.6349(9) \times 10^{-21}$	0.058(2)	0.0755(2)	0.817(6)	0.840(7)	−0.0066(2)	−0.0098(3)	-0.339(2)	5.912(30)
7F1 1	8F2 63	4392.649489(5)	$1.6475(6) \times 10^{-21}$	0.0557(1)	0.0747(1)	0.781(5)	0.795(4)	−0.0075(2)	−0.0113(1)	4.055(2)	6.975(13)
3A2 1	2A1 8	4300.367139(3)	$1.6865(5) \times 10^{-21}$	0.0671(1)	0.0844(1)	0.876(3)	0.815(2)	−0.0072(2)	−0.0091(1)	5.063(1)	7.615(10)
3F2 1	3F1 27	4316.04154(5)	$1.6898(10) \times 10^{-21}$	0.0658(2)	0.0853(4)	0.888(5)	0.783(12)	−0.0065(2)	−0.0098(3)	1.850(2)	7.569(51)
6F2 1	7F1 66	4417.887686(5)	$1.7135(6) \times 10^{-21}$	0.0631(1)	0.0797(1)	0.839(4)	0.825(2)	−0.0051(2)	−0.0085(1)	2.371(2)	4.984(11)
7A2 1	8A1 25	4431.276913(4)	$1.7966(6) \times 10^{-21}$	0.0589(1)	0.0769(1)	0.781(4)	0.809(3)	−0.0062(2)	−0.0092(1)	1.345(2)	5.788(13)
6F2 1	7F1 56	4384.393696(6)	$1.8298(16) \times 10^{-21}$	0.0606(2)	0.0753(4)	0.813(7)	0.877(14)	−0.0072(3)	−0.0104(4)	2.338(3)	6.463(50)
2F2 1	3F1 28	4362.066340(4)	$1.8630(7) \times 10^{-21}$	0.0643(1)	0.0826(2)	0.875(3)	0.775(4)	−0.0063(2)	−0.0097(2)	2.869(2)	5.800(20)
6A2 18	6A1 18	4314.186582(5)	$1.9498(8) \times 10^{-21}$	0.0656(1)	0.0821(2)	0.851(4)	0.852(5)	−0.0093(2)	−0.0127(2)	1.568(2)	10.646(19)
3A2 1	4A1 15	4380.321693(3)	$1.9561(6) \times 10^{-21}$	0.0667(1)	0.0826(1)	0.866(3)	0.853(3)	−0.0056(1)	−0.0074(1)	5.806(1)	5.479(15)
5F1 2	6F2 57	4404.405064(5)	$1.9607(9) \times 10^{-21}$	0.0636(1)	0.0804(1)	0.863(4)	0.813(3)	−0.0048(2)	−0.0077(1)	-0.801(2)	4.201(13)
2F2 1	2F1 18	4316.008955(5)	$2.0010(10) \times 10^{-21}$	0.0639(1)	0.0814(3)	0.886(4)	0.805(11)	−0.0076(2)	−0.0110(4)	-0.2580(2)	6.497(54)
5F1 1	6F2 59	4408.716934(5)	$2.0392(10) \times 10^{-21}$	0.0627(1)	0.0796(1)	0.836(4)	0.817(3)	−0.0067(2)	−0.0093(1)	2.926(2)	6.511(13)
6A2 1	6A1 22	4351.046081(3)	$2.0913(6) \times 10^{-21}$	0.0642(1)	0.0796(1)	0.841(3)	0.833(3)	−0.0056(1)	−0.0080(1)	3.586(1)	5.941(14)
3F1 1	4F2 35	4357.508018(4)	$2.1101(10) \times 10^{-21}$	0.0662(1)	0.0819(1)	0.870(3)	0.789(3)	−0.0065(2)	−0.0083(1)	2.000(2)	6.258(14)
4E 1	5E 33	4393.851488(4)	$2.1583(8) \times 10^{-21}$	0.0571(1)	0.0739(2)	0.827(3)	0.783(5)	−0.0067(1)	−0.0101(2)	2.151(1)	6.319(22)
8A1 1	9A2 24	4400.570957(6)	$2.1597(12) \times 10^{-21}$	0.0510(1)	0.0685(2)	0.746(6)	0.816(5)	−0.0088(2)	−0.0128(2)	4.948(2)	10.114(18)
6A1 1	7A2 24	4420.009234(5)	$2.3435(9) \times 10^{-21}$	0.0600(1)	0.0782(1)	0.854(4)	0.798(3)	−0.0031(1)	−0.0094(2)		1.045(17)
4F2 1	4F1 32	4315.347888(4)	$2.4502(12) \times 10^{-21}$	0.0661(1)	0.0854(3)	0.877(3)	0.746(8)	−0.0055(2)	−0.0086(3)	2.000(2)	4.048(37)
6A2 1	7A1 18	4384.376213(14)	$2.4902(91) \times 10^{-21}$	0.0629(2)	0.0798(4)	0.859(6)	0.801(13)	−0.0048(3)	−0.006(4)	-0.219(3)	6.146(52)
1F1 1	2F2 20	4348.939395(4)	$2.5544(7) \times 10^{-21}$	0.0633(1)	0.0821(1)	0.862(2)	0.767(2)	−0.0064(1)	−0.0083(1)	1.321(1)	7.702(11)
3F1 1	4F2 40	4380.651696(3)	$2.6525(8) \times 10^{-21}$	0.0661(1)	0.082(1)	0.875(3)	0.817(2)	−0.0067(1)	−0.0087(1)	1.353(1)	8.674(13)
4F2 1	5F1 48	4391.312885(4)	$2.6733(8) \times 10^{-21}$	0.0644(1)	0.0808(1)	0.859(3)	0.802(2)	−0.005(1)	−0.0082(1)	2.406(1)	2.882(13)
4A1 1	4A2 12	4339.480862(3)	$2.7357(8) \times 10^{-21}$	0.0661(1)	0.0823(1)	0.886(2)	0.810(3)	−0.007(1)	−0.0083(1)	-0.731(1)	8.767(18)
3F2 1	4F1 38	4380.145085(3)	$2.8141(7) \times 10^{-21}$	0.0653(1)	0.0818(1)	0.866(2)	0.802(4)	−0.006(1)	−0.0082(1)	3.651(1)	5.344(17)
5F2 1	6F1 56	4407.883711(4)	$2.8764(10) \times 10^{-21}$	0.0631(1)	0.0806(1)	0.855(3)	0.843(3)	−0.0077(2)	−0.0095(2)	1.363(2)	9.08(20)
6A1 1	7A2 23	4415.544438(3)	$2.9207(8) \times 10^{-21}$	0.0637(1)	0.0784(1)	0.859(2)	0.817(2)	−0.0038(1)	−0.0075(1)	4.576(1)	2.928(10)
4F1 1	5F2 46	4394.310813(3)	$3.1317(9) \times 10^{-21}$	0.0658(1)	0.0823(1)	0.868(2)	0.811(2)	−0.007(1)	−0.0096(1)	-1.427(1)	8.652(14)
6A1 1	6A2 16	4316.616458(4)	$3.2830(15) \times 10^{-21}$	0.0654(1)	0.0801(1)	0.852(2)	0.834(3)	−0.0059(1)	−0.0077(1)	3.867(1)	6.633(12)
6A2 1	7A1 21	4421.401434(4)	$3.7697(13) \times 10^{-21}$	0.0578(1)	0.0794(1)	0.874(3)	0.792(2)	−0.0086(1)	−0.0116(2)	0.066(1)	11.576(21)
4A1 1	5A2 17	4394.744960(3)	$3.9918(10) \times 10^{-21}$	0.0639(1)	0.0803(1)	0.864(2)	0.800(2)	−0.0064(1)	−0.0093(1)	6.009(1)	5.259(14)
0A1 1	1A2 5	4333.670822(3)	$4.2193(8) \times 10^{-21}$	0.0605(1)	0.0804(1)	0.801(2)	0.765(2)	−0.0065(1)	−0.0109(1)	3.501(1)	9.123(15)
3A2 1	3A1 8	4315.685886(4)	$5.3329(14) \times 10^{-21}$	0.0641(1)	0.0825(1)	0.877(2)	0.791(4)	−0.0067(1)	−0.0093(2)	3.425(1)	6.997(29)

A.2 The copyright permissions

This section includes the copyright permissions from different journals used in the thesis.

Printable License.pdf

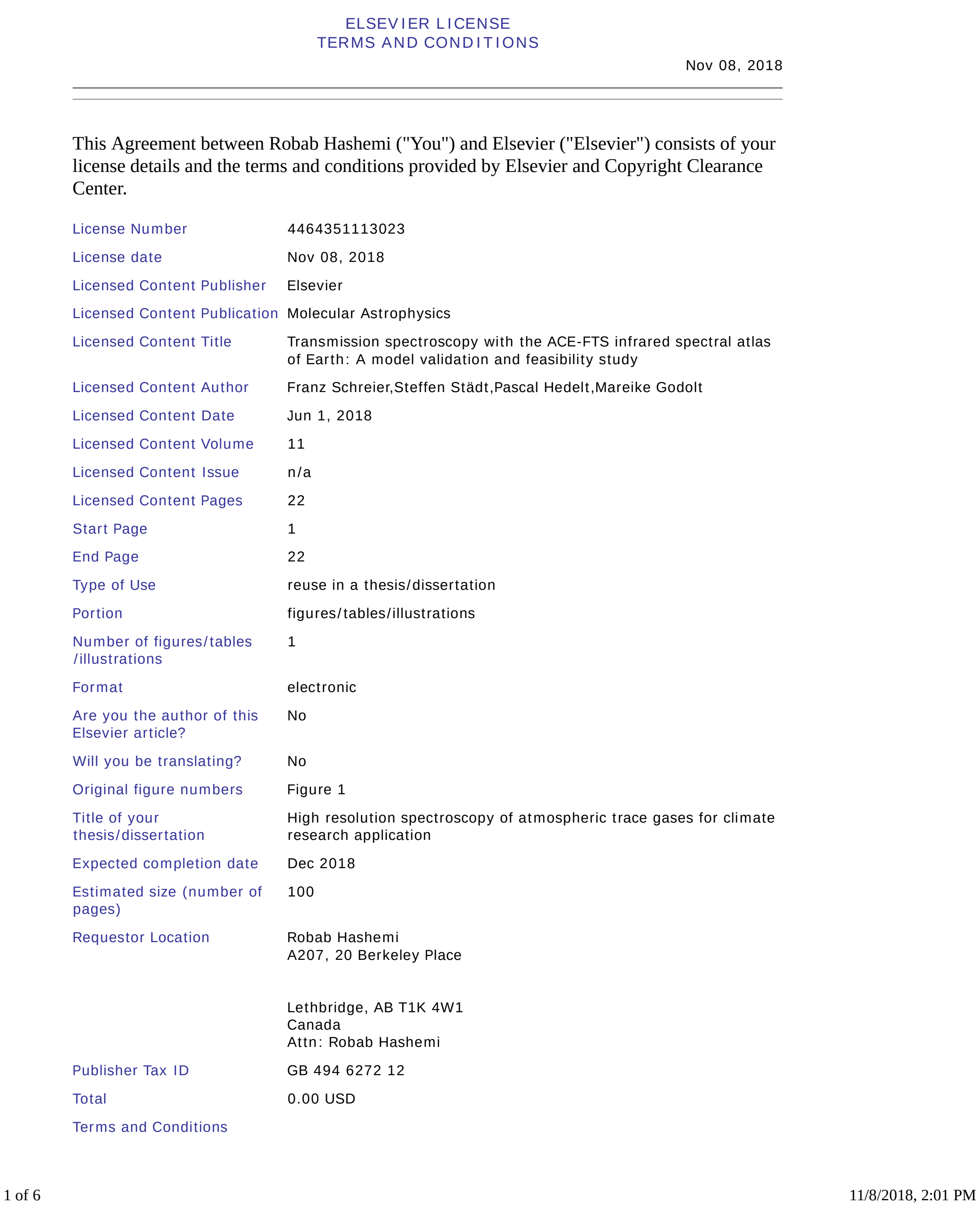

ELSEVIER LICENSE
TERMS AND CONDITIONS

Nov 08, 2018

This Agreement between Robab Hashemi ("You") and Elsevier ("Elsevier") consists of your license details and the terms and conditions provided by Elsevier and Copyright Clearance Center.

License Number	4464351113023
License date	Nov 08, 2018
Licensed Content Publisher	Elsevier
Licensed Content Publication	Molecular Astrophysics
Licensed Content Title	Transmission spectroscopy with the ACE-FTS infrared spectral atlas of Earth: A model validation and feasibility study
Licensed Content Author	Franz Schreier,Steffen Städt,Pascal Hedelt,Mareike Godolt
Licensed Content Date	Jun 1, 2018
Licensed Content Volume	11
Licensed Content Issue	n/a
Licensed Content Pages	22
Start Page	1
End Page	22
Type of Use	reuse in a thesis/dissertation
Portion	figures/tables/illustrations
Number of figures/tables /illustrations	1
Format	electronic
Are you the author of this Elsevier article?	No
Will you be translating?	No
Original figure numbers	Figure 1
Title of your thesis/dissertation	High resolution spectroscopy of atmospheric trace gases for climate research application
Expected completion date	Dec 2018
Estimated size (number of pages)	100
Requestor Location	Robab Hashemi A207, 20 Berkeley Place Lethbridge, AB T1K 4W1 Canada Attn: Robab Hashemi
Publisher Tax ID	GB 494 6272 12
Total	0.00 USD
Terms and Conditions	

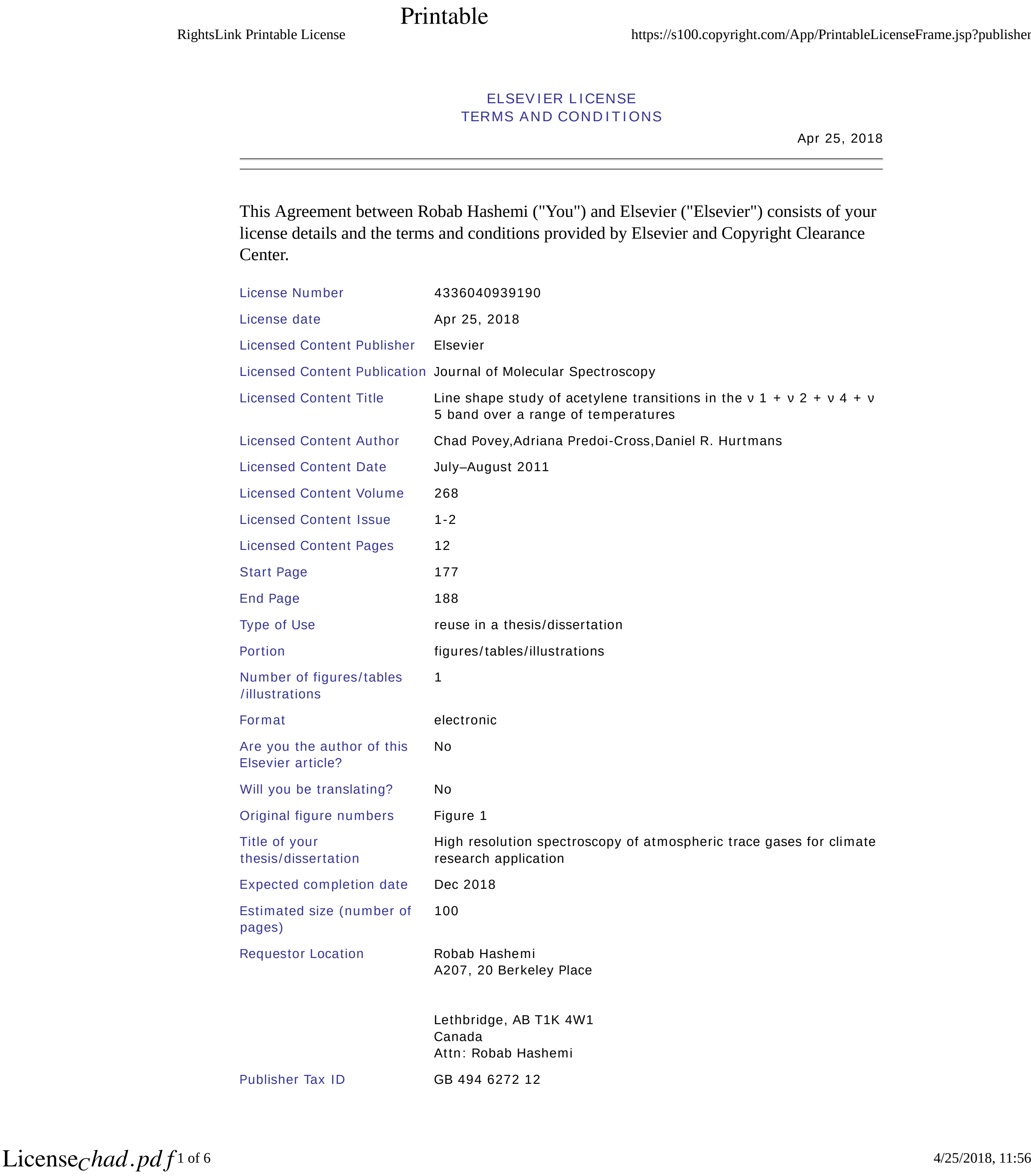

Printable

RightsLink Printable License https://s100.copyright.com/App/PrintableLicenseFrame.jsp?publisher

ELSEVIER LICENSE
TERMS AND CONDITIONS

Apr 25, 2018

This Agreement between Robab Hashemi ("You") and Elsevier ("Elsevier") consists of your license details and the terms and conditions provided by Elsevier and Copyright Clearance Center.

License Number	4336040939190
License date	Apr 25, 2018
Licensed Content Publisher	Elsevier
Licensed Content Publication	Journal of Molecular Spectroscopy
Licensed Content Title	Line shape study of acetylene transitions in the ν 1 + ν 2 + ν 4 + ν 5 band over a range of temperatures
Licensed Content Author	Chad Povey,Adriana Predoi-Cross,Daniel R. Hurtmans
Licensed Content Date	July–August 2011
Licensed Content Volume	268
Licensed Content Issue	1-2
Licensed Content Pages	12
Start Page	177
End Page	188
Type of Use	reuse in a thesis/dissertation
Portion	figures/tables/illustrations
Number of figures/tables /illustrations	1
Format	electronic
Are you the author of this Elsevier article?	No
Will you be translating?	No
Original figure numbers	Figure 1
Title of your thesis/dissertation	High resolution spectroscopy of atmospheric trace gases for climate research application
Expected completion date	Dec 2018
Estimated size (number of pages)	100
Requestor Location	Robab Hashemi A207, 20 Berkeley Place Lethbridge, AB T1K 4W1 Canada Attn: Robab Hashemi
Publisher Tax ID	GB 494 6272 12

Licensechad.pdf 1 of 6 4/25/2018, 11:56

Printable

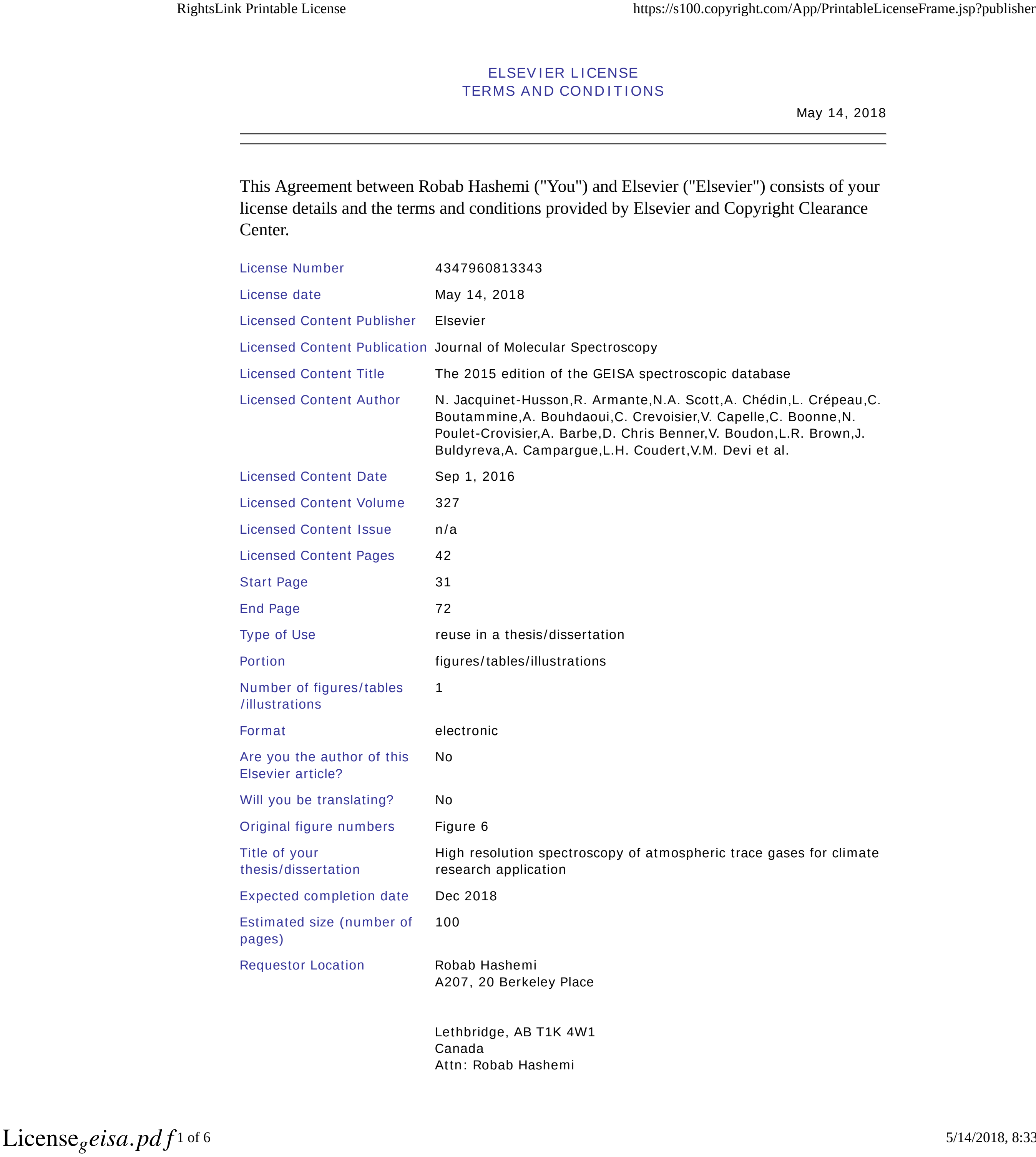

RightsLink Printable License https://s100.copyright.com/App/PrintableLicenseFrame.jsp?publisher

ELSEVIER LICENSE
TERMS AND CONDITIONS

May 14, 2018

This Agreement between Robab Hashemi ("You") and Elsevier ("Elsevier") consists of your license details and the terms and conditions provided by Elsevier and Copyright Clearance Center.

License Number	4347960813343
License date	May 14, 2018
Licensed Content Publisher	Elsevier
Licensed Content Publication	Journal of Molecular Spectroscopy
Licensed Content Title	The 2015 edition of the GEISA spectroscopic database
Licensed Content Author	N. Jacquinet-Husson,R. Armante,N.A. Scott,A. Chédin,L. Crépeau,C. Boutammine,A. Bouhdaoui,C. Crevoisier,V. Capelle,C. Boonne,N. Poulet-Crovisier,A. Barbe,D. Chris Benner,V. Boudon,L.R. Brown,J. Buldyreva,A. Campargue,L.H. Coudert,V.M. Devi et al.
Licensed Content Date	Sep 1, 2016
Licensed Content Volume	327
Licensed Content Issue	n/a
Licensed Content Pages	42
Start Page	31
End Page	72
Type of Use	reuse in a thesis/dissertation
Portion	figures/tables/illustrations
Number of figures/tables /illustrations	1
Format	electronic
Are you the author of this Elsevier article?	No
Will you be translating?	No
Original figure numbers	Figure 6
Title of your thesis/dissertation	High resolution spectroscopy of atmospheric trace gases for climate research application
Expected completion date	Dec 2018
Estimated size (number of pages)	100
Requestor Location	Robab Hashemi A207, 20 Berkeley Place Lethbridge, AB T1K 4W1 Canada Attn: Robab Hashemi

License$_geisa.pdf$ 1 of 6 5/14/2018, 8:33

- Permission to use my paper in my thesis.pdf

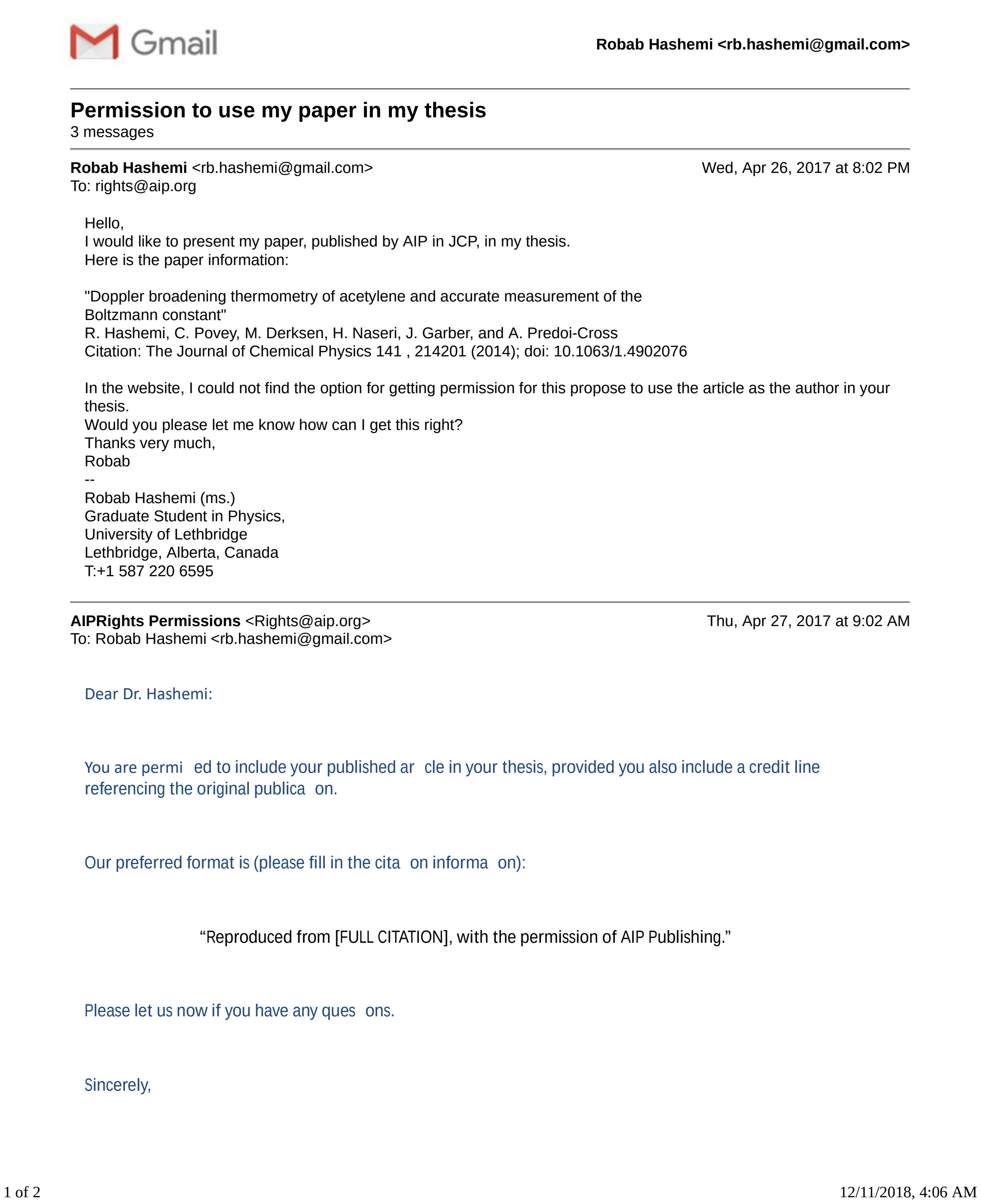

Gmail **Robab Hashemi <rb.hashemi@gmail.com>**

Permission to use my paper in my thesis
3 messages

Robab Hashemi <rb.hashemi@gmail.com> Wed, Apr 26, 2017 at 8:02 PM
To: rights@aip.org

Hello,
I would like to present my paper, published by AIP in JCP, in my thesis.
Here is the paper information:

"Doppler broadening thermometry of acetylene and accurate measurement of the Boltzmann constant"
R. Hashemi, C. Povey, M. Derksen, H. Naseri, J. Garber, and A. Predoi-Cross
Citation: The Journal of Chemical Physics 141 , 214201 (2014); doi: 10.1063/1.4902076

In the website, I could not find the option for getting permission for this propose to use the article as the author in your thesis.
Would you please let me know how can I get this right?
Thanks very much,
Robab
--
Robab Hashemi (ms.)
Graduate Student in Physics,
University of Lethbridge
Lethbridge, Alberta, Canada
T:+1 587 220 6595

AIPRights Permissions <Rights@aip.org> Thu, Apr 27, 2017 at 9:02 AM
To: Robab Hashemi <rb.hashemi@gmail.com>

Dear Dr. Hashemi:

You are permitted to include your published article in your thesis, provided you also include a credit line referencing the original publication.

Our preferred format is (please fill in the citation information):

“Reproduced from [FULL CITATION], with the permission of AIP Publishing.”

Please let us now if you have any questions.

Sincerely,

Printable

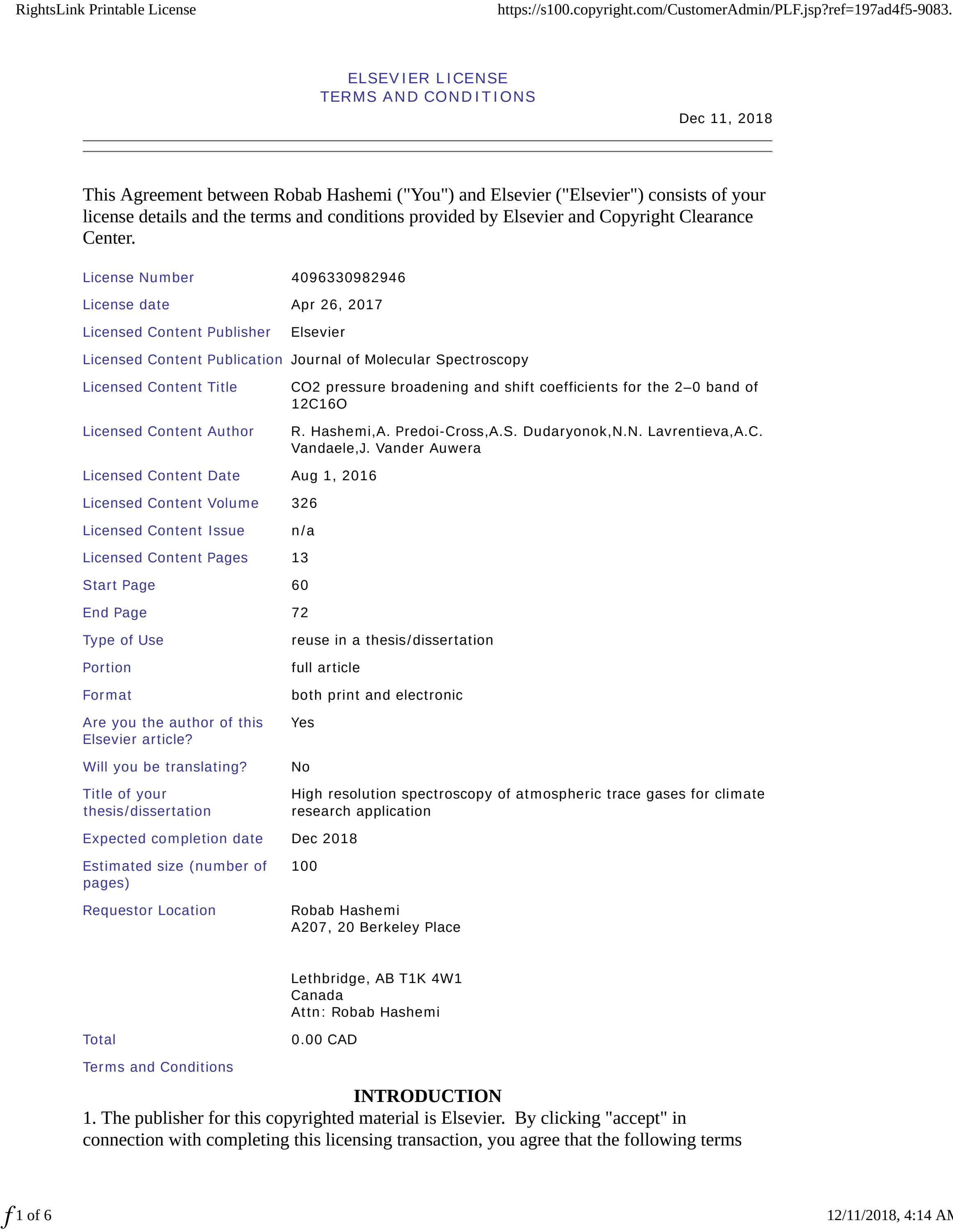

RightsLink Printable License https://s100.copyright.com/CustomerAdmin/PLF.jsp?ref=197ad4f5-9083.

ELSEVIER LICENSE
TERMS AND CONDITIONS

Dec 11, 2018

This Agreement between Robab Hashemi ("You") and Elsevier ("Elsevier") consists of your license details and the terms and conditions provided by Elsevier and Copyright Clearance Center.

License Number	4096330982946
License date	Apr 26, 2017
Licensed Content Publisher	Elsevier
Licensed Content Publication	Journal of Molecular Spectroscopy
Licensed Content Title	CO2 pressure broadening and shift coefficients for the 2–0 band of 12C16O
Licensed Content Author	R. Hashemi,A. Predoi-Cross,A.S. Dudaryonok,N.N. Lavrentieva,A.C. Vandaele,J. Vander Auwera
Licensed Content Date	Aug 1, 2016
Licensed Content Volume	326
Licensed Content Issue	n/a
Licensed Content Pages	13
Start Page	60
End Page	72
Type of Use	reuse in a thesis/dissertation
Portion	full article
Format	both print and electronic
Are you the author of this Elsevier article?	Yes
Will you be translating?	No
Title of your thesis/dissertation	High resolution spectroscopy of atmospheric trace gases for climate research application
Expected completion date	Dec 2018
Estimated size (number of pages)	100
Requestor Location	Robab Hashemi A207, 20 Berkeley Place Lethbridge, AB T1K 4W1 Canada Attn: Robab Hashemi
Total	0.00 CAD
Terms and Conditions	

INTRODUCTION

1. The publisher for this copyrighted material is Elsevier. By clicking "accept" in connection with completing this licensing transaction, you agree that the following terms

License$_CO.pdf$ 1 of 6 12/11/2018, 4:14 AM

Printable License.pdf

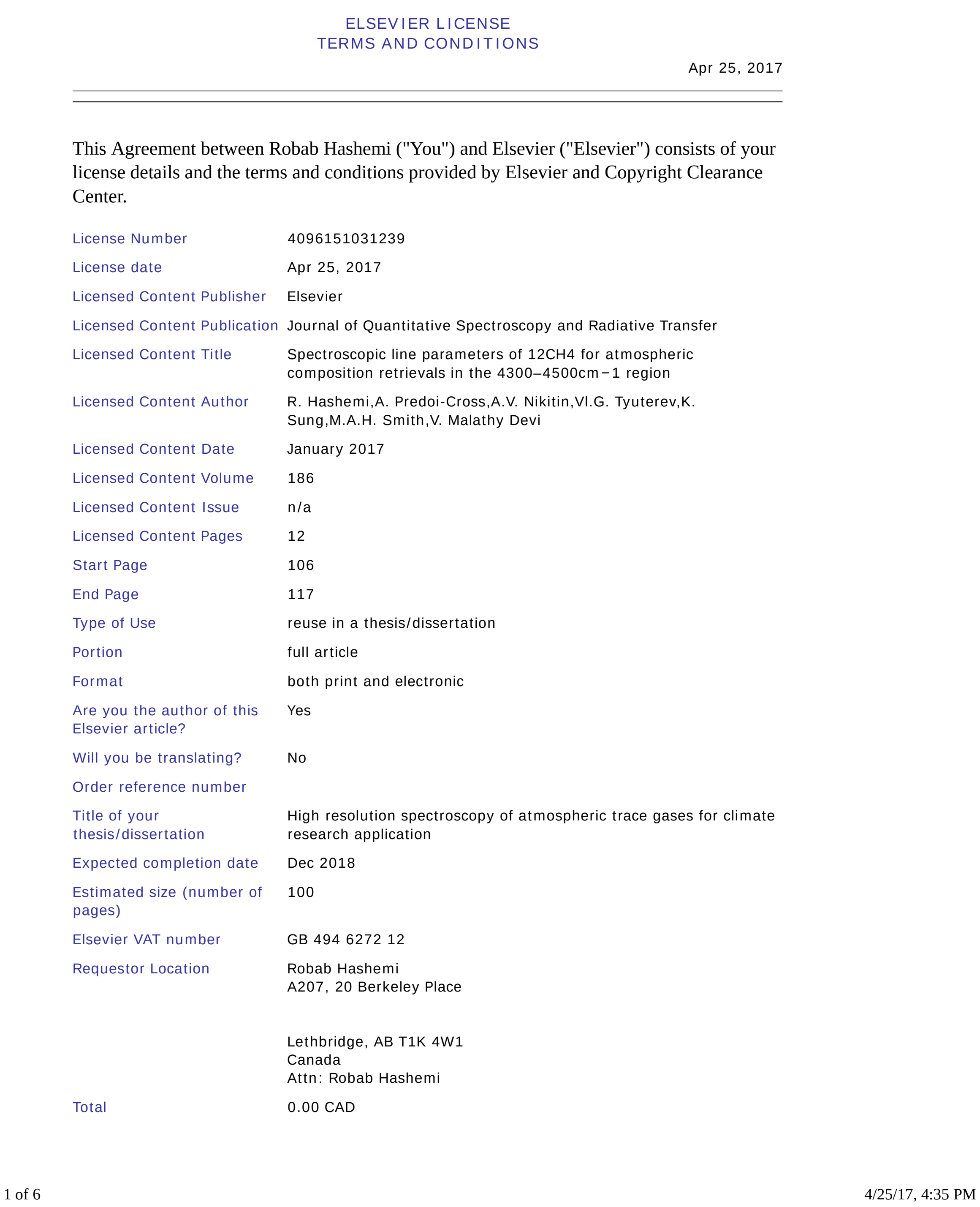

RightsLink Printable License https://s100.copyright.com/App/PrintableLicenseFrame.jsp?publisherID...

ELSEVIER LICENSE
TERMS AND CONDITIONS

Apr 25, 2017

This Agreement between Robab Hashemi ("You") and Elsevier ("Elsevier") consists of your license details and the terms and conditions provided by Elsevier and Copyright Clearance Center.

License Number	4096151031239
License date	Apr 25, 2017
Licensed Content Publisher	Elsevier
Licensed Content Publication	Journal of Quantitative Spectroscopy and Radiative Transfer
Licensed Content Title	Spectroscopic line parameters of 12CH4 for atmospheric composition retrievals in the 4300–4500cm−1 region
Licensed Content Author	R. Hashemi,A. Predoi-Cross,A.V. Nikitin,Vl.G. Tyuterev,K. Sung,M.A.H. Smith,V. Malathy Devi
Licensed Content Date	January 2017
Licensed Content Volume	186
Licensed Content Issue	n/a
Licensed Content Pages	12
Start Page	106
End Page	117
Type of Use	reuse in a thesis/dissertation
Portion	full article
Format	both print and electronic
Are you the author of this Elsevier article?	Yes
Will you be translating?	No
Order reference number	
Title of your thesis/dissertation	High resolution spectroscopy of atmospheric trace gases for climate research application
Expected completion date	Dec 2018
Estimated size (number of pages)	100
Elsevier VAT number	GB 494 6272 12
Requestor Location	Robab Hashemi A207, 20 Berkeley Place Lethbridge, AB T1K 4W1 Canada Attn: Robab Hashemi
Total	0.00 CAD

1 of 6 4/25/17, 4:35 PM